Development of Probes for Assessment of Ion Heat Transport and Sheath Heat Flux in the Boundary of the Alcator C-Mod Tokamak

by

Daniel Frederic Brunner

B.S. Engineering Physics (2008)
Rose-Hulman Institute of Technology

Submitted to the Department of Nuclear Science and Engineering
in partial fulfillment of the requirements for the degree of

Doctor of Philosophy in Applied Plasma Physics

at the

MASSACHUSETTS INSTITUTE OF TECHNOLOGY

September 2013

Author .....
Department of Nuclear Science and Engineering
August 8, 2013

Certified by .....
Brian L. LaBombard
Senior Research Scientist, Plasma Science and Fusion Center
Thesis Supervisor

Certified by .....
Dennis G. Whyte
Professor, Department of Nuclear Science and Engineering
Thesis Reader

Accepted by .....
Mujid S. Kazimi
TEPCO Professor of Nuclear Engineering
Chair, Department Committee on Graduate Students

Development of Probes for Assessment of Ion Heat Transport and Sheath Heat Flux in the Boundary of the Alcator C-Mod Tokamak

by

Daniel Frederic Brunner

Submitted to the Department of Nuclear Science and Engineering
on August 8, 2013, in partial fulfillment of the
requirements for the degree of
Doctor of Philosophy in Applied Plasma Physics

Abstract

Progress towards a viable fusion reactor will require comprehensive understanding of boundary plasma physics. Knowledge in this area has been growing, yet there are critical gaps. Measurements of the sheath heat flux transmission coefficient—a fundamental physical quantity whose theoretical value is ~ 7—have varied from 2 to 20. Values below 5 are physically impossible and have challenged the understanding of this very basic theory. In addition, measurements of ion temperature are sparse and ion energy transport is poorly understood. To this end a set of new diagnostics, including a surface thermocouple, ion sensitive probe, and retarding field analyzer, have been developed that can tolerate the extreme heat fluxes in the Alcator C-Mod boundary plasma. These probes are used to asses issues of heat flux and ion energy transport.

Systematic studies with these new tools reveal the following: A comparison of surface thermocouples and Langmuir probes confirms standard sheath heat flux theory in a tokamak for the first time. The measurement of unphysically low sheath heat flux transmission coefficients and an anomalous increase in measured divertor pressure by Langmuir probes, which is also unphysical, are found the be linked. Plasma-neutral simulations indicate that these artifacts are due to the Langmuir probe bias modifying the local plasma. Important space charge limits to measurements with ion sensitive probes are found experimentally and explored in depth with a 1D kinetic simulation. These results clarify the plasma conditions under which an ion sensitive probe may be used to measure ion temperature and/or plasma potential. The retarding field analyzer is demonstrated to be a viable ion temperature diagnostic up to the last closed flux surface in C-Mod. A 1D fluid simulations is built to interpret edge ion heat transport. At high collisionality—where the fluid approximations are valid: the simulation reproduces the measured edge ion-to-electron temperature ratio (~ 2). However, at low collisionality—where fluid approximation is not valid–the simulation is not able to reproduce the experimental temperature ratio (~ 4). The addition of kinetic heat flux limiters can bring the simulated ratio into agreement with measurements. The value of heat flux limiter is found to be consistent with that expected from kinetic theory.

Thesis Supervisor: Brian L. LaBombard
Senior Research Scientist, Plasma Science and Fusion Center

Thesis Reader: Dennis G. Whyte
Professor, Department of Nuclear Science and Engineering

Dedicated to the all of the teachers in my life.
From my formal education in Rossman Elementary School,
Central Middle School, Hartford Union High School, Rose-Hulman
Institute of Technology, and Massachusetts Institute of Technology
to everyone who taught me something out in the real world.
I am who I am today thanks to you.
For that, I am forever grateful.

ACKNOWLEDGMENTS

Of course, this work was not possible without the help of many others. Besides all of the giants of fusion and plasma physics whose shoulders I stand on today, I must thank and acknowledge the following for their contributions to this thesis:

ALCATOR C-MOD

Thanks to all of the scientists, engineers, students, technicians, and support staff. Without your hard work, there would have been no plasma at which to poke my probes. I am grateful to have you all for colleagues and wish you the best wherever the wind takes you from here.

HEAT FLUX DIAGNOSTICS

Brian LaBombard, along with some help from Josh Payne, designed the divertor module containing the heat flux diagnostics before I came to MIT. Although I was in charge of analysis and maintenance of the system, Brian deserves the credit for creating it. Additionally, I must express my gratitude to Ron Rosati, his demonstrated excellent skill in preparing the thermocouple cabling as well as turning the slow thermocouples into unsheathed, fast-response thermocouples.

LANGMUIR PROBES

Brian LaBombard is *the* Langmuir probe guru. Having 30 years of experience with them, it was a privilege to work with Brian. All of the Langmuir probe data and analysis in this thesis were due to his work.

CXRS DATA

Michael Churchill, Christian Theiler, and Bruce Lipchultz are in charge of the CXRS system on C-Mod. The data from it was originally only supposed to be the tie breaker between my ISP and RFA probes. But, when C-Mod's life got cut short, the ISP turned out the be space charge limited, and the RFA didn't have nearly enough data, I had to rely on the CXRS data for an important part of this thesis.

THOMSON DATA

Jerry Hughes and John Walk were kind enough to keep the Thomson system up and running as well as bless the data; providing a complement to the probe data where no probe dare to go.

GIRD BIAS BOARDS

The micro-Amp currents measured with the RFA would not

have been possible without the Grid Bias boards. Brian's experience with electrical circuits and instrumentation shined through in their design and Bruce Wood's diligence made them a reality.

QFLUX_1D
: Brian and Josh Payne wrote the 1D finite element software used for much of the heat analysis in this thesis.

UEDGE
: Tom Rognlien and the other architects of UEDGE have created an impressive piece of code and I must acknowledge their efforts. Maxim Umansky, with the guidance of Tom, did the "death-ray" simulations.

I am grateful to have had Brian for an advisor. His enthusiasm is endless and he was always there to help. Brian's ability to do things the right way is uncanny. Now and forever, when I run into a problem I will always think "what would Brian do?".

I thank Dennis Whyte for his careful reading of this theses and for keeping me honest. Thanks also to Ian Hutchinson for sharing his seemingly endless expertise on plasma and taking the time to read over my work. Finally I am gracious for Anne White rounding out my thesis committee. I am honored for having all four of you on my committee.

In addition to those who gave their scientific support to this thesis. I must thank everyone I have encountered around Boston; I hope that our paths may cross again. Thanks to all of the friends that I made at the Plasma Science and Fusion Center. Thanks to the crazy group of roommates I had at 47 Mecham the first two years here. Thanks to Koroush for being the perfect roommate for the final three years: almost never around, clean, and always paying the rent on time. Thanks to Nora, I don't know how I would have made it through quals without you. Thanks to Michelle, I appreciate your guidance and support. Thanks to my family–Mom, Dad, Angie, Becki, Beth, and Sarah–for their love and ability to always keep things interesting. I'm blessed to have had wonderful grandparents; they were very proud to see me get into MIT, I wish they were still around to see me get out.

Finally, thanks to Bob, Geoff, and Mike. Five years locked in the same room. You three are the closest to brothers I have ever had.

CONTENTS

LIST OF FIGURES

LIST OF TABLES

1 INTRODUCTION

1.1 WORLD ENERGY USE AND QUALITY OF LIFE

The world is ever changing. As technology and society develop, billions of people are rising out of agrarian and nomadic ways of life into a more "first-world" way of life. High standards of quality of life, as measured by the Human Development Index [15], are correlated with high power use: fig. 1. As the people in low-HDI countries rise in HDI, so will their energy consumption.

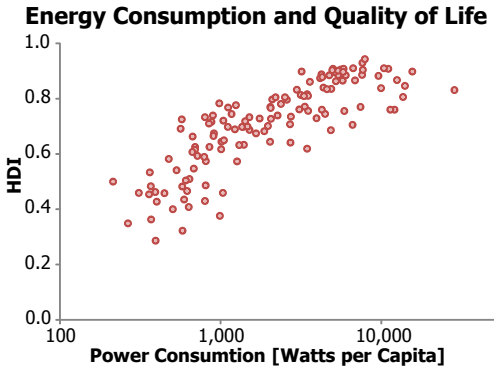

Figure 1: Quality of life (HDI) and power use go hand-in-hand.

Additionally, all but the most pessimistic studies indicate that the world population will grow for the coming century, fig. 2. Depending on the situation, it may increase by 50 % to 100 %. Great increases in energy demand will come with the increases in population and with people rising out of the third-world. BP, one of the world's largest energy suppliers, predicts that the world energy consumption will double in the next 20 years.

Energy production will need to increase to meet up with these growing demands. Although renewables such as solar and wind are appealing to the wider public, they are unlikely to be the base power of the future. Renewables are typically intermittent (requiring some sort of not-yet-existing storage mechanism to provide steady power) and their sources are far away from the demand (requiring long-distance transmission). Fossil fuels (coal, oil, gas...) are reliable for supplying base-load power on demand and there is enough fuel (especially coal) to last through the next century. Yet there is the concern of the health consequences (to both humans as well as the climate) of releasing combustion products into the atmosphere (CO_2, NO_x, particulates...).

Nuclear fission reactors also provide solid, base-load power. Conventional fuel strategies could last through the next century and more exotic strategies could extend fission's production capabilities to thousands of years. Fission's largest barrier is public perception: they are afraid of nuclear, despite it historically being the safest power source per Joule generated [10]. No one wants a power plant near them for fear of a meltdown. The US cannot even put a waste depository in one of its most remote areas. Despite the aging reactors at Fukashima doing amazingly well through one of the worst earthquakes and

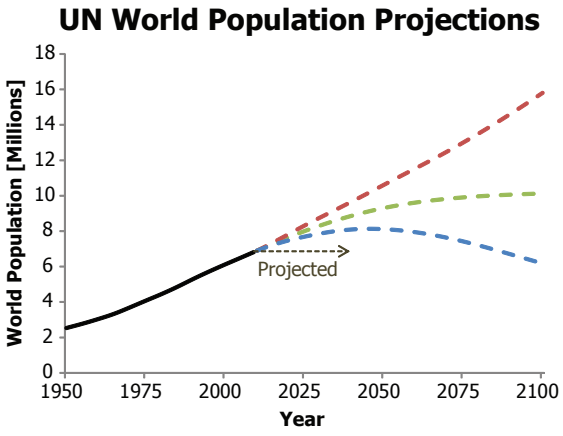

Figure 2: High, medium, and low projections of world population, spread is largely due to uncertainty in future fertility rates [19].

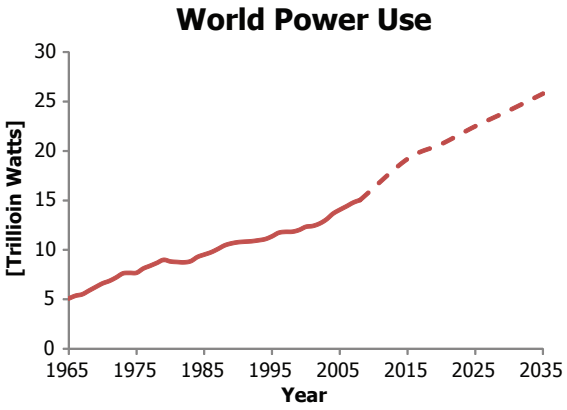

Figure 3: BP projects that world power consumption will double in the next 20 years [12, 13].

tsunamis in recorded history, the accident hurt fission's near-term future. Countries are scaling back, with Germany even proposing to close all of its facilities by the early 2020's.

Only if there were a power source that could supply base-load power with no atmospheric emission, no long-lived radioactive waste, no chance of meltdown, and a nearly inexhaustible fuel supply... ●

1.2 FUSION ENERGY

Fusion, like fission, is the transmutation (alchemy!) of nuclei into new ones. Generally, heavy elements may be fissioned, turning mass into energy; light elements may be joined or fused, also turning mass into energy. Iron is the most energetically stable element. Fission has the distinct advantage over fusion of occurring at thermal temperatures. Some of the heavier elements fission on their own, releasing neutrons. These neutrons will thermalize to near room temperature and will go on to cause other atoms to fission, releasing energy and more neutrons. And on goes the chain reaction.

Fusion, on the other hand, requires two nuclei to get close enough together such that the strong nuclear force overcomes the Coulomb repulsion of the positively charge nuclei. This needs nuclei that are so energetic (a thermal populations of ~ 10 keV for D-T) that any light element used to release energy from fusion is fully ionized: a plasma. This fact provides a difficulty but also an opportunity: a plasma this hot is not compatible with a material container, but the charge particles can be contained by a magnetic field.

Since the 1950's there has been a plethora of configurations of magnetic fields to confine plasmas. Confining a plasma with magnetic fields has been compared to holding onto Jello with rubber bands (a statement often attributed to Richard Feynman, but more likely due

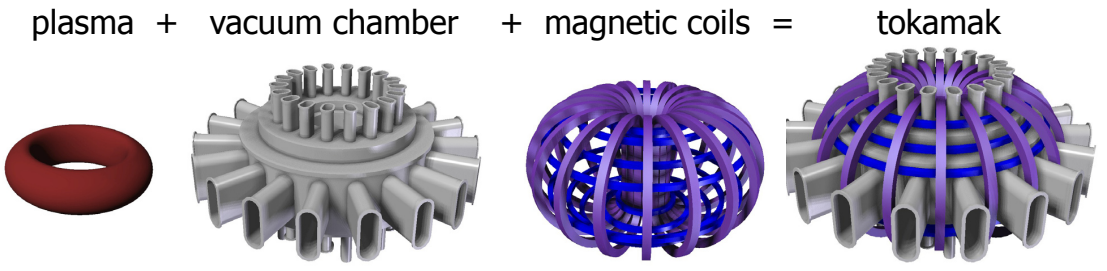

Vulcan Design Team, FED 2012.

Figure 4: A tokamak is simply a toroidal plasma isolated from the atmosphere with a vacuum chamber and held in place with the magnetic field from coils. Figure modified from [21].

to Edward Teller [22]). Jeffrey Freidberg, a leader in magnetohydrodynamics (the study of an electrically charged fluid) applied to fusion plasmas, on magnetic configurations: "Cleverness is mandatory, not an option" [11].

Advantages of fusion over fission include:

- Fuel supply is light elements (D and Li) which are so abundant as to be effectively unlimited
- No chance of meltdown due to the requirement for stellar temperatures and the lack of a chain reaction
- Relatively benign waste since the fuel cycle, as in stars, produces non-radioactive helium ash

The main disadvantage of fusion over fission is that its feasibility as an economical energy source is still uncertain. Even if it proves possible to build a fusion power plant that produces net energy, there remains the risk that it cannot compete with less expensive forms of energy.

1.3 MAGNETIC FUSION AND THE TOKAMAK

To date, the most successful magnetic confinement device has been the tokamak: a toroidal magnetic configuration with a vertical field and current in the plasma for stability and confinement, fig. 4. The toroidal configuration is necessary because the end losses of a linear system are too large. In a purely toroidal configuration ∇B drifts will cause charge separation, a vertical electric field, and outward motion of the plasma from $\vec{E} \times \vec{B}$ drift. The rotational transform of the magnetic field cancels the ∇B drift: while in the top half of the torus a given particle will drift in one direction (up or down) and while in the bottom half it will drift in the other direction.

Decades of research have gone to understanding and improving core plasma confinement and reducing cross field transport. The cross field transport from the core to the boundary are intimately linked;

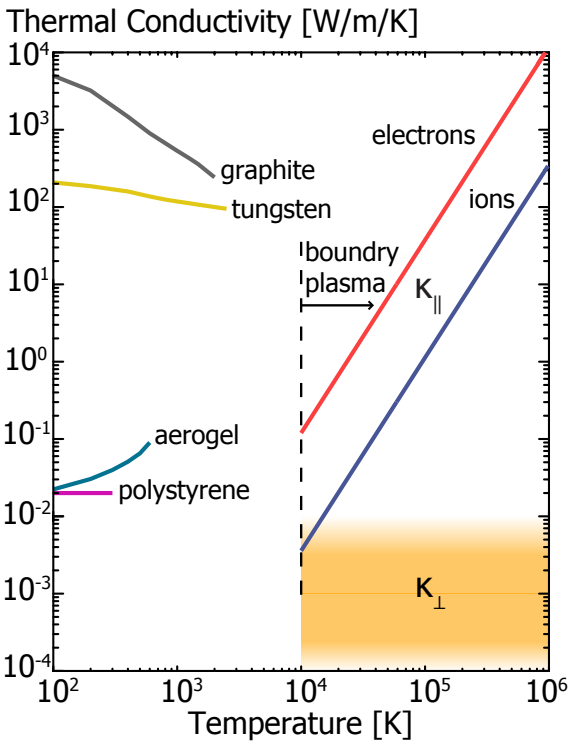

Figure 5: Thermal conductivity along ($\kappa_{||}$) and across ($\kappa_\perp$) the magnetic field typical of a fusion boundary plasma [23] along with that of common materials (graphite, tungsten, and polystyrene data from Ref. [14], aerogel data from Ref. [1]). The fusion boundary plasma is one of the most anisotropic man made materials.

the excellent cross field confinement extends to the boundary. Yet the plasma is an excellent conductor along field lines due to the absence of Lorentz force parallel to the magnetic field. In fact, a hot, magnetically confined plasma may be one of the most anisotropic materials ever created, fig. 5. This presents a challenging situation for the boundary plasma control. As plasma transports energy out of the core and into the boundary it prefers to exit to the material boundaries along the magnetic field, with little spreading across it. There is no consensus on how to predict what the parallel heat flux in a reactor will be (there are many opinions...), let alone first-principles calculations. From current measurements, our best estimates put it on order $1\,\mathrm{GW\,m^{-2}}$! One of the greatest challenges to getting a working reactor will be understanding and controlling heat transport in the boundary.

1.4 FUTURE OF FUSION RESEARCH

The future of fusion research is to push to steady-state operation. To date all experiments operating at or near reactor-level plasma parameters have been pulsed. This is due to the easy operation of a transformer to drive current and the difficulties of driving current with RF waves at reactor-level parameters. Pulse lengths were near steady-state on core plasma time scales and thus many of the reactor-relevant

core processes could be studied. The remaining big question for core plasmas on the path to a reactor is what happens when the plasma is self-heated by its own fusion products, i. e., alpha-heated; which ITER hopes to answer by attempting to achieve 500 MW of fusion power with only 50 MW of external heating [18].

Steady-state operation will push the focus to the boundary, where the plasma meets the wall. Not only will the unabated heat flux be beyond the limits of power exhaust engineering, but transient events may exceed it even more. With the current understanding of boundary physics a reactor will have gross erosion of tons of material per year. It is critical to understand the boundary plasma and how it self-organizes with the wall. There also remains questions on what effects RF waves have on the boundary plasma and vice-versa. Experiments on C-Mod consistently show that the state of the boundary plasma is intimately linked to the operation of both RF plasma heating and current drive [2, 20].

1.5 GOALS AND OUTLINE OF THESIS

A full description of the fundamental physics controlling the transport of particles and energy in the boundary of a tokamak remains unknown. Current projections of heat flux and erosion to a reactor-scale machine are highly uncertain. This is unacceptable, for either of these two parameters could limit the viability of fusion energy. Although explicitly solving these issues is beyond the scope of this thesis, there remains many areas to build towards solutions which are ripe to explore. The main goal of this thesis is understanding of two basic physics issues:

1. **Sheath Heat Flux**—The theory describing the heat flux out of the plasma through the electrostatic sheath to the first wall is relatively simple. Yet measurements confirming the theory have been elusive in tokamaks. There has been an order of magnitude variation in the sheath heat flux transmission coefficient [17]. Such a large degree of uncertainty in this key parameter is unacceptable.

2. **Ion Heat Transport**—The physics of ion heat transport in the boundary plasma remains largely unexplored. Probes able to measure the ion temperature can be challenging both to make and interpret. Thus measurements of edge ion temperature are rare. In addition, there has been no systematic comparison of edge ion temperature with simulations.

To explore these issues requires development and verification of new diagnostics capable of surviving the extreme heat flux in the boundary of Alcator C-Mod.

This thesis continues in chapter 2 with an overview of edge physics, including kinetic and fluid descriptions of edge transport. Then the physics of the plasma sheath, including the sheath heat flux transmission coefficient. Histories and descriptions of measurement techniques are then given, including the Langmuir probe, ion sensitive probe, retarding field analyzer, charge exchange recombination spectroscopy, and thermocouples.

An extensive system of thermal diagnostics—including Langmuir probes, surface thermocouples, and calorimeters—was installed in the C-Mod divertor for the 2010 DOE Joint Research Target to characterize the heat flux footprint [16]. Although that system was developed by LaBombard et al. before the inception of this thesis, a significant portion of this thesis focused on implementation and improvement of the diagnostics, see chapters 3 and 4 as well as the papers [3, 8]. The surface thermocouples proved to be extremely useful both confirming sheath heat flux theory and connecting a curious divertor over-pressure to the unphysically low values of the sheath heat flux transmission coefficient (chapter 6). A new theory implicating the divertor Langmuir probe causing the over-pressure is presented, see section 6.2 or [9]. The theory is confirmed by our collaborators using a 2D plasma-neutral fluid code, UEDGE.

Two new probes were developed to explore ion heat transport, a Retarding Field Analyzer (RFA) [7] and an Ion Sensitive Probe (ISP) [6], see chapter 3. Their geometry was optimized using 3D finite element simulations of the probes scanning through the boundary plasma. The RFA in particular is a large improvement over previous designs. The entrance slit an order of magnitude closer to the probe tip (1.7 mm versus 20 mm), maximizing measurement depth into the plasma.

The early closure of Alcator C-Mod forced a time constraint on development of the ion probes. Focus was given to the ISP due to its superior heat flux handling. However, it was found that the C-Mod ISP in its present configuration was space charge limited and thus unable to measure the ion temperature. This prompted an in depth investigation of space charge and ISPs, see chapter 7 and [5], which is also informative to other fusion experiments attempting to interpret ISP data ion sensitive probe data with respect to ion temperature. Through detailed study of ISP literature numerous other probes were found to collect current in excess of the 1D space charge limit. A 1D kinetic model was built to explore the I-V response to varying degrees of space charge and guide development of a probe which can operate in high density plasma.

The RFA operated exceptionally well and was able to measure electron and ion temperatures up to the last closed flux surface, i. e., over the extent of the boundary plasma (chapter 5). Although data is much more limited than the ISP. Electron temperature profiles overlaid that

from Langmuir probes and, most importantly, CXRS B^{5+} and RFA D^+ T_i profiles matched in a low collisionality plasma, where they are least likely to be coupled. This allows the CXRS impurity ion temperature data to be used as a proxy for the main ion temperature in heat transport studies.

A simple 1D model of coupled electron-ion heat conduction in the boundary was created, see chapter 8 and [4]. It was used to compare to experimental measurements of the upstream ion to electron temperature ratio. The 1D simulation was successfully benchmarked against the 2D plasma-neutral fluid code UEDGE. At the highest core density and edge collisionality the simulations matched the upstream temperature ratio ($T_i/T_e \sim 1.8$). However the lowest core density and edge collisionality, where the fluid assumption of Spitzer-Harm heat conduction is invalid, showed the limits of the fluid model. It was unable to reproduce the high (~ 4) ion to electron temperature ratio. The addition of heat flux limiters, an approximate kinetic correction, allows the simulation to reproduce the temperature ratio at low collisionality. The value which best matches the data (~ 0.2) is close to that given by comparison of kinetic and fluid simulations. ⋆

BIBLIOGRAPHY

[1] Pyrogel xt. Technical report, Aspen Aerogels, 30 Forbes Road, Building B, Northborough, MA 01532, 2012.

[2] S. G. Baek, R. R. Parker, S. Shiraiwa, G. M. Wallace, P. T. Bonoli, D. Brunner, I. C. Faust, A. E. Hubbard, B. LaBombard, and M. Porkolab. Measurements of ion cyclotron parametric decay of lower hybrid waves at the high-field side of Alcator C-Mod. *Plasma Physics and Controlled Fusion*, 55(5):052001, 2013.

[3] D. Brunner and B. LaBombard. Surface thermocouples for measurement of pulsed heat flux in the divertor of the Alcator C-Mod tokamak. *Review of Scientific Instruments*, 83(3):033501–033501, 2012.

[4] D. Brunner, B. LaBombard, R. M. Churchill, J. Hughes, B. Lipschultz, R. Ochoukov, T. D. Rognlien, C. Theiler, M. V. Umansky, J. Walk, and D. Whyte. Comparison of ion temperature measurements in the boundary of the Alcator C-Mod tokamak and implications for ion fluid heat flux limiters. *Plasma Physics and Controlled Fusion*, 55:095010, 2013.

[5] D. Brunner, B. LaBombard, R. Ochoukov, R. Sullivan, and D. G. Whyte. Space charge limits of ion sensitive probes. *submitted to Plasma Physics and Controlled Fusion*, 2013.

[6] D. Brunner, B. LaBombard, R. Ochoukov, and D. Whyte. Scanning ion sensitive probe for plasma profile measurements in the boundary of the Alcator C-Mod tokamak. *Review of Scientific Instruments*, 84:053507, 2013.

[7] D. Brunner, B. LaBombard, R. Ochoukov, and D. Whyte. Scanning retarding field analyzer for plasma profile measurements in the boundary of the Alcator C-Mod tokamak. *Review of Scientific Instruments*, 84(3):033502, 2013.

[8] D. Brunner, B. LaBombard, J. Payne, and J. L. Terry. Comparison of heat flux measurements by IR thermography and probes in the Alcator C-Mod divertor. *Journal of Nuclear Materials*, 415(1):S375–S378, 2011.

[9] D. Brunner, M. V. Umansky, B. LaBombard, and T. D. Rognlien. Divertor "death-ray" explained: An artifact of a Langmuir probe operating at negative bias in a high-recycling divertor. *Journal of Nuclear Materials*, 438:S1196–S1199, 2013.

[10] J. Conca. How deadly is your kilowatt?, June 2012.

[11] Jeffrey Freidberg. *Plasma Physics and Fusion Energy*. Cambridge University Press, 2007.

[12] B.P. Global. Statistical review of world energy 2009.

[13] H. Gruenspecht. International energy outlook 2011. *Center for Strategic and International Studies*, 2010.

[14] F. P. Incropera, A. S. Lavine, and D. P. DeWitt. *Fundamentals of heat and mass transfer*. John Wiley & Sons Incorporated, 5th edition, 2007.

[15] J. Klugman et al. Human development report 2011. *Sustainability and Equity: A Better Future for All*, 2011.

[16] B. LaBombard, J. L. Terry, J. W. Hughes, D. Brunner, J. Payne, M. L. Reinke, I. Cziegler, R. Granetz, M. Greenwald, I. H. Hutchinson, J. Irby, Y. Lin, B. Lipschultz, Y. Ma, E. S. Marmar, W. L. Rowan, N. Tsujii, G. Wallace, D. G. Whyte, S. Wolfe, S. Wukitch, G. Wurden, and the Alcator C-Mod Team. Scaling of the power exhaust channel in Alcator C-Mod. *Physics of Plasmas*, 18:056104, 2011.

[17] J. Marki, R. A. Pitts, T. Eich, A. Herrmann, J. Horacek, F. Sanchez, and G. Veres. Sheath heat transmission factors on TCV. *Journal of Nuclear Materials*, 363-365:382 – 388, 2007.

[18] V. Mukhovatov, M. Shimada, A. N. Chudnovskiy, A. E. Costley, Y. Gribov, G. Federici, O. Kardaun, A. S. Kukushkin, A. Polevoi, V. D. Pustovitov, Y. Shimomura, T. Sugie, M. Sugihara, and G. Vayakis. Overview of physics basis for ITER. *Plasma Physics and Controlled Fusion*, 45(12A):A235, 2003.

[19] United Nations. *World Population Prospects: The 2010 Revision. Comprehensive Tables*, volume 1. United Nations, 2010.

[20] R. Ochoukov, D. G. Whyte, D. Brunner, I. Cziegler, B. LaBombard, B. Lipschultz, J. Myra, J. Terry, and S. Wukitch. Investigation of RF-enhanced plasma potentials on Alcator C-Mod. *Journal of Nuclear Materials*, 2013.

[21] G. M. Olynyk, Z. S. Hartwig, D. G. Whyte, H. S. Barnard, P. T. Bonoli, L. Bromberg, M. L. Garrett, C. B. Haakonsen, R. T. Mumgaard, and Y. A. Podpaly. Vulcan: A steady-state tokamak for reactor-relevant plasma–material interaction science. *Fusion Engineering and Design*, 87(3):224–233, 2012.

[22] United States. Congress. Joint Committee on Reconstruction. *Hearings*, volume 8. U.S. Government Printing Office, 1960.

[23] P. C. Stangeby. *The Plasma Boundary of Magnetic Fusion Devices*. IoP Publishing, 2000.

2

PHYSICS OF THE BOUNDARY PLASMA AND PROBE MEASUREMENTS

The physics understanding of the boundary plasma has been advanced largely by the use of probes [65, 139]. A probe is an object which is physically inserted into the plasma. Plasma characteristics are determined by the response to collected current due to externally applied voltage. They can provide localized (both in time and space) measurements of many quantities of interest (density, temperature, potential, ...). Yet interpretation of probe measurements can be challenging. The plasma is often strongly affected by insertion of a probe. Understanding how the plasma interacts with the probe is necessary to understand what the plasma conditions would be without the probe present. Thus, knowledge of boundary plasma physics and probe operation have typically advanced together.

This chapter reviews the plasma physics and diagnostics that are central to this thesis. It starts with the very basic kinetic description of a plasma in section 2.1 and fluid modeling which requires kinetic corrections in collisionless regimes. The physics of the sheath—where the plasma meets the wall—is given in section 2.2. The present understanding of the physics of electron and ion transport in the boundary plasma is reviewed in section 2.3. Space charge limited current is an important concern for probe operation and is presented in section 2.4. This is followed by sections on the physics basis of the three plasma probes used in this thesis: the Langmuir probe (section 2.5), the ion sensitive probe (section 2.6), and the retarding field analyzer (section 2.7). Since its data proved to be crucial to this thesis, the basics of Charge eXchange Recombination Spectroscopy (CXRS) is in section 2.8. Finally, although not strictly a plasma probe, a brief overview of thermocouples is given in section 2.9.

2.1 BASIC BOUNDARY PHYSICS

Much of the physics in this section can be found in Refs [50, 59, 129, 139].

In an ideal world plasma simulations would include all particles in the whole tokamak over all dimensions of time (1), space (3), and velocity (3), including fine enough detail in each dimension to resolve all of the important physics. Brute-force calculations like that are computationally impossible. The challenge of doing a full-scale simulation is daunting. In a paper discussing progress at connecting

plasma simulations codes, the FACETS group (Framework Application for Core-Edge Transport Simulations) stated [24]:

> Direct simulation of the entire system is not possible due to the range of scales. The spatial scales vary from the electron gyroradius ($\approx$ 0.01 mm in the edge to $\approx$ 0.1 mm in the core) to the system size (of order several meters), i. e., by a factor 3×10^5 . The time scales vary from the electron gyroperiod (20 ps) to the discharge duration ($\approx$ 1000 s), i. e., by a factor of 6×10^{13}. Thus, a full simulation would require the integration of 3×10^{16} (spatial resolution lengths)^3 for 6×10^{13} temporal resolution periods, for a product of 2×10^{30}. With the need for of 10^{6-12} degrees of freedom per spatial resolution volume (100 per length for a modest fluid model, easily larger by 100 to resolve velocity space as well), and 10^2 floating point operations per update of a degree of freedom for one temporal resolution period, **such a fundamental simulation** will require $2 \times 10^{23-29}$ floating point operations, which even on petascale platforms, **would require $2 \times 10^{23-29}$ s, exceeding the age of the universe by a factor of 10^{6-12}**.

2.1.1 *Kinetic Equations*

To make simulations tractable on a human timescale, approximations must be made. Since there are so many particles, a statistical description of plasma transport, given by the Boltzmann equation, simplifies the situation:

$$\frac{\partial f}{\partial t} + \vec{v} \cdot \frac{\partial f}{\partial \vec{r}} + \frac{\vec{F}}{m} \cdot \frac{\partial f}{\partial \vec{v}} = \left(\frac{\partial f}{\partial t}\right)_c , \tag{1}$$

where $f(\vec{r}, \vec{v}, r)$ is the distribution function of each particles species, $\vec{r}$ is the three-dimensional position vector, $\vec{v}$ is the three-dimensional velocity vector, m is the particle mass, $\vec{F}$ describes all of the forces on the particles, and $\left(\frac{\partial f}{\partial t}\right)_c$ describes all collisions. The probability at time t of finding a particle within the volume $d\vec{r}\,d\vec{v}$ at the point $(\vec{r}, \vec{v})$ is $f(\vec{r}, \vec{v}, t)\, d\vec{r}\, d\vec{v}$. Analytic solutions to eq. (1) are impossible for all but the simplest situations.

2.1.2 *Fluid Equations*

To make computations less demanding and allow for analytic approximations in some cases, velocity moments of the distributions func-

tion are taken to get the fluid variables (density n, pressure $\vec{P}$, heat flux density $\vec{Q}$, ...):

$$n(\vec{r},t) \equiv \int f(\vec{r},\vec{v},t)\,d\vec{v}, \tag{2}$$

$$\vec{V}(\vec{r},t) \equiv \frac{1}{n(\vec{r},t)} \int \vec{v} f(\vec{r},\vec{v},t)\,d\vec{v}, \tag{3}$$

$$\vec{P}(\vec{r},t) \equiv \int m\vec{v}\vec{v} f(\vec{r},\vec{v},t)\,d\vec{v}, \tag{4}$$

$$\vec{Q}(\vec{r},t) \equiv \int \frac{mv^2}{2}\vec{v} f(\vec{r},\vec{v},t)\,d\vec{v}. \tag{5}$$

Where, $\vec{V}$ is the macroscopic fluid velocity. For isotropic plasma pressure the temperature is defined as:

$$k_B T \equiv \frac{p}{n}. \tag{6}$$

Velocity moments of eq. (1), the Boltzmann equation, provide relationships among the fluid variables. Ignoring collisions, the Vlasov equation is:

$$\frac{\partial f}{\partial t} + \vec{v}\cdot\frac{\partial f}{\partial \vec{r}} + \frac{\vec{F}}{m}\cdot\frac{\partial f}{\partial \vec{v}} = 0. \tag{7}$$

The zeroth moment is:

$$\int \left(\frac{\partial f}{\partial t} + \vec{v}\cdot\frac{\partial f}{\partial \vec{r}} + \frac{\vec{F}}{m}\cdot\frac{\partial f}{\partial \vec{v}}\right) d\vec{v} = 0. \tag{8}$$

The first term is simply the time rate of change of the density:

$$\int \frac{\partial f}{\partial t}\,d\vec{v} = \frac{\partial n}{\partial t}. \tag{9}$$

The second term is the divergence of the flux:

$$\int \vec{v}\cdot\frac{\partial f}{\partial \vec{r}}\,d\vec{v} = \frac{\partial}{\partial \vec{r}}\left(n\vec{V}\right). \tag{10}$$

So to solve for the density n we need the mean particle velocity $\vec{V}$ and thus must integrate the next higher moment:

$$\int m\vec{v}\left(\frac{\partial f}{\partial t} + \vec{v}\cdot\frac{\partial f}{\partial \vec{r}} + \frac{\vec{F}}{m}\cdot\frac{\partial f}{\partial \vec{v}}\right) d\vec{v} = \int m\vec{v}\left(\frac{\partial f}{\partial t}\right)_c d\vec{v}. \tag{11}$$

The first term is now the time rate change of the momentum flux:

$$\int m\vec{v}\frac{\partial f}{\partial t}\,d\vec{v} = m\frac{\partial}{\partial t}\left(n\vec{V}\right), \tag{12}$$

exactly what is needed to solve for the zeroth moment. However the second term is:

$$\int m\vec{v}\vec{v}\cdot\frac{\partial f}{\partial \vec{r}}\,d\vec{v} = \frac{\partial \vec{P}}{\partial \vec{r}}, \tag{13}$$

i. e., the spatial gradient of the pressure, which requires knowledge of the next higher moment.

Thus the fluid moments by themselves do not result in a closed solution, i. e., the solution to one moment always relies on knowledge of a higher moment. To make the problem tractable a "closure" mechanism must be postulated. Closure can be obtained at lower moments by making an assumption that allows a fluid variable to be written in terms of local values of other fluid variables. A frequently used assumption is that the mean free path λ between like-particle collisions is much less than the smallest system scale length. As an example, for the case of conducted heat flux along a magnetic field line, this assumption yields the Spitzer-Harm heat flux [137]:

$$\vec{q}_{SH} = -\kappa_0 T^{5/2}\frac{\partial T}{\partial \vec{r}}. \tag{14}$$

Thus the local density of heat transport can be obtained solely from local knowledge of the temperature and its spatial gradient. The thermal conductivity, $\kappa_0 T^{5/2}$, is a strong function of temperature.

2.1.3 *Flux Limits*

Although Spitzer-Harm heat flux is valid for small Knudsen number ($Kn = \lambda/L$) often, for at least part of the boundary plasma, this assumption does not hold. Kinetic limits for heat transport in fluid models have been considered for decades; see Ref. [49] for a review focusing on the tokamak boundary. The problem stems from the fact that nearly all of the heat flux is carried by the particles within the velocity range $3 < v/\sqrt{k_B T_{(e,i)}/m_{(e,i)}} < 5$. These particles have a much longer mean free path ($\lambda \propto v^4$) than the bulk of particles at much lower velocities. Thus, even for $Kn \sim 1$ or less, the majority of the heat flux is carried by particles which likely make no collisions.

To overcome this, many fluid codes employ a "heat flux limiter". That is, at high Kn the heat flux is limited to a fraction of the free-streaming value ($q_{FS(e,i)} = \alpha_{(e,i)} n v_{th(e,i)} k_B T_{(e,i)}$), where $\alpha_{(e,i)}$ is a heat flux limit factor and $v_{th(e,i)} = \sqrt{k_B T_{(e,i)}/m_{(e,i)}}$ is the thermal velocity.

Implementation of heat flux limiters in fluid codes is most often accomplished by employing the harmonic average between the Spitzer-Harm and free-streaming heat fluxes:

$$\left(q_{\parallel(e,i)}\right)^{-1} = \left(-\kappa_{0(e,i)} T_{(e,i)}^{5/2} \frac{dT_{(e,i)}}{dx}\right)^{-1} + \left(\alpha_{(e,i)} n v_{th(e,i)} k_B T_{(e,i)}\right)^{-1}, \quad (15)$$

where the free-streaming heat flux is in the same direction as the Spitzer-Harm. A fraction of the free-streaming heat flux is chosen as the limit because the heat flux is carried by hot tail electrons and cannot physically exceed a convective limit. Since there is no theoretical basis for this functional form, the heat flux limit factor α must be found through kinetic simulations. Comparisons of kinetic simulations with heat flux limited fluid simulations indicate that the harmonic average technique does not completely capture the kinetic effects and the profiles shapes are very sensitive to the value of α used [29, 47, 48]. This is because kinetic heat transport is inherently *non-local*, the heat flux cannot be determined by *local* values of the density, temperature, and/or temperature gradient as in eqs. (14) and (15). Despite these limitations, an approximate value of the flux limiting coefficient that is typically recommended in fluid codes employing eq. (15) is $\alpha = 0.2$ [1, 2, 73, 127].

We must caution the reader to be careful in interpreting $\alpha_{(e,i)}$ results from literature as it depends on the definition of $v_{th(e,i)}$. Some define it as $v_{th(e,i)} = \sqrt{k_B T_{(e,i)}/m_{(e,i)}}$ [2, 35, 47, 49, 128, 139], while others define it as $v_{th(e,i)} = \sqrt{2k_B T_{(e,i)}/m_{(e,i)}}$ [13, 25, 29, 92]. The difference of 1.4 will have a large effect on the profiles, especially for low α. In this paper we follow the standard as set out in the UEDGE [131] and SOLPS [134] user manuals: $v_{th(e,i)} = \sqrt{k_B T_{(e,i)}/m_{(e,i)}}$.

Heat flux limiters have been implemented in many edge fluid codes: UEDGE [131], EDGE2D [49], and SOLPS/B2-Eirene [134]. Their use, or lack of use, is often mentioned [26, 53, 88, 89, 90, 94, 99, 110, 120, 133]; many cite the use of $\alpha = 0.2$ due to the ITER Physics documentation [127], which is indirectly [130] cited Ref. [73] as the justification for its use. There have been a few published sensitivity scans exploring the impact of adjusting heat flux limiters on the agreement between simulated and measured parameters. It was found that adjusting the electron heat flux limiter had little impact on the upstream or downstream electron temperature and density [31]. Adjusting both the electron and ion heat flux limiters had little impact on the divertor electron and ion temperatures as well as the divertor recycling light H_α [26]. However adjusting the ion heat flux limiter had a strong impact on the poloidal ion temperature profiles [26, 31]. The effect was so strong as to prompt the authors of Ref. [31] to state:

> The quantity most affected in the simulations by the change in the heat flux limiters is the ion temperature, Fig. 14, but the dearth of existing experimental data points to an opportunity!

Additionally, comparison of CXRS impurity T_i measurements with simulations showed that heat flux limiters were likely necessary to explain the high values of T_i [98]; yet, they were not implemented due to a lack of theory for their value.

It is instructive to consider why the upstream ion temperature might be more strongly affected than the upstream electron temperature through heat flux limiters. Equation (15) may be written as:

$$q_{\parallel} = \kappa_{\text{eff}} q_{\text{SH}}, \tag{16}$$

where κ_{eff} is an effective conductivity scale factor given by:

$$\kappa_{\text{eff}} = \left(1 + \frac{q_{\text{SH}}}{q_{\text{FS}}}\right)^{-1}. \tag{17}$$

To make a comparison between the electrons and ions, we rewrite the Spitzer-Harm thermal conductivity constant, retaining the mass dependence:

$$\kappa_{o(e,i)} = \kappa'_{o(e,i)} m_{(e,i)}^{-1/2}, \tag{18}$$

where κ_o is of the same order for electrons and ions; $\kappa'_{oi}/\kappa'_{oe} = 1.7$ from Ref. [19]. We now have:

$$\begin{aligned}\kappa_{\text{eff}} &= \left(1 + \frac{\kappa'_o m^{-1/2} T^{5/2} \left|\frac{dT}{dx}\right|}{\alpha n \left(k_B T\right)^{3/2} m^{-1/2}}\right)^{-1} \\ &= \left(1 + \frac{\kappa'_o}{\alpha n k_B^{3/2}} T \left|\frac{dT}{dx}\right|\right)^{-1}.\end{aligned} \tag{19}$$

The mass dependence drops out of the effective conductivity. The most important difference between κ_{eff} for electrons versus ions is the local value of $T\left|\frac{dT}{dx}\right|$ (assuming similar values of α). Consider a case of equal parallel heat flow in the ion and electron species to the divertor target where $T_i = T_e$ (one may expect this condition in the highly collisional divertor plasma). Since $\kappa_{oi} \ll \kappa_{oe}$, the ion temperature will increase more rapidly with distance from the divertor compared to electron temperature, making $T\left|\frac{dT}{dx}\right|$ greatest for the ions. This effect feeds back into eq. (19), making κ_{eff} lower for the ions, which further increases $T\left|\frac{dT}{dx}\right|$ for the ions compared to the electrons, until the flux limiting factor dominates the ion heat flux. Thus, it is the poor thermal conductivity of the ions that makes their temperature pro-

files have sharper parallel gradients and therefore higher sensitivity to flux limiters than electrons.

2.2 BASIC SHEATH PHYSICS

Many of a plasma's peculiar characteristics come about because it is a 2-component conducting fluid where the fluid components have opposite charge signs and largely different masses. One of these peculiarities is the sheath, where the plasma meets the wall. To begin understanding this region we ask: What happens when a plasma suddenly comes into contact with an electrically floating wall? For a plasma where the ions and electrons have about the same energy ($T_i \approx T_e$), the electrons will have a much higher thermal velocity because of their lower mass ($\sqrt{m_i/m_e} \approx 60$ for deuterium). This means that the electron flux out of the plasma to the surface is much greater than the ion flux. The electrically floating wall charges up negatively until a sufficiently large electric field between the wall and the plasma retards the electron flux and increases the ion flux such that they are balanced. This is known as ambipolarity: the steady-state boundary condition that equal currents of ions and electrons leave the plasma to the wall.

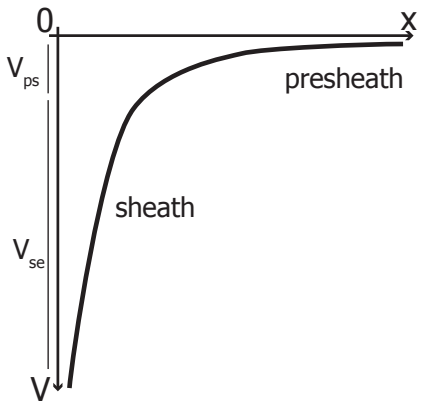

Figure 6: Basic diagram of a plasma-wall sheath. The presheath (V_{ps}) accelerates the ions to at least the sound speed. The sheath (V_{se}) retards the electron flux.

This region of charge imbalance and electric field is called the Bohm sheath, or usually just the sheath (fig. 6). The precise definition of the transition from plasma to sheath varies in the literature. It often is taken to be the point where the ion and electron densities differ or where the ions are flowing at Mach 1.

2.2.1 *Bohm Criterion*

By solving the Vlasov equation, we find that the electrons follow the Boltzmann relation in a retarding potential:

$$n_e = n_{se}\, e^{\frac{e(V-V_{se})}{k_B T_e}}, \tag{20}$$

where the subscript "se" denotes quantities at the sheath-edge and the upstream potential is defined as $V = 0$ (all potentials here are thus less than zero). Assuming that the ions have zero energy ($T_i = 0$) and originate upstream of the sheath edge at a single location, by conservation of energy we have:

$$\frac{1}{2} m_i v_{se}^2 = -eV_{se}. \tag{21}$$

Since there are no particle sources or sinks within the sheath, particle conservation gives:

$$\begin{aligned} n_i v &= \text{constant} \\ n_i v &= n_{se} v_{se} \\ n_i \sqrt{-\frac{2eV}{m_i}} &= n_{se} \sqrt{-\frac{2eV_{se}}{m_i}} \\ n_i &= n_{se} \sqrt{\frac{V_{se}}{V}}. \end{aligned} \tag{22}$$

Yet in the sheath $n_i \neq n_e$, so we must solve Poisson's equation:

$$\begin{aligned} \frac{d^2V}{dx^2} &= \frac{e}{\epsilon_o}(n_e - n_i) \\ &= \frac{e}{\epsilon_o}\left(n_{se} e^{\frac{e(V-V_{se})}{k_B T_e}} - n_{se}\sqrt{\frac{V_{se}}{V}} \right). \end{aligned} \tag{23}$$

Now, defining $\Delta \equiv V_{se} - V$ and assuming that $\frac{\Delta}{V_{se}} \ll 1$ (which is valid near the sheath entrance), we have:

$$\begin{aligned} \sqrt{\frac{V_{se}}{V}} &= \sqrt{1 + \frac{\Delta}{V_{se}}} \\ &\simeq 1 + \frac{\Delta}{2V_{se}} \\ &\simeq 1 - \frac{\Delta}{2|V_{se}|}, \end{aligned} \tag{24}$$

and:

$$\begin{aligned} e^{\frac{e(V-V_{se})}{k_B T_e}} &= e^{\frac{-e\Delta}{k_B T_e}} \\ &\simeq 1 - \frac{e\Delta}{k_B T_e}. \end{aligned} \tag{25}$$

We now have a linearized form of the Poisson equation in the sheath entrance:

$$\begin{aligned} \frac{d^2\Delta}{dx^2} &\simeq -\frac{e}{\epsilon_o} n_{se}\left(1 - \frac{e\Delta}{k_B T_e} - 1 + \frac{\Delta}{2|V_{se}|}\right) \\ &\simeq \frac{e}{\epsilon_o} n_{se}\Delta\left(\frac{e}{k_B T_e} - \frac{1}{2|V_{se}|}\right). \end{aligned} \tag{26}$$

In order for the sheath to have a monotonic solution the term in the parenthesis must be positive. The experimental observation that all sheath potentials are monotonic leads to the Bohm criterion:

$$\begin{aligned} \frac{e}{k_B T_e} &\geqslant \frac{1}{2|V_{se}|} \\ m_i v_{se}^2 &\geqslant k_B T_e \\ v_{se} &\geqslant c_s. \end{aligned} \tag{27}$$

To have a physically consistent solution the ions must enter the sheath going at least the sound speed. The full sound speed is, including non-zero (isothermal) ion temperature:

$$c_s = \sqrt{\frac{k_B (T_e + T_i)}{m_i}}. \tag{28}$$

Additionally, the length of the sheath can be approximated as follows from the Poisson equation:

$$\begin{aligned} \frac{\Delta}{L_{sheath}^2} &\approx \frac{en\Delta}{\epsilon_o} \frac{e}{k_B T_e} \\ L_{sheath} &\approx \sqrt{\frac{\epsilon_o k_B T_e}{ne^2}} \\ &\equiv \lambda_D. \end{aligned} \tag{29}$$

That is, the sheath is on order the Debye length, this should come as little surprise since the Debye length is the characteristic scale that a plasma shields electric fields.

2.2.2 *Sheath Potential*

Knowing that the ions enter the sheath at the sound speed is an important starting point for understanding other sheath properties. The particle density to the surface is:

$$\begin{aligned} \Gamma_{se} &= n_{se} v_{se} \\ &= n_{se} c_s. \end{aligned} \tag{30}$$

All of the ions that enter the sheath make it to the wall (collisions in the sheath are insignificant [63]):

$$\Gamma_{i,w} = \Gamma_{i,se}. \tag{31}$$

Electrons in the sheath have a 1-way Maxwellian flux whose density follows the Boltzmann relation:

$$\begin{aligned}\Gamma_{e,w} &= \frac{1}{4} n \bar{c}_e \\ &= \frac{1}{4} n_{se} e^{\frac{eV_w}{k_B T_e}} \sqrt{\frac{8 k_B T_e}{\pi m_e}}.\end{aligned} \tag{32}$$

Thus, with quasi-neutraility imposed at the sheath entrance, for ambipolar flux ($\Gamma_{i,w} = \Gamma_{e,w}$) to the wall:

$$\begin{aligned} n_{se} \sqrt{\frac{k_B (T_e + T_i)}{m_i}} &= \frac{1}{4} n_{se} e^{\frac{eV_w}{k_B T_e}} \sqrt{\frac{8 k_B T_e}{\pi m_e}} \\ \frac{eV_w}{k_B T_e} &= \frac{1}{2} \ln \left[2\pi \frac{m_e}{m_i} \left(1 + \frac{T_i}{T_e} \right) \right]. \end{aligned} \tag{33}$$

That is a deuterium plasma rises $V_{se} \approx 2.7 \frac{k_B T_e}{e}$ above the wall potential.

The situation is complicated slightly by a magnetic field that strikes the wall at oblique angles. The electrons remain magnetized through the sheath. The ions accelerate up through a Chodura sheath and then get demagnetized in the Bohm sheath [27]. For all but the shallowest of angles the flux along the magnetic field incident on the wall gets reduced by the sine of the angle between them. At angles approaching tangency it gets more complicated [93, 102, 145].

A useful property of the sheath is that for any biases of the wall below the floating potential (V_f, that is, the potential at which no net current flows through the sheath) the flux of ions remains constant. This feature is used by Langmuir probes in section 2.5.

2.2.3 *Sheath Heat Flux*

The sheath regulates the "escape" of plasma particles from the plasma to material surfaces. Thus the sheath also regulates the power transmitted from the plasma to the material surface. The heat flux transmitted by the sheath is comprised of three main components:

1. The forward going Maxwellian electron flux at the wall:

$$q_{e,se} = 2 k_B T_e \Gamma_{se}. \tag{34}$$

2. The energy transferred from electrons to ions through the sheath potential:

$$q_{V,se} = |eV_{se}| \Gamma_{se}. \tag{35}$$

3. The ion energy flux through the sheath is more complicated:

$$q_{i,se} = \gamma_i k_B T_e \Gamma_{se}. \tag{36}$$

If ions were simply a Maxwellian drifting at the sound speed then the ion heat flux at the sheath edge would be $\gamma_i = 3.5 T_i/T_e$. Detailed kinetic analysis with the complete ion velocity distribution indicates that $\gamma_i \approx 2.5 T_i/T_e$ may be most appropriate [139]. However, in fluid codes, where the ion velocity at the sheath edge, v_{se}, may exceed the sound speed, use of γ_i values lower than $\left(\frac{5}{2} k_B T_i + \frac{1}{2} m_i v_{se}^2\right)/k_B T_e$ result in non-monotonic ion temperature profiles to carry heat flux away from the wall.

There are important distinctions to be made here. The total electron energy flux leaving the plasma is: $q_{e,p} = (2 k_B T_e + |eV_{se}|)\Gamma_{se}$ and the total ion energy flux leaving the plasma is: $q_{i,p} = \gamma_i \Gamma_{se} T_e$. These are the appropriate boundary conditions to put on each species for a fluid code. However, the total energy flux of each species to the surface is different because of the sheath potential. At the surface the electron energy flux is: $q_{e,w} = 2 k_B T_e \Gamma_{se}$ and the ion energy flux is: $q_{i,w} = (\gamma_i k_B T_e + |eV_{se}|)\Gamma_{se}$. Thus the sheath effectively transfers kinetic energy to the ions which is important since the ion energy incident to the material surface controls the sputtering yield of the material.

Since the most common divertor measurements are T_e and J_{sat} (ion saturation current, the current collected at negative probe bias when all electrons are rejected) from Langmuir probes, a relation relating these values to the heat flux through the sheath is quite useful:

$$q_w = \gamma T_e J_{sat}. \tag{37}$$

Where γ, the sheath heat flux transmission coefficient is given by (taking the form of γ_i from kinetic simulations):

$$\gamma = 2.5 \frac{T_i}{T_e} + 2 - \frac{1}{2} \ln\left[2\pi \frac{m_e}{m_i}\left(1 + \frac{T_i}{T_e}\right)\right], \tag{38}$$

which for $T_i = T_e$ and deuterium plasma results in $\gamma \simeq 7$. A more complicated version, including secondary electron emission and non-zero sheath currents is derived in appendix A.

With independent measurements of T_e & J_{sat} along with q_w one can make an experimental test of sheath heat flux theory. This has been done in many tokamaks and is summarized in table 1, reproduced from Ref. [100]. Values greater than the nominal value of 7 can be explained with $T_i > T_e$, non-zero current through the sheath, and/or secondary electron emission. Values between 5 and 7 can be due to $T_i < T_e$ or a very small range of finite currents through the sheath. Values below 5 (the limit of $T_i \ll T_e$), however, are physically impossible. Yet, as shown in table 1, values less than 5 have been measured in

many tokamaks. The discrepancy has been attacked from all angles including:

1. Refinements to sheath heat flux theory accounting for ion collisions with neutrals within the sheath [51], which was later shown to not matter [63].

2. Difficulties in making the heat flux measurement; including IR "hot-spots" [60] and thermally detached layers [100].

3. Overestimation of T_e with Langmuir probes in the presence of a non-Maxwellian plasma [67, 138] or plasma fluctuations [132].

Clearly something must have been wrong, be it the measurements or the theory.

Table 1: Summary of experimental sheath heat flux transmission coefficients first presented in [100].

Tokamak	Range of γ	Refs.
ASDEX-U	3-8	[61]
DIII-D	2-4	[23]
JET	2-8	[108]
JT-60U	2-20	[12]
TEXT	~ 5	[140]
Tore Supra	3-8	[30]
TCV	4-8	[100]

It is important to be confident in the theory of γ. If one knew the plasma conditions at all surfaces in a magnetic fusion reactor, then the heat flux would be known to these surfaces. Since it is expected that reactors will be near engineering heat flux exhaust limits, factors of two uncertainty in γ are unacceptable. Additionally, it is used as the boundary condition in all edge fluid codes, including the one developed in section 8.2. In section 6.1 we compare Langmuir probe measurements of sheath heat flux with that from novel surface thermocouples, section 3.2, and find excellent agreement in the sheath limited regime. The surface thermocouple measurements also indicate that $\gamma \approx 2$ near detachment reproducing the results seen in other experiments (table 1). A new theory based on the Langmuir probes disturbing the local plasma is put forth, explaining the unphysical measurements, and confirmed with simulations in chapter 6. ●

2.3 TOKAMAK BOUNDARY REGIMES: ELECTRONS AND IONS

The collisionality of the boundary plasma of a tokamak is very sensitive to core plasma density [50, 95, 139]. The Knudsen number Kn (or the inverse collisionality parameter $1/\nu^*$) is defined as ratio of the mean free path between collisions $\lambda \propto T_e^{3/2}/n_e$ to a characteristic scale length of the system, be it the system length L or a local gradient scale length $\theta/(d\theta/dx)$. At the lowest core plasma density in C-Mod, the mean free path in the edge is greater than the system length ($Kn \approx 10$, $T_e \approx 50\,eV$, $n_e \approx 0.3 \times 10^{20}\,m^{-3}$ for $I_p = 0.8\,MA$ in the C-Mod divertor) and the heat flux is transported along field lines to the divertor with minimal collisions, fig. 7. This is called the "sheath-limited" heat transport regime because the rate of heat exhaust is limited by the transport through the sheath. Increasing the core density

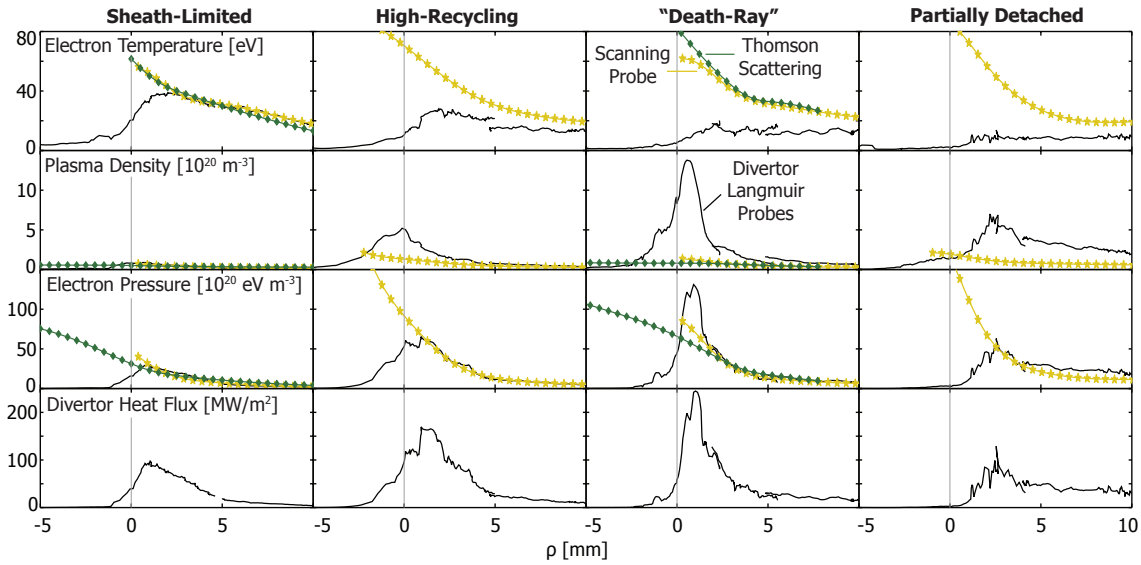

Figure 7: The four tokamak boundary regimes: (1) Sheath-limited: electron temperature and pressure map from the "upstream" scanning probe to "downstream" divertor Langmuir probes. (2) High-recycling: electron pressure still maps; yet, due to the increase in collisionality, electron temperature drops in the divertor to conduct heat flux. (3) "Death-Ray": similar to high-recycling, except for the region near the strike point. Here there is a significant increase in the measured divertor plasma density resulting in an over-pressure relative to upstream. (4) Partially detached: significant pressure drop at the strike point yet pressure maps in the far SOL ($\rho > 3\,\mathrm{mm}$).

by $\sim 50\,\%$ decreases the mean free path to the same order as the system length ($Kn \approx 1$, $T_e \approx 25\,eV$, $n_e \approx 0.6 \times 10^{20}\,m^{-3}$) or slightly less, depending on the definition of the characteristic scale length and the location where λ is evaluated. In this case, heat transport is limited by conduction—the "conduction-limited" regime—characterized by a significant parallel temperature drop while pressure remains constant along magnetic field lines. As the wall surface is approached, the local temperature falls and the local density rises in inverse proportion to the temperature; total plasma pressure must be conserved in the absence of many neutral-plasma collisions. Thus the mean free path varies along the field line. A further increase in core density by $\sim 50\,\%$ greatly increases the density at the wall surface and the rate of neutrals recycling from the wall. Momentum loss from collisions with this neutral cloud reduces the plasma pressure—the plasma enters into the "detached" regime ($Kn \lesssim 0.01$, $T_e \approx 5\,eV$, $n_e \approx 3.0 \times 10^{20}\,m^{-3}$). Since plasma density decays by orders of magnitude across field lines in the scrape-off layer (SOL), all of these regimes can exist in the boundary plasma at the same time: a detached state near the divertor strike point location, a conduction-limited state in the "near SOL", and a sheath-limited state in the "far SOL".

2.3.1 *Divertor Over-Pressure*

Just at the onset of detachment, a remarkable over-pressure condition has been reported to occur near the divertor strike point, in a region of slightly elevated T_e just above the divertor [95, 108]. This factor of ~ 2 increase in nT_e relative to "upstream" values has been dubbed the divertor "death-ray", owing to its expected enhanced heat flux. It was speculated that elevated T_e was the root cause—increasing the ionization of the neutral wind and preferentially depositing that momentum into a toroidally symmetric band of "death-ray" flux tubes near the strike point [95]. However, early modeling attempts were not able to reproduce such an effect [141] and there was no known source of the elevated T_e. The new thermal diagnostics developed as part of this thesis indicate that the "death-ray" over-pressure is localized to the Langmuir probes, and not a true axis-symmetric regime, chapter 6.

2.3.2 *Ion Transport*

The picture of parallel transport phenomena in the SOL comes from studying the electron species with Langmuir probes [95]. A corresponding investigation of the ion species has not been so thoroughly assembled. At high Knudsen number (low collisionality), we expect the ion and electron temperatures in the SOL to be weakly coupled, with T_i of order 2 to 3 times T_e (this ratio arises from a simple consideration of their relative parallel thermal conductivity), depending on the rates of ion and electron heat transport into the SOL and the flow of heat along field lines, accounting for kinetic corrections. As the Knudsen number is lowered (increased collisionality), we expect the ion and electron temperatures to become more coupled collisionally. Systematic measurements of T_i and T_e in the SOL over a range of plasma densities can therefore provide important information about the rates of cross-field and parallel heat flow and the role of kinetic corrections to heat transport in the SOL.

Systematic investigation of the upstream ion temperature (typically at the outer-midplane) have been performed in tokamaks since the mid-1980's, yet are rare [82, 83, 84, 85, 105, 152]. Downstream measurements of ion temperature are even more rare. Only recently was an RFA installed in the divertor of MAST [38, 39]. Upstream ion temperature is almost universally greater than the electron temperature and this ratio tends to increase with distance away from the core plasma [81]. This is largely due to the poor thermal conductivity of the ions. Although results are mixed, in most instances, as the core density is increased the upstream ion temperature is decreased and the upstream electron temperature is unchanged or is slightly decreased. At the lowest densities, the upstream ion temperature is

$\sim$ 3 to 8 times the upstream electron temperature (this ratio is often expressed as $\tau \equiv T_i/T_e$). At high core density the upstream ion temperature tends to converge toward the electron temperature. It is almost always noted that this convergence is due to the increasing collisionality (decreasing Kn), which allows more efficient transfer of energy between electrons and ions, a process often called equipartition.

Through extensive studies on the Alcator C tokamak with an RFA, it was found that the upstream ion to electron temperature ratio varied from $\sim$ 1.5 to 3 for low values of $\bar{n}_e/I_p$ and subsequently decreased to $\sim$ 1 at high values of $\bar{n}_e/I_p$ [152]. This quantity also appears in the Greenwald fraction: $\bar{n}_e a^2\pi/I_p$, with $\bar{n}_e$ [$10^{20}\,m^{-3}$], a [m], and I_p [MA], which has been shown to be a good ordering parameter for the edge plasma state [52]. In the DITE tokamak, both the RFA and PIMS ion to electron temperature ratios decreased from $\sim$ 6 at the lowest core densities to $\sim$ 2 at the highest in a helium plasma [105]; it was claimed that the disparity in temperature between ions and electrons was qualitatively consistent with equipartition. A decrease in the temperature ratio from $\sim$ 3 to 1 with increasing core density was seen using a Segmented Tunnel Probe in the CASTOR tokamak [85]. The CXRS measured C^{5+} impurity ion to electron temperature ratio decreased from $\sim$ 3 to 1 with increasing density in TEXTOR [64]. The impurity ion (CXRS) to electron (Langmuir probe) temperature ratio measured in JT-60U with neutral beam heating (4 MW) had no systematic change with core density, toroidal field, or plasma current, staying at $\sim$ 2 to 4 [11]. 2D fluid simulations of the FTU boundary plasma indicated that the ion to electron temperature ratio should drop with increasing core density, although they had no ion temperature measurements to check this trend [154]. The ratio of ion to electron temperature decrease with increasing core density in LHD [58].

In Tore Supra an extensive set of T_i measurements has been made with an RFA [82, 83, 84]. With deuterium plasmas over a range of Greenwald density fraction from 0.22 to 0.63 there were two trends observed. At low toroidal field ($2.4\,T \leqslant B_t \leqslant 3.1\,T$) there was *no change* in the ion to electron temperature ratio ($\sim$ 2 to 3) [82]. However, at higher toroidal field ($B_t = 3.8\,T$) the ion to electron ratio *increased* from $\sim$ 2 to 6, due almost entirely to the ion temperature increasing. The only other plasma parameter seen to increase so strongly with the change in toroidal field was the core electron temperature (there were no measurements of the core ion temperature). The reason for this coupling was not known. In a separate study at even higher field ($B_t = 4.0\,T$) the ratio of ion to electron temperature *decreased* from $\sim$ 2.5 to 1 over the same range of core density [84]. The decrease in the ratio was taken up almost exclusively by a decrease in the ion temperature. In helium plasmas in Tore Supra the ion to electron temperature ratio measured with an RFA decreased from $\sim$ 7 to 4 as core plasma density increased [83]. However at the highest densities the

ratio remained constant, which may have been due to the assumption that $Z = 2$ for all of the data. At higher densities $Z = 1$ may have been more likely, thus the ion temperature in these cases may have been over estimated and the temperature ratio may have indeed continued to decrease with increasing core density.

An "Onion-Skin" model (using conduction only, lacking convection, electron-ion equipartition, and heat flux limiters) was compared to upstream ion temperature with an RFA in JET [57]. The model used divertor Langmuir probe n and T_e as inputs (along with an assumption on T_i) and integrated up the field line. Two shots with similar densities ($2.6 \times 10^{20}\,m^{-3}$ and $3.2 \times 10^{20}\,m^{-3}$) but different neutral beam heating powers (0.8 MW and 3.3 MW) were modeled. It was found that assuming $T_i = 0.5T_e$ in the divertor for the low-power case and $T_i = T_e$ for the high-power case had the best matches between the simulated and measured upstream ion temperatures. The upstream temperature ratio was ~ 2 for both cases. This suggests that the divertor ion temperature increases with input power, a result recently seen with the divertor RFA on MAST [39].

It is important to note that upstream ion to electron temperature ratios greater than 5 have been reported regularly in the literature. Yet, within context of a fluid model for parallel ion heat flux, temperature ratios this high are difficult to reconcile and kinetic corrections to the fluid description are likely required. Integrating $\frac{dq_{SH(e,i)}}{dx} = Q_{(e,i)}$ (where $Q_{(e,i)}$, is the heat flux source) to find the upstream temperature:

$$T_{u(e,i)}^{7/2} = T_{t(e,i)}^{7/2} + \frac{7}{4} Q_{(e,i)} \frac{L}{\kappa_{0(e,i)}}. \tag{39}$$

If we assume that the upstream temperatures are greater than the divertor temperatures (thus $T_{u(e,i)}^{7/2} \gg T_{t(e,i)}^{7/2}$), the ratio of ion to electron heat flux source is:

$$\frac{Q_i}{Q_e} = \frac{\kappa_{oi}}{\kappa_{oe}} \left(\frac{T_{ui}}{T_{ue}} \right)^{7/2}, \tag{40}$$

with $\kappa_{oi}/\kappa_{oe} \approx 0.03$. This relation is shown in fig. 8. Equal electron and ion heat input into the SOL would require that $T_{ui} \approx 2.7T_{ue}$. The larger values of the upstream temperature ratio seen in experiments (> 5) would imply an ion heat flux source at least an order of magnitude higher than the electron heat flux. In many experiments, the upstream electron temperature changed very little and it was the ion temperature that decreased with an increase in Kn. In addition, the temperature ratio increases with distance into the SOL [80] and the ion temperature scale length has no clear trend with core density [84]. This temperature ratio trend implies a much larger total heat flux—despite the inputted and radiated powers being relatively constant—

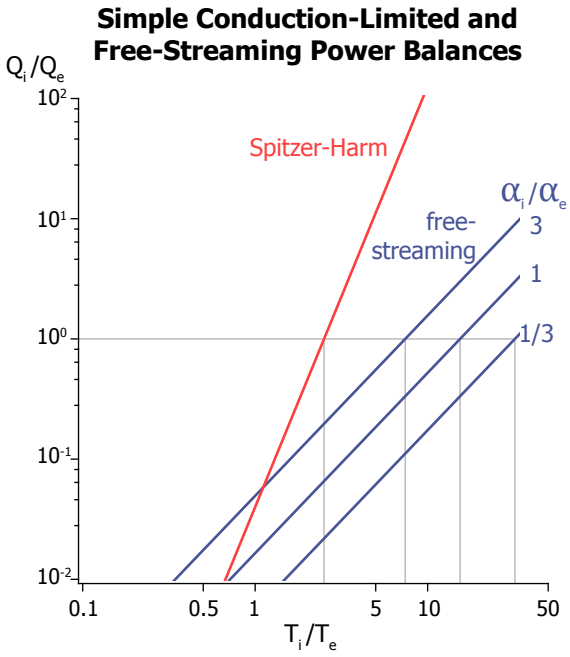

Figure 8: Ratio of ion and electron heat input into SOL (vertical axis) versus ion to electron temperature ratio (horizontal axis) for different assumptions about parallel heat transport, using simple 1D heat transport models. For the case of equal ion and electron heat transport into the SOL, ion temperature is 2.7 times the electron temperature, assuming Spitzer-Harm conduction. If a free-streaming parallel heat flux model is assumed, the T_i/T_e ratio is much higher and depends on the ratio of ion to electron heat flux limiters used to account for kinetic corrections.

clearly violating power balance. The most likely explanation for the very large values of ion temperature at high Kn is the need to include kinetic corrections to the 1D fluid heat transport model, section 2.1.3. The ratio of ion to electron heat flux source for a free-streaming assumption has a weaker dependence on the temperature ratio:

$$\frac{Q_i}{Q_e} = \frac{\alpha_i}{\alpha_e}\left(\frac{m_e}{m_i}\right)^{1/2}\left(\frac{T_{ui}}{T_{ue}}\right)^{3/2}. \tag{41}$$

This allows for a much higher upstream temperature ratio than Spitzer-Harm conduction, fig. 8.

2.4 SPACE CHARGE LIMITED CURRENT

Space charge is a crucial concern for probe measurements. These measurements inherently rely on the probe bias controlling plasma collection. However, the plasma has its own potential associated with it, fig. 9. For ion probes where the electrons must be removed from collection there are regions with large net density of ions. At low density the ion space charge is insignificant with respect to the bias potential. However, at sufficiently high density, the the ion collection becomes dominated by the potential caused by the ions rather than the external probe potential.

The phenomenon of space charge limited current is as old as plasma physics. The simplest example is current flow in a vacuum tube electronic diode, containing two electrodes (cathode and anode). The cathode is heated such that it emits electrons (via thermionic emission) into the vacuum. At negative biases of the anode with respect

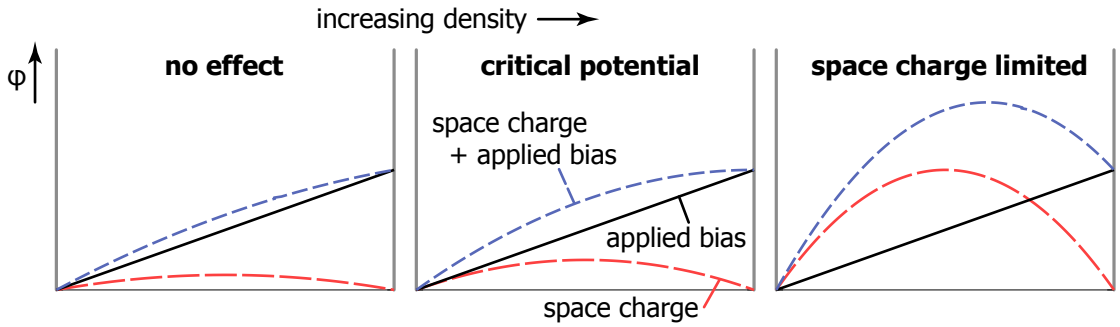

Figure 9: Simple example of space charge between two grids. For each of the three panels the left boundary is the plasma, the right boundary is the probe surface, and the area in between is the probe volume with net ion density. Left panel show the case where the density is too low to create a potential to perturb the measurement. Middle panel shows the marginal case where the density is sufficiently large enough that the potential created by the space charge is just able to reflect ions. Right panel shows case where density is so large that the space charge overwhelms the applied bias and significantly reduces the ion flux, ruining the measurement.

to the cathode, the electrons are repelled by the anode and no current flows between the two electrodes. At positive biases of the anode, the electrons are allowed to flow freely from the cathode to the anode. Thus the device acts as a diode, allowing current to flow for only one direction of bias. But flow of electrons between the two electrodes is limited, not because of the rate of thermionic emission at the cathode, but because the finite density of electrons between the electrodes produces a negative space charge potential.

The simplest form of the 1D space charge problem was solved by Child and Langmuir [97]. They considered two infinite planar electrodes separated a distance d: a grounded cathode and an anode at bias V. Electrons are emitted with zero initial velocity from the cathode. Solving Poisson's equation along with mass and energy conservation in this domain produces what is now called the Child-Langmuir Law:

$$I_{SC} = \frac{4\epsilon_0}{9}\sqrt{\frac{2e}{m}}\frac{S}{d^2}V^{3/2}. \tag{42}$$

Where I_{SC} is the space charge limited current between the plates, ϵ_0 is the permittivity of free space, e the unit charge, m the mass, and S is the surface area of the plates.

The space charge limit problem was extended for electrons emitted from the cathode with a Maxwellian velocity distribution [97]. Langmuir formulated the solution in terms of the spatial location (x) compared to the location of the potential maximum (x_m) and voltage (V) compared to the of the potential maximum (V_m). For large values

of $e(V-V_M)/k_BT$ he found the space charge limited current density to be described by:

$$I_{SC} = \frac{4\epsilon_o}{9}\sqrt{\frac{2e}{m}}\frac{S}{(x-x_M)^2}(V-V_M)^{3/2}\left(1+2.658\sqrt{\frac{k_BT}{e(V-V_M)}}\right), \quad (43)$$

with the finite temperature correction contained in the second term.

Space charge has been thoroughly considered for retarding field analyzers and we have designed ours to deal with it, sections 3.3.3 and 3.3.4. On the other hand, space charge has not been a serious concern for the ion sensitive probe in the literature and ours was designed without provisions for it. Yet, after careful examination of the data we find the ion sensitive probe measurements to be almost perfectly described by space charge physics, which renders it useless for measuring the ion temperature (although changes to the geometry might have allowed it to operate properly). Issues concerning space charge limits and ion sensitive probes are discussed in detail in chapter 7.

2.5 LANGMUIR PROBES

The Langmuir probe is the oldest and one of the simplest plasma diagnostics. It is the work horse of boundary plasma measurements. Simply an electrically isolated conductor that can be biased and have the current measured, it can measure electron temperature, density, and (indirectly) plasma potential.

The net current flux parallel to the magnetic field to the surface is:

$$\begin{aligned} J &= e(\Gamma_i - \Gamma_e) \\ &= e\left(\frac{1}{4}n_{se}e^{\frac{eV_f}{k_BT_e}}\sqrt{\frac{8k_BT_e}{\pi m_e}} - \frac{1}{4}n_{se}e^{\frac{eV}{k_BT_e}}\sqrt{\frac{8k_BT_e}{\pi m_e}}\right) \\ &= e\frac{1}{4}n_{se}e^{\frac{eV_f}{k_BT_e}}\sqrt{\frac{8k_BT_e}{\pi m_e}}\left(1-e^{\frac{e}{k_bT_e}(V-V_f)}\right) \\ &= en_{se}c_s\left(1-e^{\frac{e}{k_bT_e}(V-V_f)}\right) \\ &= J_{sat}\left(1-e^{\frac{e}{k_bT_e}(V-V_f)}\right). \end{aligned} \quad (44)$$

With $J_{sat} \equiv en_{se}c_s$. Thus for a measured I-V values can be fit for J_{sat}, T_e, V_f. With an assumption or independent measurement of T_i and knowing the projected area of the magnetic field incident on the

probe, values can also be calculated for n_{se}. The plasma potential can be estimated from standard sheath theory eq. (33):

$$\begin{aligned} V_P &= V_f - \frac{1}{2}\frac{k_B T_e}{e} \ln\left[2\pi\frac{m_e}{m_i}\left(Z + \frac{T_i}{T_e}\right)\right] \\ &\simeq V_f + 2.7\frac{k_B T_e}{e}. \end{aligned} \tag{45}$$

And the heat flux parallel to the magnetic field, section 2.2.3, is given by:

$$q_w = \gamma T_e J_{sat}. \tag{46}$$

To understand how a Langmuir probe works in a tokamak, consider a small, electrically isolated section of the vacuum vessel. The current flowing through the probe must connect through the plasma back to the vacuum vessel somewhere. For a magnetized plasma, in the limit of no cross field electrical conductivity ($\sigma_\perp = 0$), that current must return through the sheath on the opposite end of the field line. Thus the return area is limited to the size of the probe and the maximum current it can pass is the ion saturation current. With a symmetric I-V it would operate like a double probe. However, in tokamak experiments a symmetric I-V is not seen. The probe collects more electron saturation current than ion saturation current. The cross field conductivity is clearly not zero. The current spreads across field lines to an area much larger than the probe, where the maximum current *density* is still limited to the ion saturation current, but now the area is not restricted to the flux tube.

Magnetic fields can make Langmuir probe interpretation challenging. The ion saturation current decreases with $\sin\theta$ over most angles between the magnetic field and the probe surface. However, at shallow angles the ion saturation current no longer decreases.

Using an array of tiltable Langmuir probes, Matthews did a dedicated set of experiments in the DITE tokamak exploring the changes to the I-V and fitted parameters over a range of incident angles [104]. The ratio of ion to electron saturation current dropped rapidly to below unity as the magnetic field becomes tangent to the surface. The electron saturation current dropped with the sine of the angle whereas the ion saturation current stopped decreasing when the angle was $\lesssim 5°$. The resulting fit for electron temperature increased by a factor of ~ 2 as the angle decreased. The floating potential increased to very near the plasma potential. To avoid these challenges in interpreting probe measurements at glancing angles the C-Mod Langmuir probes are constructed with their current collection areas proud to the local magnetic field. The divertor probes present a surface $\sim 10°$ into the magnetic field.

One of the major drawbacks of Langmuir probes is that they only measure T_e, not T_i. The ion temperature requires a more complicated

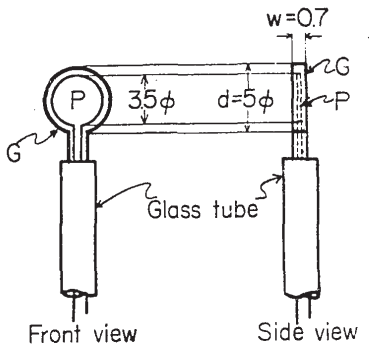

Figure 10: Diagram of Katsumata's original ISP. Copyright 1967 The Japan Society of Applied Physics [72]. Reproduced with permission.

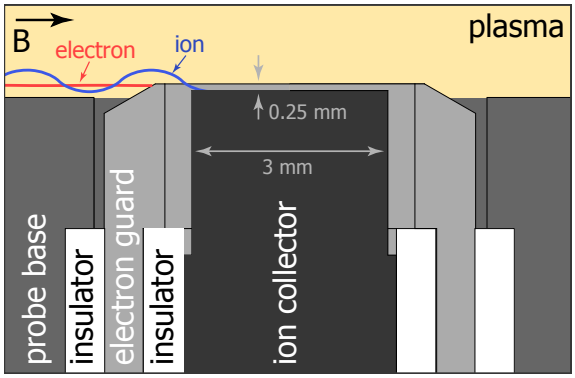

Figure 11: Cross section of the C-Mod ISP showing typical path of ions and electrons. The Guard magnetically shadows electrons from reaching the Collector.

probe to isolate the ions from the electrons. The subject of the following sections is how different probe configurations attempt to isolate electrons and ions by geometry (ISP in section 2.6) or electro-statically (RFA in section 2.7).

2.6 ION SENSITIVE PROBE

Ion sensitive probes have been in use since the early days of magnetic fusion research. They were originally developed by Katsumata (fig. 10) to interrogate ions and the plasma potential in RHITOP III, a figure 8 torus [72]. Their use has been extended to Q-machines [45, 69, 70, 109, 117], tokamaks [4, 6, 7, 8, 10, 20, 21, 22, 33, 34, 36, 115, 116, 135, 146, 147], mirror machines [44, 107, 136], a simple plasma device [9], stellarators [17, 42, 43, 66], ECH plasmas [15, 62], linear plasma devices [5, 18, 41, 114, 119, 142], a torsatron [5], a magnetron [5], and even an unmagnetized plasma [118].

At the most basic level, an ISP uses the large difference in Larmor radii ($\rho = \sqrt{2mk_BT}/ZeB$, with m the mass, k_B Boltzmann's constant, T the temperature, Ze the charge, and B the magnetic field) between ions and electrons: $\rho_i/\rho_e = \sqrt{m_i/m_e} \approx 60$, for $T_i = T_e$ in deuterium. An ISP typically consists of two concentric cylinders with their axes normal to the magnetic field, see fig. 11. The inner cylinder (here called the Collector, in other works called the P-electrode) is recessed at least the electron Larmor radius behind the outer cylinder (here called the Guard, in other works called the Wall or G-electrode). The recess prevents line-of-sight access by the electrons along the magnetic field to the Collector. In principle the only current appearing on the Collector is that due to ions. In practice it is found that the Guard needs to be biased slightly positive with respect to the Collector [71]. Additionally, the Collector must be about an ion Larmor radius behind the Guard for proper operation.

2.6.1 *Ion Temperature*

Positive bias of the Collector electrostatically repels ions, much like a negatively biased Langmuir probe repels electrons (albeit in the presence of a constant ion flux for Langmuir probes). Sweeping the Collector bias samples an energy integral of the ion energy distribution perpendicular to the magnetic field. For a Maxwellian energy distribution the resulting I-V relationship is an exponential,

$$I_C = \begin{cases} I_o & V \leqslant V_p \\ I_o \, e^{-\frac{eZ(V-V_p)}{k_B T_i}} & V > V_p \end{cases} . \tag{47}$$

Information about the density is captured in I_o [34, 44, 70], although a quantitative relationship is complicated by probe geometry as well as the ratio of parallel to perpendicular ion temperature $T_{i,\parallel}/T_{i,\perp}$.

An assumption must be made on the effective ion charge, Z, to get T_i from a fit of eq. (47) to the data. Kinetic simulations of ion collection by an RFA have been made to investigate the impact of a C^{4+} impurity fraction, ranging from 0 % to 100 % in an otherwise pure $Z = 1$ plasma [80]. If Z in eq. (47) is taken to be that of a pure plasma, a less than 20 % error in T_i will occur for impurity fractions up to 50 %. Although the details of particle collection are different, it is likely that similar results apply for the ISP.

Measurements of ion temperature from ISPs have been found to be consistent with other diagnostics; including favorable comparisons with the plate temperature and collisionless theory in a Q-machine [69, 70], spectroscopic Ba^+ measurements in W II A stellarator [66], a Faraday cup on the DIVA tokamak [116], a gridded analyzer in the MIX 1 mirror machine [107], a CNPA in the GAMMA-10 mirror machine [136], and a segmented tunnel probe in the CASTOR tokamak [4]. During Alfven wave heating in the TCA tokamak the ISP T_i increased by 50 % and the time history qualitatively followed a neutral particle analyzer [36]. Comparison of an ISP with an end loss ion spectrometer in the TMX-U mirror machine matched with no auxiliary heating, while the ISP measured hotter ion temperature during ion cyclotron resonance heating—a strong indication that it measures the perpendicular ion energy component [44]. Use of a gridded ISP allowed the probe to be used like an RFA and measure the parallel ion energy distribution by turning the probe into the magnetic field [117]. In a steady plasma the parallel and perpendicular distributions matched. But, in the presence of an excited instability expected to anisotropically heat the plasma, only the perpendicular ion distribution was changed.

There also have been discrepancies. The ISP-inferred ion temperature in a Q machine was consistently higher than the plate tempera-

ture and theory [109]. Comparison of an RFA data point (~ 30 eV) and an ion sensitive probe profile (~ 18 eV at the RFA position) showed disagreement between the measurement techniques in the WEGA tokamak [37, 103].

2.6.2 *Plasma Potential*

There have been multiple ways in which an ISP has been used to measure the plasma potential. In his original paper Katsumata used an ISP that collected both ions and electrons. He indicated that the plasma potential was at a weakly defined knee [72]. Falabella, using an ISP that collected only net ions, had great success in matching fitted V_p from eq. (47) to plasma potential measurements from a thallium beam probe over nearly 1 kV range [44].

Adámek used an ISP with an insulating Guard, called a Ball-Pen Probe (BPP) to measure the plasma potential [8]. He proposed that if the electron saturation current ($I_{sat,e}$) could be reduced such that it was about the same as the ion saturation current ($I_{sat,i}$) that the probe would float at the plasma potential:

$$V_f = V_p - \frac{k_B T_e}{e} \ln\left(\frac{I_{sat,e}}{I_{sat,i}}\right), \tag{48}$$

with V_f the floating potential and T_e the electron temperature. This ratio is typically much greater than unity for a standard Langmuir probe in a deuterium plasma (with $T_i = T_e$ the probe floats at $\sim 2.7\frac{k_B T_e}{e}$ below the plasma potential). Recessing the BPP Collector behind an insulating Guard reduces the electron saturation current such that it is about the same as the ion [8]. Initially it was found that the plasma potential given by a BPP was much lower than that of a Langmuir probe (a difference of about 40 V) [8]. Further comparisons of the same BPP to an emissive probe showed that the two measurements tracked each other. But the BPP systematically measured a higher potential (about $0.7\frac{k_B T_e}{e}$, or 6 V) [7]. This difference accounted for by including space charge limiting the emissive probe current [153]. In Ref. [135] BPPs with different diameters (1 mm, 2 mm and 4 mm) were tested. Variations in their floating potential were observed and attributed to the probes being on different flux surfaces. BPP measurements of plasma potential were also performed during the large plasma fluctuations known as ELMs [6].

A thorough study of the importance in geometry of a BPP in low-temperature magnetized plasmas was performed in Mirabelle [18]. In this device the electrons were magnetized yet the ions were unmagnetized (ion-ion collision frequency much greater than cyclotron frequency); unlike the typical tokamak plasma where both electrons and ions are magnetized. It was shown that the BPP plasma potential measurement agreed with that measured by a Langmuir probe (us-

ing the location of the maximum of the first derivative of the Langmuir probe I-V) for a certain range of probe diameter and retraction depth as well as magnetic field strength. Smaller diameter probes were able to measure the plasma potential over a wider range of magnetic field yet required a more precise retraction depth than larger diameter probes. It was suggested that the radius of the probe should be smaller than the Debye length to prevent enhanced electron collection through $\vec{E} \times \vec{B}$ drift. Additionally, the probe radius should be much smaller than the electron Larmor radius to sufficiently reduce the electron flux onto the Collector. The floating BPP was also found to be close to the plasma potential in a magnetron, linear plasma device, and torsatron, each a low-temperature magnetized plasma with different electron energy distribution functions (Druyvesteynian, double Maxwellian, and Maxwellian, respectively) [5].

Ochoukov compared a more traditionally swept ISP with an emissive probe both in a linear plasma device [114] and a tokamak [115]. The Guard and Collector were swept together with a constant offset bias. By comparing to an independent potential measurement of an emissive probe, the plasma potential was identified as the point where the probe current decayed to zero when the Collector was biased either above or below the Guard. It was mentioned in Ref. [114] that the collected current was three orders of magnitude in excess of the space charge limit. Thus, it is quite clear that the current should go to zero when a space charge limited probes is at the plasma potential, as is demonstrated in chapter 7.

2.6.3 *Variations on the Ion Sensitive Probe*

Although an ISP with two concentric electrodes is the most common, there have been many variations on this design. The variations can be split into three categories:

1. Ball-Pen Probes—has an insulator for a Guard and the Collector is often conical.

Although it was originally created to measure the plasma potential, as described above, ion temperature measurements have also been attempted with a swept BPP [3]. Here an exponential with a current offset, much like a Langmuir probe measurement of T_e, was fit to the I-V with positive current collected (sign convention for this work was positive current is net electrons collected). This technique relies on a constant flux of electrons to the probe through the whole fitting region. If the electron flux is not yet saturated by the point of positive current, this technique would yield an over-estimate of the ion temperature. This technique is advantageous because it only requires one electrode to make an ion temperature measurement, however it would greatly benefit from benchmarking by other techniques.

A BPP-like "hollow" probe was used in an unmagnetized processing plasma [118]. The recessed probe reduced the electron saturation flux, allowing for the break in slope of the I-V at ion beam energy to be more easily found. Comparisons of ion beam energy with an electrostatic energy analyzer (RFA) and a planar probe were quite good. The hollow probe had the advantage of being much smaller and easily managed than with the RFA within the processing plasma.

2. ISPs with a grid over the Guard—the grid ensures that no electrons are allowed within the probe volume.

Four ISPs have had a grid over the Guard [9, 62, 107, 117]. A grid over the Guard can ensure that no plasma electrons are allowed to the Collector by either increasing the geometric shadowing or presenting apertures smaller than the Debye length to shield out any potentials from within the probe volume penetrating into the plasma. However, depending on the bias arrangement, secondary electrons from the Guard grid may make it to the Collector. In Ref. [107] the gridded Guard was grounded. In Refs. [9, 117] the gridded Guard was held at a negative bias to reject plasma electrons; making the probe more like a traditional RFA than an ISP. In Ref. [117] the ISP was even turned face-on into the magnetic field and used as an RFA, with very similar results for both directions. In Ref. [62] the Guard and Collector were swept together. Without the grid there was a large electron current to the Collector through the whole bias sweep; with the grid electron collection was eliminated.

3. ISPs with more than two electrodes—an additional electrode has been useful in controlling electrons and exploring their collection.

There have been many ISPs built with more than two electrodes [22, 44, 68, 71, 107, 119, 136, 142]. Two had multiple Collectors to explore the $\vec{E} \times \vec{B}$ drift pattern of electrons [68, 71, 142]. In Refs. [68, 71] two concentric Collectors were used to show that only the Collector biased more positively collected net electron current. In Ref. [142] the Collector was split into two D-shaped electrodes. It was demonstrated that the electron current was stronger on one side as predicted by the $\vec{E} \times \vec{B}$ drift model.

In Ref. [107] an additional secondary suppressor ring (Repeller) was installed between the gridded Guard and the Collector. It was thought that biasing the Repeller would prevent secondary electrons generated on the probe wall from getting to the Collector. With the Repeller unbiased, the Collector had net electron current at high bias. With the suppressor biased above the Collector, the Collector had no regions of net electron current. Biasing the Repeller above the Collector gives it essentially the same function as the Guard in a standard ISP. Thus it is not entirely clear that the grounded, gridded Guard

was necessary. The net electron collection may have not been due to secondary electrons but due to incomplete electron attenuation by the grid, allowing plasma electrons to $\vec{E} \times \vec{B}$ drift onto the Collector.

The ISP in Ref. [136] also contained a Repeller electrode, although in this case to repel secondary electrons generated at the Collector. In measuring current, secondary electrons leaving the Collector look the same as ions arriving. When the Repeller was switched from biasing above the Collector (not returning the secondary electrons to it) to biasing below the Collector (returning secondary electrons to it) it was found that the Collector current decreased; indicating that it functioned as expected. The relative bias between the Collector and Guard was not given; however, in this arrangement it is clear that the Repeller is not acting as a Guard as it may have been in Ref. [107]. But it is not entirely clear whether it is indeed returning secondary electrons to the Collector or pulling ions away as both would have the same effect on the current.

The ISP in Ref. [44] had three concentric electrodes. The outermost was left floating and the inner two as a normal Guard and Collector pair. The purpose of the floating electrode was not stated. Similarly, the original C-Mod ISP had a floating electrode around the Guard section 3.3.5. The hope with the C-Mod ISP was to bias the other electrodes with respect to the floating potential and ride on top of the plasma fluctuations. It was found that the density fluctuations were more problematic than the floating potential fluctuations. So the floating electrode was replaced with a Langmuir probe kept in ion saturation. The Collector current was normalized to the ion saturation signal to normalize out the plasma density fluctuations. The ISP in Ref. [119] also had a Langmuir probe kept in ion saturation. However, this signal was used as a threshold to identify when the probe was in or outside of a density fluctuation (blob). The ISP data was then binned into data in blobs or not in blobs. The temperature was found to be higher within the blobs.

2.6.4 *Modeling of Ion Sensitive Probes*

Finite element methods were used to model space charge in Ref. [44]. The potential was calculated assuming a sheet charge at each spatial point. Results in the limit of low-temperature were found to be consistent within 10 % of the Child-Langmuir formula. Graphs were presented giving the voltage increase (normalized to ion temperature) and plotted versus the tip voltage (normalized to ion temperature) for various ion temperatures at two densities. The higher density and lower temperatures displayed larger relative voltage increases. A simulated I-V curve was shown demonstrating that the space charge rounded the usually sharp transition between the ion saturation and exponential regions. Simulated rounding was more

pronounced than experimental, indicating experimental space charge may not have been as strong as the simulation predicted.

In Ref. [136] numerical calculation of ion orbits using a Monte Carlo technique were performed with the real probe geometry. A correction factor as a function of ion temperature was found to relate the probe current collected to density. The potential profile in front of the probe was calculated with the finite element method. It was found that the ion temperature from fitting the simulated I-V was 20 % lower than the inputted ion temperature. Both the simulated and experimental I-Vs had rounded knees typical of a space charge limited probe. However space charge limited current was not discussed in context of the experiment or simulation.

There have been Particle-In Cell (PIC) simulations of ion sensitive probes [40, 86, 87]. A 2D simulation that modeled an ISP as an infinitely long channel explored the $\vec{E} \times \vec{B}$ drift of electrons around the probe [40]. It was demonstrated that equipotential surfaces connected the Collector to the plasma outside the probe when the Collector was biased above the Guard. Electrons flowed along the equipotential surfaces to the Collector. Due to the asymmetry in the drift (the electric field points in opposite directions on opposite sides of the probe), the electrons are collected predominately on one side of the probe. When the Collector and Guard were biased together, the equipotential surfaces no longer connected from the plasma to the Collector and there was no electron current to the Collector.

Similar $\vec{E} \times \vec{B}$ drift results were also seen by Komm in 3D PIC simulations (figs. 12 and 13) [86]. Komm also found that the temperature from an exponential fit to a simulated I-V was within 3 % of the injected ion temperature. Initial 2D simulations of a BPP were published in [87].

An additional mechanism that can distort the I-V characteristic is selective loss of ions due to probe geometry, an issue considered in Refs. [34, 109] and extensively in Ref. [44]. Ignoring distortions to the ion trajectories due to the probe bias, ions with a Larmor radius less than the probe recess ($\rho_i < d$) should not make it to the Collector. This geometric shadowing would simply truncate the distribution, giving lower fitted saturation current and higher plasma potential.

Geometric shadowing of particle collection also depends on the pitch angle, only ions with a high enough parallel velocity for a given perpendicular velocity can make it past the Guard and onto the Collector. Pitch angle shadowing has a more complicated effect on the I-V. A numerical analysis of ion orbits and collection was performed in Ref. [143]. This was done assuming that the potential inside the probe volume was unaffected by the ion space charge and that there were no electrons in the probe volume. It was found that the optimal probe geometry to minimize errors in fitting an exponential to the I-V was a probe radius: $r \simeq 1.5\rho_i$, and probe recess distance: $d \simeq 0.15\rho_i$

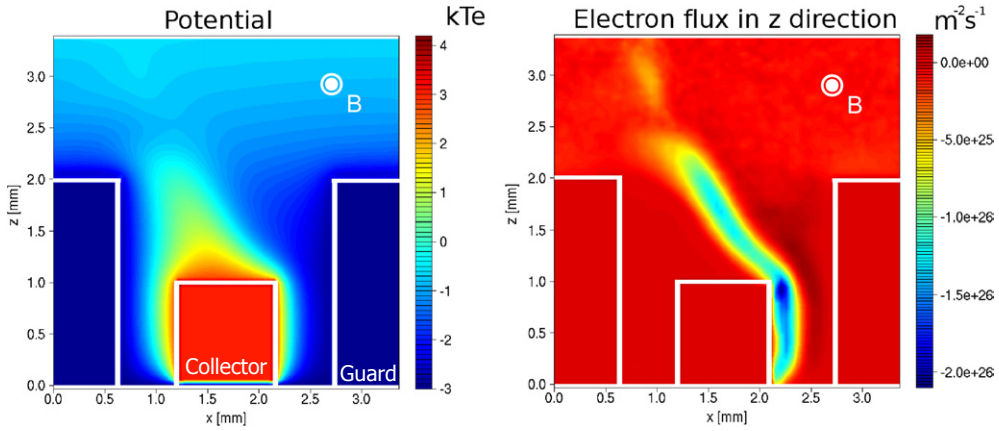

Figure 12: PIC simulation of electrons $\vec{E} \times \vec{B}$ drifting into the Collector. When the Guard potential is less than the Collector, the electrons $\vec{E} \times \vec{B}$ drift along equipotentials to the Collector. Reproduced with permission from [86].

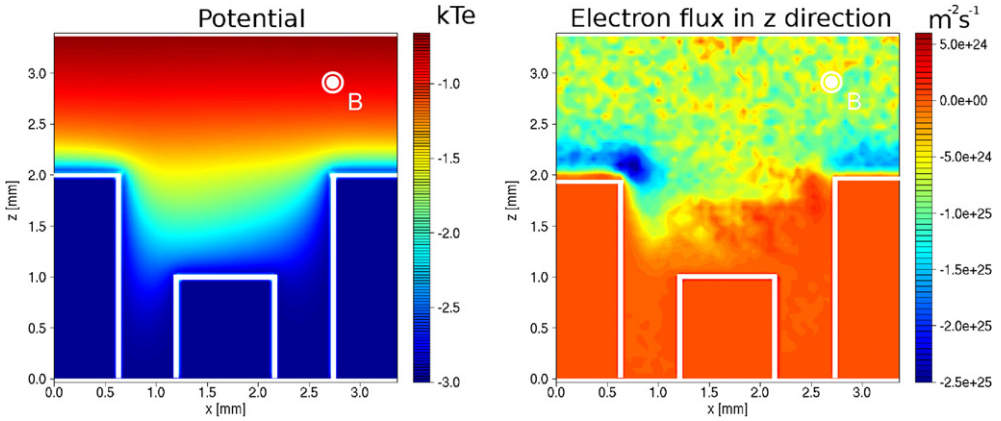

Figure 13: PIC simulation of an ISP. When the Guard potential is greater than or equal to the Collector, no potential surface from the plasma connects to the Collector. Thus no electrons may $\vec{E} \times \vec{B}$ drift to the Collector. Reproduced with permission from [86].

(much smaller than what is typically constructed). For the range of probe geometries simulated ($0.5 < {}^{r}/_{\rho_i} < 5.0$ and $0.1 < {}^{d}/_{\rho_i} < 1.0$) the degree of I-V distortion depended only on the recess distance, d, with stronger rounding at larger d. The rounding due to selective shielding of ions shown in these simulations is much less pronounced than that due space charge limited current and it unlikely to significantly affect probe measurements.

2.7 RETARDING FIELD ANALYZER

RFAs have been the most widely used diagnostic of T_i in tokamaks [32, 37, 38, 55, 56, 57, 74, 75, 76, 78, 79, 80, 81, 82, 83, 84, 91, 101, 102, 103, 106, 111, 112, 113, 121, 122, 123, 124, 125, 144, 149, 150, 151, 152]. They are also used in other plasma physics experiments, and thus have many design and operation considerations. However, here we focus on concerns specific, but not all unique, to magnetic fusion devices and especially to tokamaks.

A retarding field analyzer uses a series of biased grids to interrogate the energy distribution of a desired plasma species (i. e., ions or electrons). Typically, plasma ions and/or electrons enter the analyzer volume through a narrow slit. The slit width is chosen to be on order the Debye length ($\lambda_D = \sqrt{\epsilon_0 k_B T/ne^2}$), typically 5 µm to 50 µm in the boundary of C-Mod) to insure that no internal biases are seen by the plasma and that all particles that enter the probe have passed through a well-defined sheath potential structure. If the slit is wider than a few λ_D then a full sheath potential drop is not developed and the electric field in front of the probe is not uniform. Parallel ion energy is converted into perpendicular and proper operation is lost [121]. In low-energy density plasmas a grid, thin foil, or micro-channel plate may serve as the Slit plate. However, a more robust design is necessary for C-Mod plasmas.

2.7.1 *Ion Temperature*

In measuring T_i (see fig. 14) the voltage of Grid 1 (V_1) rejects ions without sufficient energy to overcome it. Grid 2 is held at a sufficiently negative voltage (V_2) such that no plasma electrons may reach the Collector. It is crucial that Grid 2 be at the lowest potential in the system so secondary electrons (which have an assumed limited kinetic energy) emitted from the Collector return (as well as those released from ions rejected by Grid 1 impacting the rear of the Slit). This ensures that the only current to the Collector is due to ions with enough energy to overcome V_1. Secondary electrons from Grid 2 could contribute to the Collector current, but in practice their current is insignificant because of the low net yield from ions impacting the rear of the grid. Sweeping V_1 produces a current on the Collector

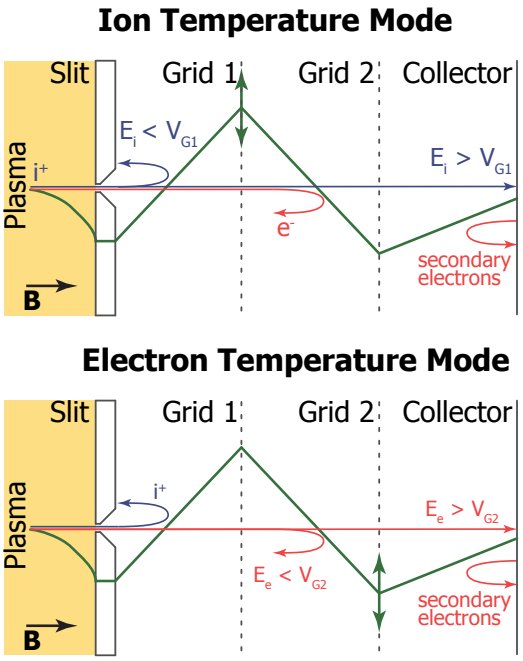

Figure 14: Typical operating modes of a 2-grid retarding field analyzer. Each diagram shows a 2D slice through the probe volume. The green line approximates the potential structure through the probe body. Is both cases the Slit is shown as floating. Plasma forms a sheath over the Slit plate. When measuring the ion temperature, electrons are rejected from the Collector by a very negative Slit and/or Grid 2. Grid 1 is swept; only ions with enough energy to overcome the Grid 1 bias are incident on the Collector. When measuring the electron temperature, Grid 1 is biased very positive to reject all ions from the Collector. Grid 2 is swept; only electrons with enough energy to overcome the Grid 2 bias are incident on the Collector. In both scenarios, Grid 2 is always more negative than the Slit or Collector to ensure that secondary electrons formed at the Collector are recollected. Ion- or electron-induced secondary electrons from Grid 2 could also contribute to the Collector current but are assumed to be negligible.

that corresponds to a velocity moment of the ion distribution function for ions with energy parallel to the magnetic field above the bias potential,

$$I_C = A_{slit} e Z \int_{\sqrt{2eZV_1/m_i}}^{\infty} \xi_{total} v_{\|} f(v_{\|})\, dv_{\|}, \tag{49}$$

where I_C is the current on the Collector, A_{slit} is the area of the slit, e is the unit electric charge, Z is the charge of the ions, m_i is the ion mass, ξ_{total} is the total system ion transmission factor, and $f(v_{\|})$ is the ion distribution function in velocity parallel to the magnetic field which depends on T_i. In an ideal system the distribution function may be inferred by differentiation the I-V characteristic with respect to voltage. In reality, the quality of the data is not good enough to differentiate (due to both noise and the present inability to sweep faster than turbulent fluctuations). A new regularization technique has been developed to get the distribution function without differentiating [77]. Although more typically a model I-V characteristic function is fitted to the data to extract the ion temperature. For a half-Maxwellian distribution shifted by the sheath voltage, a functional form for the Collector current is:

$$I_C = \begin{cases} I_o & V_1 \leqslant V_S \\ I_o\, e^{-\frac{eZ(V_1 - V_S)}{k_B T_i}} & V_1 > V_S \end{cases}, \tag{50}$$

where $I_o = A_{slit} J_{sat} \xi_{total}$. It is assumed that ξ_{total} is a weak function of parallel ion velocity. A fit of eq. (50) to the experimental data results

in a value for T_i/Z, along with I_o and V_s; hence an assumption must be made for the charge of the plasma species. Kinetic simulations of ion collection by a RFA have been made to investigate the impact of a C^{4+} impurity fraction ranging from 0 % to 100 % in an otherwise pure $Z = 1$ plasma [80]. If Z in eq. (50) is taken to be that of a pure plasma, a less than 20 % error in T_i will occur for impurity fractions up to 50 %.

Care must be taken in interpreting T_i measurements in flowing plasma and under conditions when the ion distribution function can be anisotropic along field lines. Measurements in Alcator C with a double-sided RFA, Janus, noted that T_i was asymmetric looking "upstream" (facing into the flow) versus "downstream" (facing away from the flow) along field lines [151]. The physical mechanism was unknown at the time, but asymmetries were well documented over a wide range of plasma conditions. Since then, at least one mechanism that can cause directional asymmetries has become understood. Using the kinetic model of Chung and Hutchinson [28] Valsaque et al. found that a flowing plasma would make the T_i measurements appear asymmetric [148]. In the absence of the disturbing probe, T_i was found to be well represented by the arithmetic average of the upstream and downstream ion temperatures. This model has been extended by Gunn et al. to include ion-ion collisions, demonstrating that the apparent temperature asymmetry depends on, in addition to the plasma flow, the ratio of ion to electron temperature and the collisionality [54]. Motivated by these observations, we have gone to exceptional effort to fit two RFAs within a single probe head.

2.7.2 *Electron Temperature*

In addition to measuring T_i, the RFA can be used to explore T_e. Comparisons between T_e measured with an RFA and a Langmuir probe are generally favorable [151]. The RFA has the advantage of its measured current being due to only electrons whereas a Langmuir probe relies on a constant ion current through its sweep below the floating potential. Thus any departure from the exponential typically used to fit experimental RFA data, eq. (51) discussed below, is due to a non-Maxwellian electron energy distribution. With a Langmuir probe there remains the ambiguity to whether the departure from an exponential is due to a non-Maxwellian electron population or changes in the ion current collected.

The electron temperature may also be found by changing the bias arrangement of the grids (see fig. 14). A functional fit to electron collection data is analogous to eq. (50):

$$I_C = \begin{cases} I_o \, e^{\frac{e(V_2 - V_S)}{k_B T_e}} & V_2 \leqslant V_S \\ I_o & V_2 > V_S \end{cases}, \tag{51}$$

Although, here ξ_{total} is different for electrons versus ions. Directional asymmetries in electron temperature have also been seen in scrape-off layer plasmas. In Alcator C-Mod, electron temperature asymmetries on the high field side midplane were associated with poloidally asymmetric heat transport [96]. Due to ballooning-like transport the majority of plasma in the SOL originates at the outer midplane. The plasma that transports into the flux tubes on either side of the probe could be from two different sources, one side dominated by hot plasma from the core and the other side from the cold electrons rejected by the sheath voltage in the divertor and from ions created from cold, recycling neutrals. Thus a two-sided RFA could be used to study the physics of asymmetric heat transport. Although separating the effects of asymmetric heat transport and apparent asymmetries due to a flowing plasma may be challenging.

2.7.3 *Single Particle Motion*

RFA operation and analysis relies on undisturbed, single-particle motion within the probe cavity such that the ion distribution function is not appreciably changed from that outside the probe. Wan, Nachtrieb, and Kocan [83, 112, 152], among others, have done extensive work demonstrating that, for typical slit and grid geometries, selective removal of ion orbits does not significantly affect fitted T_i nor do misalignments to the magnetic field up to $\sim 10°$. It is also important that the ions are collisionless within the probe. Following Nachtrieb [112], the mean time between collisions for deuterium ions in the external plasma at 50 eV and $10^{18}\,m^{-3}$ is $\sim 40\,\mu s$, much longer than the time for a particle to transverse the length of the analyzer, $\sim 10\,ns$; therefore ion-ion collisions and a redistribution of ion energies within the probe are highly unlikely. Unless the neutral density in the analyzer greatly exceeds the ion density, ion-neutral collisions are also unlikely. Thus the distribution of ions within the probe is that of those fallen through a sheath and eq. (50) is a valid functional form to fit to experimental data.

2.8 CHARGE EXCHANGE RECOMBINATION SPECTROSCOPY

CXRS measurements of impurity ion temperature utilize the interaction between a light impurity ion and a neutral particle [46, 65]. In a charge exchange collision, the neutral particle donates its electron to the ionized impurity. The electron is captured in an excited state and radiatively decays. Due to the finite ion temperature, this line radiation is Doppler broadened, fig. 15. The ion temperature is found from a 3-Gaussian fit to the spectrum, taking into account Zeeman splitting due to the magnetic field [16]. Spatial localization is provided by a "cross-beam" technique, i. e., a local source of neutrals to donate CX electrons that is viewed perpendicularly, be it a high-energy neutral beam or thermal gas puff.

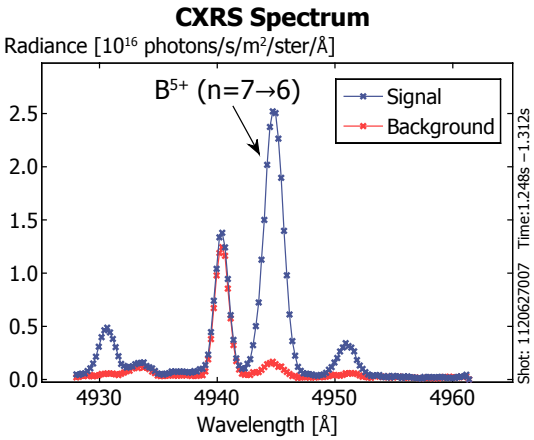

Figure 15: CXRS spectrum from C-Mod. The background is subtracted from the active signal and a 3-part Gaussian, taking Zeeman splitting into account, is fitted to the spectrum to get the B5+ ion temperature.

2.9 THERMOCOUPLES

Thermocouples are one of the most widely used temperature measurement devices [14, 126]. They are simply a pair of dissimilar metal wires and a voltage measurement. However, since their performance relies on the thermojunction—where the two metals meet—to come into thermal equilibrium with what is being measured, this restricts their use in fusion reactors to regions where they can survive.

The basic physics of a thermocouple is as follows. A temperature gradient in a conductor generates a potential gradient:

$$\nabla V_{emf} = -S\nabla T, \tag{52}$$

with S the Seebeck coefficient. Diffusion of the charge carriers is impeded by scattering, which is energy dependent. Thus the hotter charge carriers have a different scattering cross section than the colder. Because the details of this scattering is different for different materials, the Seebeck coefficient is also different. Since the voltage generated depends on the temperature gradient, it must be taken with reference to a known temperature. This is often done with an ice-point compensated circuit where the thermocouple leads connect to the circuit at a known temperature, section 4.1.1.

To understand why a thermocouple needs two metals, consider two different cases, fig. 16:

1. A metal wire with the open ends held at temperature T_1 and the middle at temperature T_2

2. Two joined metal wires with the open ends held at T_1 and the closed ends held at T_2

In both cases, by eq. (52), there will be a thermoelectric voltage generated between T_1 and T_2. In the first case, since each leg has the same Seebeck coefficient, the voltages will be the same magnitude and opposite sign in each leg (i. e., $V_1 - V_2 = V_3 - V_2$). No net voltage will be generated across the open end. In the second case, since each leg is a different metal with a different Seebeck coefficient, the voltage magnitudes will be different. Thus there will be a net voltage generated across the open ends (i. e., $V_1 - V_2 \neq V_3 - V_2$). ⋆

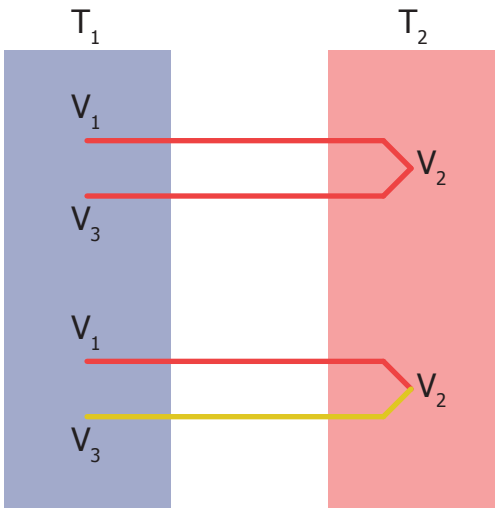

Figure 16: A thermocouple needs to be made out of metals with different Seebeck coefficients. If they are the same (top), then the net voltage generated is zero. If they are different (bottom), then there is a net voltage generated.

BIBLIOGRAPHY

[1] Z. Abou-Assaleh, J. P. Matte, T. W. Johnston, and R. Marchand. Fokker-Planck modelling of edge plasma near the neutralizer plate in a tokamak. *Contributions to Plasma Physics*, 32(3-4):268–272, 1992.

[2] Z. Abou-Assaleh, M. Petravic, R. Vesey, J. P. Matte, and T. W. Johnston. Non-local transport in a tokamak plasma divertor with recycling. *Contributions to Plasma Physics*, 34(2-3):175–179, 1994.

[3] J. Adámek, J. Horacek, H. W. Müller, R. Schrittwieser, M. Tichy, A. H. Nielsen, and The ASDEX-U Team. Fast ion temperature measurements using ball-pen probes in the SOL of ASDEX Upgrade during L-mode. In *38th EPS Conference on Plasma Physics*, 2011.

[4] J. Adámek, M. Kočan, R. Pánek, J. P. Gunn, E. Martines, J. Stöckel, C. Ionita, G. Popa, C. Costin, J. Brotánková, R. Schrittwieser, and G. Van Oost. Simultaneous measurements of ion temperature by segmented tunnel and Katsumata probe. *Contributions to Plasma Physics*, 48(5):395–399, 2008.

[5] J. Adámek, M. Peterka, T. Gyergyek, P. Kudrna, M. Ramisch, U. Stroth, J. Cavalier, and M. Tichỳ. Application of the ball-pen probe in two low-temperature magnetised plasma devices and in torsatron TJ-K. *Contributions to Plasma Physics*, 53(1):39–44, 2013.

[6] J. Adámek, V. Rohde, H. W. Müller, A. Herrmann, C. Ionita, R. Schrittwieser, F. Mehlmann, J. Stöckel, J. Horacek, J. Brotánková, and ASDEX Upgrade Team. Direct measurements of the plasma potential in ELMy H-mode plasma with ball-pen probes on ASDEX Upgrade tokamak. *Journal of Nuclear Materials*, 390-391:1114 – 1117, 2009.

[7] J. Adámek, J. Stöckel, I. Duran, M. Hron, R. Panek, M. Tichy, R. Schrittwieser, C. Ionita, P. Balan, E. Martines, and G. Van Oost. Comparative measurements of the plasma potential with the ball-pen and emissive probes on the CASTOR tokamak. *Czechoslovak Journal of Physics*, 55:235–242, 2005.

[8] J. Adámek, J. Stöckel, M. Hron, J. Ryszawy, M. Tichy, R. Schrittwieser, C. Ionita, P. Balan, E. Martines, and G. Oost. A novel approach to direct measurement of the plasma potential. *Czechoslovak Journal of Physics*, 54:C95–C99, 2004.

[9] W. E. Amatucci, D. N. Walker, G. Ganguli, D. Duncan, J. A. Antoniades, J. H. Bowles, V. Gavrishchaka, and M. E. Koepke. Velocity-shear-driven ion-cyclotron waves and associated transverse ion heating. *Journal of Geophysical Research*, 103(A6):11711, 1998.

[10] R. Armstrong, Å. Fredriksen, E. Grønvoll, D. Batani, A. Galassi, and F. Pisani. Measurements of ion temperature in weakly ionized, steady-state plasmas. *Physics Essays*, 10(3):483–491, 1997.

[11] N. Asakura, Y. Koide, K. Itami, N. Hosogane, K. Shimizu, S. Tsuji-Iio, S. Sakurai, and A. Sakasai. SOL plasma profiles under radiative and detached divertor conditions in JT-60U. *Journal of Nuclear Materials*, 241-243:559 – 563, 1997.

[12] N. Asakura, K. Shimizu, N. Hosogane, K. Itami, and S. Tsuji. Recycling enhancement with n_e and q_{eff} in high density discharges on JT-60U. *Nuclear Fusion*, 35(4):381–398, 1995.

[13] A. A. Batishcheva, O. V. Batishchev, S. I. Krasheninnikov, D. J. Sigmar, M. M. Shoucri, and I. P. Shkarofsky. Fokker-Planck simulation of electron transport in SOL plasmas with ALLA code. *Contributions to Plasma Physics*, 36(2-3):235–239, 2006.

[14] Robin E Bentley. *Handbook of Temperature Measurement Volume 3: The Theory and Practice of Thermoelectric Thermometry*. Springer, 1998.

[15] T. Bisong, M. Zhibin, S. Wulin, W. Zhenhui, C. Hong, and W. Jianhua. Measurement of ion parameters by ion sensitive probe in ECR plasma. *Plasma Science and Technology*, 13(1):68, 2011.

[16] A. Blom and C. Jupén. Parametrization of the Zeeman effect for hydrogen-like spectra in high-temperature plasmas. *Plasma Physics and Controlled Fusion*, 44(7):1229, 2002.

[17] G. Böhm, B. Kampmann, and H. Schulüter. Measurements with an ion-sensitive probe in stationary RF-discharges of stellarator configuration. *Physics Letters A*, 70(5):413–415, 1979.

[18] G. Bousselin, J. Cavalier, J. F. Pautex, S. Heuraux, N. Lemoine, and G. Bonhomme. Design and validation of the ball-pen probe for measurements in a low-temperature magnetized plasma. *Review of Scientific Instruments*, 84(1):013505–013505, 2013.

[19] S. I. Braginskii. Transport processes in a plasma. *Reviews of Plasma Physics*, 1:205, 1965.

[20] J. Brotánková, J. Adámek, J. Stöckel, E. Martines, G. Popa, C. Costin, R. Schrittwieser, C. Ionita, G. Van Oost, and L. Van

De Peppel. A probe-based method for measuring the transport coefficient in the tokamak edge region. *Czechoslovak Journal of Physics*, 56(12):1321–1327, 2006.

[21] D. Brunner, B. LaBombard, R. M. Churchill, J. Hughes, B. Lipschultz, R. Ochoukov, T. D. Rognlien, C. Theiler, M. V. Umansky, J. Walk, and D. Whyte. Comparison of ion temperature measurements in the boundary of the Alcator C-Mod tokamak and implications for ion fluid heat flux limiters. *Plasma Physics and Controlled Fusion*, 55:095010, 2013.

[22] D. Brunner, B. LaBombard, R. Ochoukov, and D. Whyte. Scanning ion sensitive probe for plasma profile measurements in the boundary of the Alcator C-Mod tokamak. *Review of Scientific Instruments*, 84:053507, 2013.

[23] D. Buchenauer, J. W. Cuthbertson, J. A. Whaley, J. D. Miller, J. G. Watkins, R. Junge, W. P. West, and D. N. Hill. Sheath physics study using the divertor materials evaluation system (DiMES) on DIII-D. *Proceedings of the Tenth Topical Conference on High Temperature Plasma Diagnostics*, 66(1):827–829, 1995.

[24] J. R. Cary, J. Candy, J. Cobb, R. H. Cohen, T. Epperly, D. J. Estep, S. Krasheninnikov, A. D. Malony, D. C. McCune, L. McInnes, A. Pankin, A. Balay, J. A. Carlsson, M. R. Fahey, R. J. Groebner, A. H. Hakim, S. E. Kruger, M. Miah, A. Pletzer, S. Shasharina, S. Vadlamani, D. Wade-Stein, T. D. Rognlien, A. Morris, S. Shende, G. W. Hammett, K. Indireshkumar, A. Yu Pigarov, and H. Zhang. Concurrent, parallel, multiphysics coupling in the FACETS project. In *Journal of Physics: Conference Series*, volume 180, page 012056. IOP Publishing, 2009.

[25] P. J. Catto and K-E. Yeoh. Long mean free path modifications of electron heat conduction. *Contributions to Plasma Physics*, 38(1-2):207–212, 1998.

[26] A. V. Chankin, D. P. Coster, R. Dux, Ch. Fuchs, G. Haas, A. Herrmann, L. D. Horton, A. Kallenbach, M. Kaufmann, Ch. Konz, K. Lackner, C. Maggi, H. W. Müller, J. Neuhauser, R. Pugno, M. Reich, and W. Schneider. SOLPS modelling of ASDEX upgrade H-mode plasma. *Plasma Physics and Controlled Fusion*, 48(6):839, 2006.

[27] R. Chodura. Plasma–wall transition in an oblique magnetic field. *Physics of Fluids*, 25(9):1628–1633, 1982.

[28] K-S. Chung and I. H. Hutchinson. Kinetic theory of ion collection by probing objects in flowing strongly magnetized plasmas. *Physics Review A*, 38(9):4721–4731, Nov 1988.

[29] R. H. Cohen and T. D. Rognlien. Finite mean-free-path effects in tokamak scrape-off layers. *Contributions to Plasma Physics*, 34(2-3):198–203, 1994.

[30] L. Costanzo, J. P. Gunn, T. Loarer, L. Colas, Y. Corre, Ph. Ghendrih, C. Grisolia, A. Grosman, D. Guilhem, P. Monier-Garbet, R. Reichle, H. Roche, and J. C. Vallet. Analysis of energy flux deposition and sheath transmission factors during ergodic divertor operation on Tore Supra. *Journal of Nuclear Materials*, 290-293:840 – 844, 2001.

[31] D. P. Coster, X. Bonnin, B. Braams, D. Reiter, R. Schneider, and the ASDEX Upgrade Team. Simulation of the edge plasma in tokamaks. *Physica Scripta*, T108(T108):7, 2004.

[32] D. B. Crockett, P. E. Phillips, W. A. Craven, A. J. Wootton, A. S. Wan, and T. F. Yang. Edge parameters from an energy analyzer and particle transport on TEXT-U. *Review of Scientific Instruments*, 66(1):366–368, 1995.

[33] R. P. da Silva and I. C. Nascimento. Simultaneous measurement of ion and electron temperatures in the scrape-off layer of a small tokamak. *Review of Scientific Instruments*, 62(11):2700–2708, 1991.

[34] R. P. da Silva, I. C. Nascimento, Jr. D. F. da Cruz, and A. Hershcovitch. Electrostatic ion probe for tokamak-plasma-edge diagnostic. *Review of Scientific Instruments*, 57(9):2205–2209, 1986.

[35] M. Day, B. Merriman, F. Najmabadi, and R. W. Conn. The effect of heat flux limiting on divertor fluid models. *Contributions to Plasma Physics*, 36(2-3):419–423, 1996.

[36] A. de Cambrier, G. A. Collins, P. A. Duperrex, A. Heym, F. Hofmann, Ch. Hollenstein, B. Joye, R. Keller, A. Lietti, J. B. Lister, F. B. Marcus, J. M. Moret, S. Nowak, A. Pochelon, W. Simm, and S. Veprek. Alfven wave heating on TCA. In *Proccedings of the 4th International Symposium on Heating in Toroidal Plasmas, International School of Plasma Physics and ENEA, Rome, March 21-28*, volume 310, pages 137–152, 1984.

[37] Mohamed El Shaer. *Plasma De Bord Dans un Tokamak Mesures et Simulation Numerique Application au Chauffage Hybride du Plasma de WEGA*. PhD thesis, L'Universite Scientifique et Medicale de Grenoble, June 1981.

[38] S. Elmore, S. Y. Allan, A. Kirk, G. Fishpool, J. Harrison, P. Tamain, M. Kočan, R. Gaffka, R. Stephen, J. W. Bradley, and the MAST Team. Upstream and divertor ion temperature measurements on MAST by retarding field energy analyser. *Plasma Physics and Controlled Fusion*, 54(6):065001, 2012.

[39] S. Elmore, S. Y. Allan, A. Kirk, A. J. Thornton, J. R. Harrison, P. Tamain, M. Kočan, and J. W. Bradley. Scrape-off layer ion temperature measurements at the divertor target in MAST by retarding field energy analyser. *Journal of Nuclear Materials*, 438:S1212–S1215, 2013.

[40] N. Ezumi. PIC simulation of the motion of plasma around ion sensitive probes. *Contributions to Plasma Physics*, 41(5):488–493, 2001.

[41] N. Ezumi, Zh. Kiss'ovski, W. Bohmeyer, and G. Fussmann. Ion sensitive probe measurement in the linear plasma device PSI-2. *Journal of Nuclear Materials*, 337-339:1106 – 1110, 2005.

[42] N. Ezumi, S. Masuzaki, N. Ohno, Y. Uesugi, S. Takamura, and LHD Experimental Group. Ion temperature measurement using an ion sensitive probe in the LHD divertor plasma. *Journal of Nuclear Materials*, 313-316:696 – 700, 2003.

[43] N. Ezumi, K. Todoroki, T. Kobayashi, K. Sawada, N. Ohno, M. Kobayashi, S. Masuzaki, and Y. Feng. Particle transport measurements in the LHD stochastic magnetic boundary plasma using Mach probes and ion sensitive probe. *Journal of Nuclear Materials*, 415(1):S430–S432, 2011.

[44] S. Falabella and A. W. Molvik. Ion temperature measurements on TMX-U using a gridless electrostatic analyzer. *Review of Scientific Instruments*, 61(7):1892–1899, 1990.

[45] Ambrogio Fasoli. *Study of Wave-Particle Interaction from the Linear Regime to Dynamical Chaos in a Magnetized Plasma*. PhD thesis, Ecole Polytechnique Federale de Lausanne, 1993.

[46] R. J. Fonck, D. S. Darrow, and K. P. Jaehnig. Determination of plasma-ion velocity distribution via charge-exchange recombination spectroscopy. *Physical Review A*, 29(6):3288, 1984.

[47] A. Froese, T. Takizuka, and M. Yagi. Kinetic particle simulation study of parallel heat transport in scrape-off layer plasmas over a wide range of collisionalities. *Plasma and Fusion Research*, 5(0):26–26, 2010.

[48] A. Froese, T. Takizuka, and M. Yagi. PIC simulation study of heat transport kinetic factors in scrape-off layer plasmas. *Contributions to Plasma Physics*, 52(5-6):534–538, 2012.

[49] W Fundamenski. Parallel heat flux limits in the tokamak scrape-off layer. *Plasma Physics and Controlled Fusion*, 47(11):R163, 2005.

[50] W. Fundamenski. *Power Exhaust in Fusion Plasmas*. Cambridge University Press, 2010.

[51] A. H. Futch, G. F. Matthews, D. Buchenauer, D. N. Hill, R. A. Jong, and G. D. Porter. Effects of neutral gas collisions on the power transmission factor at the divertor sheath. *Journal of Nuclear Materials*, 196-198:860 – 864, 1992.

[52] M. Greenwald. Density limits in toroidal plasmas. *Plasma Physics and Controlled Fusion*, 44(8):R27, 2002.

[53] B. Gulejová, R. A. Pitts, M. Wischmeier, R. Behn, D. Coster, J. Horacek, and J. Marki. SOLPS5 modelling of the type III ELMing H-mode on TCV. *Journal of Nuclear Materials*, 363:1037–1043, 2007.

[54] J. P. Gunn, V. Fuchs, and M. Kočan. A kinetic model of retarding field analyser measurements in strongly magnetized, flowing, collisional plasmas. *Plasma Physics and Controlled Fusion*, 55(4):045012, 2013.

[55] J. P. Gunn, V. Petrzilka, A. Ekedahl, V. Fuchs, E. Gauthier, M. Goniche, M. Kočan, J.-Y. Pascal, and F. Saint-Laurent. Measurement of lower hybrid hot spots using a retarding field analyzer in Tore Supra. *Journal of Nuclear Materials*, 390-391:904 – 906, 2009.

[56] J. P. Gunn, V. Petržílka, V. Fuchs, A. Ekedahl, M. Goniche, J. Hillaret, M. Kočan, and F. Saint-Laurent. Radial-poloidal mapping of the energy distribution of electrons accelerated by lower hybrid waves in the scrape-off layer. In *AIP Conference Proceedings*, volume 1187, page 391, 2009.

[57] H. Y. Guo, G. F. Matthews, S. J. Davies, S. K. Erents, L. D. Horton, R. D. Monk, and P. C. Stangeby. Ion temperature measurements in JET boundary plasmas using a retarding field analyser. *Contributions to Plasma Physics*, 36(S1):81–86, 1996.

[58] Y. Hayashi, N. Exumi, S. Masuzaki, H. Tanaka, M. Kobayashi, K. Sawada, N. Ohno, and the LHD Experiment Group. Edge and divertor plasma measurements with ion sensitive and Mach probes in LHD. *Journal of Nuclear Materials*, 438:S1228–S1231, 2013.

[59] Per Helander and Dieter J. Sigmar. *Collisional Transport in Magnetized Plasmas*. Cambridge University Press, 2005.

[60] A. Herrmann, M. Balden, W. Bohmeyer, and D. Hidebrandt. Investigation of infrared emission from carbon microstructure on a 30 micron spatial scale. *Physica Scripta*, 2004(T111):98, 2006.

[61] A. Herrmann, M. Laux, D. Coster, J. Neuhauser, D. Reiter, R. Schneider, M. Weinlich, and ASDEX-Upgrade Team. Energy transport to the divertor plates of ASDEX-Upgrade during

ELMy H-mode phases. *Journal of Nuclear Materials*, 220-222:543 – 547, 1995.

[62] T-Y. Hsieh, E. Kawamori, and Y. Nishida. Pure ion current collection in ion sensitive probe measurement with a metal mesh guard electrode for evaluation of ion temperature in magnetized plasma. *Review of Scientific Instruments*, 84(2):023502, 2013.

[63] T. Q. Hua and J. N. Brooks. Analysis of the tokamak sheath region with in-sheath ionization and transport of surface emitted particles. *Physics of Plasmas*, 1(11):3607–3613, 1994.

[64] A. Huber, A. Pospieszczyk, B. Unterberg, M. Brix, P. Mertens, V. Philipps, and B. Schweer. Spectroscopic measurements of the ion temperature profile in front of a limiter in TEXTOR-94. *Plasma Physics and Controlled Fusion*, 42:569, 2000.

[65] I. H. Hutchinson. *Principles of Plasma Diagnostics*. Cambridge University Press, 1990.

[66] P. Javel, G. Muller, A. v.H. von Oordt, and U. Weber. Wave propagation and RF plasma heating near and above the lower hybrid frequency in the W II A stellarator. In *Proccedings of the 7th European Conference on Controlled Fusion and Plasma Physics*, page 147, 1975.

[67] M. A. Jaworski, M. G. Bell, T. K. Gray, R. Kaita, J. Kallman, H. W. Kugel, B. LeBlanc, A. G. McLean, S. A. Sabbagh, V. A. Soukhanovskii, D. P. Stotler, and Surla V. Modification of the electron energy distribution function during lithium experiments on the National Spherical Torus Experiment. *Fusion Engineering and Design*, 2012.

[68] I. Katsumata. Ion temperature measurements of cesium plasma by ion sensitive probe. *Annual Review of Institute of Plasma Physics Japan*, 76, 1966-1967.

[69] I. Katsumata. Direct measurement of ion temperature by ion sensitive probe. *Annual Review of Institute of Plasma Physics Japan*, 59, 1967-1968.

[70] I. Katsumata. A measurement of $T_{i\perp}$ of Ba plasma in a Q-machine. *Proccedings of 3rd International Conference on Quiescent Plasmas, Elisinore September 20-24*, page 374, 1971.

[71] I. Katsumata. A review of ion sensitive probes. *Contributions to Plasma Physics*, 36(S1):73–79, 1996.

[72] I. Katsumata and M. Okazaki. Ion sensitive probe—A new diagnostic method for plasma in magnetic fields. *Japanese Journal of Applied Physics*, 6:123, 1967.

[73] S. A. Khan and T. D. Rognlien. Thermal heat flux in a plasma for arbitrary collisionality. *Physics of Fluids*, 24:1442, 1981.

[74] H. Kimura, H. Maeda, N. Ueda, M. Seki, H. Kawamura, S. Yamamoto, M. Nagami, K. Odajima, S. Sengoku, and Y. Shimomura. Heat flux to the material surfaces in a tokamak. *Nuclear Fusion*, 18:1195, 1978.

[75] H. Kimura, K. Odajima, T. Sugie, and H. Maeda. Application of multigrid energy analyzer to the scrape-off layer plasma in DIVA. *Japanese Journal of Applied Physics*, 18(12):2275–2281, 1979.

[76] M. Kočan, S. Y. Allan, S. Carpentier-Chouchana, P. de Marné, S. Elmore, T. Franke, J. P. Gunn, A. Herrmann, A. Kirk, M. Kubič, T. Lunt, H. W. Muller, R. A. Pitts, V. Rohde, and the ASDEX Upgrade Team. Ion energies and currents of type I and mitigated ELMs in the ASDEX Upgrade far scrape-off layer. *Nuclear Fusion*, 52:023016, 2012.

[77] M. Kočan, S. Y. Allan, S. Carpentier-Chouchana, P. de Marné, S. Elmore, J. P. Gunn, A. Herrmann, A. Kirk, M. Kubič, T. Lunt, H. W. Müller, R. A. Pitts, V. Rohde, and the ASDEX Upgrade Team. Inter-ELM ion transport in the ASDEX Upgrade far scrape-off layer. *Contributions to Plasma Physics*, 53(1):22–26, 2013.

[78] M. Kočan, F. P. Gennrich, A. Kendl, H. W . Müller, and the ASDEX Upgrade Team. Ion temperature fluctuations in the ASDEX Upgrade scrape-off layer. *Plasma Physics and Controlled Fusion*, 54(8):085009, 2012.

[79] M. Kočan and J. P. Gunn. Comparison of scrape-off layer profiles in outboard-versus inboard-limited plasmas in Tore Supra. *Plasma Physics and Controlled Fusion*, 52:045010, 2010.

[80] M. Kočan and J. P. Gunn. Influence of impurities on ion temperature measurements in the tokamak scrape-off layer by retarding field analysers. *Plasma Physics and Controlled Fusion*, 53:085016, 2011.

[81] M. Kočan, J. P. Gunn, S. Carpentier-Chouchana, A. Herrmann, A. Kirk, M. Komm, H. W. Müller, J. Y. Pascal, R. A. Pitts, V. Rohde, P. Tamain, and ASDEX Upgrade and Tore Supra Teams. Measurements of ion energies in the tokamak plasma boundary. *Journal of Nuclear Materials*, 415(1):S1133–S1138, 2011.

[82] M. Kočan, J. P. Gunn, J.-Y. Pascal, G. Bonhomme, P. Devynck, I. Duran, E. Gauthier, P. Ghendrih, Y. Marandet, B. Pegourie, and J.-C. Vallet. Measurements of scrape-off layer ion-to-electron temperature ratio in Tore Supra ohmic plasmas. *Journal of Nuclear Materials*, 390-391:1074 – 1077, 2009.

[83] M. Kočan, J. P. Gunn, J.-Y. Pascal, G. Bonhomme, C. Fenzi, E. Gauthier, and J.-L. Segui. Edge ion-to-electron temperature ratio in the Tore Supra tokamak. *Plasma Physics and Controlled Fusion*, 50(12):125009 (10pp), 2008.

[84] M. Kočan, J. P. Gunn, J.-Y. Pascal, and E. Gauthier. Ion temperature measurements in the Tore Supra scrape-off layer using a retarding field analyzer. *Contributions to Plasma Physics*, 50:836, 2010.

[85] M. Kočan, R. Panek, J. Stockel, M. Hron, J. P. Gunn, and R. Dejarnac. Ion temperature measurements in the tokamak scrape-off layer. *Journal of Nuclear Materials*, 363-365:1436 – 1440, 2007.

[86] M. Komm, J. Adámek, R. Dejarnac, J. P. Gunn, and Z. Pekarek. Transport of electrons in the tunnel of an ion sensitive probe. *Plasma Physics and Controlled Fusion*, 53:015005, 2011.

[87] M. Komm, J. Adámek, Z. Pekarek, and R. Pánek. Particle-In-Cell simulations of the ball-pen probe. *Contributions to Plasma Physics*, 50(9):814–818, 2010.

[88] V. Kotov, D. Reiter, R. A. Pitts, S. Jachmich, A. Huber, D. P. Coster, and JET-EFDA contributors. Numerical modelling of high density JET divertor plasma with the SOLPS4.2 (B2-EIRENE) code. *Plasma Physics and Controlled Fusion*, 50(10):105012, 2008.

[89] V. Kotov, D. Reiter, and S. Wiesen. Self-consistent modeling of X-point MARFE and divertor detachment. *Journal of Nuclear Materials*, 438:S449–S452, 2013.

[90] M. Kotschenreuther, P. Valanju, S. Mahajan, L. J. Zheng, L. D. Pearlstein, R. H. Bulmer, J. Canik, and R. Maingi. The super X divertor (SXD) and a compact fusion neutron source (CFNS). *Nuclear Fusion*, 50(3):035003, 2010.

[91] M. Kočan, J. P. Gunn, M. Komm, J.-Y. Pascal, E. Gauthier, and G. Bonhomme. On the reliability of scrape-off layer ion temperature measurements by retarding field analyzers. *Review of Scientific Instruments*, 79(7):073502, 2008.

[92] S. I. Krasheninnikov. Superthermal particles and electron thermal conductivity. *Soviet Physics JETP*, 94:17, 1988.

[93] N. S. Krasheninnikova and X. Tang. Equilibrium properties of the plasma sheath with a magnetic field parallel to the wall. *Physics of Plasmas*, 17(6):063508, 2010.

[94] A. S. Kukushkin, H. D. Pacher, G. W. Pacher, G. Janeschitz, D. Coster, A. Loarte, and D Reiter. Scaling laws for edge plasma

parameters in ITER from two-dimensional edge modelling. *Nuclear Fusion*, 43(8):716, 2003.

[95] B. Labombard, J. A. Goetz, I. Hutchinson, D. Jablonski, J. Kesner, C. Kurz, B. Lipschultz, G. M. McCracken, A. Niemczewski, J. Terry, A. Allen, R. L. Boivin, F. Bombarda, P. Bonoli, C. Christensen, C. Fiore, D. Garnier, S. Golovato, R. Granetz, M. Greenwald, S. Horne, A. Hubbard, J. Irby, D. Lo, D. Lumma, E. Marmar, M. May, A. Mazurenko, R. Nachtrieb, H. Ohkawa, P. O'Shea, M. Porkolab, J. Reardon, J. Rice, J. Rost, J. Schachter, J. Snipes, J. Sorci, P. Stek, Y. Takase, Y. Wang, R. Watterson, J. Weaver, B. Welch, and S. Wolfe. Experimental investigation of transport phenomena in the scrape-off layer and divertor. *Journal of Nuclear Materials*, 241-243:149 – 166, 1997.

[96] B. LaBombard, J. E. Rice, A. E. Hubbard, J. W. Hughes, M. Greenwald, J. Irby, Y. Lin, B. Lipschultz, E. S. Marmar, C. S. Pitcher, N. Smick, S. J. Wolfe, S. M. Wukitch, and the Alcator Group. Transport-driven scrape-off-layer flows and the boundary conditions imposed at the magnetic separatrix in a tokamak plasma. *Nuclear Fusion*, 44(10):1047, 2004.

[97] I. Langmuir and K. T. Compton. Electrical discharges in gases Part II. Fundamental phenomena in electrical discharges. *Review of Modern Physics*, 3:191–257, Apr 1931.

[98] A. Loarte, A. S. Kukushkin, H. D. Pacher, D. P. Coster, R. Schneider, N. Asakura, K. Itami, B. LaBombard, B. Lipschultz, C. F. Maggi, R. D. Monk, G. D. Porter, M Shimada, M. Sugihara, and J. L. Terry. Comparison of B2-EIRENE calculations with multi-machine experimental measurements. *Journal of Nuclear Materials*, 266:1123–1128, 1999.

[99] R. Marchand. Finite element modelling of transport in a tokamak edge and divertor. *Plasma Physics and Controlled Fusion*, 44(6):871, 2002.

[100] J. Marki, R. A. Pitts, T. Eich, A. Herrmann, J. Horacek, F. Sanchez, and G. Veres. Sheath heat transmission factors on TCV. *Journal of Nuclear Materials*, 363-365:382 – 388, 2007.

[101] G. F. Matthews. A combined retarding field analyser and E×B probe for measurement of ion and electron energy distribution in tokamak edge plasmas. *Journal of Physics D: Applied Physics*, 17:2243, 1984.

[102] G. F. Matthews. Ion diagnostics for the tokamak boundary. *Vacuum*, 42(12):769 – 773, 1991.

[103] G. F. Matthews. Tokamak plasma diagnosis by electrical probes. *Plasma Physics and Controlled Fusion*, 36(10):1595–1628, 1994.

[104] G. F. Matthews, S. J. Fielding, G. M. McCracken, C. S. Pitcher, P. C. Stangeby, and M. Ulrickson. Investigation of the fluxes to a surface at grazing angles of incidence in the tokamak boundary. *Plasma Physics and Controlled Fusion*, 32(14):1301–1320, 1990.

[105] G. F. Matthews, R. A. Pitts, G. M. McCracken, and P. C. Stangeby. Edge ion analysis in DITE. *Nuclear Fusion*, 31(8):1495, 1991.

[106] Guy Matthews. *The Measurement of Ion Temperature in Tokamak Edge Plasmas*. PhD thesis, Wolfson College, 1984.

[107] M. J. McCarrick, R. F. Ellis, M. Koepke, and R. P. Majeski. Perpendicular ion energy analyzer for hot-ion plasmas. *Review of Scientific Instruments*, 56(7):1463–1464, 1985.

[108] R. D. Monk, A. Loarte, A. Chankin, S. Clement, S. J. Davies, J. K. Ehrenberg, H. Y. Guo, J. Lingertat, G. F. Matthews, M. F. Stamp, and P. C. Stangeby. Interpretation of ion flux and electron temperature profiles at the JET divertor target during high recycling and detached discharges. *Journal of Nuclear Materials*, 241-243:396 – 401, 1997.

[109] R. W. Motley and T. Kawabe. Energy analysis of cesium ions in a Q machine. *Physics of Fluids*, 14:1019, 1971.

[110] D. Moulton, W. Fundamenski, S. Wiesen, G. Corrigan, P. Belo, G. Maddison, and C. Giroud. EDGE2D-EIRENE modelling of the inter-ELM phase of H-mode plasmas on JET. *Journal of Nuclear Materials*, 415(1):S509–S512, 2011.

[111] R. Nachtrieb, B. LaBombard, and E. Thomas. Omegatron ion mass spectrometer for the Alcator C-Mod tokamak. *Review of Scientific Instruments*, 71(11):4107–4118, 2000.

[112] Robert Thomas Nachtrieb. *Ion Mass Spectrometry on the Alcator C-Mod tokamak*. PhD thesis, Massachusetts Institute of Technology, 2000.

[113] I. S. Nedzelskiy, C. Silva, H. Figueiredo, H. Fernandes, and C. A. F. Varandas. Compact retarding field energy analyzer for the tokamak ISTTOK boundary plasma. *Review of Scientific Instruments*, 77(10):10E729, 2006.

[114] R. Ochoukov, D. G. Whyte, B. Lipschultz, B. LaBombard, and S. Wukitch. Interpretation and implementation of an ion sensitive probe as a plasma potential diagnostic. *Review of Scientific Instruments*, 81(10):10E111, 2010.

[115] R. Ochoukov, D. G. Whyte, B. Lipschultz, B. LaBombard, and S. Wukitch. Interpretation and implementation of an ion sensitive probe as a plasma potential diagnostic on Alcator C-Mod. *Journal of Nuclear Materials*, 415:S1143–S1146, 2010.

[116] K. Odajima, H. Kimura, H. Maeda, and K. Ohasa. Measurement of ion temperature in scrape-off layer with Katsumata probe. *Japanese Journal of Applied Physics*, 17(7):1281–1282, 1978.

[117] M. Oertl, H. Störi, and R. Hatakeyama. A small electrostatic retarding field energy analyzer with compensating differentiation circuit. *Journal of Applied Physics*, 51(3):1431–1434, 1980.

[118] Y. Ohtsu and N. Wakita. A simple hollow probe for monitoring ion-beam energy in processing plasmas. *Measurement Science and Technology*, 21, 2010.

[119] K. Okazaki, H. Tanaka, N. Ohno, N. Ezumi, Y. Tsuji, and S. Kajita. Measurement of ion and electron temperatures in plasma blobs by using an improved ion sensitive probe system and statistical analysis methods. *Review of Scientific Instruments*, 83(2):023502, 2012.

[120] L. W. Owen, J. M. Canik, R. J. Groebner, J. D. Callen, X. Bonnin, and T. H. Osborne. Comparing 1.5 D ONETWO and 2D SOLPS analyses of inter-ELM H-mode plasma in DIII-D. *Nuclear Fusion*, 50(6):064017, 2010.

[121] R. A. Pitts. Retarding field energy analysis for ion temperature measurement in the tokamak edge. *Contributions to Plasma Physics*, 36(S1):87–93, 1996.

[122] R. A. Pitts, R. Chavan, S. J. Davies, S. K. Erents, G. Kaveney, G. F. Matthews, G. Neill, J. E. Vince, and I. Duran. Retarding field energy analyzer for the JET plasma boundary. *Review of Scientific Iinstruments*, 74(11):4644–4657, 2003.

[123] R. A. Pitts, W. Fundamenski, S. K. Erents, Y. Andrew, A. Loarte, C. Silva, and JET-EFDA contributors. Far SOL ELM ion energies in JET. *Nuclear Fusion*, 46(1):82–98, 2006.

[124] R. A. Pitts and G. F. Matthews. Real time, in-situ measurements of secondary electron emission in DITE. *Journal of Nuclear Materials*, 176:877–882, 1990.

[125] Richard Anthony Pitts. *Ion Energy, Sheath Potential and Secondary Electron Emission in the Tokamak Edge*. PhD thesis, University of London, November 1990.

[126] Daniel D. Pollock. *Thermocouples: Theory and Properties*. CRC Press LLC, 1991.

[127] D. E. Post, K. Borrass, J. D. Callen, et al. ITER Documentation Series No. 21. *ITER Physics (International Atomic Energy Agency, Vienna)*, 1991.

[128] G. J. Radford. The application of moment equations to scrape off layer plasmas. *Contributions to Plasma Physics*, 32(3-4):297–302, 1992.

[129] Hannes Risken. *Fokker-Planck Equation*. Springer, 1989.

[130] T. D. Rognlien. *Private communication*, 2013.

[131] T. D. Rognlien, M. E. Rensink, and G. R. Smith. User manual of UEDGE edge-plasma transport code. *Lawrence Livermore National Lab. Report No. UCRL-ID-137121*, 2000.

[132] D. L. Rudakov, J. A. Boedo, R. A. Moyer, P. C. Stangeby, A. McLean, and J. G. Watkins. Effect of electron temperature fluctuations on slowly swept Langmuir probe measurements. *Review of Scientific Instruments*, 75(10):4334–4337, 2004.

[133] O. Schmitz, T. E. Evans, M. E. Fenstermacher, H. Frerichs, M. W. Jakubowski, M. J. Schaffer, A. Wingen, W. P. West, N. H. Brooks, M. Groth, I. Joseph, C. J. Lasnier, R. A. Moyer, H. Stoschus, B. Unterberg, J. G. Watkins, K. H. Burrell, J. S. deGrassie, K. H. Finken, P. Gohil, Y. Fend, M. Lehnen, S. A. Mordijck, A. Nicolai, T. H. Osborne, D. Reiter, U. Samm, K. H. Spatschek, E. A. Unterberg, R. Wolf, and the DIII-D and TEXTOR Teams. Three dimensional transport analysis for ELM control experiments in ITER similar shape plasmas at low collisionality in DIII-D. *Proccedings of the 35th EPS Conference on Plasma Physics, in Crete, Greece, June 9-13, 2008*, 2008.

[134] R. Schneider, X. Bonnin, K. Borrass, D. P. Coster, H. Kastelewicz, D. Reiter, V. A. Rozhansky, and B. J. Braams. Plasma edge physics with B2-Eirene. *Contributions to Plasma Physics*, 46(1-2):3–191, 2006.

[135] R. Schrittwieser, C. Ionita, J. Adamek, J. Stockel, J. Brotankova, E. Martines, G. Popa, C. Costin, L. van de Peppel, and G. van Oost. Direct measurements of the plasma potential by Katsumata-type probes. *Czechoslovak Journal of Physics*, 56, 2006.

[136] T. Sekine, T. Saito, Y. Tatematsu, T. Yasuoka, H. Ikegami, D. Nagai, K. Nozaki, M. Ichimura, H. Higaki, and T. Cho. Ion measurement of the edge plasma in the GAMMA10 tandem mirror device with an ion sensitive probe. *Review of Scientific Instruments*, 75(10):4317–4319, 2004.

[137] L. Spitzer Jr and R. Härm. Transport phenomena in a completely ionized gas. *Physical Review*, 89(5):977, 1953.

[138] P. C. Stangeby. A problem in the interpretation of tokamak Langmuir probes when a fast electron component is present. *Plasma Physics and Controlled Fusion*, 37(9):1031–1037, 1995.

[139] P. C. Stangeby. *The Plasma Boundary of Magnetic Fusion Devices*. IoP Publishing, 2000.

[140] D. Storek and K. W. Gentle. Accurate measurement and interpretation of the heat flux to the divertor in TEXT Upgrade. *Nuclear Fusion*, 41(1):1–9, 2001.

[141] D. P. Stotler, R. A. Vesey, D. P. Coster, C. F. F. Karney, B. LaBombard, B. Lipschultz, C. S. Pitcher, and R. Schneider. Coupled Monte Carlo neutral–fluid plasma simulation of Alcator C-Mod divertor plasma near detachment. *Journal of Nuclear Materials*, 266:947–952, 1999.

[142] R. M. Sullivan, R. Ochoukov, and D. G. Whyte. Internal physics of the ion-sensitive probe. *Journal of Nuclear Materials*, 438:S1253–S1256, 2013.

[143] Akira T. and Yuichi T. Ion temperature measurement using ion-sensitive probe. *Japanese Journal of Applied Physics*, 44(6A):4128–4132, 2005.

[144] P. Tamain, M. Kočan, J. Gunn, A. Kirk, J. Y. Pascal, and M. Price. Ion energy measurements in the scrape-off layer of MAST using a retarding field analyzer. *Journal of Nuclear Materials*, 415(1):S1139–S1142, 2011.

[145] D. D. Tskhakaya, P. K. Shukla, B. Eliasson, and S. Kuhn. Theory of the plasma sheath in a magnetic field parallel to the wall. *Physics of Plasmas*, 12(10):103503–103503, 2005.

[146] K. Uehara, R. Fukumoto, A. Tsushima, and H. Amemiya. Evaluation of ion temperature using ion sensitive probe in the boundary plasma of the JFT-2M tokamak. *Journal of the Physical Society of Japan*, 72(11):2804–2810, 2003.

[147] K. Uehara, A. Tsushima, H. Amemiya, and JFT-2M Group. Direct measurement of ion behavior using modified ion sensitive probe in tokamak boundary plasma. *Journal of the Physics Society of Japan*, 66:921–924, 1997.

[148] F. Valsaque, G. Manfredi, J. P. Gunn, and E. Gauthier. Kinetic simulations of ion temperature measurements from retarding field analyzers. *Physics of Plasmas*, 9(5):1806–1814, 2002.

[149] A. S. Wan, B. LaBombard, B. Lipschultz, and T. F. Yang. Directional asymmetries in the Alcator C edge plasma. *Journal of Nuclear Materials*, 145:191–195, 1987.

[150] A. S. Wan, B. Lipschultz, F. S. McDermott, and J. L. Terry. The effect of ICRF on the Alcator C scrape-off layer plasma. *Journal of Nuclear Materials*, 162-164:292 – 299, 1989.

[151] A. S. Wan, T. F. Yang, B. Lipschultz, and B. LaBombard. Janus, a bidirectional, multifunctional plasma diagnostic. *Review of Scientific Instruments*, 57(8):1542–1551, 1986.

[152] Alan Szu-Hsin Wan. *Ion and electron parameters in the Alcator C tokamak scrape-off region*. PhD thesis, MIT, 1986.

[153] M. Y. Ye and S. Takamura. Effect of space-charge limited emission on measurements of plasma potential using emissive probes. *Physics of Plasmas*, 7:3457, 2000.

[154] R. Zagorski, V. Pericoli, and L. Pieroni. Numerical modelling of impurity production in the FTU tokamak scrape-off layer. *Contributions to Plasma Physics*, 34(2-3):466–471, 1994.

3

HARDWARE

The extreme heat flux in the boundary of Alcator C-Mod presents a great opportunity to study plasma physics at reactor-relevant parameters. It also puts great demand on the probes which will operate within it. The high plasma temperature ($\sim 100\,\mathrm{eV}$) and density ($\sim 10^{20}\,\mathrm{m^{-3}}$) places extreme heat flux ($> 100\,\mathrm{MW\,m^{-2}}$) on the probe surfaces (table 2 gives the approximate range of boundary plasma parameters encountered in Alcator C-Mod). Not only must the probes meet basic physics requirements to operate properly, they must also survive the heat flux such that they do not ruin the plasma and the plasma does not ruin them. Only a handful of materials are allowed in the ultra-high vacuum chamber due to limits on outgassing. This necessitates using materials with the best thermal performance and a design focused on optimal heat flux handling. This chapter describes the design for the high-heat flux environment of C-Mod of embedded thermocouples (section 3.1), surface thermocouples (section 3.2), as well as ion sensitive probe and retarding field analyzer scanning probes (section 3.3).

Table 2: Typical deuterium plasma parameters extremes in a 5 T magnetic field.

	Near SOL	Far SOL
$n\ [\mathrm{m^{-3}}]$	10^{20}	10^{17}
$T_i\ [\mathrm{eV}]$	100	5
$T_e\ [\mathrm{eV}]$	50	5
$\rho_i\ [\mu\mathrm{m}]$	410	91
$\rho_e\ [\mu\mathrm{m}]$	4.7	1.5
$\lambda_D\ [\mu\mathrm{m}]$	5.2	53
$q_{\parallel}\ [\mathrm{MW\,m^{-2}}]$	570	0.01

3.1 TILE AND CALORIMETER EMBEDDED THERMOCOUPLES

As part of the 2010 Department of Energy Joint Research Target to measure the divertor heat flux footprint [19, 20] the C-Mod first wall was instrumented with an extensive set of heat flux diagnostics. Thermocouple arrays were installed in tiles at the lower inner and outer divertors (including thermally isolated calorimeters in the lower outer divertor for finer spatial scale energy measurements). Thermocouples were installed in the outboard main limiters, including the full limiter between G- and H-ports, the split limiter between A- and B-ports, and the diagnostic limiter at K-port. After the spring 2012 opening the new rotated J-Antenna limiter was also instrumented. Thermocouples were not installed in the flat-plate upper divertor because of the extensive modifications needed to place them there.

The heat flux instrumentation in the lower outer divertor is comprised of nine surface thermocouples, seven Langmuir probes, thirteen calorimeters, and ten tile thermocouples—all in view of an IR thermographic camera (fig. 17). The diagnostics are placed in a 12°

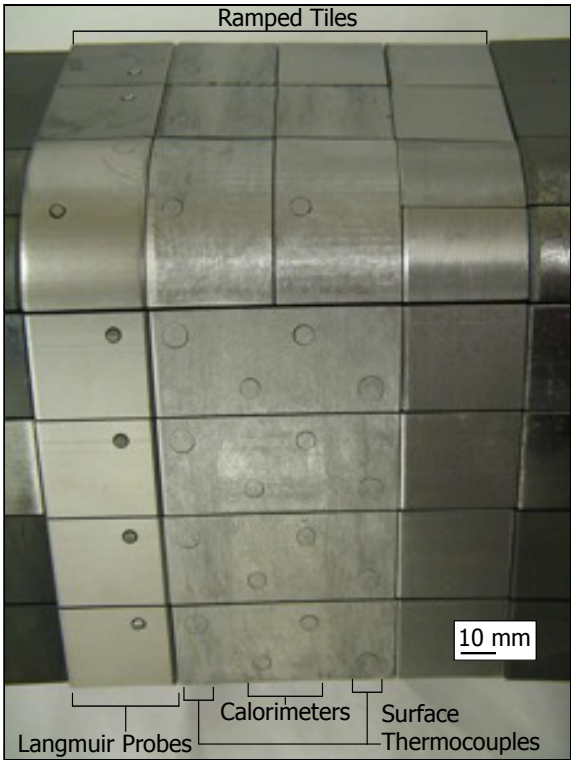

Figure 17: 12° toroidal section of the lower outer divertor module instrumented with heat flux sensors.

toroidal section of the divertor. The divertor is of greatest interest because it receives the highest local heat flux. The magnetic field angle with respect to the divertor surface is typically less than 1°. The majority of plasma heat flux is carried along field lines, thus misalignments of tiles and divertor modules can cause magnetic shadowing of surfaces. To eliminate shadowing, the tiles and thermal sensors of this special 12° section are ramped an additional 2° into the magnetic field. This has the added benefit of increasing the heat flux signal. Placement of the diagnostics within the same 12° toroidal sector removes uncertainties that arise in assuming toroidal symmetry; which may have been the main contribution to the disagreement between Langmuir probes and IR heat flux in Ref. [8].

The embedded thermocouples proved to be very useful:

1. The outer divertor thermocouples provided a calibration base temperature for the (non ice-point compensated) surface thermocouples [6], see section 4.2.2.

2. The outer divertor thermocouples also provided a calibration temperature for the IR camera, a necessity due to shot-to-shot changes of the surface emissivity [37].

3. Calorimeters measure divertor profiles of the shot-integrated energy deposition, allowing for an important check on the surface thermocouple and IR thermographic calculations, section 5.1.

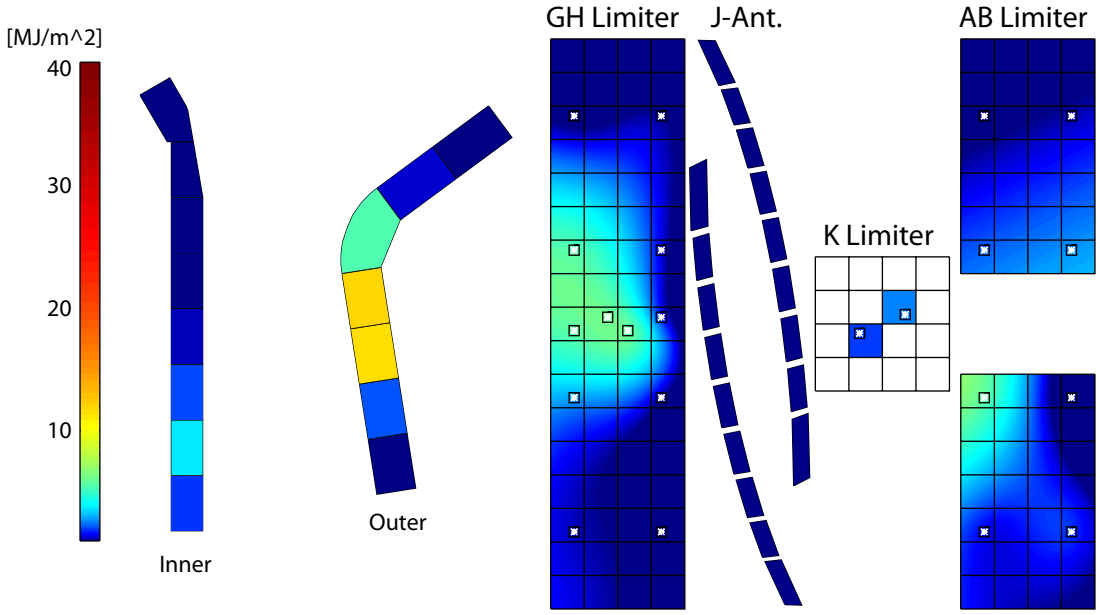

Figure 18: An example of the energy deposition pattern to the first wall surfaces of C-Mod displayed after the shot on the "big board" in the C-Mod control room (this from a 2 s shot with 1 MW ohmic and 4 MW ICRF input power). Limiter tile thermocouple locations are indicated with a white asterisk inclosed in a black square (when a thermocouple goes open, this symbol automatically disappears). The AB and GH limiter energy patterns are a thin-plate spline fit through the thermocouple points. The K limiter does not have enough points to fit a spline. Limiter views are looking out in major radius. The inner and outer divertor views are poloidal cross sections through the tiles.

4. Following each shot the limiter thermocouples displayed where the energy was deposited and if it were too much, fig. 18; giving feedback to tokamak operators what the damaging shots were.

5. The embedded divertor thermocouples allowed for investigation of the in/out divertor energy asymmetries. Especially the large energy fluxes to the inner divertor during I-mode experiments in reversed field [36].

6. Energy deposition values were also stored in a database, which allows for explorations of long-term trends, section 5.1..

3.1.1 *Design*

The calorimeters are 4.8 mm diameter by 18 mm long (length varies by tile) molybdenum cylinders with a hole drilled from the back to within 5 mm from the front surface, fig. 19 and fig. 20. A type-K thermocouples is inserted through this hole. An Inconel sleeve provides partial thermal isolation of the calorimeter from the tile. The thermal conductivity of Inconel is about an order of magnitude less than molybdenum. In addition, the sleeve has holes drilled in it to reduce the effective area heat flux has to flow through it; creating a bottleneck to heat flux leaking out of the calorimeter. A hole in the sleeve

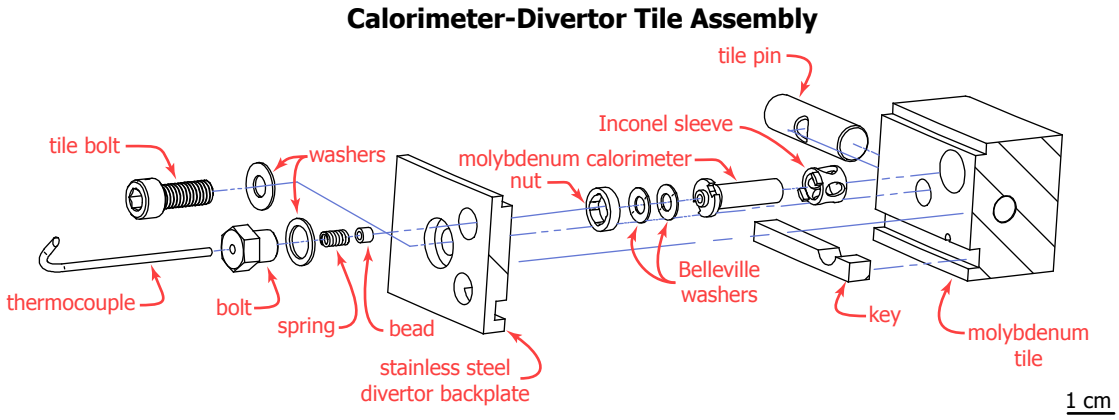

Figure 19: CAD line drawing of the calorimeter-divertor tile assembly. The calorimeter is thermally isolated from the tile by the Inconel sleeve. Tabs in the sleeve and calorimeter maintain alignment between them. A circular notch in the sleeve fits into the tile pin. These two constraints insures that the calorimeter is not free to rotate. The calorimeter is held in the tile with a nut and a pair of Belleville washers. A bolt-spring-bead system keeps the thermocouple pressed into good thermal contact with the back of the calorimeter. The bead is crimped onto the thermocouple sheath, trapping the spring between the bead and bolt. (mechanical design by Josh Payne and Brian LaBombard)

also serves to lock the calorimeter in place and prevent it from rotating. This is important because the calorimeters are filed flush to the ramped tiles. Any rotation would expose a leading edge and increase the plasma heat flux collected. The calorimeter is pressed in place with a nut threaded into the back of the tile and a pair of Belleville washers, which allow for thermal expansion of the system without loosening of the nut.

The thermocouple must remain in good thermal contact with the back of the calorimeter, fig. 20. This is accomplished with a bead and spring system. The bead is crimped onto the thermocouple sheath, locking the spring between the bead and nut. Screwing the nut into the divertor back plate compresses the spring and pushes the thermocouple into the calorimeter. The same system is used for all of the tile thermocouples.

Analysis of calorimeter measurements is presented in section 4.1.2. Comparisons to surface thermocouple and IR energy deposition are in section 5.1.

3.1.2 *Importance of Tip for Adequate Time Response*

The thermocouples were type-K, composed of chromel (90 % nickel, 10 % chromium) and alumel (95 % nickel, 2 % manganese, 2 % aluminium, 1 % silicon). Type-K was used because of its temperature range (−200 °C to 1250 °C) and its relative inexpensiveness—allowing to run the chromel-alumel wire pair all the way from the thermojunction to the electronics rack (> 10 m). At the rack the voltage was converted using an ice-point compensated circuit (section 4.1.1) allowing the embedded thermocouples to measure the absolute temperature.

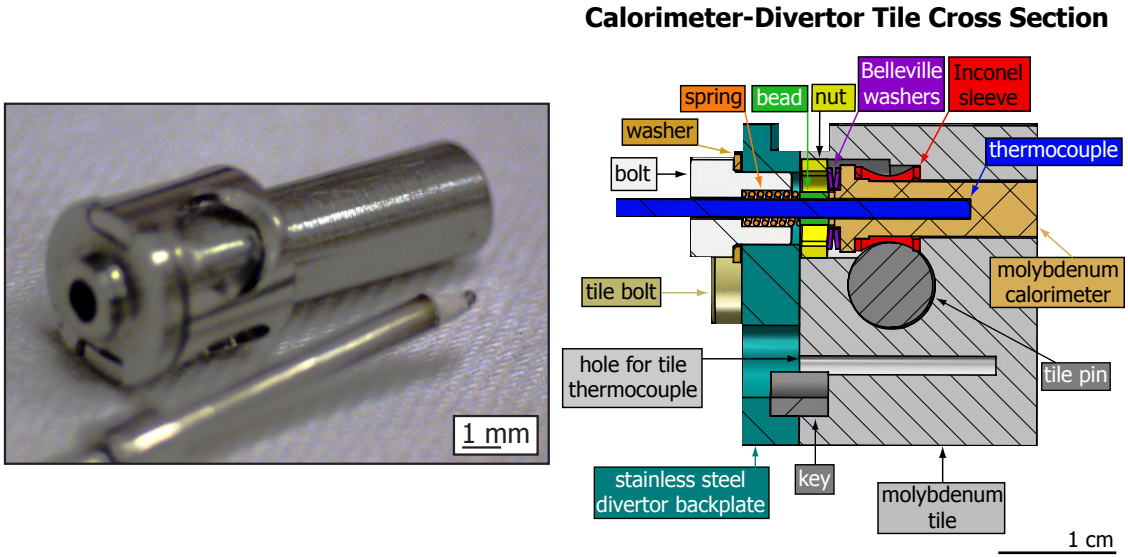

Figure 20: Image of the calorimeter and thermocouple (left). CAD cross section of the calorimeter-divertor tile assembly (right). Here it can easily been seen how the cut-out in the Inconel sleeve locks the calorimeter into the tile pin. Additionally, the action of the spring pressing the thermocouple into the calorimeter is shown.

Figure 21: Photograph of the two styles of embedded thermocouples used in C-Mod. The center and right are the original, stainless steel sheathed thermocouples. The right thermocouple's sheath was filed back to reveal the thick ~2 mm stainless steel tip that was severely detrimental to its time response. The left most thermocouple is the "fast-response" thermocouple made to replace the sheathed. The stainless steel tip was removed and the wires were joined in a low-mass thermojunction for superior time response. Ceramic potting was used behind the tip to keep the wires in place.

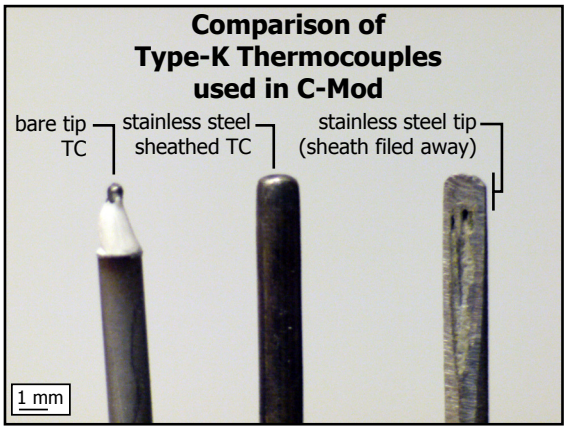

Figure 22: Comparison of the temperature response for the stainless steel sheathed thermocouple tip and the bare tip for two plasma shots with similar energy depositions. Heat flux was incident on the calorimeter from 0.5 s to 1.5 s. The stainless steel slows down the thermocouple response significantly. The late-time temperature is so different because of the large temperature drop across the stainless steel sheath to the thermojunction.

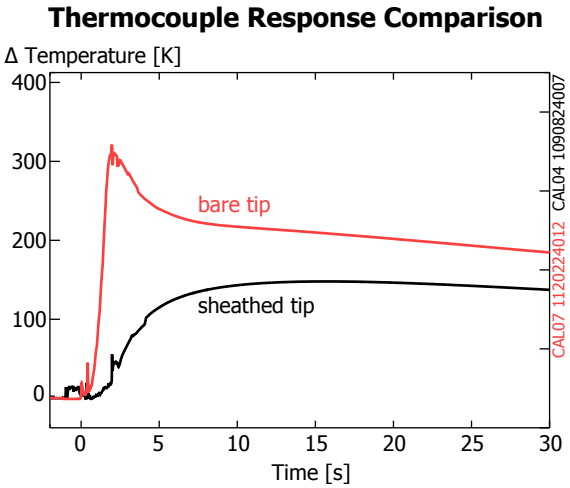

Two versions of the embedded thermocouples were used. The first iteration was a standard thermocouple sheathed in stainless steel, fig. 21. Thermal analysis of these thermocouples revealed their time response to be severely lacking [8], fig. 22.

It was found through inspection of a thermocouple, by partially removing the stainless steel sheath with a file, that the thermojunction was placed behind $\sim 2\,\mathrm{mm}$ of stainless steel. To accurately measure the transient temperature response of a medium, the thermocouple must have a thermal diffusivity (α) an order of magnitude higher than that medium [32]. Thus the stainless steel sheath ($\alpha \approx 4 \times 10^{-6}\,\mathrm{m^2\,s^{-1}}$) completely prevents adequate time-response measurements in the molybdenum ($\alpha \approx 5 \times 10^{-5}\,\mathrm{m^2\,s^{-1}}$) tiles and calorimeters. Following this we implemented a new version of the thermocouple, fig. 21, one that lacked the stainless steel sheath and pressed the thermojunction in direct contact with the molybdenum tile/calorimeter. Its time response was greatly improved, fig. 22. See section 4.1.2 for a description of how the calorimeter-thermocouple system is modeled to calculate the deposited energy.

3.2 SURFACE THERMOCOUPLES

Surface thermocouples (or "self-renewing thermocouples" [28]) are different from standard thermocouples, the thermojunction is formed in a very thin layer at the surface of the sensor. This is typically done by embedding two electrically insulated and dissimilar metallic wires into a carrier body and allowing them to come into electrical contact only at the very surface. This construction leads to a fast thermal time response and is particularly useful if one wants to characterize the surface temperature evolution of an actual component in service. In this case, one simply makes the carrier body out of the same material as the component under test. In addition, this construction also enables a simple computation of the incident heat flux to the component; the measured surface temperature evolution is applied as a boundary condition to a time-dependent thermal transport model of the component under test. In fusion plasmas, it is this latter quantity, the incident heat flux, which is most desired for assessing plasma thermal loads.

Originally developed to measure gun-bore surface temperatures [4], surface thermocouples have since been used for heat flux measurements in rocket nozzles [24, 28], shock tunnels and tubes [22, 25], diesel engines [2], and reentrant vehicles [14]. A recent investigation of surface thermojunction formation and the subsequent time response is given in Ref. [9]. To our knowledge, Alcator C-Mod is the first use of surface thermocouples in a fusion reactor experiment. They were first tried in Alcator C-Mod in the mid 1990s but were not used extensively due to poor signal quality [3, 11]. We have since

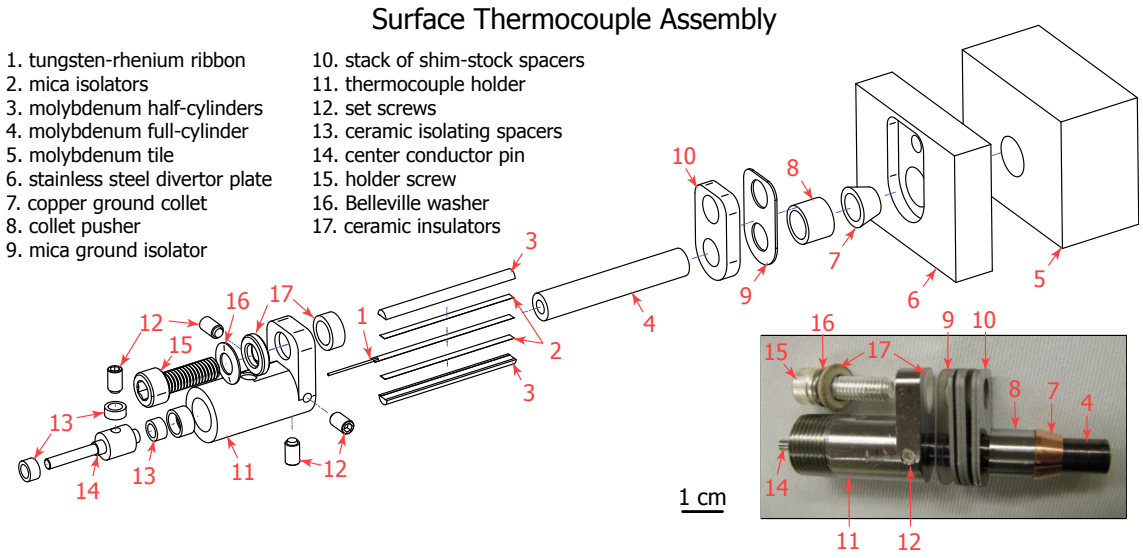

Figure 23: The 1 cm scale bar is for both the line drawing and inset photograph. The 74 % tungsten-26 % rhenium ribbon (1) is electrically isolated with mica sheets (2) from the molybdenum probe body (3). This in turn is swaged into a 6.35 mm diameter molybdenum tube (4); forming a customized version of a "self-renewing thermocouple" supplied by NANMAC Corp. Filing the surface of the sensor initiates the thermojunction. The copper collet (7) grounds the molybdenum sensor body to the molybdenum tile with low electrical resistance. Insulators (9 and 17) isolate the stainless steel probe body from ground. The threaded holder (11) allows for a removable coaxial connection.(mechanical design by Brian LaBombard and Ned Mucic)

made substantial improvements to that original design, allowing them to be used for routine measurements in the C-Mod tokamak—a very harsh environment for such sensors.

3.2.1 *Design*

Surface thermocouples are typically made with two parallel ribbons to form the thermojunction. But this would necessitate bringing the signal out via twisted-pair leads, which is inferior to the use of a coaxial cable. In general, wire loops in low-voltage signal pathways must be minimized in a tokamak environment because, by Faraday's Law, time-varying magnetic fields induce voltage in the loops. Therefore, any transition from a two-ribbon sensor to a coaxial cable would be problematic because of the small wire loop formed at the connection. Our surface thermocouples and cables all have a coaxial geometry to avoid this effect, figs. 23 and 24. The surface thermocouples are grounded at only one point to avoid ground loops.

The surface thermocouples are an adaptation of a standard product that is commercially available from NANMAC Corporation, the patented E12 series "self-renewing thermocouple" [28]. However, unlike the two-ribbon design of the E12 product line, we requested that NANMAC build a set of sensors with only a single 74 % tungsten-26 % rhenium ribbon (2 mm wide by 50 µm thick) embedded into two

molybdenum half-cylinders (figs. 23 and 24). This coaxial geometry is important because, as stated above, it minimizes EMF pickup from the tokamak's rapidly changing magnetic fields. Mica strips keep the ribbon electrically insulated from the molybdenum body. The assembly is held together by swaging it into a 6.35 mm outside diameter molybdenum cylinder.

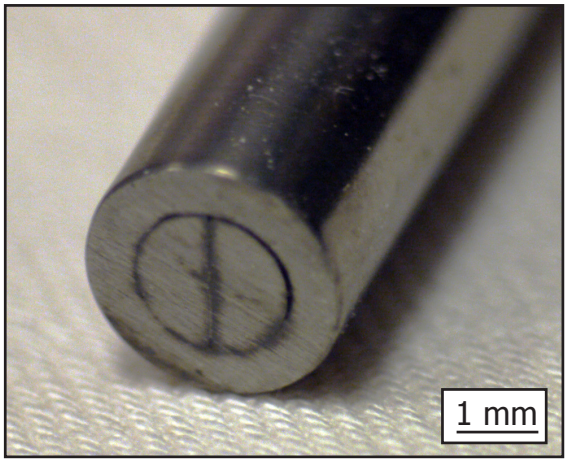

Figure 24: Photograph of plasma-facing side of surface thermocouple. The tungsten-rhenium ribbon is pressed between the two D-shaped molybdenum half cylinders.

Each surface thermocouple is bolted to the divertor structure with a custom stainless steel mount. The mount connects to a standard 50 Ω ceramic-insulated cable by a threaded, removable coaxial cable connector. The depth of the surface thermocouple body into the divertor is adjusted with a series of stainless steel shims until its face is just proud of the divertor tile surface. A diamond file is then used to file the surface thermocouple flush to the tile surface. This initiates the thermojunction between the tungsten-rhenium and molybdenum by bending small slivers of molybdenum over the ribbon. We find that this thermojunction can be reliably maintained, regardless of the plasma exposure conditions. Although there are some unresolved failures of proper surface thermocouple operation, see section 4.2.3.

Since we are only interested in recording rapid changes in surface temperature from a plasma pulse, unlike the type-K embedded thermocouple system we do not need to select lead wires that match the Seebeck coefficients of the thermojunction metals. Thermal calibration of the entire circuit, with its various thermojunctions along the electrical pathway, would be impractical and is not needed. Instead, our scheme for measurements with surface thermocouples relies on all thermojunctions, except for that at the surface, to remain at constant temperature throughout the pulse. The most likely thermojunction to violate this assumption is the one between the surface thermocouple molybdenum body and its stainless steel holder. Using a semi-infinite body approximation [23] (the time for a 1 % temperature change at a distance x from the surface: $t \approx x^2/16\alpha$ with $\alpha \approx 5.4 \times 10^{-5}\,\mathrm{m^2\,s^{-1}}$ for molybdenum and a surface thermocouple of length $x \approx 35$ mm) the time scale for the back thermojunction to change by 1 % is ~ 1.4 s, which is longer than the typical pulse flat top of 1.0 s. Thus, the overall change in the sensor's EMF is due to that of the molybdenum/tungsten-rhenium thermojunction alone. It is only necessary to know the surface temperature before the plasma pulse in order to look up the proper starting point on the voltage-to-temperature calibration curve, section 4.2.2.

The surface thermocouple electronics are described in section 4.2.1. Processing of surface thermocouple data is in section 4.2.2. Comparison of surface thermocouple to calorimeter energy deposition is in section 5.1. Use of surface thermocouples to confirm sheath heat flux transmission coefficient theory is presented in section 5.1. Surface thermocouples demonstrate that there is no heat flux associated with the divertor "death-ray", chapter 6.

3.2.2 *Importance of Proper Grounding*

There are strong currents (a few 100 kA m^{-2} parallel to the magnetic field) in the edge plasma of Alcator C-Mod that connect the inner and outer divertor [16]. The heat flux to the divertor surface is partially carried by these currents. Thus, in order to insure that the surface thermocouple receives the same heat flux as the divertor surface, its body must be grounded to the divertor. Yet in the first version of the surface thermocouple sensor mount, it was found that the plasma-induced current caused a voltage on the same order of the thermal electromotive force signals (EMF). This is because the current flowed through the electrically resistive stainless steel holder to the ground (see fig. 23). Propagation of this fictitious thermal EMF through the thermal analysis resulted in a large positive spike of heat flux at plasma initiation and a negative spike at plasma termination, making the measurements difficult to interpret, fig. 25.

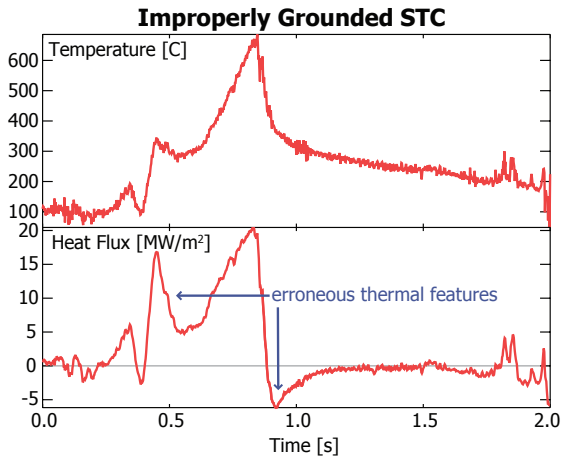

Figure 25: Temperature and heat flux from an improperly grounded surface thermocouple. The plasma current flowing to ground through the stainless steel mount generates a voltage which adds to the thermojunction EMF. Propagating this through the heat flux analysis generates erroneous positive and negative spikes in heat flux.

Negative surface heat fluxes are not expected. This would imply that a power flux comparable to the incident plasma flux is leaving the surface. The leading candidate for this would be radiation from the probe. The power radiated by a grey body is:

$$P = \epsilon \sigma T^4, \tag{53}$$

with the molybdenum emissivity $\epsilon \approx 0.1$ and the Stephen-Boltzmann constant $\sigma = 5.67 \times 10^{-8}\,W\,m^{-2}\,K^{-4}$. As in fig. 25, if the surface was 500 °C then the radiated power would be $P \approx 2\,kW\,m^{-2}$; about three orders of magnitude less than erroneous negative heat flux.

Plasma current density in the C-Mod boundary can be on order $0.5 \times 10^6\,A\,m^{-2}$, with a 3° attack angle and a surface thermocouple with cross sectional area $3 \times 10^{-5}\,m^2$, the current passing through the surface thermocouple is 0.78 A. The thermal resistivity of molyb-

denum and stainless steel are approximately $\rho_{Mo} \approx 10^{-8}\,\Omega\,m$ and $\rho_{SS} \approx 10^{-6}\,\Omega\,m$, with lengths of $\sim 3 \times 10^{-2}\,m$ the resistances are $R_{Mo} \approx 10^{-5}\,\Omega$ and $R_{SS} \approx 10^{-3}\,\Omega$. Thus the voltages in each section are $V_{Mo} \approx 7.8 \times 10^{-6}\,V$ and $V_{SS} \approx 7.8 \times 10^{-4}\,V$. This voltage is added to the molybdenum/tungsten-rhenium thermojunction voltage. Putting it through the calibration calculation ($\sim 16\,\mu V\,°C^{-1}$, section 4.2.2), the resulting spurious temperature increases due to each of the molybdenum and stainless steel portions of the surface thermocouple bodies are $\Delta T_{Mo} \approx 0.5\,°C$ and $\Delta T_{SS} \approx 50\,°C$. The change due to the molybdenum section is imperceptible while the change due to the stainless steel section is comparable to the temperature changes due to plasma heat flux, significantly altering the heat flux calculations, fig. 25. E. g., a surface heat flux of $1\,MW\,m^{-2}$ for 1 s results in a 60 °C surface temperature change for molybdenum.

The present design electrically grounds the sensor through the molybdenum thermocouple body (via a copper ground collet, fig. 23). Since the copper has a much smaller resistance than the stainless steel, the potential difference caused by the current is eliminated and hence the anomalously generated heat flux is also eliminated. With this proper ground placement, no negative heat fluxes are measured with the surface thermocouples.

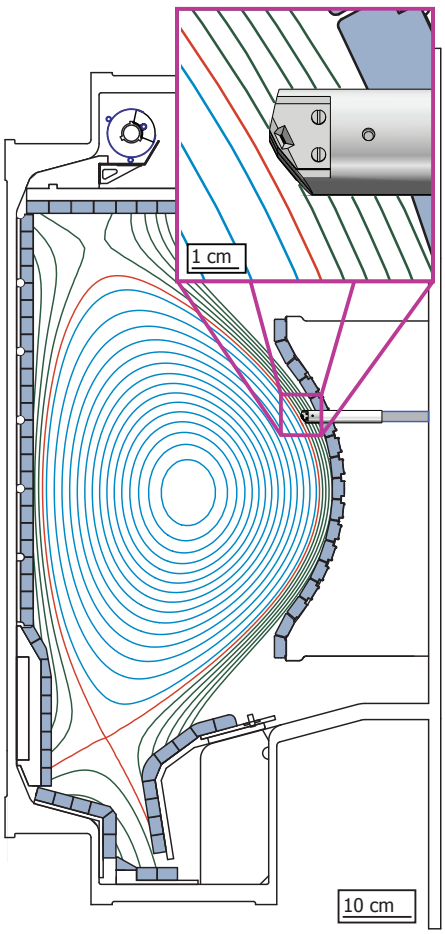

Figure 26: Cross section of Alcator C-Mod with RFA scanning probe.

3.3 DESIGN OF RFA AND ISP SCANNING PROBE HEADS

3.3.1 *Overview of Scanning Probe System*

The horizontal scanning probe system has been on C-Mod for many years with both Langmuir probe (see Refs. [17, 18, 20] among others) and magnetic probe heads (see Ref. [35]); fig. 26 presents a cross section of C-Mod highlighting the location of the scanning probe.

Radial motion of the probe head into and out of the plasma is performed with a pneumatic cylinder. Vacuum is maintained by a set of fast-action bellows. The system allows for up to three scans to the same depth (separated by at least 0.2 s to allow return of the probe to its rest position before the next scan starts) or one "dwell" scan to a fixed depth for the whole shot (usually 0.5 s for ramp-up, 1.0 s of flat top, and 0.5 s for ramp-down). The probe may be scanned up to, and sometimes to a few millimeters inside, the last closed flux surface in ohmically-

heated plasmas; dwell scans are limited to further out into the SOL due to the intense, steady plasma heating of the probe head. Accurate targeting relies on repeatable shots with a steady boundary. The scanning probe depth is targeted based on the plasma equilibrium of a previous shot that must be repeated.

All C-Mod probes are baked under vacuum at 150 °C (or higher if the materials allow) for a couple of days to remove water vapor and verify high-vacuum (low-outgassing) compatibility. After baking, probes are stored in a desiccant container under rough vacuum, $\lesssim 0.5\,\mathrm{atm}$ (380 torr), to prevent reabsorption of water vapor. The horizontal scanning probe drive system has its own gate valve and turbo pump. This allows us to change the probe head after a day of experiments. Back-filling dry nitrogen through the probe system while changing the probe head and storing probes in the desiccant box aids in reducing turnaround time. The system is usually pumped down overnight (to ~ 1 µtorr) in time for the next day's experiments.

3.3.2 *List of Materials Used*

The extreme heat fluxes along with operation in an ultra-high vacuum are the two most important factors in choosing materials for probe construction. Thus materials are primarily chosen on their ability to survive high heat flux and low vapor pressure. Metals used include:

MOLYBDENUM
: Has superior thermal properties (melting temperature $T_{melt} = 2896\,\mathrm{K}$ and thermal conductivity $\kappa \approx 138\,\mathrm{W\,m^{-1}\,K^{-1}}$) yet it is still machinable with standard carbide tooling. In practice TZM (99.40 % molybdenum, 0.50 % titanium, 0.08 % zirconium, and 0.02 % carbon) is used in place of pure molybdenum. It has similar thermal and improved structural properties. Due to its machinability, TZM is used for the majority of plasma-exposed parts.

TUNGSTEN
: Has the highest melting temperature of any element ($T_{melt} = 3695\,\mathrm{K}$, $\kappa \approx 173\,\mathrm{W\,m^{-1}\,K^{-1}}$) yet is challenging to machine. It is very brittle at room temperature and electro-discharge machining (EDM, also called spark-erosion) or laser-cutting typically need to be employed. EDM is more expensive than standard machining, thus tungsten parts are kept simple and limited to those experiencing the most extreme heat flux.

STAINLESS STEEL
: Has poor thermal properties ($T_{melt} \approx 1700\,\mathrm{K}$, $\kappa \approx 17\,\mathrm{W\,m^{-1}\,K^{-1}}$) but is inexpensive and easy to machine. Stainless steel is used wherever high heat flux performance is not needed.

SILVER
: ($T_{melt} \approx 1235\,K$) silver plated screws are used wherever possible. The silver reduces galling in the lubrication-free environment of high vacuum.

BERYLLIUM COPPER
: Used for removable electrical contacts due to good electrical conductivity and resiliency as a spring (high yield strength).

Insulators used include:

BORON NITRIDE
: Has very high thermal conductivity for an insulator (depending strongly on type, $\kappa \approx 100\,W\,m^{-1}\,K^{-1}$) and sublimates at $\sim 2000\,K$ in vacuum. It has a very low thermal expansion coefficient. Boron nitride is very soft, so it is easily machined, but not to high precision.

ALUMINA (ALUMINUM OXIDE)
: Has good thermal performance for an electric insulator ($T_{max} = 2345\,K$, $\kappa \approx 30\,W\,m^{-1}\,K^{-1}$). It is very hard and may be precision ground to better than $\pm 5\,\mu m$.

MICA
: Silicate mineral that may easily be cleaved into sheets $< 25\,\mu m$ thick. It has a high maximum temperature ($T_{max} = 972\,K$) and excellent voltage stand-off ($20\,V\,\mu m^{-1}$). Easily laser-cut into complex patterns.

TEFLON
: Fluoropolymer used mainly as a wire insulator, softens as it approaches its melting temperature, $T_{melt} = 600\,K$.

PEEK
: Thermoplastic that retains structural integrity to near its melting temperature, $T_{melt} = 616\,K$.

3.3.3 *RFA Design*

An exploded view of the RFA head design is shown in fig. 27; pictures of the head are shown in figs. 28 and 29. The probe was constructed out of a 22.2 mm outside diameter (OD) TZM cylinder, limited to this size by the 25.4 mm inside diameter (ID) scanning probe guide tube. The probe face is angled to 26° in the R-Z plane such that the slit is aligned to the typical flux surfaces 111 mm above the outer-midplane—the location of the scanning probe drive, fig. 26. The probe faces are angled 8.5° in the Z-ϕ plane so the surface normal of the slit is parallel to the magnetic pitch angle of the standard 5.4 T, 0.8 MA plasma equilibrium. The pitch angle changes less than 0.5° over the

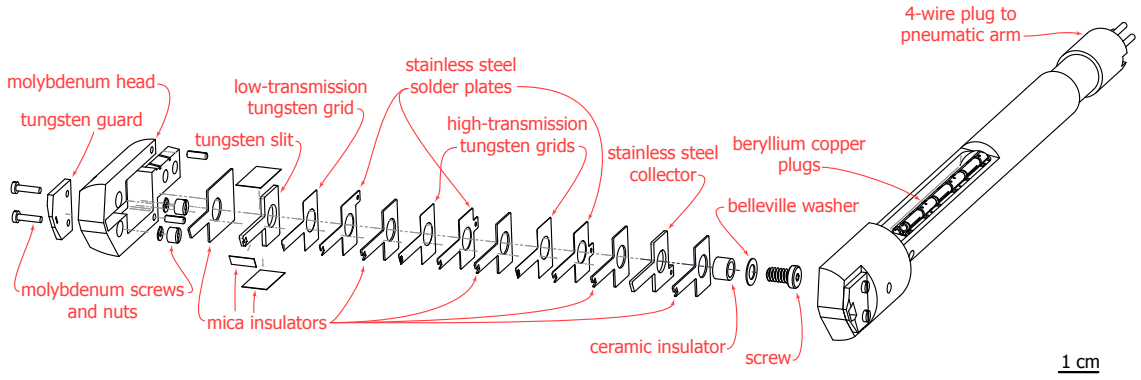

Figure 27: Line drawing of the retarding field analyzer probe. The "West" side is exploded while the "East" side remains assembled. Pictured is the stack assembly of electrodes and insulators which is held in the molybdenum probe head with a screw. The tungsten guard plate, held on with molybdenum nuts and bolts, protects the internal components. The electrodes are attached with wires (not pictured) to the beryllium copper plugs. The scanning probe system allows for only 4 independent electrodes, whereas the retarding field analyzer probe head has two distinct analyzers (each with 4 electrodes); the plugs allow for flexible operation of which electrodes are connected. The boron nitride sleeve is removed for clarity.

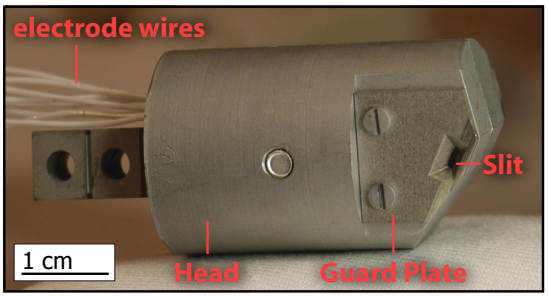

Figure 28: Photograph of an assembled RFA head. The wires from the internal components are coming out the left side of the probe.

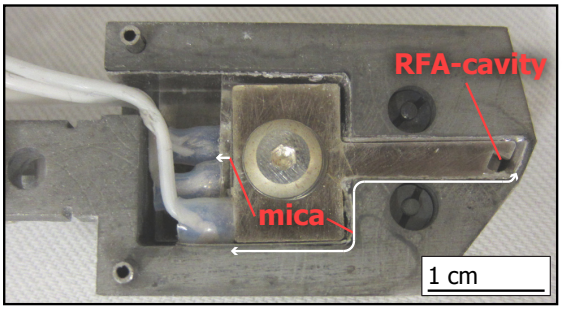

Figure 29: Photograph of one half of a RFA head. Mica is placed all around the RFA stack (over-lapping in the corners) to prevent it from arcing to the molybdenum head. The mica must also extend beyond the back of the stack (where the wires are soldered) to prevent arcing there.

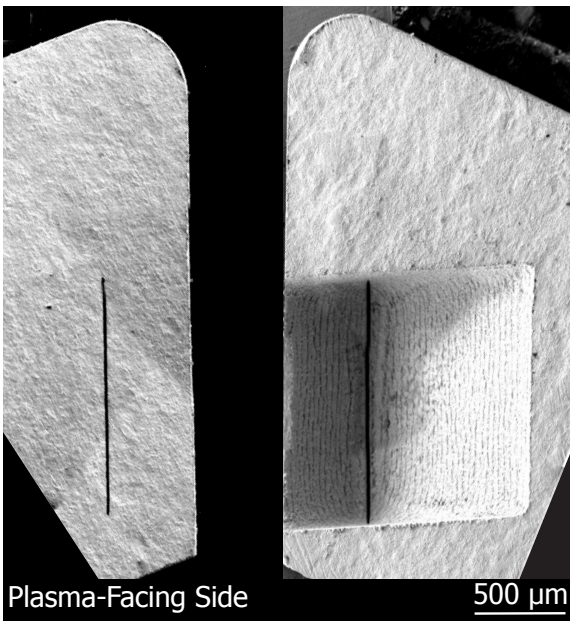

Figure 30: Composite SEM images of a 1 mm thick tungsten Slit plate. (Left) Plasma facing side. The wedge-relief (right) reduces energy-dependent reduction in transmission of ions through the slit (Larmor radius typically ~ 200 µm) while retaining enough mass to tolerate the plasma-deposited energy. The relief was formed by plunge-EMD eroding to ~ 25 µm of the opposite face. At the bottom of this valley is a 16 µm wide laser-cut slit. The slit is narrower than the Debye length to ensure that a sheath forms across it. The slit is aligned with the local flux surface.

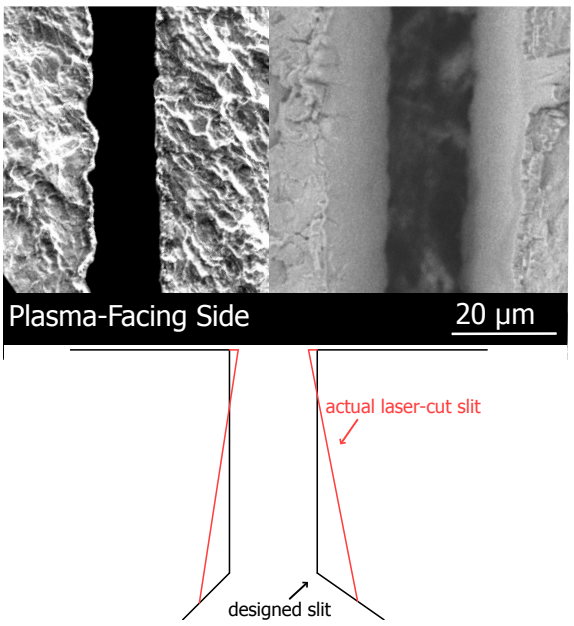

Figure 31: Composite SEM image of slit. Plasma facing side (left) and wedge-relief (right). The slit is slightly wider at the rear due to the laser cutting. This should increase the ion transmission over a perfectly straight slit

course of a typical spatial scan and less than $\pm 5°$ among extremes in equilibria used in these experiments. Misalignments caused by these changes are unlikely to affect ion transmission through the slit and probe operation [15].

The probe is composed of layers, each playing a specific role. The two TZM head halves provide machinable, high heat flux bases. Attached to each head half is a 1.5 mm thick tungsten Guard plate used to protect the Slit plate from high heat flux. Guard plates are held to the head with molybdenum screws and nuts from Thermoshield [38]. Split lock washers are used to keep the molybdenum screw in tension through thermal expansion; although a Belleville washer is preferred, it could not be used due to space restrictions. A wedge-shaped aperture 2 mm by 0.41 mm, formed by plunge EDM [1], exposes the Slit plate through the Guard plate. The wedge-aperture is stopped 0.2 mm before going through, to avoid a thin corner which would easily melt. The Guard plate reduces the total energy deposited on the Slit, reducing the peak temperature of this delicate component.

The Slit plate, figs. 30 to 32, provides an aperture into the cavity yet maintains a sheath over the aperture. It is a 1 mm thick tung-

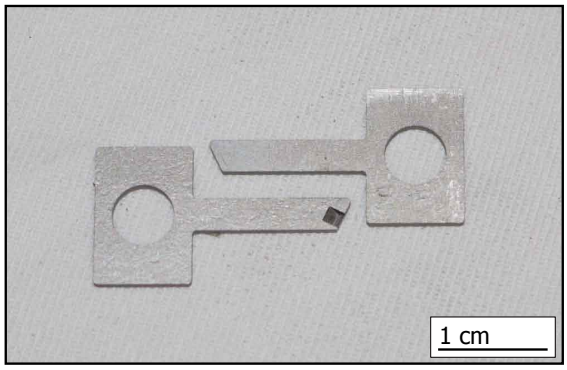

Figure 32: Image of the full Slit plate. Top is the plasma facing side and bottom is the side with the wedge relief.

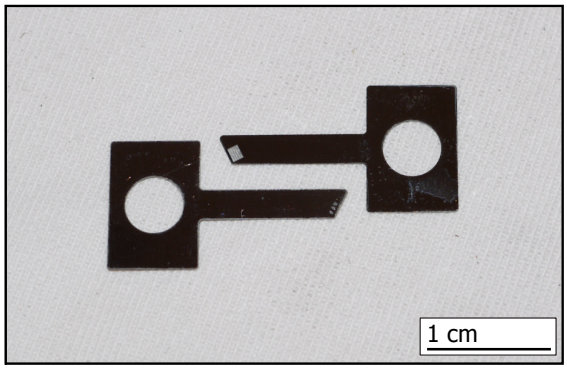

Figure 33: Full image of grids. Top is the high transmission grid and bottom is the low transmission grid.

sten plate with a 45° wedge plunge EDM eroded from the back to within 25 µm of the plasma-facing side. The wedge-relief provides space for ion transmission yet leaves sufficient material, compared to a foil with a slit, to drain the energy and prevent melting the slit. At the bottom of the wedge is a laser-cut aperture-which starts at ~ 25 µm wide and narrows to 16 µm at the face, fig. 31. This is a natural result of the laser-cutting process and an improvement over the design of a straight aperture; the ions are less selectively lost [15]. The Slit plate is electrically isolated and thus floating from the probe head and the Guard plate by a 400 µm thick layer of laser cut mica. The slit is aligned with the local magnetic flux surface (26° in the R-Z plane).

To reduce the plasma flux into the cavity such that it does not exceed the space-charge limit (section 3.3.4) there is a low-transmission grid placed directly behind the Slit plate, figs. 33 to 35. The grid is a laser-cut [29] 25 µm thick tungsten foil. Three 20 µm wide slits are cut orthogonal to the slit to ensure that some particles have at least an optical path from the plasma through the Slit and low-transmission grid into the cavity. The slits are spaced 500 µm ($\sim 2\rho_i$) to minimize overlap of the transmitted ion beams. This grid reduces transmission of plasma into the probe cavity by 95 %.

The high transmission grids, figs. 33 to 35, supply the potentials to retard charged particles yet must be transparent enough to not overly attenuate the flux. The high transmission grids are also laser-cut from 25 µm thick tungsten foil. The spacing of the grid wires is picked such that no matter the misalignment, at least one of the apertures has an optical path from the low-transmission grid to the Collector. The high-transmission grid is composed of 25 µm wires with 200 µm by 40 µm spaces, for an optical transparency of 54 % and total exposed area of 2.25 mm². The grids are electrically isolated by 400 µm thick layers of laser-cut mica. Since it is challenging to solder to tungsten, each grid is pressed against a 200 µm thick stainless steel "solder" plate. The stainless steel plates contain a tab with a hole to which a Teflon-

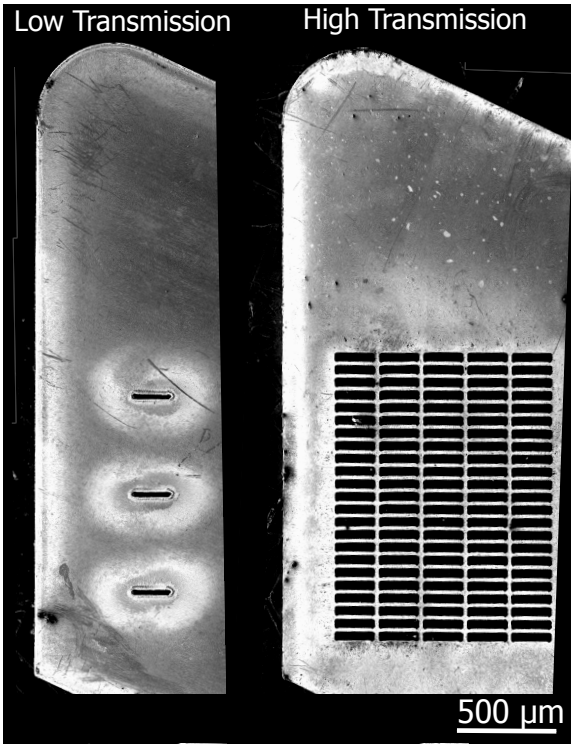

Figure 34: Composite SEM images of the low and high transmission grids. Both grids were formed by laser-cutting 25 µm thick tungsten foil. The low transmission grid can be used to attenuate the plasma flux into the probe to reduce it to below the space-charge limit. The high transmission grid (~ 54 % transparent) provides the bias to reject plasma electrons/ions.

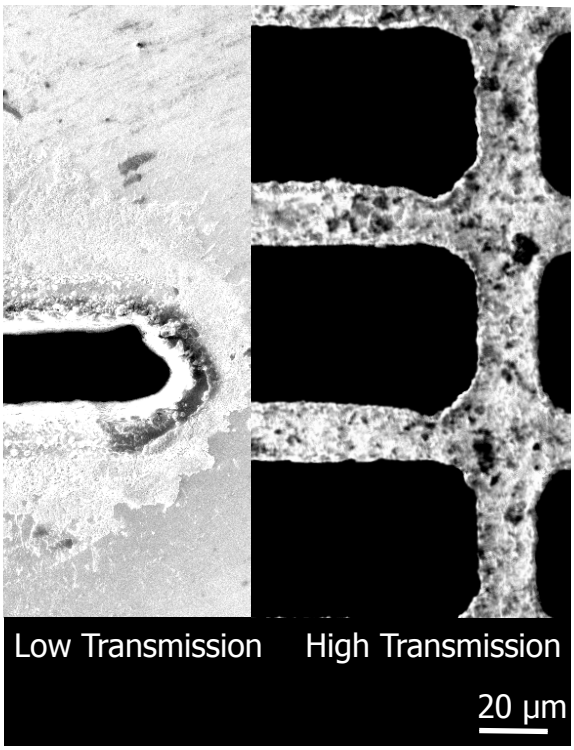

Figure 35: Close-up composite SEM image of grids. Left is the low transmission and right is the high transmission grid.

coated copper wire is soldered, fig. 29. The Collector is also a stainless steel plate. The tabs for each of the stainless steel plates are offset from each other to avoid interference among the wires. The total distance from the front of the Slit to the front of the Collector is 2.875 mm and the distance between the grids is 0.6 mm. It is advantageous to keep the grid spacing to a minimum: the allowed space charge current decreases with the inverse square of the spacing (section 2.4) [21].

The stack of electrodes (fig. 36) is held to the probe head with a silver-coated screw electrically isolated from the stack with an alumina cylinder, fig. 29. A Belleville washer ensures the screw stays tensioned through the large thermal excursions experienced by the probe. A stack of mica grid insulators is used to electrically isolate the Belleville washer from the Collector. Large clearances among the stack of components and the alumina cylinder allows the stack to be adjusted within the probe head to ensure proper alignment of the Slit plate behind the Guard plate. The mica around the 3 sides of the front of the stack allows for fine positioning of the stack (mica is easily cleaved into sheets ~ 25 µm thick). It is crucial that the mica overlap around corners and completely surround the stack. When assembled with only butt joints in the corners there was severe arcing among grid components and the molybdenum head. In places where the stack is not pressed against mica, such as the area around the tabs, it was necessary to extend the mica in between the grids out past the ends of the solder plates to prevent arcing there, fig. 29.

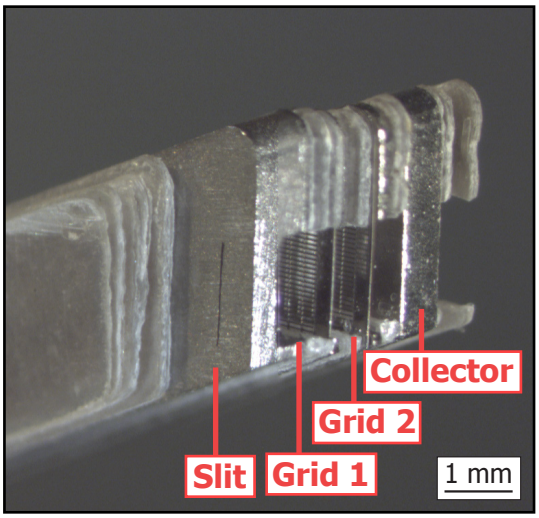

Figure 36: Close-up image of the RFA electrodes. The rest of the head is removed to show the arrangement of the electrodes.

Having such a tightly closed stack, there was concern about trapping of neutral gas within the probe cavity. This issue has been considered in other RFA designs [5, 30]. Anomalous current was thought to be caused by electron impact ionization of trapped neutral gas. The JET RFA contains holes specifically for exhausting neutral gas [30]. Despite operating in dense plasma ($\sim 10^{20}\,m^{-3}$), no sign of anomalous current, possibly due to breakdown of neutral gas, is observed. This may be due to the pre-baking (mentioned above) of the RFA head before installation.

The rear of the probe body is of the same construction as all other scanning probes. The probe head is held to a stainless steel core tube with two ceramic pins. Full electrical isolation is insured with mica sheets. Due to the large currents in the SOL and subsequent $\vec{J} \times \vec{B}$ forces during off-normal events, e. g., disruptions, it is important that the probe head remain floating. The core tube is isolated

from plasma contact with a boron nitride tube, necessary because the core tube is grounded through the probe drive. The boron nitride tube also captures the ceramic pins in place. Differential thermal expansion between the stainless steel core tube and boron nitride tube is accommodated with wave washers pre-loaded to 90 N. Alignment between the two head halves is maintained with press fit pins. Total probe alignment is ensured through asymmetric-matching keys and pins in the core tube and probe drive.

The RFA scanning probe head had to be fully compatible with the present probe drive system. This limits it to 4 independently biased electrodes due to space and vacuum feedthrough limitations within the scanning tube. This means that either one side may be biased and diagnosed completely or, to run double-sided, some electrodes must be biased in parallel and their currents recorded together. To accommodate the need for different bias arrangements the RFA was built to be flexible. Each electrical element in the stack is connected by a 22 AWG Teflon coated wire to a beryllium copper plug. The beryllium copper plugs may be attached in multiple configurations to the 4 stainless steel wires within the core tube, limited to two plugs per wire due to space constraints. This allows multiple electrodes to be biased together (e. g., Grid 1 on both sides shares the same voltage) and configurations may easily be changed with only partial disassembly of the probe (removal of the boron nitride tube). The wires and plugs within the core tube were originally electrically isolated from each other and the tube with fiberglass sock. This material was found to be unreliable and later replaced with Teflon heat-shrink tubing.

3.3.4 *Space Charge Limits*

Given the high densities ($> 10^{19}\,m^{-3}$) typical of the edge of Alcator C-Mod, space-charge limited current (section 2.4) is the biggest challenge to proper operation of the retarding field analyzer, beyond simply surviving the heat flux. After the electrons are rejected, only ions remain between the grids. This ion beam has its own potential structure. If the ion beam is sufficiently dense, its space-charge potential will overwhelm the bias of the grids—thus the true retarding potential is not known to the operator and the resulting data is essentially useless for determining T_i. Space charge limits are not a concern for electrons for these measurements; for deuterium and $T_i = T_e$ the limit is higher by $\sqrt{m_i/m_e} \approx 60$ (eq. (42)).

For a hypothetical case near the separatrix, where the density is the highest and thus space charge limits are most likely, we assume

$T_i = 100\,\mathrm{eV}$, $T_e = 50\,\mathrm{eV}$, and $n = 10^{20}\,\mathrm{m}^{-3}$. The total ion flux through the slit is given by:

$$I_{slit} = A_{slit}\frac{en}{2}\sqrt{\frac{k_B\left(ZT_e + T_i\right)}{m_i}}\,. \tag{54}$$

For the prescribed conditions $I_{slit} = 16\,\mathrm{mA}$. This is a pessimistic assumption, given that a portion of the ion flux is attenuated going through the slit. To asses if the RFA is operable in these plasma conditions, this value of I_{slit} must be compared to a model of space charge within the probe volume. If I_{slit} exceeds the calculation of space charge limited current, the probe would likely not function as an ion temperature diagnostic.

To calculate a more realistic value for space charge limited current than the 1D Child Langmuir limit Nachtrieb [27] used the Green function to solve the Poisson equation. He derived a relationship for the space charge potential of a rectangular volume of charge within a conducting, rectangular box, both of arbitrary size. The origin is centered in the middle of the box such that the grids are located at $x = \pm a$, the sides of the box are $y = \pm b$ and $z = \pm c$. The space charge is located within the volume defined by $-a' \leqslant x \leqslant a'$, $-b' \leqslant y \leqslant b'$, $-c' \leqslant z \leqslant c'$. The charge density spans the length of the box such that $a' = a$. The other dimensions of the charge volume are either determined by the slit width and height or the area to which the charge expands (about the size of the Larmor radius).

He considered the case where the space charge potential was about equal to the ion energy at the origin ($e\phi\,(0,0,0) \approx k_B T_i$) and the beam moved at the ion thermal velocity $\left(v = \sqrt{k_B T_i/m_i}\right)$:

$$I_{max} \approx \frac{8\epsilon_0}{e}\frac{b'c'}{a_2}\sqrt{\frac{(k_B T_i)^3}{m_i}}\frac{1}{F\,(a,b,c,a',b',c')}. \tag{55}$$

The shape function:

$$F\,(a,b,c) = \frac{2}{a^2}\sum_{l,m,n=0}^{\infty}\frac{8}{k_{lmn}^2}\frac{(-1)^l}{k_l a}\frac{\sin\left(k_m b'\right)}{k_m b}\frac{\sin\left(k_n c'\right)}{k_n c}\,, \tag{56}$$

with

$$\begin{aligned} k_l &= \left(l + \frac{1}{2}\right)\frac{\pi}{a}, \\ k_m &= \left(m + \frac{1}{2}\right)\frac{\pi}{b}, \\ k_l &= \left(n + \frac{1}{2}\right)\frac{\pi}{c}, \\ k_{lmn}^2 &= k_l^2 + k_m^2 + k_n^2. \end{aligned} \tag{57}$$

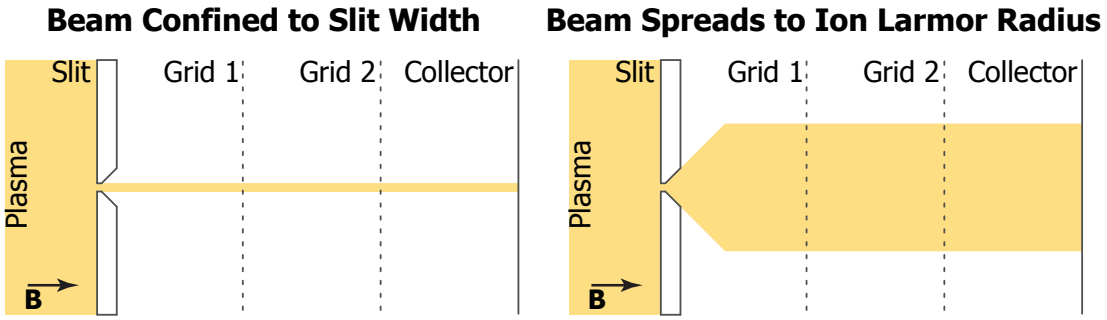

Figure 37: Ions confined to the slit width (left) and spreading to the ion Larmor radius (right). A more realistic assumption for space charge is that the ions, after entering the probe volume, spread to the Larmor radius. This allows for a higher total current.

For the new C-Mod RFA (section 3.3), the half-dimensions are: $a = 0.305\,\text{mm}$ and $b = c = 0.75\,\text{mm}$. Assuming that the ions are confined to the projected area of the slit (fig. 37): $a' = a = 0.305\,\text{mm}$, $b' = 0.008\,\text{mm}$, and $c' = 0.75\,\text{mm}$. Thus the shape function is $F \approx 0.037$. For the hypothetical case near the separatrix the space charge limited current is $I_{max} \approx 0.84\,\text{mA}$. The ion current through the slit (16 mA) is about 19 times greater than this calculation of space charge limited current. The probe under these assumptions will not be able to measure the ion temperature.

A more realistic and less conservative assumption is that the beam spreads out to about its Larmor radius, $\sim 0.3\,\text{mm}$ for this case, as shown in fig. 37. For a beam $2\rho_i$ wide the shape function is $F \approx 0.82$, larger because the beam is less of a ribbon (aspect ratio closer to unity). The space charge limited current in this case, assuming the ion beam is broadened, is now $I_{max} = 1.9\,\text{mA}$. The incident current through the slit (16 mA) still exceeds this more realistic calculations of the space charge limit.

This leads to the only conclusion that the ion flux through the slit must be attenuated. To do this we have created an extremely low transmission grid to be placed behind the Slit plate, section 3.3.3. This low transmission grid is a 25 µm thick tungsten foil with three laser cut 20 µm slits spaced 510 µm (approximately two ion gyroradii) apart. Since the total height of the slit is 1.5 mm, the optical transmission is approximately $\xi_{LT} \approx 3 \times {}^{0.02\,\text{mm}}/_{1.5\,\text{mm}} = 0.04$. The new ion current through the low transmission grid is $I_{LT} = \xi_{LT} I_{slit} = 0.64\,\text{mA}$, one third of the space charge limit (1.9 mA), assuming the beam broadens to the ion gyroradius. Thus, if the attenuation of ion flux through the slit is not enough to get the current in the probe below the space charge limit ($\sim 1\,\text{mA}$) we will use the low transmission grid to reduce it further.

An additional technique for mitigating the space charge potential is to enforce a greater bias between the grids [26]. This is typically done by keeping the Slit at a very negative potential (often in ion saturation at a $-100\,\text{V}$ to $-300\,\text{V}$) while sweeping Grid 1. As opposed to keeping

the Slit floating or grounded, this increased negative bias can reduce the relative maximum of the space charge potential between the grids to below the ion retarding grid potential. A simple estimate of the necessary voltage for a given current density and grid spacing can be found with the Child-Langmuir Law, section 2.4. This technique was not implemented on the C-Mod RFAs.

3.3.4.1 *Limiter RFA*

Lower Hybrid Current Drive (LHCD) is currently thought to be the most viable method to extend tokamak operation to steady state [31]. Lower hybrid heating extends the tail of the electron energy distribution. Extensive studies with LHCD at C-Mod have demonstrated an anomalous drop in current drive as density is increased [39, 40]. There is evidence of large changes to the boundary plasma during LHCD. The RFA has been demonstrated to be an important tool for exploring the SOL during LH operation; demonstrating both changes to fluctuations [12] and non-Maxwellian electrons [13]. But, the outer midplane scanning probe on C-Mod doesn't map magnetically to the LH launcher (both systems are located near the midplane of horizontal ports separated ~ 72° toroidally). To explore direct interactions, we have installed a RFA assembly on the side of a limiter which maps magnetically to the launcher in all plasmas (separated by ~ 40° toroidally).

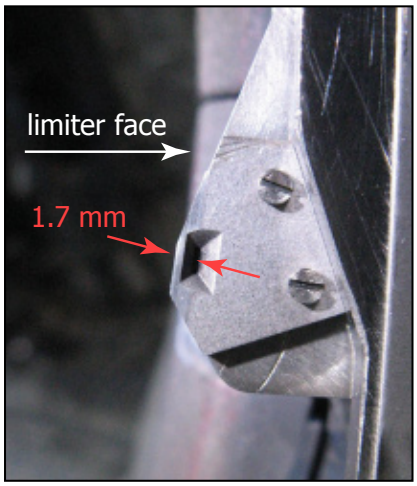

Figure 38: Retarding field analyzer mounted on the side of a limiter. Components are identical to that of the scanning retarding field analyzer, except that it is one-sided.

The retarding field analyzer fixed to the side of a limiter has identical internal components to the scanning probe head, fig. 38. It is held in a TZM and stainless steel box. The tip of the probe is flush with the limiter surface, placing the slit 1.7 mm behind the limiter. Given that the limiter tiles here never melt, we were confident that the RFA would be safe from melting. Signals are carried out on 50 Ω coaxial cable. To reduce displacement currents induced by the cable capacitance, the shields are biased at the same voltage as the center conductor. To facilitate this, the 4 cables are wrapped in fiberglass sock and then encased in a flexible stainless steel tube. They attach to the probe box with SMA connectors. The SMA connectors are attached to the probe body with a PEEK block to electrically isolate the shield from ground (which allows the shield to be biased). Teflon wires join the stainless steel plates in the stack to the center pin of the SMA connectors.

Since this RFA was attached to the side of the limiter and thus only accessible for repair during manned access it was a challenge to get it operating. There is very limited data with it during LH operation. However, interesting observations were made [7].

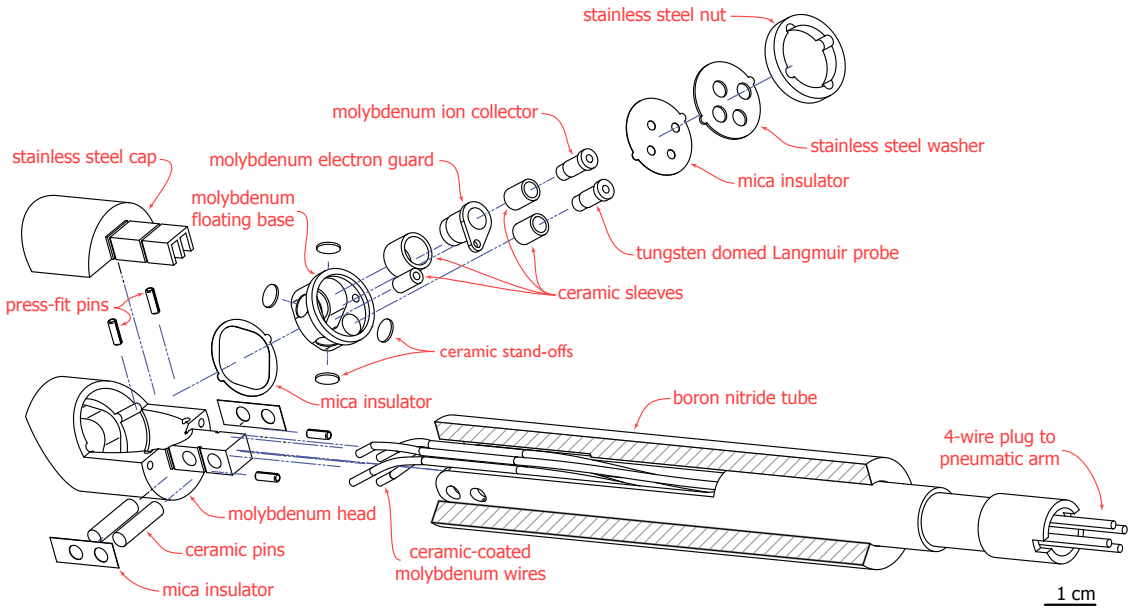

Figure 39: Exploded view of the ion sensitive probe. The Collector, Guard, and Langmuir probe are located and electrically isolated with precision-machined (±15 µm diameter) alumina ceramic cylinders. Depths are adjusted by filing the length of the cylinders down to ±5 µm. The stainless steel nut holds the entire assembly in the TZM head. Behind the head is the standard Alcator C-Mod scanning probe arm. The ceramic pins and mica insulators insure that the plasma-exposed probe head remains floating from ground.

3.3.5 *ISP Design*

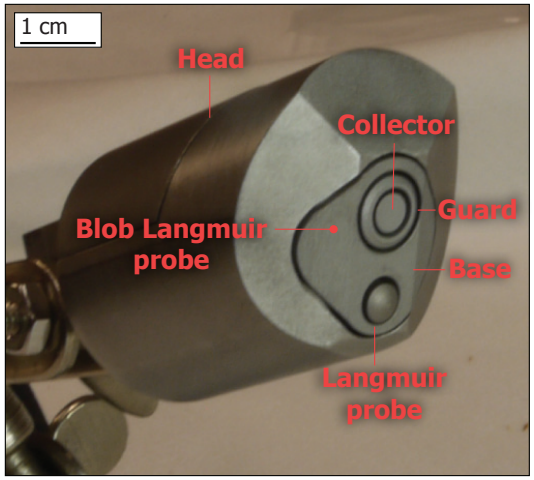

Figure 40: Plasma-facing view of the assembled ion sensitive probe head. Although not part of this assembly, the location of the Blob Langmuir probe is shown.

The ISP was constructed out of a 22.2 mm outside diameter (OD) TZM cylinder figs. 39 and 40, limited to this size by the 25.4 mm inside diameter (ID) scanning probe guide tube. The probe face is angled to 26° in the R-Z plane such that it is tangent to the typical flux surfaces 111 mm above the outer-midplane—the location of the scanning probe. The cylindrical symmetry of the ion sensitive and Langmuir probes makes alignment to the pitch of the magnetic field unnecessary.

The Langmuir probe is a 3 mm OD cylinder 0.69 mm proud of the probe head, presenting a domed surface to the plasma. The Langmuir probe was made with tungsten because it is easily created by EDM (due to simple cylindrical geometry) and it receives the highest heat flux. The other parts: Base, Guard, and Collector, were all made of TZM due to their complicated geometry. All parts are electrically isolated from each other with precision ground (±15 µm diameter) alumina cylinders. The Col-

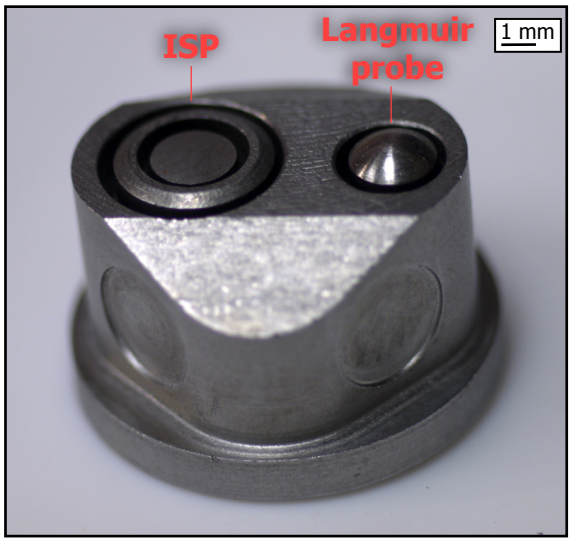

Figure 41: Front view of the ion sensitive probe sub-assembly.

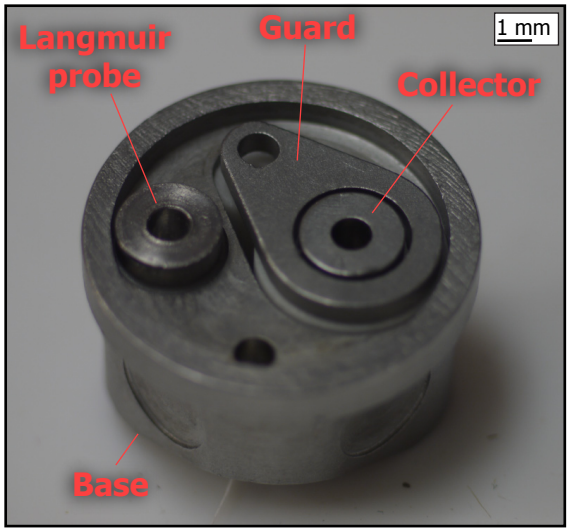

Figure 42: Rear view of the ion sensitive probe sub-assembly. The cylindrical ceramic sleeves can be seen behind the metal parts. Molybdenum wires with a cross-hatch pattern cut into their tips plug into each of the four holes.

lector is a 3 mm OD cylinder, its height with respect to the Guard is set to ± 5 µm by filing the alumina cylinder to length. The Guard is a 3.8 mm ID, 5.6 mm OD cylinder with the tip chamfered to spread the heat flux to a larger surface area. The Guard may be adjusted to any height relative to the probe Base; it is typically kept flush to minimize the electron current collected at strong positive bias. Figure 41 shows the electrodes assembled from the front and fig. 42 shows the rear.

This recess height of the Collector is typically set to the ion Larmor radius. However, at a depth of 100 µm electron current on the Collector was measured despite it being held at a bias less than the Guard, possibly due to slight misalignments in the scanning probe system relative to the magnetic field. At a depth of 200 µm there was no electron current detected on the Collector. Given the probe dimensions, the Collector should be magnetically shadowed for misalignments of up to 2°. The change in angle over the typical scan is $\sim 0.5°$ with respect to the Collector surface normal. Although the pitch angle can change $\pm 5°$ over the full range of magnetic configurations possible in C-Mod, it changes less than 2° with respect to the Collector surface normal.

The Langmuir probe and ion sensitive probes are contained within a Base that is electrically isolated from the head and connected (in the first version) to one of the four scanning probe electrodes. The relative location of parts within the head is maintained by having lips on the parts such that a retaining ring screwed in from the back presses and locks them in place. Electrical isolation of the Base from the head is maintained with domed, alumina buttons on the four sides and

laser-cut mica on the face and back of the Base. An additional laser cut stainless steel "washer" that matched the pattern of the mica allows the retaining nut to be tightened down without ruining the mica sheet.

With this setup, it was envisioned that the Langmuir and ion sensitive probes could be biased with respect to the Base, allowing them to float on top of the plasma floating potential fluctuations. Through initial operations it was found that the density fluctuations due to the arrival of plasma blobs (order unity plasma fluctuations transporting plasma particles and energy from the edge plasma into the boundary) during an I-V sweep was a greater challenge, causing difficulties in fitting eq. (47) to the I-V data.

Modifications were made to address the density fluctuations. An additional hole was drilled through the Base, placed 4.75 mm (center-to-center) along a field line connected between the outer-midplane and the center of the ion sensitive probe Collector. The Base wire was replaced with an alumina-coated 1.75 mm OD tungsten wire (same as that used for older Langmuir probe heads) that went through the new hole. The wire was filed flush with the surface of the Base, presenting a surface angled $\sim 30°$ into the magnetic field. This new Langmuir probe is kept in ion saturation, such that the Collector current can be normalized to it to reduce the deleterious effects of density fluctuations, section 4.3.2.3.

Each electrical element of the ISP head has a 1.60 mm ID hole, into which plug 1.75 mm OD diameter wires. The wires have cross patterns cut into their faces which allow them to be press-fit into the larger holes. The wires are coated in flame-sprayed alumina (save for the ends) to maintain electrical isolation. The rear of the probe body is of the same construction as all other scanning probes, including the RFA (section 3.3.3).

3.3.6 *Optimization With Thermal Simulations*

Alcator C-Mod presents a particularly challenging environment to make probe measurements: the heat flux parallel to the magnetic field can exceed $0.5\,\mathrm{GW\,m^{-2}}$ on the open field lines of the boundary and has an exponential fall-off to the wall with an e-folding length of only a few millimeters. There is a fine line between making a good measurement and ruining the probe. It is desirable that the probe be able to scan as deep into the plasma as possible without melting. Melting not only destroys the probe, ruining the known collection area and possibly shorting out electrodes, it injects impurities into the plasma, changing the very plasma trying to be measured. The physics that sets critical gradients near the LCFS is crucial to understanding the edge plasma [17, 20]. A probe that can operate within this space is much more useful than one that cannot.

The probe geometry was optimized for heat flux handling using the finite element code COMSOL [10]. 3D geometry was imported directly from the CAD program Solid Edge [33]. Coupling of these two powerful programs allowed for quick optimization of geometry; iterations could be performed in less than 15 min. To approximate the time variation of surface heat flux of the probe plunging through the exponential profile, the heat flux function in COMSOL was defined as:

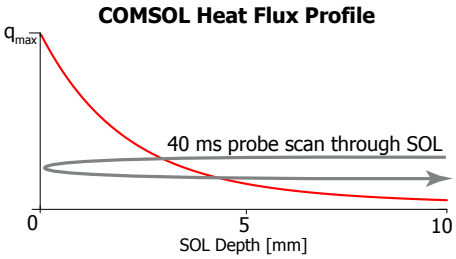

Figure 43: COMSOL SOL profile.

$$q_{\parallel}(t, x, y, z) = q_{max}\,\mathrm{tri}(t)\, e^{-x/\lambda} \tag{58}$$

where q_{max} is the peak heat flux, λ is the heat flux e-folding length, and $\mathrm{tri}(t)$ is a triangle function with a duration of the scan time (fig. 43). For the retarding field analyzer simulations these values were set to 0.4 GW m^{-2}, 4 mm, and 40 ms, respectively. For the ion sensitive probe simulations these values were set to 0.7 GW m^{-2}, 4 mm, and 40 ms, respectively. The probe was orientated such that coordinates $\hat{x}$ and $\hat{y}$ correspond to coordinates $\hat{\rho}$ and $\hat{B}$, shown in fig. 44. To simulate the heat flux arriving parallel to the magnetic field, $q_{\parallel}$ was multiplied on each plasma-exposed surface by the magnitude of the unit surface normal of the probe in the direction parallel to the magnetic field, $|\hat{n}_y|$. Temperature dependent material properties were used, which is an important detail: over the temperature range of interest (room to melting) the thermal conductivities and heat capacities of tungsten and molybdenum change by at least a factor of 2. Using the room temperature values results in an over-optimistic prediction of the heat flux which a probe may handle.

These simulations neglected heat flux perpendicular to the magnetic field as well as radiation-both from the plasma and the probe. Plasma radiation is much lower than the plasma heat flux. With external heating it is typically $\lesssim 0.5$ MW m^{-2}; however the probes will mostly be operated in ohmically heated plasmas where plasma radiation is ~ 0.02 MW m^{-2}. Thermal radiation from the probe is also relatively low at reasonable/expected operating temperatures. At tungsten's melting temperature (3695 K) its black body emitted power (with emissivity 0.04) is 4.2 MW m^{-2}.

Two design features were optimized for the RFA:

1. Peak heat flux handled without melting, especially the slit—this would allow the probe to operate deeper into the plasma.

2. Distance of the slit to the front of the probe—it is advantageous to keep the slit as close to the front of the probe as possible. Probe depth into the plasma is limited exclusively by plasma heating of the tip. Thus, the closer the slit is to the front of the probe, the deeper into the plasma measurements may be made.

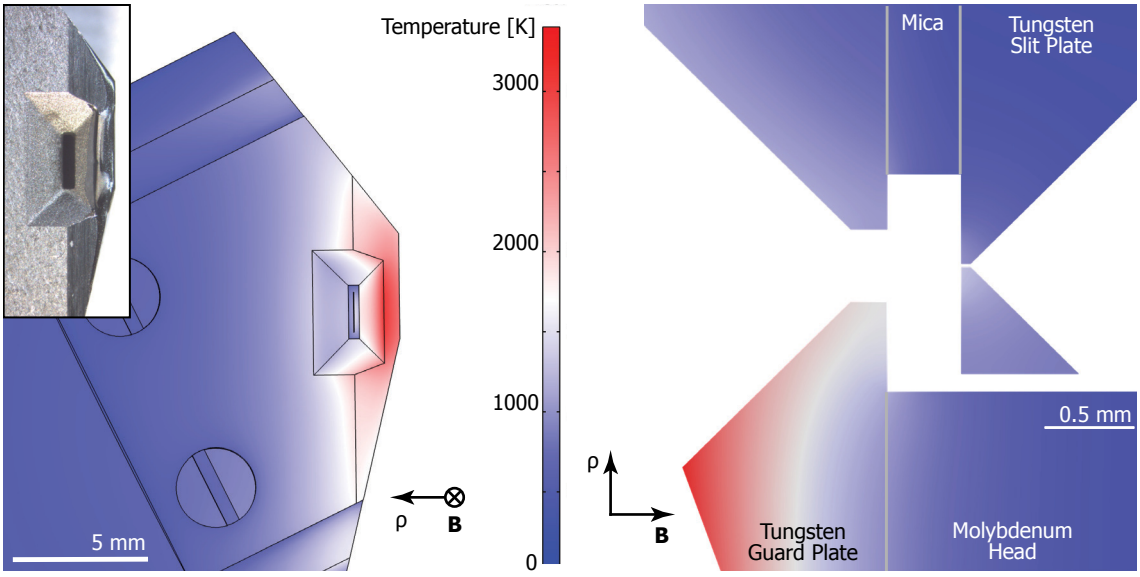

Figure 44: Results of finite element simulation (COMSOL) of plasma heat flux incident on retarding field analyzer probe. It simulated the probe plunging into the exponential heat flux of the boundary plasma to a peak heat flux of 0.4 GW m^{-2}. Pictured is the temperature at its peak, just after full insertion. (Left) The surface temperature of one face; the peak temperature is concentrated at the front of the probe. (Right) A slice through the middle of the slit; here it can be seen that the Guard plate reduces the plasma energy incident on the slit—preventing melting of this crucial component. At the time-scale of the scan, the Guard plate is nearly semi-infinite, a thicker plate will not improve performance. (Inset) A photo of a partially melted Guard, scanned to the LCFS; demonstrating the melt pattern expected from the simulation.

Simulation results are shown in figs. 44 and 45 for the optimized probe geometry. The peak heat flux of 0.4 GW m^{-2} is essentially the limit at which this probe can be operated (unless one can demonstrate proper operation is maintained with a Slit plate not normal to the magnetic field—a likely possibility given that the sheath is still developed).

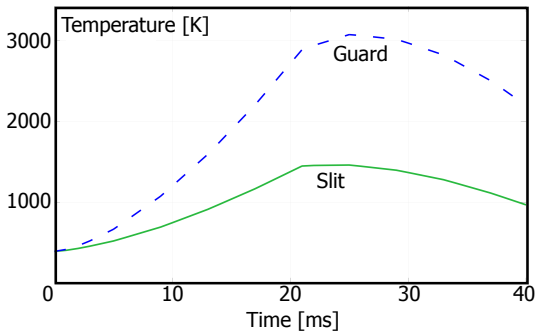

Figure 45: Peak surface temperatures over the scan of the Guard and Slit for the same finite element simulation as fig. 44. The Guard protects the delicate Slit from melting.

Preventing the Slit from melting was relatively easy; placement of a sacrificial tungsten Guard plate in front of the Slit with an aperture limits the total energy on the Slit. This allows the plasma energy deposited on the Slit to diffuse away from the Slit to areas not exposed, rather than build up around the wedge relief. Design feature 2 was more challenging, fundamentally limited by the fact that this was the region of largest heat flux. The best that could be done was make the Guard plate thick enough that it was nearly semi-infinite on the time scale of the scan (1.5 mm, also limited in thickness by space constraints) and to ensure that there were no sharp corners, which are "bottlenecks" to heat conduction.

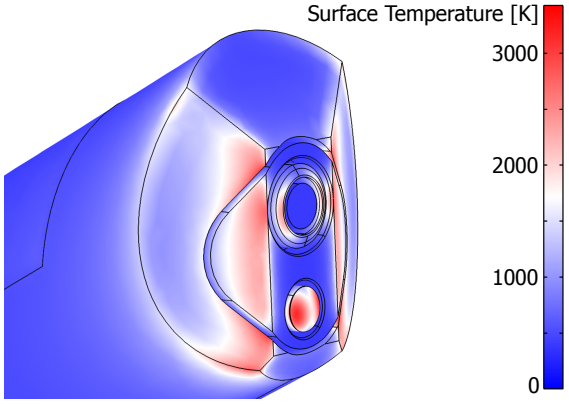

Figure 46: Results of finite element simulation in COMSOL of the ion sensitive probe plunging the scrape-off layer to a peak heat flux of 0.7 GW m^{-2}. Surface temperature at its peak (t = 25 ms).

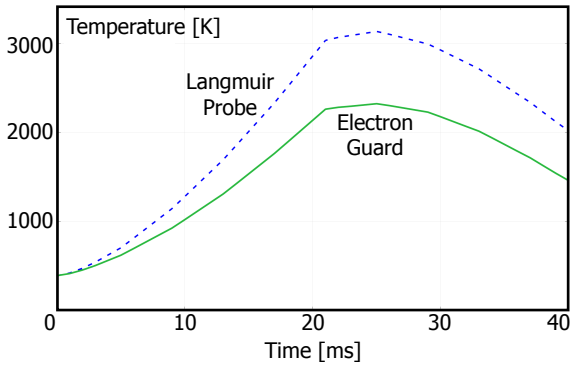

Figure 47: Peak temperature of the tungsten Langmuir probe and TZM Guard over the plunge. Although the tungsten Langmuir probe reaches the highest temperature, scan depth will be limited by all of the other TZM parts due to their lower melting temperature (2896 K versus 3695 K).

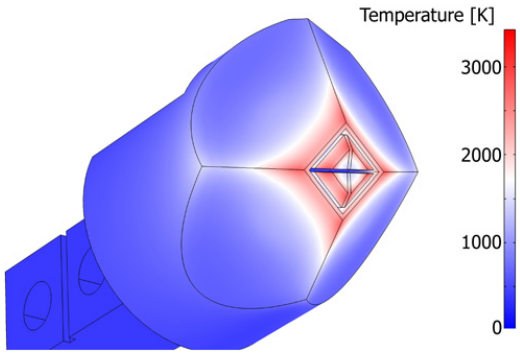

Figure 48: Time slice at peak surface temperature in COMSOL simulation of Mach Langmuir probe head at the same parameters as the ISP in fig. 46.

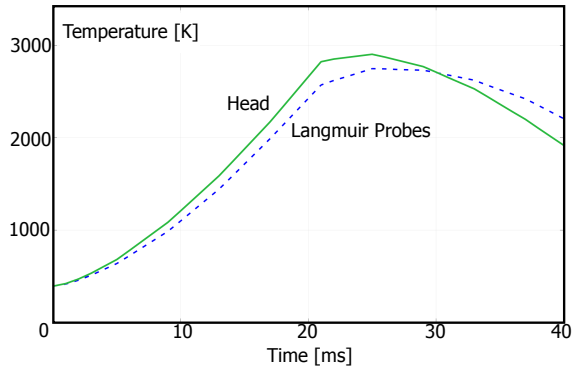

Figure 49: Temperature response of Mach probe head and Langmuir probes in COMSOL simulation.

The ISP simulations readily showed the regions that needed improvement. Most of the optimization was in trade-offs between making surfaces nearly tangent to the magnetic field to reduce the normal heat flux and keeping material thick enough such that there was enough thermal mass to drain the energy. Given the short time scale, 40 ms, bodies thicker than ~ 2 mm were essentially semi-infinite. Making the parts any thicker would not reduce the peak surface temperature. The simulation results of the final probe design are shown in figs. 46 and 47. Performance could be increase by substituting tungsten for the TZM parts, an unlikely change because manufacturing the tungsten parts would likely increase costs an order of magnitude.

For comparison, the current "high-heat flux"' Mach Langmuir probe head [34] can survive a simulated peak heat flux of ~ 0.7 GW m^{-2}, figs. 48 and 49. It is likely that the RFA can remain operational past a peak heat flux of 0.4 GW m^{-2}, despite melting; any molten tung-

sten on the Guard plate will drip down away from the Slit. On the other hand, the Langmuir probe and ISP must be operated below their peak heat flux; melting will ruin the known areas of the probe and may electrically short out elements. ⋆

BIBLIOGRAPHY

[1] Adron Tool Corp. P.O. Box 960, Menomonee Falls, WI, 53051, www.adron.com.

[2] A. C. Alkidas and R. M. Cole. Transient heat flux measurements in a divided-chamber diesel engine. *Journal of Heat Transfer*, 107(2):439–444, 1985.

[3] N. P. Basse, A. Dominguez, E. M. Edlund, C. L. Fiore, R. S. Grantez, A. E. Hubbard, J. W. Hughes, I. H. Hutchinson, J. H. Irby, B. LaBombard, L. Lin, Y. Lin, B. Lipschultz, J. E. Liptac, E. S. Marmar, D. A. Mossessian, R. R. Parker, M. Porkolab, J. E. Rice, J. A. Snipes, V. Tang, J. L. Terry, S. M. Wolfe, S. J. Wukitch, and K. Zhurovich. Diagnostic Systems on Alcator C-Mod. *Fusion Science and Technology*, 51, 2007.

[4] D. A. Bendersky. A special thermocouple for measuring transient temperatures. *Mechanical Engineering*, 75:117, 1953.

[5] C. Bohm and J. Perrin. Retarding-field analyzer for measurements of ion energy distributions and secondary electron emission coefficients in low-pressure radio frequency discharges. *Review of Scientific Instruments*, 64(1):31–44, 1993.

[6] D. Brunner and B. LaBombard. Surface thermocouples for measurement of pulsed heat flux in the divertor of the Alcator C-Mod tokamak. *Review of Scientific Instruments*, 83(3):033501–033501, 2012.

[7] D. Brunner, B. LaBombard, R. Ochoukov, and D. Whyte. Scanning retarding field analyzer for plasma profile measurements in the boundary of the Alcator C-Mod tokamak. *Review of Scientific Instruments*, 84(3):033502, 2013.

[8] D. Brunner, B. LaBombard, J. Payne, and J. L. Terry. Comparison of heat flux measurements by IR thermography and probes in the Alcator C-Mod divertor. *Journal of Nuclear Materials*, 415(1):S375–S378, 2011.

[9] D. R Buttsworth. Assessment of effective thermal product of surface junction thermocouples on millisecond and microsecond time scales. *Experimental Thermal and Fluid Science*, 25(6):409–420, 2001.

[10] COMSOL Inc. 1 New England Executive Park, Suite 350, Burlington, MA 01803, www.comsol.com.

[11] S. Gangadhara, B. Labombard, B. Lipschultz, and N. Pierce. Novel surface thermocouple probes for divertor heat flux measurement. In *Bulletin American Physical Society*, volume 41, 1996.

[12] J. P. Gunn, V. Petrzilka, A. Ekedahl, V. Fuchs, E. Gauthier, M. Goniche, M. Kočan, J.-Y. Pascal, and F. Saint-Laurent. Measurement of lower hybrid hot spots using a retarding field analyzer in Tore Supra. *Journal of Nuclear Materials*, 390-391:904 – 906, 2009.

[13] J. P. Gunn, V. Petržílka, V. Fuchs, A. Ekedahl, M. Goniche, J. Hillaret, M. Kočan, and F. Saint-Laurent. Radial-poloidal mapping of the energy distribution of electrons accelerated by lower hybrid waves in the scrape-off layer. In *AIP Conference Proceedings*, volume 1187, page 391, 2009.

[14] C. T. Kidd. High heat flux measurements and experimental calibrations/characterizations. *In NASA. Langley Research Center, The 1992 NASA Langley Measurement Technology Conference: Measurement Technology for Aerospace Applications in High-Temperature Environments*, pages 31–50, 1992.

[15] M. Kočan, J. P. Gunn, M. Komm, J.-Y. Pascal, E. Gauthier, and G. Bonhomme. On the reliability of scrape-off layer ion temperature measurements by retarding field analyzers. *Review of Scientific Instruments*, 79(7):073502, 2008.

[16] B. Labombard, J. A. Goetz, I. Hutchinson, D. Jablonski, J. Kesner, C. Kurz, B. Lipschultz, G. M. McCracken, A. Niemczewski, J. Terry, A. Allen, R. L. Boivin, F. Bombarda, P. Bonoli, C. Christensen, C. Fiore, D. Garnier, S. Golovato, R. Granetz, M. Greenwald, S. Horne, A. Hubbard, J. Irby, D. Lo, D. Lumma, E. Marmar, M. May, A. Mazurenko, R. Nachtrieb, H. Ohkawa, P. O'Shea, M. Porkolab, J. Reardon, J. Rice, J. Rost, J. Schachter, J. Snipes, J. Sorci, P. Stek, Y. Takase, Y. Wang, R. Watterson, J. Weaver, B. Welch, and S. Wolfe. Experimental investigation of transport phenomena in the scrape-off layer and divertor. *Journal of Nuclear Materials*, 241-243:149 – 166, 1997.

[17] B. LaBombard, J. W. Hughes, N. Smick, A. Graf, K. Marr, R. McDermott, M. Reinke, M. Greenwald, B. Lipschultz, J. L. Terry, D. G. Whyte, S. J. Zweben, and Alcator C-Mod Team. Critical gradients and plasma flows in the edge plasma of Alcator C-Mod. *Physics of Plasmas*, 15(5):056106, 2008.

[18] B. LaBombard, J. E. Rice, A. E. Hubbard, J. W. Hughes, M. Greenwald, J. Irby, Y. Lin, B. Lipschultz, E. S. Marmar, C. S. Pitcher, N. Smick, S. J. Wolfe, S. M. Wukitch, and the Alcator Group. Transport-driven scrape-off-layer flows and the boundary conditions imposed at the magnetic separatrix in a tokamak plasma. *Nuclear Fusion*, 44(10):1047, 2004.

[19] B. LaBombard, J. L. Terry, J. W. Hughes, D. Brunner, J. Payne, M. Reinke, I. Cziegler, S. Zweben, R. Granetz, M. Greenwald, I. H. Hutchinson, J. Irby, Y. Lin, B. Lipschultz, Y. Ma, E. S. Marmar, N. Mucic, W. Parkin, S. Pierson, R. Rosati, R. Rowan, H. Savelli, J. Stillerman, N. Tsujii, R. Viera, G. Wallace, D. G. Whyte, S. Wolfe, S. Wukitch, G. Wurden, and J. Zaks. Boundary layer heat transport experiments in Alcator C-Mod in support of the FY2010 US DoE Joint Research Target, 2010.

[20] B. LaBombard, J. L. Terry, J. W. Hughes, D. Brunner, J. Payne, M. L. Reinke, I. Cziegler, R. Granetz, M. Greenwald, I. H. Hutchinson, J. Irby, Y. Lin, B. Lipschultz, Y. Ma, E. S. Marmar, W. L. Rowan, N. Tsujii, G. Wallace, D. G. Whyte, S. Wolfe, S. Wukitch, G. Wurden, and the Alcator C-Mod Team. Scaling of the power exhaust channel in Alcator C-Mod. *Physics of Plasmas*, 18:056104, 2011.

[21] I. Langmuir and K. T. Compton. Electrical discharges in gases Part II. Fundamental phenomena in electrical discharges. *Review of Modern Physics*, 3:191–257, Apr 1931.

[22] V. Menezes and S. Bhat. A coaxial thermocouple for shock tunnel applications. *Review of Scientific Instruments*, 81(10):104905, 2010.

[23] A. F. Mills. *Heat Transfer*. Irwin Publishing, Homewood, IL, 1992.

[24] C. E. Moeller, M. C. Noland, B. L. Rhodes, and Midwest Research Institute. *NASA contributions to development of special-purpose thermocouples: A survey*, volume 5050. Technology Utilization Division, National Aeronautics and Space Administration, 1968.

[25] H. Mohammed, H. Salleh, and M. Z. Yusoff. Design and fabrication of coaxial surface junction thermocouples for transient heat transfer measurements. *International Communications in Heat and Mass Transfer*, 35(7):853 – 859, 2008.

[26] A.W. Molvik. Large acceptance angle retarding-potential analyzers. *Review of Scientific Instruments*, 52(5):704–711, 1981.

[27] R. Nachtrieb, B. LaBombard, and E. Thomas. Omegatron ion mass spectrometer for the Alcator C-Mod tokamak. *Review of Scientific Instruments*, 71(11):4107–4118, 2000.

[28] J. Nanigian and D. Nanigian. A unique thermocouple to measure the temperatures of squibs, igniters, propellants and rocket nozzles. In *Proceedings of SPIE*, volume 6222, pages 622203–1, 2006.

[29] PhotoMachining Inc. 4 Industrial Drive, Unit #40, Pelham, NH, 03076, www.photomachining.com.

[30] R. A. Pitts, R. Chavan, S. J. Davies, S. K. Erents, G. Kaveney, G. F. Matthews, G. Neill, J. E. Vince, and I. Duran. Retarding field energy analyzer for the JET plasma boundary. *Review of Scientific Iinstruments*, 74(11):4644–4657, 2003.

[31] F. M. Poli, C. E. Kessel, M. S. Chance, S. C. Jardin, and J. Manickam. Ideal MHD stability and performance of ITER steady-state scenarios with ITBs. *Nuclear Fusion*, 52(6):063027, 2012.

[32] Y. Rabin and D. Rittel. A model for the time response of solid-embedded thermocouples. *Experimental Mechanics*, 39(2):132–136, June 1999.

[33] Siemens PLM Software Inc. 5800 Granite Parkway, Suite 600, Plano, TX 75024, `www.plm.automation.siemens.com/en_us/products/velocity/solidedge`.

[34] N. Smick and B. LaBombard. Wall scanning probe for high-field side plasma measurements on Alcator C-Mod. *Review of Scientific Instruments*, 80(2):023502, 2009.

[35] J. A. Snipes, B. LaBombard, M. Greenwald, I. H. Hutchinson, J. Irby, Y. Lin, A. Mazurenko, and M. Porkolab. The quasi-coherent signature of enhanced Dα H-mode in Alcator C-Mod. *Plasma Physics and Controlled Fusion*, 43(4):L23, 2001.

[36] J. L. Terry, B. LaBombard, D. Brunner, J. W. Hughes, M. L. Reinke, and D. G. Whyte. Heat-flux footprints for I-mode and EDA H-mode plasmas on Alcator C-Mod. *Journal of Nuclear Materials*, 2013.

[37] J. L. Terry, B. LaBombard, D. Brunner, J. Payne, and G. A. Wurden. Divertor IR thermography on Alcator C-Mod. *Review of Scientific Instruments*, 81(10):10E513–10E513, 2010.

[38] Thermo Shield. 361 Grove Dr., Portola Valley, CA 94028, `http://www.thermoshield-us.com`.

[39] G. M. Wallace, I. C. Faust, O. Meneghini, R. R. Parker, S. Shiraiwa, S. G. Baek, P. T. Bonoli, A. E. Hubbard, J. W. Hughes, B. L. LaBombard, C. Lau, Y. Ma, M. L. Reinke, J. L. Terry, D. G. Whyte, J. C. Wright, S. J. Wukitch, R. W. Harvey, A. E. Schmidt, A. P. Smirnov, and J. R. Wilson. Lower hybrid current drive at high density in the multi-pass regime. *Physics of Plasmas*, 19:062505, 2012.

[40] G. M. Wallace, A. E. Hubbard, P. T. Bonoli, R. W. Harvey, J. W. Hughes, B. L. LaBombard, O. Meneghini, R. R. Parker, A. E. Schmidt, S. Shiraiwa, A. P. Smirnov, D. G. Whyte, J. R. Wilson, J. C. Wright, S. J. Wukitch, and the Alcator C-Mod Team. Lower

hybrid current drive at high density in Alcator C-Mod. *Nuclear Fusion*, 51:083032, 2011.

4

DATA ACQUISITION AND PROCESSING

Careful consideration must be made for the biasing and measurement electronics: the probes need to measure µA-level currents within meters of MW-level RF antenna. The short scale-length of plasma parameters (a few mm) in conjunction with the high heat flux requires that the probe move in and out of the plasma quickly ($\sim 1\,\mathrm{m\,s^{-1}}$) and the bias swept quickly ($\sim 2\,\mathrm{kHz}$) to resolve the gradients. Additionally, the plasma is quite turbulent in the edge, with fluctuation amplitudes (e. g., $\tilde{n}/n$) up to order unity and fluctuation frequencies up to $\sim 1\,\mathrm{MHz}$. Large currents in the edge and changing magnetic fields require careful consideration of probe grounding.

4.1 EMBEDDED THERMOCOUPLES

4.1.1 *Electronics*

To allow for direct measurement of the embedded (calorimeter and tile) temperatures type-K (Chromel and Alumel) wires are run all the way from the thermojunction, through the vacuum feedthrough, and to the electronics rack. In the rack are custom thermocouple boards, fig. 50, which contain ice point compensation circuits. These circuits output a $10\,\mathrm{mV\,°C^{-1}}$ signal. Thermocouple signals are digitized on DTAcq DT196 units at 400 kHz. An RC-filter on the input of the boards removes high frequency noise.

This setup is more susceptible to voltage pickup from changing magnetic fields than the coaxial surface thermocouple system (sec-

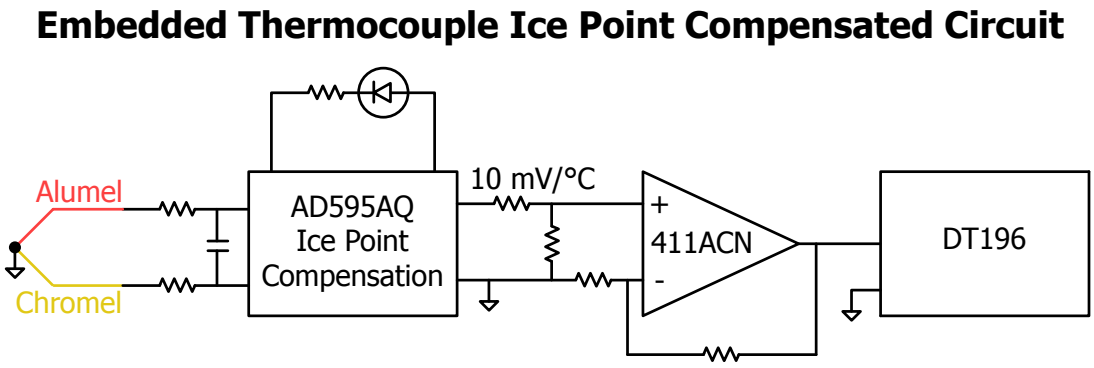

Figure 50: Embedded thermocouple circuit. The thermocouple is grounded directly at the measurement location. Chromel and Alumel wires are run all the way from the thermocouple junction to the ice point compensated chip. The ice point chip outputs $10\,\mathrm{mV\,°C^{-1}}$. An LED light turns on if the thermocouple is not grounded. Signals are digitized on DT196 units at 400 kHz. (circuit designed by Brian LaBombard)

tion 3.2). The type-K cabling in vessel is a wire pair in ceramic insulation and a stainless steel sheath. The wire pair presents a non-zero area for pick up of the time changing magnetic fields, especially so at the vacuum feedthrough where spade plugs were used. The feedthrough was orientated such that the plugs were parallel to the poloidal field to minimize pick up. However, since the embedded thermocouples were primarily used for integrated energy deposition measurements, the loss of information due to the exclusion of data during the toroidal field ramps (which occur from the end of the plasma pulse to ~ 2.5 s after) was inconsequential.

4.1.2 *Data Processing*

The calorimeters were originally envisioned to measure the divertor heat flux. That is, from the temperature history at the location of the thermocouple, it was hoped to measure the temperature history of the calorimeter at the thermocouple location, calculate the heat flux that passed through that location, place that heat flux and temperature as a back boundary condition on a simulation of the tip of the calorimeter, and finally calculate the surface heat flux. But, as shown in section 3.1, the time response of the thermocouples was insufficient to accurately measure the temperature change at their location. Even the bare-tip fast response thermocouples were too slow to infer the heat flux.

Despite the lack of time resolution the thermocouples still provide information regarding total energy deposited by the plasma onto the non-cooled plasma-facing components. I. e., the plasma exposure during a pulse is the only energy source or sink available to alter the temperature of the probes. Accurate knowledge of the geometry and material properties of the system allow for modeling and calculation of the total energy deposited on the calorimeters. The energy incident on a simple 1D model of the calorimeters, including the delayed response of the thermocouples, is iterated until the simulated temperature response most closely matches the experiment. Changing over from the slow-response to fast-response thermocouples greatly improved confidence with this modeling.

Nearly all data analysis at C-Mod is done with code written in IDL [9, 21]. To stream-line the modeling and calculation of energy deposition a finite element heat flux program, QFLUX_1D, was created by LaBombard and Payne in IDL. It allows for temperature dependent thermal properties and different materials, lengths, and cross-sectional areas at each node. An example output from QFLUX_1D is given in fig. 51. Any two sets of boundary conditions (the temperature or heat flux at the front or rear of the simulation domain) may, and must, be specified.

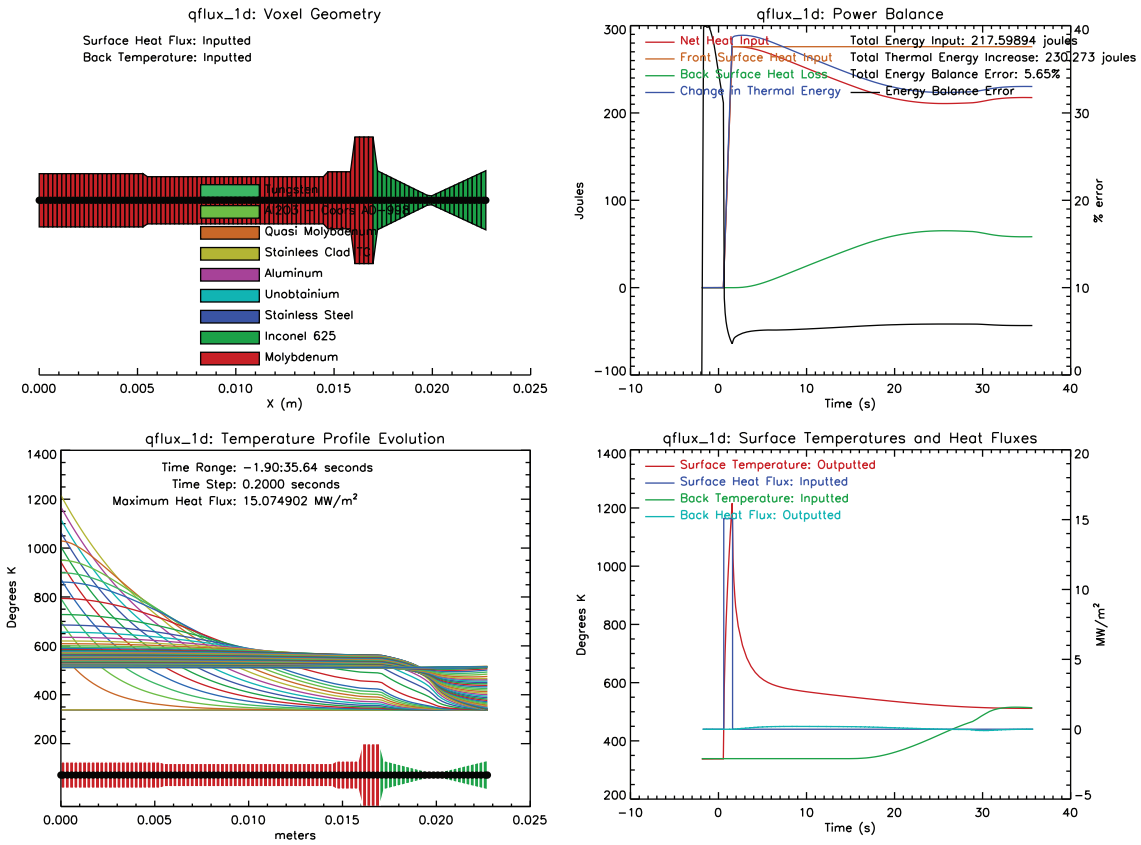

Figure 51: An example output from a QFLUX_1D simulation of a calorimeter. Upper-left panel is a diagram of the material model, showing the materials available for simulation and those used for each node. It also shows the relative cross-sectional area for each node. Bottom-left panel is the the temperature profile history through the model. Upper-right panel are calculations of power balance. Bottom-right panel are the two inputed boundary conditions and the two outputted boundary conditions resulting from the calculations.

Accurate measurements were made of the tile and calorimeter geometry, including depth of the thermocouple tip from the plasma-facing surface and the mass of each component. This data was translated into cross-sectional areas as a function of length in each 1D model. Care was taken to ensure that the mass of each individual 1D model was the same as that measured. Any error in the mass would translate into systematic errors in the calculated energy.

The slow response of the thermocouples requires a two-step analysis. The first step is to apply a square-wave heat flux pulse from 0.5 s to 1.5 s, replicating plasma-flattop, to the plasma-facing side of the calorimeter or tile model. The exact shape of this heat pulse is not important because the precise temporal information is lost as the energy diffuses through the system. A triangle waveform with the same total energy as the square waveform has the same temperature history at the location of the thermocouple. The back boundary condition for the tile simulations is a constant heat flux (but very small in comparison to the plasma heat flux) estimated by the late-time (after 20 s) thermal decay measured by the thermocouple. The back boundary condition for the calorimeter system, placed on the interface between the Inconel sleeve and the tile, is the temperature at this location in the surrounding tile from the tile energy deposition simulation.

The temperature time history from the first step at the location of the thermocouple within the calorimeter/tile is then input into the second step. It is used as the front boundary condition on a simulation of the thermocouple body. The thermocouple body is a 1.5 mm diameter stainless steel cylinder that is long enough (50 mm) such that the back temperature does not change appreciably on the time scale of the simulation. For example, taking a stainless steel body initially at 350 K with thermal diffusivity $\alpha = 4 \times 10^{-6}\,\mathrm{m^2\,s^{-1}}$ the 1D heat equation for an applied constant surface temperature of 550 K indicates that at 50 mm into the stainless steel body the temperature increases by only 0.2 K in 30 s. Thus the boundary condition there, be it constant temperature or zero heat flux, does not matter.

From this simulation the temperature profile through the thermocouple body is calculated. The temperature time histories at varying depths (finite element nodes) in the thermocouple body are compared to the measured temperature time history. The node with the minimum error between the time histories is selected as the best match between the measurement and simulation. Time points during large changes in the toroidal field are not considered because of the large voltage pickup. These two steps are iterated until a given surface heat flux and depth into the thermocouple body gives the minimum error between the measured and simulated temperature profiles. This 2-step simulation assumes that the thermocouple body drains an insignificant amount of energy from the calorimeter/tile system.

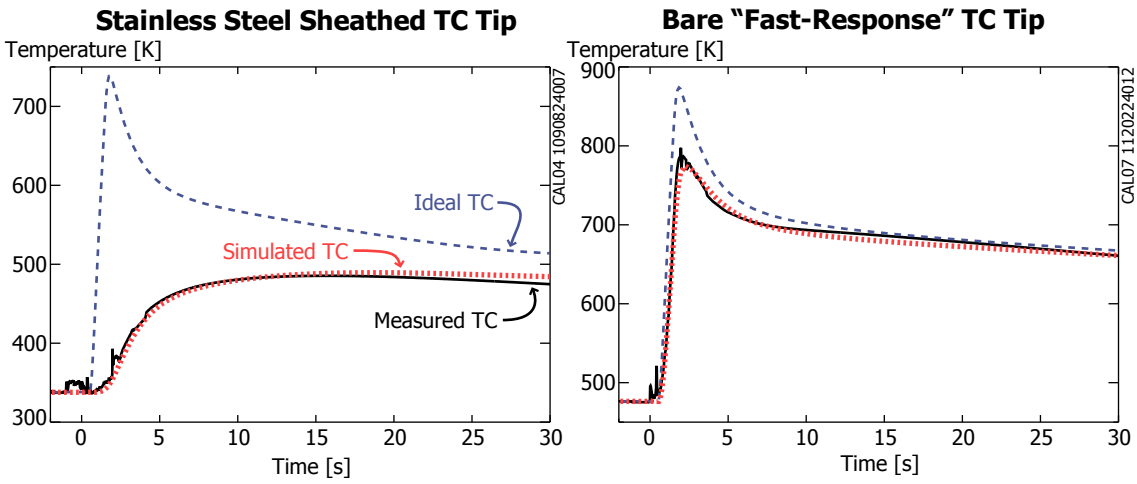

Figure 52: A comparison of the time response of the two different styles of the thermocouples and the results of attempts to calculate the energy deposited on the calorimeters. Both having very similar calculated energy deposition (289 J and 276 J). Left panel is the slow-time response thermocouple and the results of a simulation (as discussed in the text). Right panel is the fast-response thermocouple. The line labeled "Ideal TC" indicates the temperature in the calorimeter at the location of the thermocouple, i. e., the temperature that a thermocouple with sufficiently fast thermal response would measure.

A comparison for this energy calculation technique for both the slow-response stainless steel sheathed (289 J calculated deposited energy) and fast-response bare tip (276 J calculated deposited energy) thermocouples is given in fig. 52. Although the calculated deposited energy varies by less than 5 % between these two different cases, the difference in thermocouple tip gives very different time responses. The bare tip fast-response thermocouple is now much closer to the ideal thermocouple (i. e., the simulated temperature response at the thermocouple location or what a thermocouple would measure if it had sufficient time response). In both instances the time delay of the thermocouple is well modeled by the simulations. The major difference between these simulations is the depth of the of the best-fit temperature profile for each of the simulated thermocouples: 3.3 mm into the slow-response and 0.5 mm into the fast-response. The depth from this slow-response simulation (3.3 mm) is close to that of the actual thermocouple stainless steel tip (~ 2 mm, fig. 21). The thermal resistance of the stainless steel tip causes a large temperature drop from the tile to the thermojunction. If the measured temperature were taken to be what the tile actually was, this would cause a significant (> 20 %) underestimate of the deposited energy.

This energy deposition measurement technique is generally successful. Total energy deposited in comparison with IR thermography and surface thermocouples is quite good, section 5.1. •

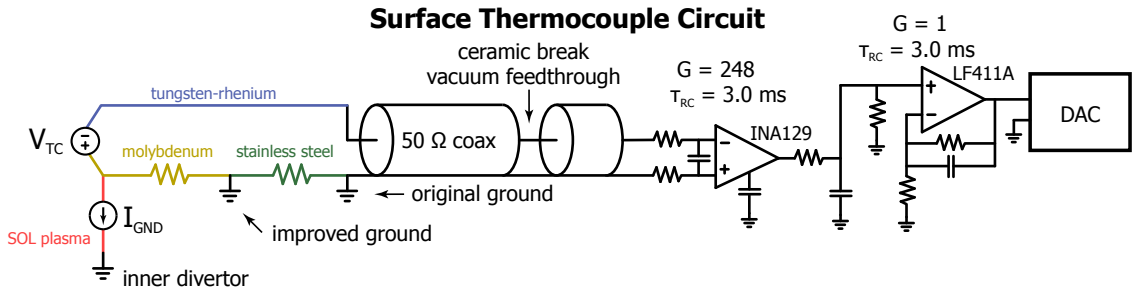

Figure 53: The thermal EMF (V_{TC}) is generated at the molybdenum/tungsten-rhenium thermojunction. No other thermojunctions change temperature through the pulse. The voltage is transmitted via a 50 Ω coax to a high common-mode rejection instrumentation amplifier with a gain of 248. The differential input RC filter has a 3 ms time constant. The signal is put through a unity gain circuit with further filtering (3 ms time constant) and then digitized on a D-tAcq ACQ196 unit at 400 kHz. Both the original and improved grounding points are shown (ground taken to be the vacuum vessel potential). With the old grounding method, plasma-induced currents would flow though the stainless steel thermocouple holder, contributing a voltage that was of the same order and sign of V_{TC}, leading to erroneous temperature measurements. In the present design the current path through the stainless steel is eliminated and the molybdenum body is shorted directly to ground. The voltage generated by the plasma-induced current flowing through the molybdenum is much less than V_{TC}. (circuit designed by Brian LaBombard)

4.2 SURFACE THERMOCOUPLES

The surface thermocouples are a novel type of thermocouple whose design was discussed in section 3.2. They are not ice point compensated and rely on calibration to the embedded thermocouples before each shot. Since they directly measure the surface temperature evolution, they provide an unambiguous boundary condition for calculation of the surface heat flux.

4.2.1 *Electronics*

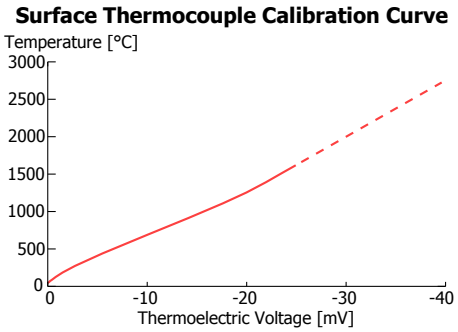

Figure 54: Custom molybdenum/74 % tungsten-26 % rhenium thermocouple junction calibration curve supplied by NANMAC. Data is given to 1600 °C and extrapolated thereafter.

The surface thermocouple signal is carried on a standard 50 Ω silicon-dioxide insulated coaxial cable through a ceramic-insulated coaxial vacuum feedthrough (fig. 53). The voltage signal, which is on the order of a few mV, is processed by custom-built circuit boards. First, it is differentially filtered with a simple RC filter, $\tau_{RC} = 3.0$ ms, to attenuate high frequency noise. A high common-mode rejection differential amplifier (INA129) is then used to amplify the thermoelectric EMF by a factor of 248. Finally, the signal passes through a unity-gain amplifier (LF411A) to provide additional filtering ($\tau_{RC} = 3.0$ ms) and to send the signal to a compact PCI data acquisition system. We employ a D-tAcq ACQ196 digitizer [3] operating at a 400 kHz sampling rate.

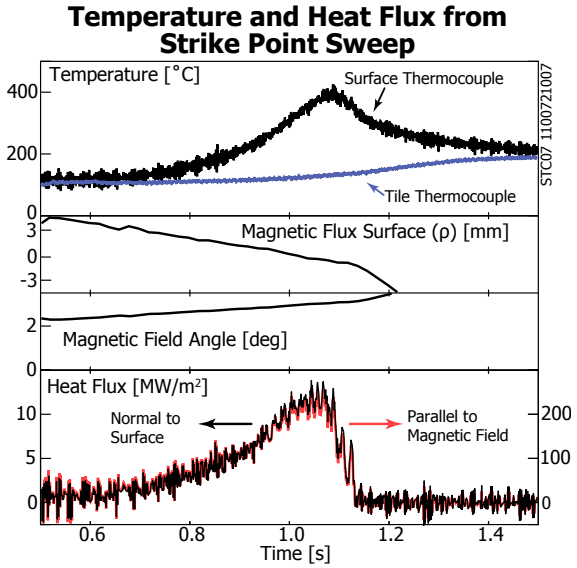

Figure 55: A cross-calibration procedure is performed on each discharge, which forces the surface thermocouple temperature to agree with the tile thermocouple temperature before the plasma pulse. The time evolution of both signals is shown in the top panel. Using output from the EFIT plasma equilibrium reconstruction code, the magnetic flux surface label (ρ) and magnetic field line inclination angle on each surface thermocouple is recorded (second and third panel). Local heat flux density normal to the surface thermocouple surface is computed from a 1D heat transport model of the surface thermocouple cylinder with temperature-dependent thermal parameters. This quantity and its equivalent heat flux density flowing along magnetic field lines are shown in the bottom panel.

4.2.2 *Data Processing*

NANMAC supplied a custom voltage-to-temperature calibration, for the non-standard molybdenum/74 % tungsten-26 % rhenium thermojunction (~16 $\mu V\,°C^{-1}$fig. 54), with data supplied over the range of 30 °C to 1600 °C and then linearly extrapolated to higher temperatures. Note that using the tungsten-rhenium as the center conductor results in a decrease in voltage representing an increase in temperature. Before each plasma pulse the surface thermocouple voltage is cross-calibrated using type-K thermocouples that are a part of the overall divertor diagnostic package, fig. 55. The surface thermocouple voltage before the shot is set to be the voltage corresponding to the temperature as indicated by the embedded thermocouple nearest to it. Since Alcator C-Mod operates with a ~20 min time delay between plasma pulses, there is more than sufficient time for the surface thermocouples, their surrounding divertor tiles, and embedded type-K thermocouples to achieve thermal equilibrium by the start of the following plasma pulse (characteristic time scale for thermal diffusion across 50 mm of molybdenum, $\alpha = 54.3 \times 10^{-6}\,m^2\,s^{-1}$, is ~ 3.5 s). There remains a poloidal pattern of temperature among the divertor tiles due to the high thermal resistance of the stainless steel back plate joining them and the relatively low rate of radiative cooling once the tiles have equilibrated in temperature after the shot.

During a typical plasma pulse, the "footprint", i. e., the spatial pattern, of the plasma-surface heat flux is interrogated in detail by slowly sweeping it (via programmed changes in the plasma's magnetic equilibrium, more specifically moving the position of the x-point out in major radius) over the surface thermocouple sensor array. This produces time traces of surface temperature, plasma flux surface position, and magnetic field angle for a given sensor, such as those

shown in the top three panels of fig. 55. Heat flux is calculated using QFLUX_1D. The surface temperature time history is imposed as the front-surface boundary condition. Since there remains noise of the order of ±50 °C (top panel of fig. 55), the temperature is digitally filtered with a time constant of $\tau_{RC} = 0.8\,\text{ms}$ before input to thermal analysis. Energy loss due to surface thermal radiation is neglected because it is much less than the incident plasma heat flux ($q_{radiation} \sim 10^4\,\text{W m}^{-2}$ at $T_{surf} \sim 1000\,°\text{C}$ compared to $q_{plasma} \sim 10^7\,\text{W m}^{-2}$). A zero heat flux boundary condition is applied to the back surface since the thermocouple body is essentially semi-infinite on the time scale of the pulse. The time evolution of the magnetic field in the tokamak, and in particular at the sensor locations, is derived from the EFIT plasma equilibrium code [12]. This output allows the equivalent heat flux flowing along magnetic field lines to be computed (bottom panel in fig. 55) along with the mapping of that field line into the SOL, as it passes the outer equatorial midplane (ρ-coordinate in second panel of fig. 55 with the location of the last-closed flux surface corresponding to $\rho = 0$).

Unlike the poorly grounded first version of the surface thermocouple (section 3.2.2), this version shows no negative heat flux (fig. 55). This is an important advantage over IR thermography. Negative heat fluxes are often seen when IR thermography is used in tokamaks [13]. This is thought to be due to the thermal emission coming from a poor thermal connection between a plasma-deposited surface layer and the bulk plasma facing component. A thermal resistance is added to the thermal modeling of the IR thermography and adjusted to remove negative heat flux. This is undesirable because it adds an unknown fitting parameter (i. e., the thermal properties of the layer) into the thermal calculation which degrades the integrity of the surface heat flux calculation. The thermocouples are not prone to this issue because although the IR radiation is dominated by the poorly connected thermal layers the voltage generated at the thermojunction is due to the bulk metals who's thermal response can be accurately modeled.

The three largest potential sources for error in the surface thermocouple electrical signal are:

1. Voltage pick-up from large, time-varying magnetic fields
2. Temperature changes at other thermojunctions in the circuit during the plasma pulse
3. Voltage generated by plasma-induced current flowing to ground through resistive sensor leads

These effects have been largely minimized by the sensor's design, as can be assessed by studying the behavior of the sensor signals.

Observations that the surface thermocouple is operating properly may be made through comparison of measurements with and with-

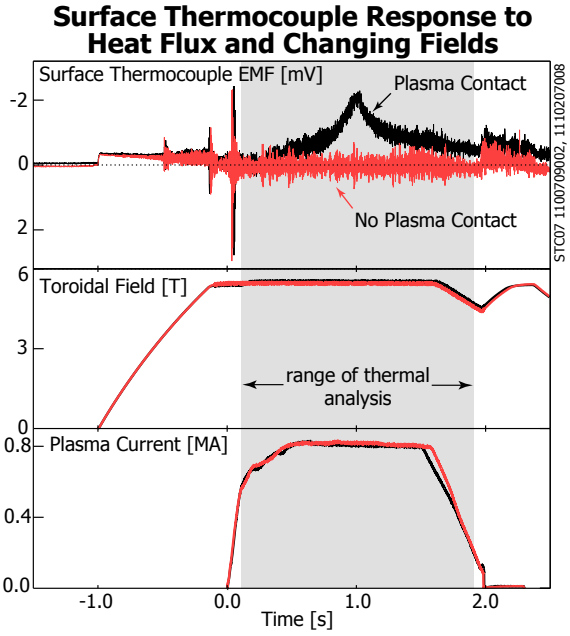

Figure 56: Comparison of raw surface thermocouple voltages for a pulse with plasma contacting the surface thermocouple sensor and one without plasma contact (top panel). Both pulses have nearly identical toroidal field (middle panel) and plasma current (bottom panel). There is a small sensitivity to the rate of toroidal field ramp-up and ramp-down, but neither affects the thermal analysis. The heat flux calculation starts after the toroidal field ramp-up induced voltage returns to its starting value and ends before the ramp-down. The sensor does not pick up any voltage contribution from plasma current ramps, as seen by the lack of a response during the case with no plasma contact. This lack of voltage change also indicates that only the surface thermojunction, and none of the others in the circuit, changes its temperature over a plasma pulse. From this comparison we are confident that the voltage response of the sensor during flattop is entirely due to changes in its surface temperature.

out plasma contact (fig. 56). Unless the surface thermocouple is directly exposed to plasma contact, the sensor voltage remains relatively constant in time over the period when thermal analysis is performed. This demonstrates that the changing magnetic fields associated with routine tokamak operation do not affect the surface thermocouple analysis and that only the surface thermojunction is changing temperature. The lack of a temperature change at the thermojunction between the surface thermocouple and its stainless steel mount is demonstrated by the QFLUX_1D thermal simulations that use the surface temperature to calculate heat flux.

Surface thermocouple measurements compare well with other diagnostics: the total energy fluence agrees with calorimeters, section 5.1. Because we are confident in their measurements of surface heat flux, surface thermocouples, along with Langmuir probe measurements of the divertor plasma, have demonstrated excellent confirmation of sheath heat flux theory, section 6.1. Surface thermocouples also show where Langmuir probe measurements fail, chapter 6; demonstrating that the divertor "death-ray" is localized to the Langmuir probes.

4.2.3 *Performance Under Heating and Transients*

We had initially found that voltage pick-up during ion-cyclotron range of frequencies (ICRF) heating in Alcator C-Mod [2] precluded the use of surface thermocouples. Small levels of voltage pick-up were seen when ICRF antennas are tuned to 80 MHz. The pick-up voltage increases when the antennas are tuned to 50 MHz. However, adding RF-shorts to the vacuum feedthrough allowed operation during ICRF, fig. 57. Since the surface thermocouples are grounded at the divertor,

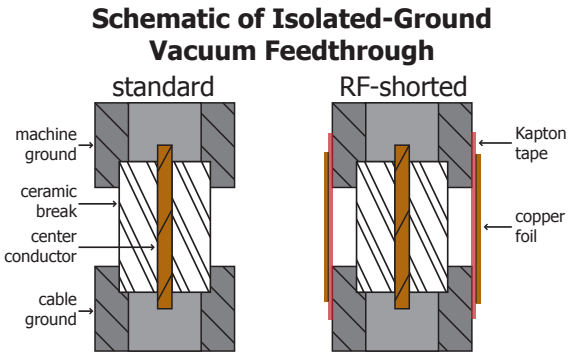

Figure 57: Schematic of the surface thermocouple feedthroughs with and without RF-shorts. On the left is the standard ceramic stand-off vacuum feedthrough. On the right is the feedthrough modified to still be DC-open on the ground, but RF-shorted.

the ground at the feedthrough must be open to prevent large ground loops. This is accomplished with a ceramic feedthrough, which is essentially an open circuit to all frequencies. Kapton tape was wrapped around the feedthrough and covered with copper foil, it was made sure that DC stand-off was maintained. With this setup the RF fields easily passed through the Kapton tape and through the copper foil to ground. The surface thermocouple measurements were much improved and useable during ICRF.

There is no pick-up seen during operation of lower hybrid heating or lower-hybrid current drive [2] (both at 4.6 GHz), allowing surface thermocouple analysis to be performed in these discharges.

Measurements of surface heat flux during a plasma disruption, i. e., a rapid loss of plasma confinement [22], would be of great interest. In these events in C-Mod, the plasma stored energy (~ 100 kJ) is transferred from the plasma to the wall in ~ 1 ms. Surface melting is a concern when so much energy is released in so little time. Unfortunately, we have found that the voltage response during a disruption typically overwhelms the thermal signal, fig. 58, with large positive and negative spikes. Data of Edge Localized Mode (ELM) heat flux was also unavailable with the surface thermocouples. ELMs are edge oscillations which release a significant fraction of the plasma stored energy (~ 10 %) in a very short time (~ 1 ms) and are of great concern for large machines like ITER. The C-Mod equilibrium in which ELMs are most readily produced ("JFT2M" shape, very high lower triangularity with the lower x-point pulled near the inner divertor) places the outer strike point off the divertor face and into the slot. In this configuration no ELM heat flux reaches the outer divertor.

Although surface thermocouples are very robust, surviving thousands of plasma pulses and numerous full current disruptions, some do fail. The two most common failures shown fig. 59, which depicts three poloidally separated thermocouples during the same plasma pulse. The top panel is an example of a good thermal response to plasma heat flux. The middle panel is a failure mode where the signal saturates the digitizer and occasionally has sawtooth oscillations. The bottom panel is an example of a failure where some features coordinate with changing magnetic fields.

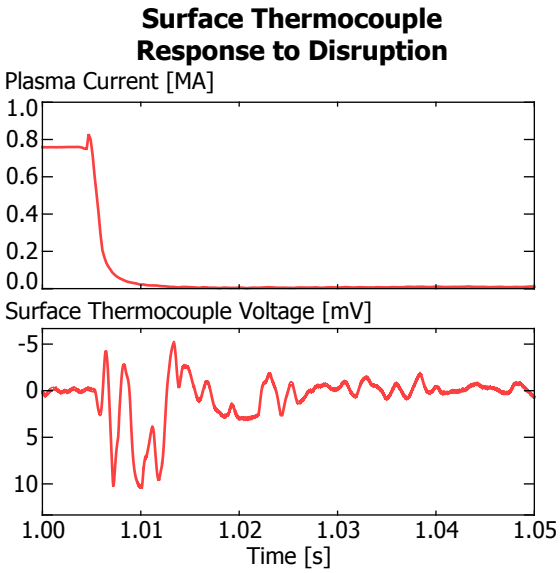

Figure 58: Failure of a surface thermocouple to measure the disruption heat flux.

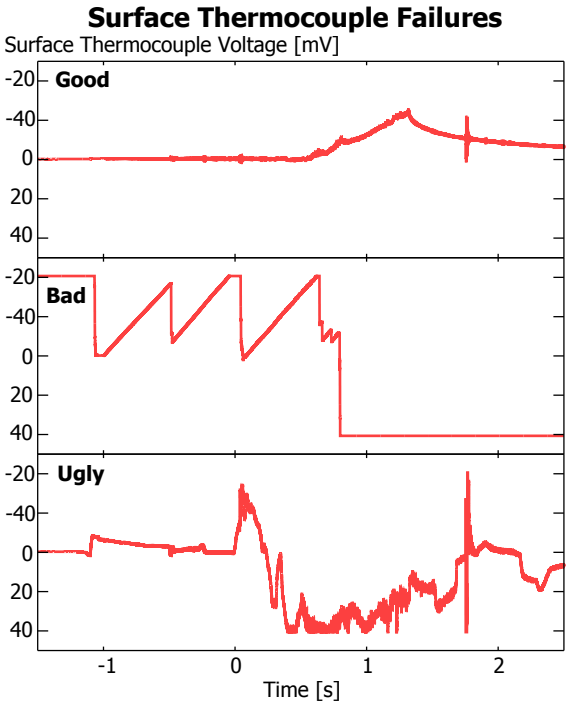

Figure 59: Various failures of the surface thermocouple during a standard LSN shot with plasma flat-top from 0.5 s to 1.5 s. Signals are from three poloidally separated thermocouples during the same shot.

The cause(s) of these failure modes are not known. But once a surface thermocouple failed, it stayed in that state for the remainder of the campaign. All surface thermocouples were checked before instillation. A mount was constructed which pressed the surface thermocouple face into a thin sheet of copper. The copper was heated for ~ 10 s with a blow torch and the voltage response was recorded. All surface thermocouples had nearly the same response. It would be very advantageous for future surface thermocouple use to understand these failures, because once a thermocouple is installed in the experiment, it is in there until the next manned access.

All thermocouples depicting these two failures (1) with signals railed at the digitizer limits or (2) with positive voltages (negative temperatures) were marked as "inactive" and their data not analyzed. All surface thermocouple data used in this thesis was benchmarked against calorimeter deposited energy to ensure proper performance.

4.3 ISP AND RFA

The low signal levels of the ISP and especially of the RFA along with the need to bias probe electrodes with respect to each other prompted the creation of new bias electronics. We have also developed a new

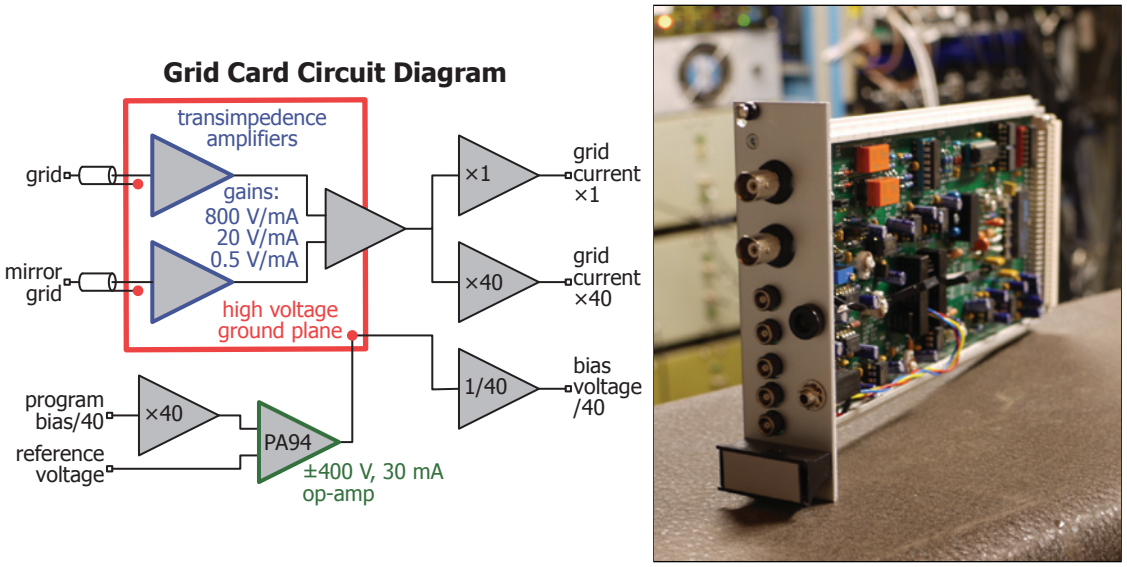

Figure 60: Photograph of the new Grid Card and a simplified circuit diagram. A high voltage ground plane is driven by a PA94 op-amp. This voltage sets the voltage on "grid" and "mirror grid". It also can be used to bias the coaxial shields of the cables. The PA94 responds to the difference between a programmed voltage and a reference voltage (which can be another probe bias, a floating probe, or ground) at its inputs. Variable gain transimpedance amplifiers measure the grid current. A "mirror" grid can be implemented to negate the displacement current due to the probe capacitance. The card outputs measurements of the high voltage (divided by 40) as well as the probe current (at both 1 and 40 times, for a larger dynamic range). (circuit designed by Brian LaBombard)

technique using a Fourier transform to subtract non-plasma signal from the current measurements. The biggest impediment to quality measurements is the lack of an ability to sweep the probes faster than the plasma fluctuations and turbulence, thus the measured quantities are averages over these fluctuations.

4.3.1 *Electronics*

New custom electronics (Grid Bias cards) were developed to control the ion sensitive probe and retarding field analyzer, see fig. 60. The new electronics provide a low-current (100 nA to 100 mA) measurement capability that complements the high-current (1 mA to 20 A) Langmuir probe cards already employed at C-Mod. It uses a PA94 high voltage (±400 V) op-amp, with the current output limited to between 30 mA to 100 mA, depending on the configuration. Each Grid Bias card allows for a programmed voltage waveform to be outputted with respect to an input reference voltage. The reference voltage can be from the floating potential of another probe, the bias being applied to another probe, or ground. To cover the wide range of edge densities on C-Mod, the Grid Bias cards have adjustable gain transimpedance amplifiers (from 0.5 V mA^{-1} to 800 V mA^{-1}) which may be adjusted before each shot. To further increase the dynamic range,

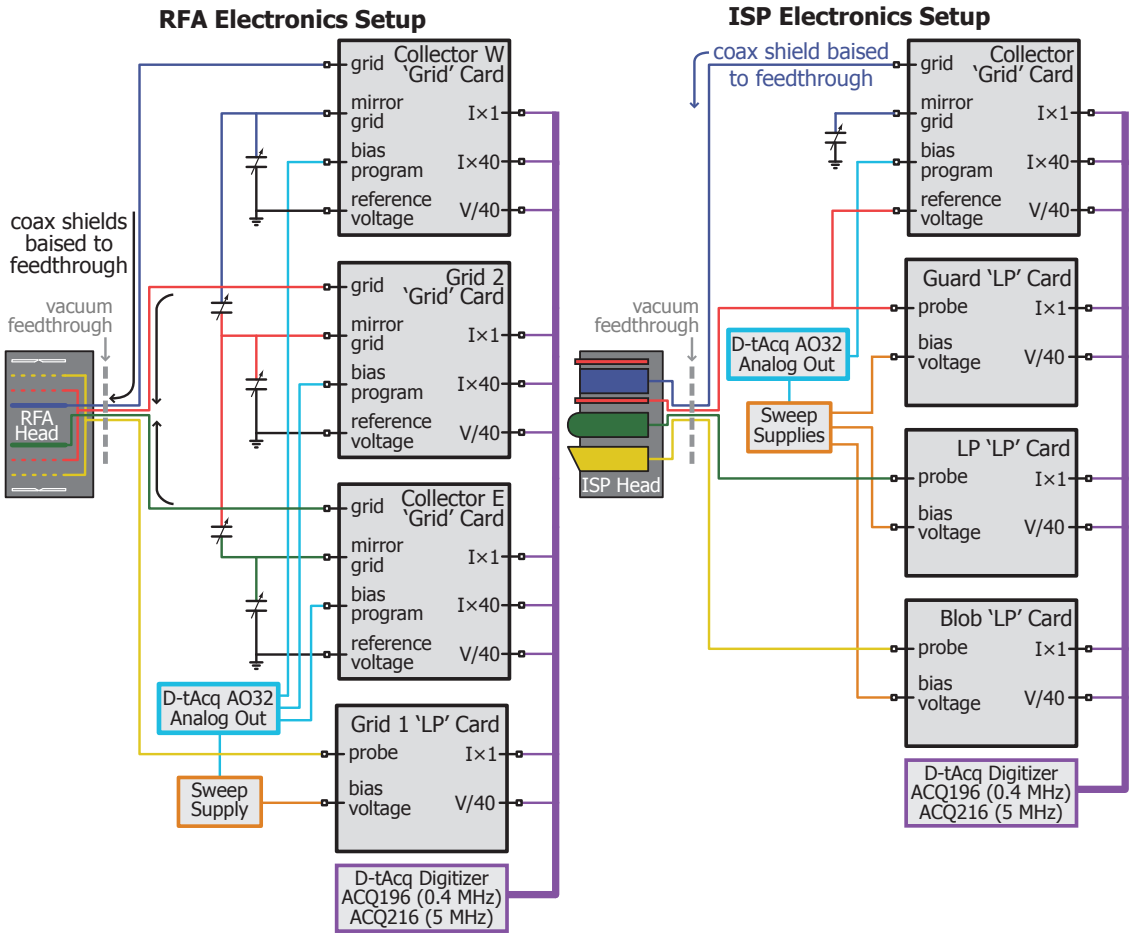

Figure 61: Diagrams of the ISP and RFA electronic systems. An analog output sends waveforms to the Grid card and sweep power supplies. Each Langmuir probe card may be controlled by a different sweep power supply. In the setups shown the ISP Collector was biased with respect to the Guard and the RFA Grids were biased in parallel. The coaxial cable shields that were connected to Grid cards were biased at the same voltage as the center conductor to reduce displacement currents. A variable capacitor attached to the mirror circuit was used to offset the remaining displacement currents. The RFA had a network of capacitors to balance the capacitive coupling among the electrodes

Grid Bias cards output current measurements channels at both $I \times 1$ and $I \times 40$.

The Grid Bias cards apply identical biases to their "grid" and "mirror grid" inputs while reporting only the difference in currents from each. The "mirror grid" is connected to a "dummy" probe circuit. It applies the bias voltage to the same electronics as the probe. But, instead of being connected to the probe, this circuit is connected to a network of capacitors (fig. 61) tuned to mirror the capacitances of the probe. For the fast voltage sweeps used (typically $\pm 300\,\mathrm{V}$ triangle sweep at $2\,\mathrm{kHz}$), $\sim 1\,\mathrm{mA}$ of displacement current is generated for every $400\,\mathrm{pF}$ of uncompensated capacitance.

Diagrams of the whole ISP and RFA probes & electronics systems are shown in fig. 61. Waveforms are outputted by a D-tAcq AO32 analog output unit [3] to the individual Grid Bias cards and sweep power

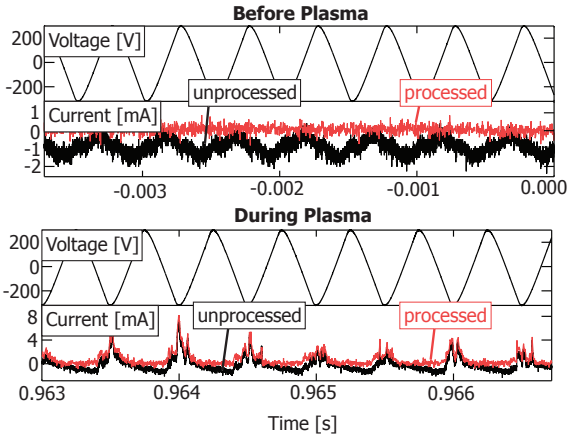

Figure 62: Removal of the residual displacement current from current measurement. Applied ISP voltage and Collector current before the plasma is shown in the top panels. A Fourier transform is taken from the signals to get the complex circuit impedance. This impedance is then applied to the during-plasma voltage to get the circuit current. The circuit current is then subtracted from the total current to get that due to the plasma alone. Although this process is not important near the separatrix, where plasma current dominates, is it important in the far scrape-off layer where the signal is low and the circuit response distorts the measurement signal.

supplies. Each of our sweep power supplies are typically $\sim \pm 200\,\mathrm{V}$ and $\pm 1\,\mathrm{A}$ and may bias multiple Langmuir probe cards. Each Langmuir probe card can be biased by one of three sweep supplies. The Collector is on a Grid Bias card; all other elements, due to their larger currents, are on Langmuir probe cards. The cable shields are biased at the same voltage as the center conductor to the vacuum feedthrough on the scanning probe drive ($\sim 7\,\mathrm{m}$) to reduce capacitive currents. Within the probe drive the cable shields are grounded ($\sim 2\,\mathrm{m}$). The limiter RFA cable shields are biased at the same voltage as the center conductor all the way to the RFA. Current and voltage signals are digitized on D-tAcq ACQ196 (0.4 MHz) and ACQ216 (5.0 MHz) units [3]. The slower digitizer is used for analysis of the data immediately after the plasma pulse and the faster digitizer is used for final processing of the data. All of the RFA probe signals are digitized at 0.4 MHz. Due to channel limitations, only the scanning RFA V and $\mathrm{I} \times 1$ signals are digitized at 5.0 MHz.

4.3.2 *Data Processing*

4.3.2.1 *Removal of Circuit Current*

After digitization, residual displacement currents from uncompensated cable capacitance are subtracted through software analysis of the I-V, fig. 62. The probe is biased with its programmed waveform and the current and voltage signals are digitized for $\sim 0.5\,\mathrm{s}$ before the plasma pulse. From this data a Fourier transform is applied to the current and voltage (without plasma) to estimate the complex circuit impedance for frequencies less than 100 kHz. Then the Fourier transform of the voltage is taken for the whole plasma pulse. This, combined with the circuit impedance, determines the current due to the circuit alone for the whole shot. Subtracting this current in the time domain from the total current for the whole shot leaves only

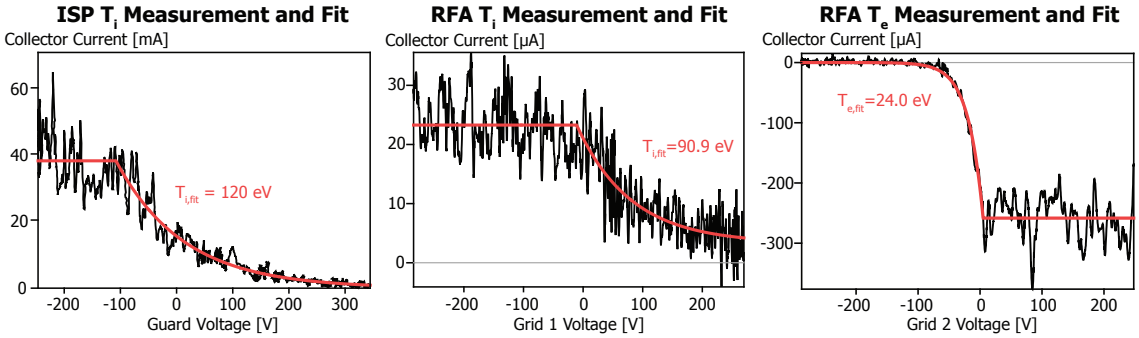

Figure 63: Example fits to ISP and RFA I-V.

that due to the plasma. DC-offsets are also removed as a result of this digital processing.

4.3.2.2 *Fitting Characteristics to Data*

As stated in chapter 2, the ISP and RFA both measure an integral of the velocity distribution function. This could, in principle, be differentiated to directly get the velocity distribution function. However, in practice, plasma fluctuations and measurement noise makes differentiation impractical. Thus we fit analytic functions, eqs. (47) and (50), to the experimental data. We use MPFIT [14] which uses the Levenberg-Marquardt Algorithm [16] to calculate the non-linear least squares fit of the functional forms to the experimental data. Example fits are shown in fig. 63.

Comparison of RFA ion temperature data with CXRS is good, section 5.2. RFA electron temperature measurements also agree with Langmuir probe and Thomson scattering, section 5.3. Although the fitted ISP ion temperature is quite close to the RFA and CXRS ion temperatures, closer inspection of the data reveals it to be space charge limited an thus unable to measure the ion temperature, chapter 7.

4.3.2.3 *Issues of Measurements in a Turbulent Plasma*

Although outside the scope of this thesis, some comments must be made on making probe measurements in fluctuating plasmas. The boundary plasma of a tokamak is a violent place, with fluctuation amplitudes (e. g., , $\tilde{n}/n$) on order unity and fluctuation frequencies up to ~ 1 MHz. There are a couple of ways of dealing with this:

1. Sweep the probe voltage slower than the fluctuations and "average" over them. This is the most common technique due to its simplicity. The challenge here is how the fluctuations get translated through the non-linear I-V. Depending on the relative phase of the temperature and plasma potential fluctuations, this can either under- or over-estimate the electron temperature

from fitting the I-V [20]. Using plasma fluctuation data generated from a gyrofluid code it was found that RFA measurements must either be swept as fast as the fluctuations or the sweeps must be conditionally binned to accurately reflect the plasma temperature [6].

2. Take lots of data, sort it by some metric indicating the strength of the fluctuation, and then fit the I-V of the sorted data (sometimes called conditional averaging). This has been done with both RFAs [10] and ISPs [19]. There is a balance between getting enough data for good statistics and still having the ability to make profile measurements.

3. Use multiple electrodes at various biases. This is most often done with three Langmuir probes ("triple probe" [8]); the major disadvantage is the uncertainty of spatial locality of fluctuations over the three probes. A technique has also been employed with an RFA comparing the relative currents of the last grid and collector [18]. Keeping the collector biased above the last grid means that it does not collect some of the lower energy ions that the grid does. The two currents (properly normalized) are taken as two points on the I-V.

4. Sweep the bias faster than the fluctuations. This has been attempted with a ball-pen probe [1], although only to 50 kHz. But to truly keep up with the $\sim$ 1 MHz plasma fluctuations requires special electronics. One such system is the mirror Langmuir probe [11]; which switches between three bias states of a Langmuir probe with active feedback of the bias states and a measurement bandwidth of $\sim$ 1 MHz.

It is clear that the field of probe measurements must progress to accurate measurements of turbulent fluctuations for a better understanding of plasma transport. However, this thesis is primarily focused on the development and validation of diagnostics robust enough to survive in reactor-level heat fluxes. Thus we use the first technique of sweeping slower than the fluctuations and acknowledge that it may skew the data.

An issue on fitting equations not considered in the literature: the least-squares process fundamentally assumes that any deviations from the model are due to normally distributed errors. This may hold true for noise within the electronics. However it is clearly a poor assumption for plasma fluctuations which are Gamma distributed [4, 5]. Since plasma fluctuations are skewed positively, minimizing the least-squared difference between the fitting function and the experimental data will return a fit higher than the true "background". A technique using the maximum likelihood method for Gamma distributions would likely be more appropriate [7].

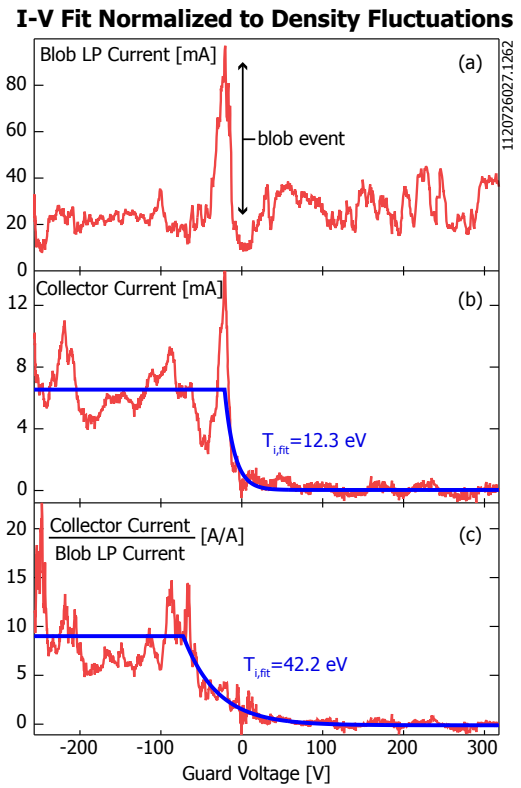

Figure 64: I-V characteristics demonstrating benifit of normalizing to density fluctuations. A Langmuir probe very close to the ion sensitive probe is kept in ion saturation to measure the density fluctuations (panel a). A large density fluctuation (blob) hits the probe as the ISP is going through the exponential part of its sweep. The minimum error fit to the raw Collector current is dominated by this density fluctuation. Normalizing the Collector current to the density fluctuations improves the fit (panel c).

One technique of dealing with turbulent fluctuations that was implemented was normalization of density fluctuations. Fitting eq. (47) to the Collector current verses the Guard voltage can be troublesome during blob events; the decaying tail sometimes provide a better (lower RMS error), albeit incorrect, fit (fig. 64). Here we adopt a technique following [15, 17] of using the slit plate of an RFA in ion saturation to continuously measure the density fluctuations. Normalizing the Collector current to the ion saturation current reduces the effect of density fluctuations. For the ISP, a Langmuir probe provides the ion saturation current signal.

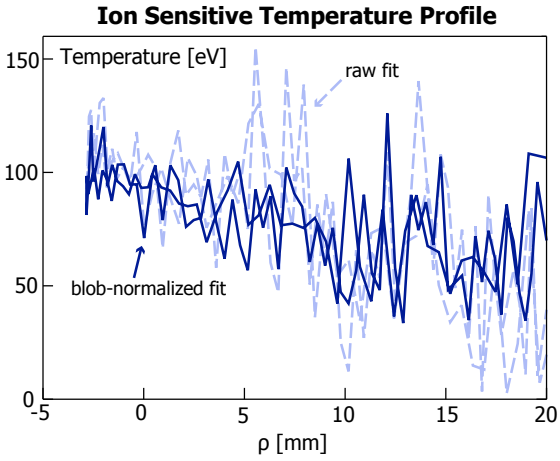

Figure 65: Demonstrated help of normalizing out blob fluctuations. Two profiles of ion temperature are shown: the dashed line is from fits to the ISP I-V. The solid line is from fits the ISP I-V normalized to the Blob LP current. The density fluctuation normalization reduces scatter of the data across the SOL.

Figure 64 shows the utility of this technique. During this sweep a large blob hits the probe. Without the normalization, the software finds the e-folding temperature (12.3 eV) to be associated with the blob decay. Despite the model being a good fit to the data, it is clearly not representative of the plasma conditions. Normalizing the Collector current to the Blob Langmuir probe current improves the fit. Examining over the entire SOL profile (see fig. 65), it is clear that the technique of normalizing the I-V characteristic reduces the scatter of fitted T_i values. This technique assumes that the temperature change during a blob effects the I-V less than the density.

Although, after this data processing was done, it was found that the ISP I-V was not representative of the ion temperature but was space charge limited (chapter 7). The magnitude of the space charge limited current collected at a given bias does not depend on the local density but on the plasma potential. This normalization technique was still useful because the plasma temperature and density fluctuations tend to be correlated and the space charge limited current varies close to linear with the potential ($I \propto V^{3/2}$).

The Blob Langmuir probe was set to a floating condition to see if the ISP, drawing $\sim$ 1 A of current from the plasma, affected the plasma potential. It would be unfortunate if it did; the bias voltage would not truly represent the repelling voltage experienced by ions. It was found that the floating voltage of the Blob Langmuir probe oscillated < 5 V, synchronized with the bias of the ISP, mostly due to capacitive coupling between the probe electrodes (as was evident when the probe was out of the plasma). Given the ISP was biased through a $\pm$300 V sweep, we are confident that the ISP bias is not significantly disturbing the surrounding plasma. ⋆

BIBLIOGRAPHY

[1] J. Adámek, J. Horacek, H. W. Müller, R. Schrittwieser, M. Tichy, A. H. Nielsen, and The ASDEX-U Team. Fast ion temperature measurements using ball-pen probes in the SOL of ASDEX Upgrade during L-mode. In *38th EPS Conference on Plasma Physics*, 2011.

[2] P. T. Bonoli, R. Parker, S. J. Wukitch, Y. Lin, M. Porkolab, J. C. Wright, E. Edlund, T. Graves, L. Lin, J. Liptac, A. Parisot, A. E. Schmidt, V. Tang, W. Beck, R. Childs, M. Grimes, D. Gwinn, D. Johnson, J. Irby, A. Kanojia, P. Koert, S. Marazita, E. Marmar, D. Terry, R. Vieira, G. Wallace, J. Zaks, S. Bernabei, C. Brunkhorse, R. Ellis, E. Fredd, N. Greenough, J. Hosea, C. C. Kung, G. D. Loesser, J. Rushinski, G. Schilling, C. K. Phillips, J. R. Wilson, R. W. Harvey, C. L. Fiore, R. Granetz, M. Greenwald, A. E. Hubbard, I. H. Hutchinson, B. LaBombard, B. Lipschultz, J. Rice, J. A. Snipes, J. L. Terry, and S. M. Wolfe. Wave-particle studies in the ion cyclotron and lower hybrid ranges of frequencies in Alcator C-Mod. *Fusion Science and Technology*, 51(3):401–436, 2007.

[3] D-tAcq Solutions Ltd. James Watt Building, Scottish Enterprise Technology Park, East Kilbride, G75 0QD, SCOTLAND, UK, `www.d-tacq.com`.

[4] O. E. Garcia. Blob transport in the plasma edge: A review. *Plasma and Fusion Research*, 4:019–019, 2009.

[5] O. E. Garcia. Stochastic modeling of intermittent scrape-off layer plasma fluctuations. *Physical Review Letters*, 108(26):265001, 2012.

[6] F. P. Gennrich, M. Kočan, and A. Kendl. Numerical investigation on the validity of ion temperature measurements by a retarding field analyzer in turbulent plasma. In *39th EPS Conference & 16th International Congress on Plasma Physics*, 2012.

[7] J. A. Greenwood and D. Durand. Aids for fitting the gamma distribution by maximum likelihood. *Technometrics*, 2(1):55–65, 1960.

[8] I. H. Hutchinson. *Principles of Plasma Diagnostics*. Cambridge University Press, 1990.

[9] Interactive Data Language. `http://www.exelisvis.com/ProductsServices/IDL.aspx`.

[10] M. Kočan, F. P. Gennrich, A. Kendl, H. W . Müller, and the ASDEX Upgrade Team. Ion temperature fluctuations in the ASDEX Upgrade scrape-off layer. *Plasma Physics and Controlled Fusion*, 54(8):085009, 2012.

[11] B. LaBombard and L. Lyons. Mirror Langmuir probe: A technique for real-time measurement of magnetized plasma conditions using a single Langmuir electrode. *Review of Scientific Instruments*, 78(7):073501, 2007.

[12] L. L. Lao, H. St. John, R. D. Stambaugh, A. G. Kellman, and W. Pfeiffer. Reconstruction of current profile parameters and plasma shapes in tokamaks. *Nuclear Fusion*, 25(11):1611, 1985.

[13] J. Marki, R. A. Pitts, T. Eich, A. Herrmann, J. Horacek, F. Sanchez, and G. Veres. Sheath heat transmission factors on TCV. *Journal of Nuclear Materials*, 363-365:382 – 388, 2007.

[14] C. B. Markwardt. Non-linear least squares fitting in IDL with MPFIT. *arXiv preprint arXiv:0902.2850*, 2009.

[15] Guy Matthews. *The Measurement of Ion Temperature in Tokamak Edge Plasmas*. PhD thesis, Wolfson College, 1984.

[16] J. J. Moré. The Levenberg-Marquardt algorithm: Implementation and theory. In *Numerical Analysis*, pages 105–116. Springer, 1978.

[17] Robert Thomas Nachtrieb. *Ion Mass Spectrometry on the Alcator C-Mod tokamak*. PhD thesis, Massachusetts Institute of Technology, 2000.

[18] I. S. Nedzelskiy, C. Silva, P. Duarte, and H. Fernandes. Ion temperature fluctuation measurements using a retarding field analyzer. *Review of Scientific Instruments*, 82(4):043505–043505, 2011.

[19] K. Okazaki, H. Tanaka, N. Ohno, N. Ezumi, Y. Tsuji, and S. Kajita. Measurement of ion and electron temperatures in plasma blobs by using an improved ion sensitive probe system and statistical analysis methods. *Review of Scientific Instruments*, 83(2):023502, 2012.

[20] D. L. Rudakov, J. A. Boedo, R. A. Moyer, P. C. Stangeby, A. McLean, and J. G. Watkins. Effect of electron temperature fluctuations on slowly swept Langmuir probe measurements. *Review of Scientific Instruments*, 75(10):4334–4337, 2004.

[21] B. Stern. Interactive Data Language. *Proceedings of Space*, pages 20191–4400, 2000.

[22] M. Sugihara, M. Shimada, H. Fujieda, Yu. Gribov, K. Ioki, Y. Kawano, R. Khayrutdinov, V. Lukash, and J. Ohmori. Disruption scenarios, their mitigation and operation window in ITER. *Nuclear Fusion*, 47(4):337, 2007.

5

COMPARISON OF MEASUREMENTS AMONG DIAGNOSTICS

The extensive set of edge diagnostics in C-Mod presents a unique opportunity to both validate measurements and elucidate the regimes where techniques fail. In the process of comparing measurements among different diagnostics, this thesis work has identified which diagnostics can be trusted and which diagnostics must be treated with caution or interpreted differently. The energy deposition measurements from the calorimeters, surface thermocouples, and IR thermography are found to agree, section 5.1. Through comparison of CXRS and ISP ion temperature profiles it is shown that the ISP profile is not representative of the ion temperature, section 5.2. The CXRS impurity temperature profile is shown to be representative of the main fuel in the edge through comparison with RFA measurements. RFA and Langmuir probe electron temperature profiles match, section 5.3. Comparison of the flush-mounted Guard and proud Langmuir probe on the ISP head shows that the flush probe overestimates the electron temperature by up to a factor of 2, section 5.3. Plasma potential measurements by the ISP and Langmuir probes indicate that the ISP is not operating as an ion temperature diagnostic but is space charge limited, section 5.4.

5.1 ENERGY DEPOSITION

Utilizing the extensive array of sensors installed on C-Mod's outer divertor (chapter 3), it is possible to perform a number of comparisons among the surface heat flux diagnostics. One important crosscheck is with the calorimeter sensors. This signal is too slow to be used to infer surface heat fluxes directly. Yet, because the sensors are thermally isolated, their overall change in temperature is a reliable measure of the time-integrated surface heat flux density, section 4.1.2. This quantity is computed for each calorimeter, accounting for its mass and exposed surface area. For comparison, a corresponding time-integration of the surface heat flux signal derived from the surface thermocouple data is performed. It is found that the surface thermocouple-derived and calorimeter-derived energy flux densities agree within 15 % (fig. 66).

The data in fig. 66 is from all non-disruptive shots in the L-mode 2010 JRT experiments, which span a wide range of edge parameter space from sheath-limited to detached. The agreement over a wide range of plasma-deposited energies, and hence different plasma exposures, indicate that not only is the thermal analysis of the calorimeters

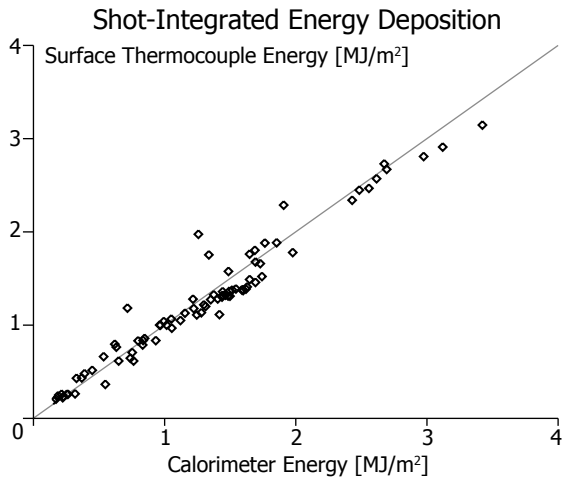

Figure 66: Comparison of the energy deposited on a surface thermocouple and neighboring calorimeter for all of the L-Mode pulses taken for the 2010 Joint Research Target [7]. Calorimeter energy flux is calculated using the temperature difference of a thermally isolated molybdenum slug with an embedded thermocouple. Surface thermocouple energy flux is found by integrating the surface heat flux, which was calculated from the surface temperature evolution. Values typically agree to better than 15 %.

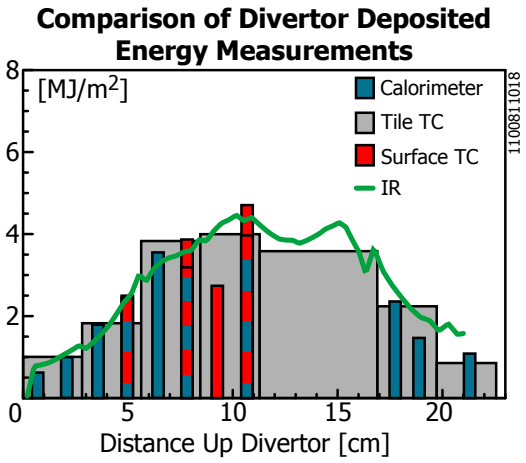

Figure 67: Comparison of the energy deposited on the divertor by different calorimeters, tile thermocouples, surface thermocouples, and IR camera, all showing excellent agreement over the height of the divertor (8 T, 1.2 MA, low recycling shot).

functioning properly but that the surface thermocouples are indeed measuring the proper energy flux. With this result in hand we have been able to do in depth investigation of sheath heat flux, chapter 6.

In addition to the calorimeters and surface thermocouples, the tile thermocouples and IR thermography can also be used to asses the energy deposition. In fig. 67 is a profile of the energy deposition measurements by these diagnostics up the plate of the outer divertor. There is some variation in the profile due to non-uniform heat flux over the ramped tiles (calorimeters and surface thermocouples near the bottom of the ramp tend to get less energy flux). Yet there is good agreement among the diagnostics over the entire span of the outer divertor.

The thermocouples in the inner and outer divertors along with those in the limiters allow for assessment of total-machine energy balance. This is presented for an ICRF-heat discharge in fig. 68. Power balance is typically in the 75 % to 100 % range in lower single-null discharges, fig. 69. The energy deposition in upper single-null or inner wall limited discharges is not well-accounted for due to the lack of thermocouples in these locations.

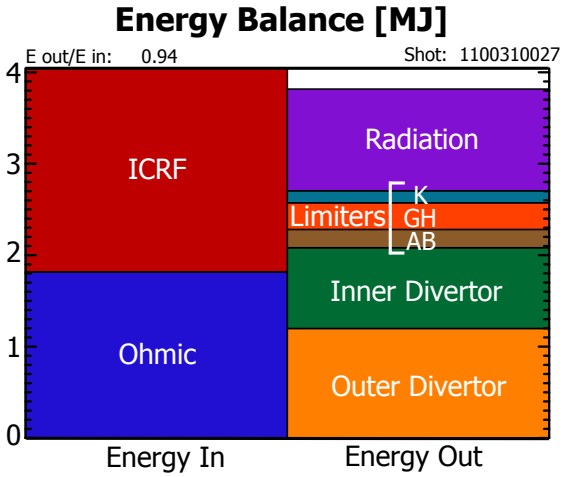

Figure 68: The embedded thermocouples allow for energy deposition measurements of most of C-Mod's surfaces. Along with radiated energy from bolometry, we are able to account for most of the inputted energy, here for a single ICRF-heated discharge.

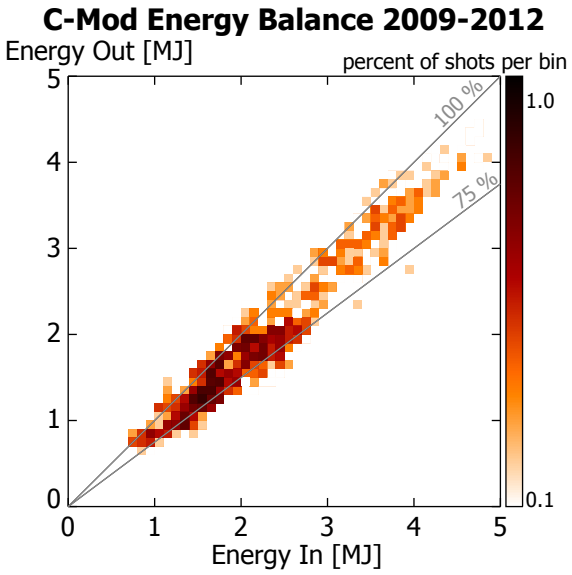

Figure 69: Total C-Mod energy balance for 3130 shots. "Energy In" is the sum of ohmic, ICRF, and LH injected energy. "Energy Out" is the sum of thermocouple deposited energy measured at the inner & outer divertors; the AB, GH, & K limiters; as well as the radiated power. All shots are lower-single null (secondary seperatrix < 0 mm and right and left gaps > 0.5 mm) and survived into ramp-down (pulse time > 1.4 s).

5.2 ION TEMPERATURE

Since the ion sensitive probe has not been benchmarked to measure ion temperature in high density plasmas, it is important to compare measurements over a wide range of conditions. Unfortunately due to limited run time, there is no retarding field analyzer data on identical shots to benchmark the ion sensitive probe, so the CXRS B^{5+} ion temperature will have to suffice. Quality ISP and CXRS data was obtained with a density scan from $\bar{n}_e = 0.6 \times 10^{20}\,m^{-3}$ to $1.8 \times 10^{20}\,m^{-3}$ (Greenwald fraction: $\bar{n}_e/n_G = 0.12$ to 0.35).

Temperature profiles from the CXRS, ISP, Langmuir probe, and Thomson scattering for the lowest and highest densities are presented in fig. 70. Only the CXRS profile changes significantly over this density range. At first glance this would call into question these measurements of the impurity ion temperature. However, the trend seen in nearly all other edge measurement of the main ion temperature (section 2.3.2) is for it to decrease with increasing core density. Thus it is the ISP profiles which are suspect: they do not change at all—save for an increase in scatter due to increased edge fluctuations—over this large change in core density. This, along with the observation that the ISP plasma potential was near where the I-V decayed to zero (section 5.4) likely indicate that the ISP is space charge limited and

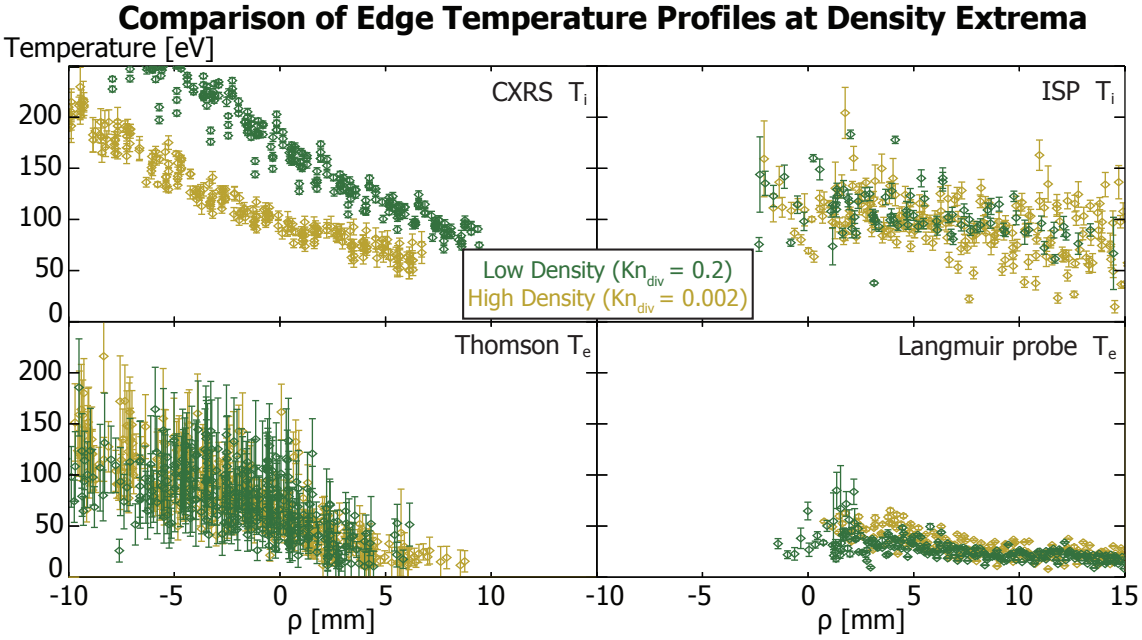

Figure 70: Comparison of CXRS (top-left) and ISP (top-right) T_i along with Thomson (bottom-left) and Langmuir probe (bottom-right) T_e profiles for low- (green) and high-density (yellow) cases. As the density increases the CXRS T_i profile decreases, the ISP profile increases in scatter, the Thomson profile remains unchanged, and the Langmuir probe profile remains unchanged (save for a slight increase near $\rho \approx 4\,\text{mm}$).

unable to measure T_i. These issues are further explored in chapter 7. It is remarkable and somewhat suspicious that the erroneous ISP T_i measurements were so close to the CXRS.

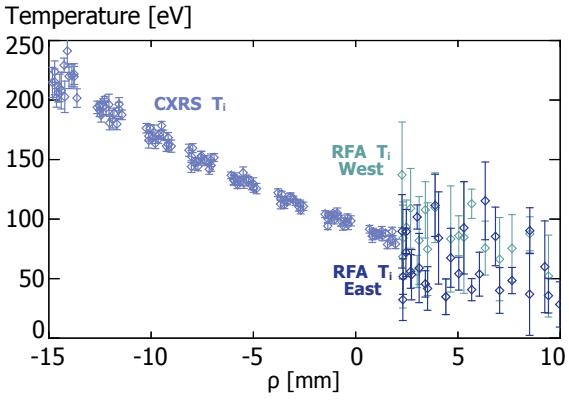

Figure 71: Comparison of the CXRS and RFA T_i temperature profiles. The RFA measurements of T_i are in good agreement with the CXRS.

The RFA data are much more sparse, with only a single good comparison with CXRS. Yet the profiles do appear to match in the SOL, as shown in fig. 71, albeit with considerable scatter in the RFA T_i. Current collected by the RFA is well below that of the space charge limit, section 3.3.4, so its T_i measurements should be trustworthy. The RFA samples plasma from both directions along magnetic field lines. Data are split into "West" (facing the outer midplane and outer divertor along the magnetic field) and "East" (facing the inner divertor along the magnetic field). The parallel Mach number in this location is typically low (< 0.2) and thus effect of an apparent temperature asymmetry due to flows ($< 10\,\%$) should be below the scatter in these data [15]. The West side appears to have a higher average T_i, this could be indicative of asymmetric heat transport.

The CXRS-RFA comparison shown in fig. 71 is at the same sheath-limited edge regime as the lowest density case in the CXRS-ISP den-

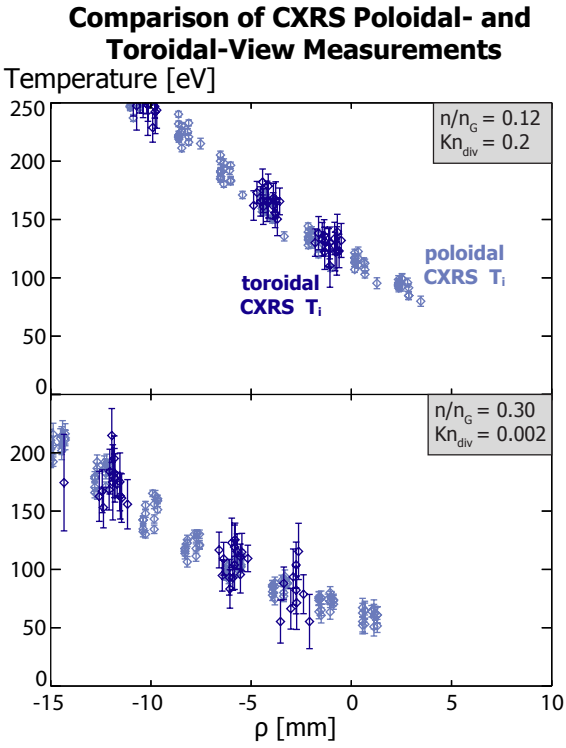

Figure 72: Comparison of the toroidal and poloidal CXRS B^{5+} T_i profiles for low- and high-density cases. In both cases the toroidal profile was shifted $-2\,mm$ such that the brightness profiles overlaid. The data indicate that the B^{5+} T_i distribution function is isotropic in the confined plasma.

sity scan: $Kn_{div} \approx 1$ (at lower plasma current and density $I_p = 0.6\,MA$ and $\bar{n}_e = 5.5 \times 10^{20}\,m^{-3}$ for the CXRS-RFA versus $I_p = 0.8\,MA$ and $\bar{n}_e = 7.5 \times 10^{20}\,m^{-3}$). This is fortunate because it samples the collisionality regime in which the boron is least likely to thermally couple to the deuterium. The data shows that B^{5+} is at, or very near to, thermal equilibrium with the deuterium and therefore is a good proxy for the main ion temperature. In comparison to electron-ion coupling, the similar masses of boron and deuterium results in more efficient energy coupling. An evaluation of the B^{5+}-D^+ equilibration time [9, 14] compared to the SOL dwell time at these parameters ($n = 0.5 \times 10^{20}\,m^{-3}$, $T_i = 115\,eV$, and assuming $T_{B^{5+}} = T_{D^+}$) reveals that these species should be in approximate thermal equilibrium: $\tau_{B^{5+}-D^+} c_s/L \approx 0.001$. Strong coupling would still be justified without the assumption of $T_{B^{5+}} = T_{D^+}$.

Finally, we must consider the possibility that the B^{5+} distribution function might be anisotropic in the boundary. If so, measurements of B^{5+} T_i from the poloidally-viewing CXRS system would need to be treated with caution. Kinetic simulations clearly show temperature anisotropies along open field lines, with $T_\parallel/T_\perp < 1$ for high Kn [4, 5]. In addition, DIII-D CXRS C^{6+} T_i profiles can actually increase with distance into the SOL [8], which may be due to trapped orbits from the top of the pedestal [1]. A comparison of the C-Mod CXRS poloidal- and toroidal-views is shown in fig. 72. It indicates that B^{5+} is essentially isotropic over the range of Kn considered here, at least in within the confined plasma. This indicates that any tem-

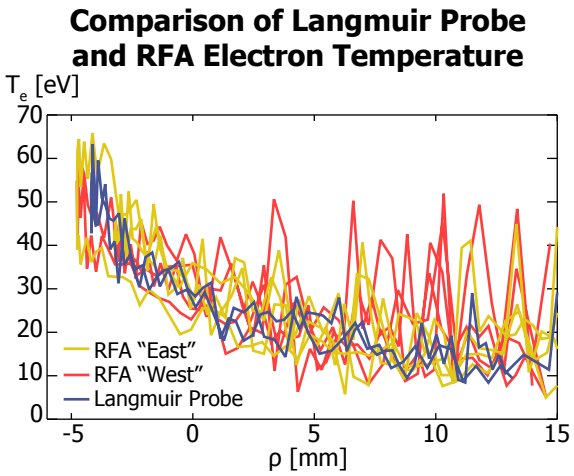

Figure 73: Comparison of the electron temperature measured with a Langmuir Probe (on the ISP head) and an RFA. There is good agreement between the two different techniques. The RFA does have more scatter in the far SOL due to the low signal there. Measurements are from two nearly identical shots ($B_t = 5.4\,T$, $I_p = 0.8\,MA$, $\bar{n}_e = 0.4 \times 10^{20}\,m^{-3}$).

perature asymmetry which may exist along open field lines in the SOL does not extend within the LCFS, where the ion heat transport analysis will be focused. •

5.3 ELECTRON TEMPERATURE

With the addition of the RFA C-Mod now has 3 different ways of measuring the edge electron temperature. Previous comparisons of the Langmuir probe with Thomson scattering have been successful [6]. This agreement still remains valid with the new domed Langmuir probe on the ISP head, fig. 70. RFA electron temperature measurements have generally been consistent with Langmuir probes [16]. We find good agreement between the Langmuir probe and RFA electron temperature measurements, fig. 73.

Often times the ISP Guard is used to measure the electron temperature. The Guard on the C-Mod ISP presents an opportunity to compare a flush Langmuir probe (i. e., a Langmuir probe with its surface tangent to the magnetic field) to a proud probe. Measurements with a tilting array of Langmuir probes on the DITE tokamak clearly indicated that the Langmuir probe I-V changes as a the angle between a probe and the magnetic field becomes tangent [10]. The fitted electron temperature approximately doubled when the probe was tangent. The Guard on our ion sensitive probe was made flush to the head to keep its electron currents within power supply limits. The fitted electron temperature for the flush Guard is much more scattered that the proud Langmuir probe and exceeds it by a factor of 1 to 2, fig. 74. The measurements here are consistent with those from Matthews. This will be important for design of an ISP and interpretation of measurements. If the Guard is to be used as a Langmuir probe, it must be at least partially proud to ensure proper operation. •

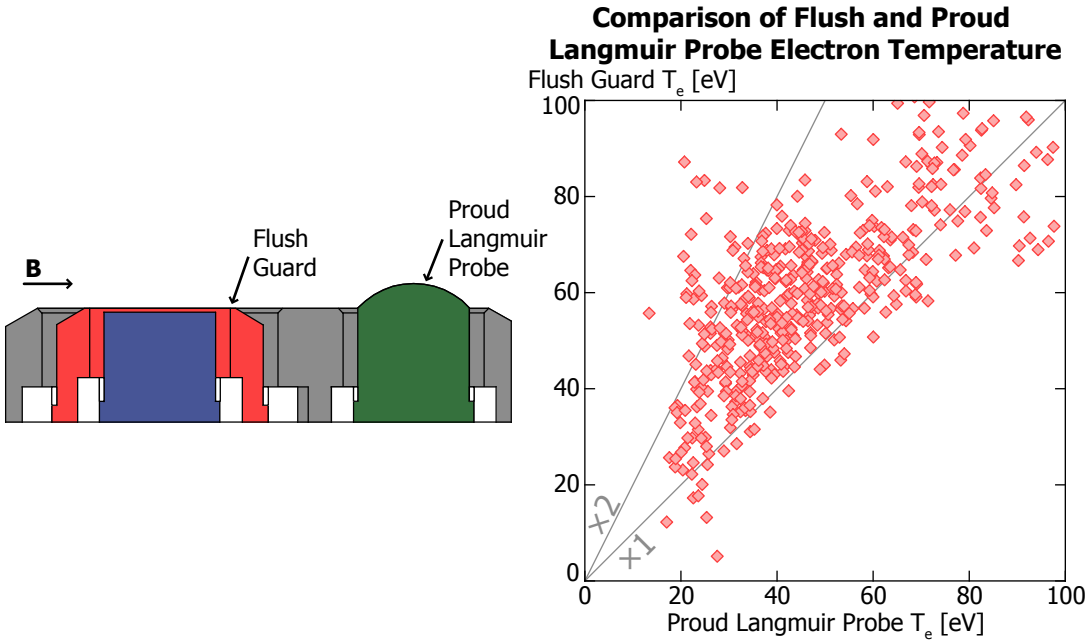

Figure 74: Comparison of the electron temperature measured with a proud and flush Langmuir probe. The Guard on the ISP head can be used as a Langmuir probe. However, because its surface is tangent to the magnetic field, fits of electron temperature exceed that from a proud Langmuir probe from factors of 1 to 2.

5.4 PLASMA POTENTIAL

As stated in section 2.6, there are two ways in which an ISP can measure the plasma potential. For an ISP that is not dominated by space charge V_p is at the break in slope between the saturation and exponential decay [3]. For an ISP that is dominated by space charge V_p is where the current decayed to zero [11]. Comparison can be made to the Langmuir probe, which independently infers the plasma potential at $V_p \approx V_f + 2.7 k_B T_e/e$. The break in slope of the C-Mod ISP measurements are far below (typically 100 V to 200 V) the Langmuir probe plasma potential. On the other hand the point where the ISP I-V decays to zero matches up very well with the Langmuir probe plasma potential over most of the boundary, fig. 75. The data diverges from agreement at the lowest potentials, corresponding to locations behind the main plasma limiter. Previous comparisons of ISP and Langmuir probe plasma potential data behind the limiter showed similar disagreement [2]. The disagreement may be due to the short connection length behind the limiter (< 1 m); a full pre-sheath may not have the opportunity to form in such a situation [13].

When properly interpreted, the space charge limited ISP correctly measures the plasma potential as compared to the standard Langmuir probe analysis. This interpretation has been successfully compared to emissive probes in C-Mod [12] and is based on the idea that as the ISP Guard potential is swept above the plasma potential, it

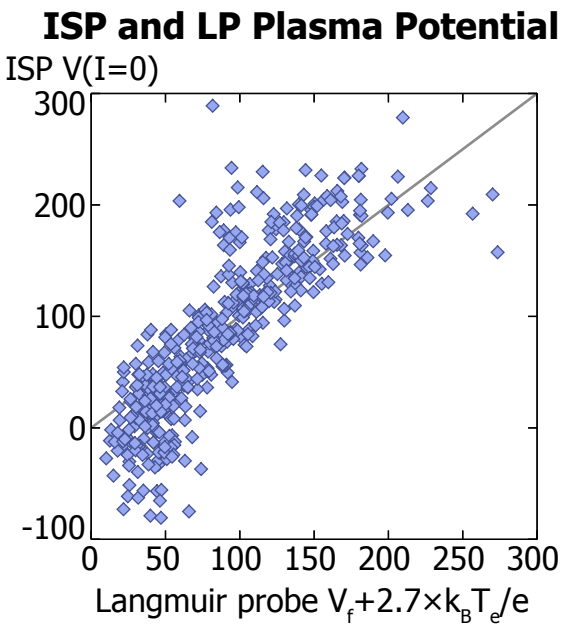

Figure 75: Comparison of the plasma potential measured with the Langmuir probe (standard method of $V_p = V_f + 2.7\frac{k_B T_e}{e}$) and the ISP by the method of Ochoukov (the bias potential where the Collector voltage is zero). There is good agreement between the two measurements over much of the range. The lower values were in the shadow of the limiter, where the disagreement may be due to the short connection length (< 1 m).

electrostatically disallows positive charge accumulation in the probe volume and thus all net charge collection, either ions or electrons, is precluded. Of particular importance is the suppression of electron current at the Collector, which must arise from space charge effects in the probe volume allowing electrons to $\vec{E} \times \vec{B}$ drift to the Collector. This indicates that space charge effects must be playing a critical role in this ISP. Further examination and quantification of space charge effects in chapter 7 will indicate that the ion collection is indeed dominated by space charge. This has the important implication that the ISP is its present form is unable to measure T_i. ⋆

BIBLIOGRAPHY

[1] D. Battaglia, J. A. Boedo, K. H. Burrell, C. S. Chang, J. S. deGrassie, B. A. Grierson, R. J. Groebner, and W. M. Solomon. Interpretive full-f edge transport calculations for DIII-D. In *U.S.–E.U. Joint Turbulence Task Force Workshop Santa Rosa, California*, 2013.

[2] D. Brunner, B. LaBombard, R. Ochoukov, and D. Whyte. Scanning ion sensitive probe for plasma profile measurements in the boundary of the Alcator C-Mod tokamak. *Review of Scientific Instruments*, 84:053507, 2013.

[3] S. Falabella and A. W. Molvik. Ion temperature measurements on TMX-U using a gridless electrostatic analyzer. *Review of Scientific Instruments*, 61(7):1892–1899, 1990.

[4] A. Froese, T. Takizuka, and M. Yagi. Kinetic particle simulation study of parallel heat transport in scrape-off layer plasmas over a wide range of collisionalities. *Plasma and Fusion Research*, 5(0):26–26, 2010.

[5] A. Froese, T. Takizuka, and M. Yagi. PIC simulation study of heat transport kinetic factors in scrape-off layer plasmas. *Contributions to Plasma Physics*, 52(5-6):534–538, 2012.

[6] B. LaBombard, J. W. Hughes, D. Mossessian, M. Greenwald, B. Lipschultz, J. L. Terry, and the Alcator C-Mod Team. Evidence for electromagnetic fluid drift turbulence controlling the edge plasma state in the Alcator C-Mod tokamak. *Nuclear Fusion*, 45(12):1658, 2005.

[7] B. LaBombard, J. L. Terry, J. W. Hughes, D. Brunner, J. Payne, M. L. Reinke, I. Cziegler, R. Granetz, M. Greenwald, I. H. Hutchinson, J. Irby, Y. Lin, B. Lipschultz, Y. Ma, E. S. Marmar, W. L. Rowan, N. Tsujii, G. Wallace, D. G. Whyte, S. Wolfe, S. Wukitch, G. Wurden, and the Alcator C-Mod Team. Scaling of the power exhaust channel in Alcator C-Mod. *Physics of Plasmas*, 18:056104, 2011.

[8] C. J. Lasnier, K. H. Burrell, J. S. DeGrassie, A. W. Leonard, R. A. Moyer, G. D. Porter, and J. G. Watkins. Scrape-off layer features of the QH-mode. *Journal of Nuclear Materials*, 313:904–908, 2003.

[9] K. D. Marr, B. Lipschultz, P. J. Catto, R. M. McDermott, M. L. Reinke, and A. N. Simakov. Comparison of neoclassical predictions with measured flows and evaluation of a poloidal impurity density asymmetry. *Plasma Physics and Controlled Fusion*, 52(5):055010, 2010.

[10] G. F. Matthews, S. J. Fielding, G. M. McCracken, C. S. Pitcher, P. C. Stangeby, and M. Ulrickson. Investigation of the fluxes to a surface at grazing angles of incidence in the tokamak boundary. *Plasma Physics and Controlled Fusion*, 32(14):1301–1320, 1990.

[11] R. Ochoukov, D. G. Whyte, B. Lipschultz, B. LaBombard, and S. Wukitch. Interpretation and implementation of an ion sensitive probe as a plasma potential diagnostic. *Review of Scientific Instruments*, 81(10):10E111, 2010.

[12] R. Ochoukov, D. G. Whyte, B. Lipschultz, B. LaBombard, and S. Wukitch. Interpretation and implementation of an ion sensitive probe as a plasma potential diagnostic on Alcator C-Mod. *Journal of Nuclear Materials*, 415:S1143–S1146, 2010.

[13] P. C. Stangeby. *The Plasma Boundary of Magnetic Fusion Devices*. IoP Publishing, 2000.

[14] B. A. Trubnikov. Particle interactions in a fully ionized plasma. *Reviews of Plasma Physics*, 1:105, 1965.

[15] F. Valsaque, G. Manfredi, J. P. Gunn, and E. Gauthier. Kinetic simulations of ion temperature measurements from retarding field analyzers. *Physics of Plasmas*, 9(5):1806–1814, 2002.

[16] Alan Szu-Hsin Wan. *Ion and electron parameters in the Alcator C tokamak scrape-off region*. PhD thesis, MIT, 1986.

6

ASSESSMENT OF SHEATH HEAT FLUX

The heat flux through the sheath is a key edge parameter, the basic physics of which is covered in some detail in section 2.2.3. The sheath heat flux transmission coefficient is a physical model used to account for the kinetic effects of heat flux through a sheath in terms of local fluid variables. It is crucial to understand the physics in the model as it is used as the heat flux boundary condition for fluid simulations of the edge plasma. Especially so because there are strict engineering limits on the surface heat flux that may limit a fusion reactor's viability as an economic energy source.

Table 3: Summary of experimental sheath heat flux transmission coefficients first presented in [13].

Tokamak	Range of γ	Refs.
ASDEX-U	3-8	[7]
DIII-D	2-4	[3]
JET	2-8	[15]
JT-60U	2-20	[1]
TEXT	~ 5	[21]
Tore Supra	3-8	[4]
TCV	4-8	[13]

There have been challenges in measuring this very fundamental quantity in tokamak experiments, table 3. Its nominal value should be ~ 7, yet it has been experimentally measured by factors of 3 higher and lower. Values below 5 are physically impossible, beyond the limit of $T_i \ll T_e$.

With the surface thermocouples (section 3.2) we have a unique tool to directly asses the sheath heat flux. Surface thermocouple energy deposition was successfully benchmarked against calorimetry over all divertor regimes in C-Mod, section 5.1. So we are confident in using its heat flux measurements. Separated 1 cm from the surface thermocouples are an array of proud Langmuir probes which measure the local plasma conditions (electron temperature T_e, ion saturation current J_{sat}, and ground current J_{gnd}).

Using these diagnostics it is demonstrated in the sheath limited regime that sheath heat flux theory does indeed hold in a tokamak, section 6.1. However the often-made assumption of a floating surface is poor. We present a version of the sheath heat flux equation which accounts for the non-zero current flowing through the sheath. At higher edge collisionality in the conduction-limited (or high recycling) regime, agreement with the sheath heat flux model is still fair, although measurements indicate that $T_i \ll T_e$ may be applicable.

Just before the onset of divertor detachment (i. e., a loss of plasma pressure along magnetic field lines) the experimentally measured heat transfer coefficient is found to decrease below the minimum theoretically allowed value of $\gamma \approx 5$ (when $T_i \ll T_e$). Coincident with this behavior is the detection of excess plasma pressure ($\sim 2\times$) on divertor Langmuir probes relative to those upstream—a situation seen before on C-Mod called the "death-ray" [9]. This is the first time that the low

sheath heat flux transmission coefficient and divertor over-pressure have been linked. A new theory is proposed to explain the excess pressure and heat flux as measured by the Langmuir probe as due to the probe bias itself, section 6.2. This theory was tested by M. V. Umansky with 2D plasma-neutral fluid simulations, section 6.3.

6.1 EXPERIMENTAL TEST OF SHEATH HEAT FLUX THEORY

Using a combination of "upstream" and divertor Langmuir probes, divertor surface thermocouples, and divertor calorimetry probes, we have systematically explored the relationship between sheath heat flux values and pressure mappings in deuterium plasmas. A limited set of data in helium is also available.

Upstream T_e and n_e are measured with a pneumatically driven scanning Langmuir probe at 11 cm above the outer-midplane [10]. These measurements are not affected by the "death-ray" phenomena because the local conditions do not support it: electron temperature is too high (typically 20 eV to 70 eV), neutral density is low (sheath-limited regime), and magnetic field lines have a large angle-of-attack with respect to the probe surface ($\sim 30°$) where, unlike in an axisymmetric divertor, the ion-neutral interaction does not lead to the generation of a strong "neutral wind" [9]. The upstream profiles of T_e and n_e measured with the Langmuir probe match well with those measured by Thomson scattering, see fig. 77. These profiles are mapped to the flux surface coordinate, ρ, which is the distance into the scrape-off layer measured at the outer midplane. Some shifts in the profiles (few mm) are sometimes needed in order for the electron temperature profile to be consistent with power balance and for the electron pressure profiles to agree [11]. These shifts are within the uncertainties of EFIT [12] magnetic reconstruction.

6.1.1 *Extension of Theory to Grounded Surface*

The theory for heat flux through a plasma-wall sheath is well developed [19]:

$$q = \gamma k_B T_e J_{sat}. \tag{59}$$

Where the sheath heat flux transmission coefficient, γ, is almost always given by its theoretical value to an electrically isolated, floating surface: $\gamma \approx 7.5$, section 2.2.3.

However, the divertor surface in a tokamak is rarely electrically isolated. It is almost always grounded to the vacuum vessel. Thus it becomes an important part of an electric circuit involving the scrape-off layer. Significant currents, at times on order the ion saturation current, flow through the boundary connecting through the divertors and vac-

uum vessel. These are due to both parallel Pfirsch-Schlüter currents required for MHD force balance [17] and thermoelectric currents [9]. Thermoelectric currents arise because asymmetric edge energy transport causes a difference in inner and outer divertor electron temperature on the same flux surface. Since the sheath potential is a function of electron temperature ($\sim 2.7 k_B T_e/e$) this causes an asymmetry in the sheath potential which drives the thermoelectric current.

Some works express the sheath heat flux transmission coefficient to a biased surface as a function of the voltage [19, 24]. This is useful for linear devices where the ion temperature is cold and the target is biased to increase the incident ion energy. For a tokamak boundary plasma, it is more appropriate to express it for a grounded surface with net current flux parallel to the magnetic field through the sheath (J_{gnd}). This relation is derived in appendix A and expressed in a convenient form for Langmuir probe measurements as a function of the ratio of the ground current to the ion saturation current, J_{gnd}/J_{sat}:

$$\gamma = 2.5\frac{T_i}{ZT_e} + 2\frac{1-\frac{J_{gnd}}{J_{sat}}}{1-\delta_e} - \ln\left[\sqrt{2\pi\frac{m_e}{m_i}\left(Z+\frac{T_i}{T_e}\right)}\frac{1-\frac{J_{gnd}}{J_{sat}}}{1-\delta_e}\right]. \quad (60)$$

$J_{gnd}$is measured as the current density to a proud Langmuir probe when it is held at zero bias with respect to the divertor. Positive J_{gnd} corresponds to net ion collection by the divertor.

Both the ion temperature (T_i) and the secondary electron emission coefficients (δ_e) are not measured in the divertor of C-Mod. Recent measurements with an RFA in the divertor of MAST indicated $T_i \approx T_e$ in ohmic plasmas [6]. Secondary electron emission is assumed to be zero. The small grazing angle of the magnetic field line with respect to the surface ($\sim 2°$) makes prompt recapture of emitted electrons likely [19, 23], which effectively makes $\delta_e \approx 0$ even if secondary electrons are produced at the metal divertor surfaces. The heat transfer coefficient value that is customarily assumed for a deuterium plasma, $\gamma \approx 7.5$, comes from the assumptions $T_i = T_e$ and $\delta_e = 0$ along with a floating surface ($J_{gnd} = 0$).

6.1.2 *Measurements of Sheath Heat Flux*

Comparison of adjacent surface thermocouples and Langmuir probes for a deuterium plasma in the low density sheath-limited regime yields excellent agreement with sheath theory (figs. 76 and 77). These results show that a floating surface assumption ($J_{gnd} = 0$) is not always appropriate for a grounded divertor. The current at the outer divertor (in the magnetic configuration with the ∇B-drift pointed to the active divertor) is net electron because the outer divertor has higher electron temperature than the inner divertor. The sheath potential is suppressed and thus more electrons leak through. This electron

Figure 76: Plasma parameters and derived parallel heat flux density profiles obtained from sweeping the "heat flux footprint" over a surface thermocouple and Langmuir probe in close proximity. Horizontal axis is ρ, the magnetic flux surface label, mapped to the outer midplane. The plasma-induced ground current (J_{gnd}) at the outer divertor increases the sheath heat flux coefficient to ~11, 50 % above the nominal floating value of ~7.5 (dashed line). Using this calculated value of the sheath heat flux transmission coefficient, the heat flux profiles from the Langmuir probe and surface thermocouple are in excellent agreement across the entire footprint.

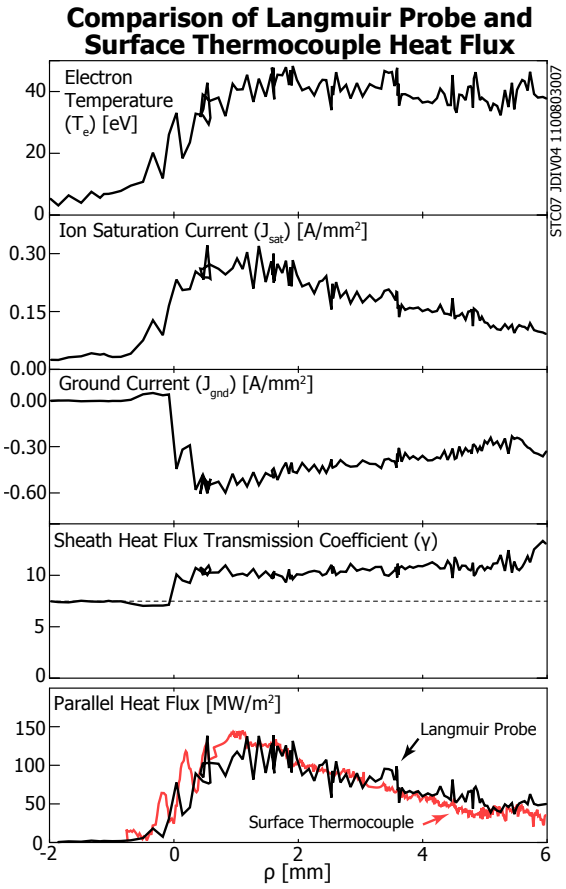

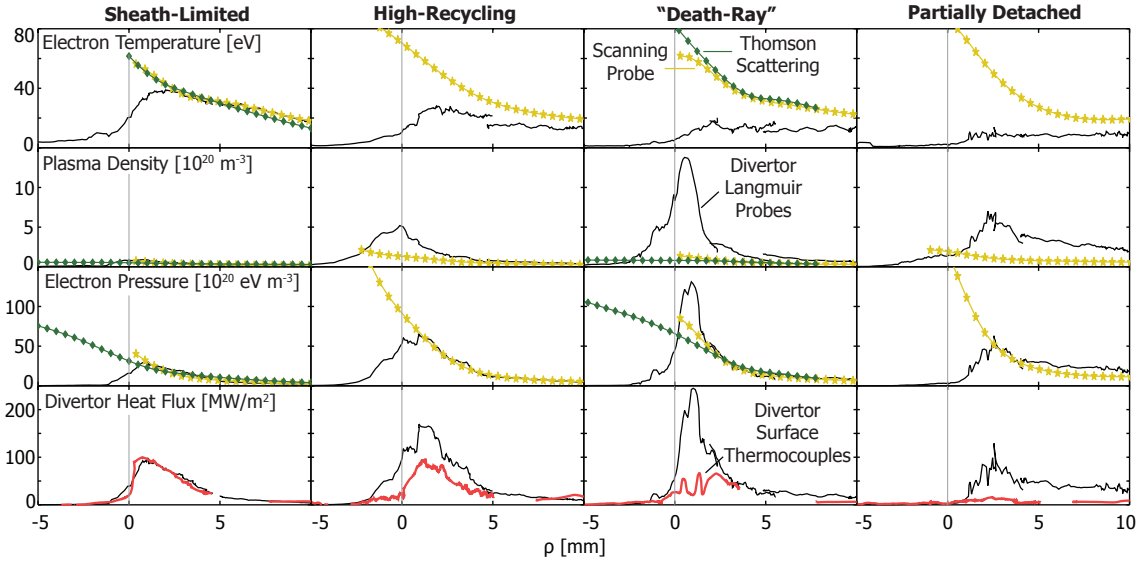

Figure 77: Surface thermocouple (red), Langmuir probe (black divertor, yellow upstream), and Thomson scattering (green) measurements in four boundary regimes: (1) Sheath-limited: sheath heat flux, including the effects of net current, agrees well with surface thermocouples. (2) High-recycling: sheath heat flux departs from the surface thermocouples, suggesting that the ion temperature is dropping relative to the electron temperature. (3) "Death-Ray": sheath heat flux strongly disagrees with surface thermocouples. (4) Partially detached: surface thermocouple signals at noise.

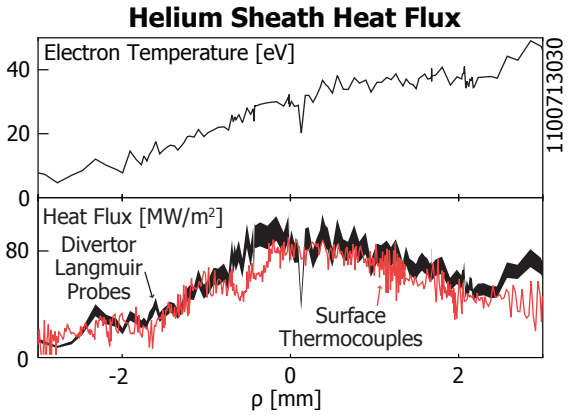

Figure 78: Sheath heat flux profiles typically agree very well for pure helium plasmas, here in the low-recycling regime. The black band spans $Z = 1$ to 2 (top to bottom) in sheath heat flux transmission equation.

current is balanced by a net ion current on the inner divertor. The ground current in this instance increases the heat flux by nearly 50 %, almost consistently through the whole SOL. The upstream electron temperature and density profiles measured by the Langmuir probes and Thomson scattering match. Pressure maps from upstream to the divertor. Since the edge collisionality is so low the heat flux is transported without a significant parallel electron temperature gradient and the upstream and divertor electron temperature profiles map.

The agreement for sheath heat flux in a helium plasma in the sheath-limited regime is also excellent, fig. 78. Equation (60) requires an assumption on the charge Z of the ions. The range of $Z = 1$ to 2 is indicated as the thickness of the line in fig. 78. Since eq. (60) is a weak function of Z the assumption of Z has a small effect on the final value of sheath heat flux.

Although the confirmation of sheath heat flux theory in sheath-limited plasmas is excellent, as the core density increases so does the disagreement.

In the high-recycling (conduction-limited) regime the shape of the surface thermocouple and Langmuir probe heat flux profiles are the same, fig. 79. However the Langmuir probe profile over-predicts the sheath heat flux with the assumption that $T_i \approx T_e$. This may indicate that $T_i \ll T_e$ and that the divertor ion temperature in the high-recycling regime is dominated by cold recycling deuterium. However, in this high collisionality divertor, it is expected that the ions are well-coupled to the electrons. So, perhaps this disagreement is just the beginning of a bigger problem as discussed below.

When T_e falls sufficiently low ($\sim 10\,\mathrm{eV}$, third column in fig. 77 and second column in fig. 79), divertor Langmuir probes report a spike in nT_e, ~ 2 times the "upstream" value. When this was discovered, before the instillation of the thermal diagnostics, it was dubbed the "death-ray" due to its apparent enhanced heat flux. Yet, nearby surface thermocouples now measure a very low surface heat flux, one that is indicative of a detached plasma—clearly not a "death-ray" with respect to high localized heat flux. The experimentally inferred sheath heat

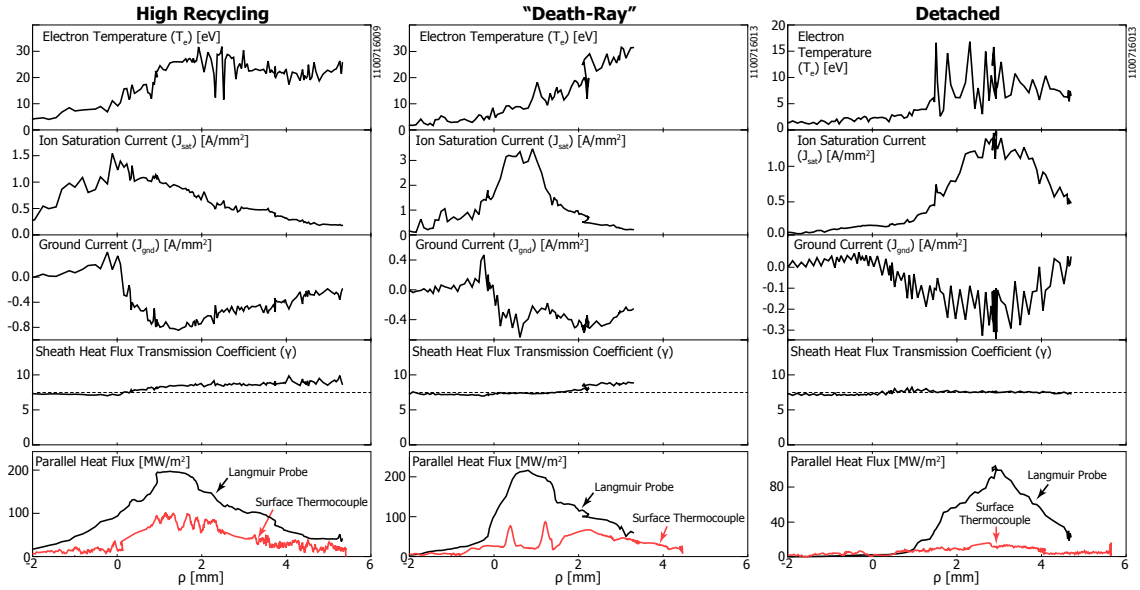

Figure 79: Heat flux transmission coefficient in high recycling, "death-ray", and detached regimes. The agreement between theory and experiment gets worse as the core density increases.

flux transmission coefficient is ~ 2. The surface thermocouples are measuring the correct total energy flux in this regime, as confirmed by the calorimeters. In addition, the upstream Langmuir probe and Thomson profiles still match. The odd-measurement out is the divertor Langmuir probe.

At even higher core plasma density the divertor begins to detach (fourth column in fig. 77 and third column in fig. 79). In this regime the momentum loss with neutrals is great enough to cause a pressure drop from upstream to the divertor. In this regime the surface thermocouples measure almost no heat flux—at least a factor of 10 less than in the sheath-limited regime. However the Langmuir probes still indicate a heat flux nearly the same as in the sheath-limited regime! The experimentally inferred sheath heat flux transmission coefficient would be ~ 1.

6.1.3 *Discussion*

Given that the divertor Langmuir probes disagree with both pressure mapping to upstream (during the "death-ray") and local heat flux (in all but the sheath-limited regime), it seems that they are the diagnostic that is not being interpreted properly. But how?

The most cited cause is the sensitivity of Langmuir probes to a small population of hot electrons [8, 18]. It is likely, due to their higher velocity, that hot electrons are able to travel the length of the SOL without a collision and will not be subject to the same temperature gradient that the bulk of electrons experience. This is supported by measurements in DIII-D which showed the divertor Langmuir probes

to measure the electron temperature about twice as high as Thomson scattering [20]. Yet, we find that the Langmuir probe I-V remains a single exponential over all four regimes, fig. 80, with no sign of non-Maxwellian electrons.

If the Langmuir probes were indeed measuring a non-Maxwellian electron distribution with a hot tail, then the T_e from the I-V fit would be higher than an effective "bulk" temperature. However, if the electron distribution was non-Maxwellian with a hot tail then the plasma potential would be enhanced to repel these hot electrons—increasing the energy with which the ions impact the divertor surface. How these two processes (over-calculation of T_e and under prediction of the plasma potential) balance out is up to the details of the electron energy distribution. It is not clear that they would balance out to an experimentally measured $\gamma < 2$. Perhaps it is time to go beyond considering how a Langmuir probe may be sensitive to plasma conditions and consider what effect the probe bias has on the local plasma conditions. ●

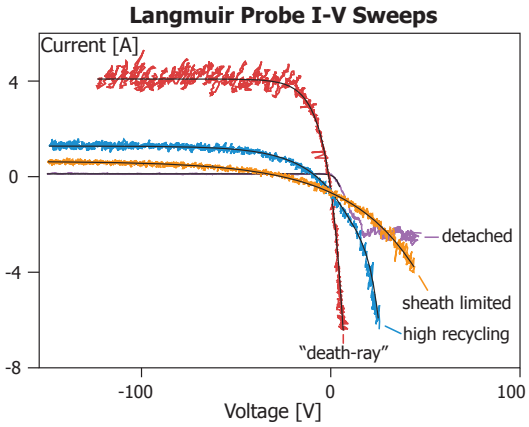

Figure 80: I-Vs for all edge regimes.

6.2 THEORY FOR EXCESS ION COLLECTION

C-Mod lacked thermal measurements in the divertor at the time that the "death-ray" was discovered. Thus it was not known to be limited to the Langmuir probes. It was speculated that the divertor over-pressure was caused by ionization of neutrals flowing with large toroidal velocities (since ion-neutral momentum coupling is strong in this regime). They deposited their momentum on magnetic flux surfaces that, for some unknown reason, had slightly elevated temperatures ($T_e > 5\,\text{eV}$, ionization dominant) relative to the rest of the divertor profile ($T_e < 5\,\text{eV}$, charge-exchange dominant) [9]. Moreover, the phenomenon was assumed to occur in an axisymmetric band, affecting the whole divertor. But with the new surface thermocouple sensors installed on C-Mod, we now see that the "death-ray" is not an axisymmetric effect. Instead, it is likely restricted to just the magnetic flux tube intercepted by the Langmuir probe.

An attempt at modeling the "death-ray" as an axisymmetric phenomena with a coupled Monte Carlo neutral–fluid plasma simulation was done by Stotler [22]. The over-pressure could simply be turned on by adjusting the recycling coefficient from 0.8 to 0.9. It was found that the over-pressure was supported by radial transport of parallel momentum. However, the simulated over-pressure was only $\sim 33\,\%$, compared to the $\sim 100\,\%$ over-pressure typically seen in experiments.

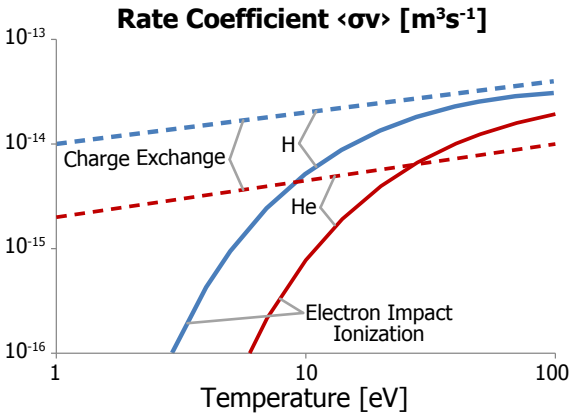

Figure 81: Atomic data for H and He. The "death-ray" depends on both charge exchange on electron impaction ionization. Both of which have at least an order of magnitude difference between hydrogen and helium. So it was thought that the "death-ray" may behave differently in each species.

And the simulation indicated a spike in D_α emission that was absent in the experiment.

It is clear that the "death-ray" is due to an anomalous measurement from the divertor Langmuir probes: the calorimeters and surface thermocouples clearly do not measure the excess energy flux that should be associated with the "death-ray" and that the upstream scanning probe profiles match Thomson scattering. The original theory behind the "death-ray" was partially correct. The missing point was the source of elevated electron temperature. But, now it is known that the "death-ray" is localized to the Langmuir probe, which must be the source of elevated electron temperature.

Normally the sheath serves to cool the scrape-off layer electrons. It repels the low-energy electrons and lets the high-energy ones through. However, a Langmuir probe swept through ion saturation no longer allows the high-energy electrons to exhaust through the sheath, effectively forming an insulating boundary condition. Thus the local electron temperature rises. Within this temperature range (5 eV to 10 eV) the electron impact ionization of hydrogen is a exponentially sensitive function of electron temperature, fig. 81. The neutrals, coupled to the ions through charge-exchange collisions and flowing at a significant fraction of the local sound speed, are ionized by the elevated electron temperature and deposit their momentum in the the local flux tube.

Based on this understanding that the "death-ray" depends on ionization and charge exchange—two atomic processes—one may expect the "death-ray" to behave differently in hydrogen and helium. In addition hydrogen recycles from the divertor as a diatomic molecule and helium recycles as an atom. There is a limited set of divertor data for pure helium obtained during other experiments in C-Mod in sheath-limited and low recycling regimes; yet there remains a good match with sheath heat flux, fig. 78. During a run day dedicated to the study of divertor conditions in helium, it was difficult to obtain pure helium plasmas: deuterium was needed for breakdown and there remained deuterium recycling from the first wall from previous experiments. Preliminary results indicate that the "death-ray" over-pressure

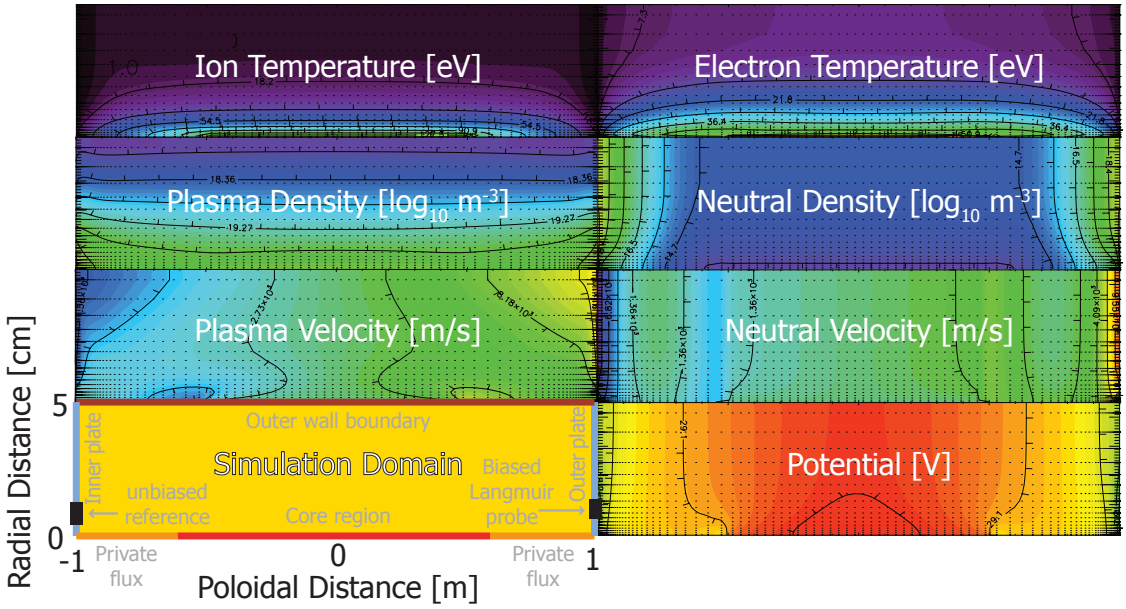

Figure 82: 2D contours of edge plasma fluid variables from UEDGE simulation of biased Langmuir probe. (simulations by M. V. Umansky)

was reduced in these mixed deuterium-helium plasmas from pure deuterium. However, without a precise measurement of the relative amounts of helium and deuterium, the result is not conclusive. •

6.3 PLASMA-NEUTRAL SIMULATION OF EXCESS ION COLLECTION

A collaboration between the PSFC (D. Brunner and B. LaBombard) and LLNL (M. V. Umansky and T. D. Rognlien) was formed to test the theory of the "death-ray" divertor over-pressure with simulations [2, 25]. M. V. Umansky used UEDGE, a numerical code created to model tokamak edge plasmas. It finds steady-state solutions (or can solve for the time-evolution) of a system of fluid equations for density, parallel momentum, and energy of plasma and neutrals [16]. The anomalous radial transport is typically modeled by ad-hoc transport coefficients chosen to match experimentally observed radial plasma profiles. An additional equation is used for electric current continuity.

The C-Mod edge plasma is modeled as an axisymmetric rectangular slab, fig. 82. The poloidal (2 m) and radial (5 cm) dimensions of the edge plasma as well as the toroidal (5 T) and poloidal fields (0.5 T) roughly match that of C-Mod. Radial boundary conditions model the influx of energy and particles and outflow to the wall. Sheath boundary conditions are used on the poloidal boundaries (target plates). Plasma profiles at the midplane were set to closely match those of a typical "death-ray". The divertor coefficient recycling was adjusted such that the divertor temperature was in the range where experimental "death-rays" are found, $T_e \approx 5$ eV.

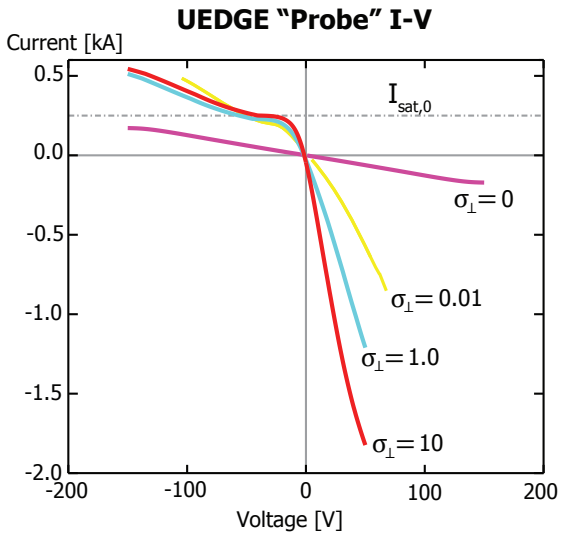

Figure 83: I-V curves calculated in UEDGE for several values of the effective perpendicular conductivity $\sigma_\perp$ (shown in $[\Omega^{-1}\,m^{-1}]$. With $\sigma_\perp = 0$ the curve is symmetric, for finite $\sigma_\perp$ an asymmetric curve is produced. (figure modified from [25])

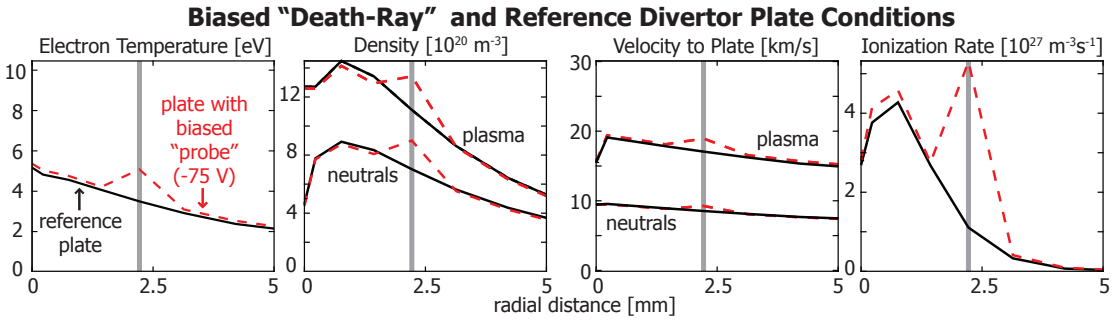

Figure 84: Divertor plate profiles of plasma conditions from UEDGE simulation for plate with "probe" biased at -75 V (red dashed) and unbiased reference plate (solid black); probe location denoted by vertical grey line. The probe bias increases the electron temperature—greatly increasing the ionization of neutrals. Overpressure is supported by charge-exchange collisions coupling the neutral velocity to half the plasma velocity. (simulations by M. V. Umansky)

The Langmuir probe is modeled as a biased axisymmetric strip on one of the target plates by adjusting the potential of one boundary node and measuring the net current collected at that node. There is no first-principles model for electric conductivity perpendicular to the magnetic field ($\sigma_\perp$) in magnetized plasma. If $\sigma_\perp$ was zero, the current collected by a Langmuir probe biased positive with respect to the chamber would be limited to the ion saturation current drawn on the sheath at the opposite end of the field line connected to the probe (section 2.5). Yet, in C-Mod edge plasma experiments a Langmuir probe's current-voltage (I-V) trace is clearly asymmetric—that is, the current collected at positive bias exceeds the ion saturation current, fig. 80. The current must be transported across the magnetic field and $\sigma_\perp$ is clearly not zero. The perpendicular conductivity was adjusted such that the asymmetry in the UEDGE simulated Langmuir probe I-V approximately matched that seen in experiments: $\sigma_\perp = 1\,\Omega^{-1}\,m^{-1}$, fig. 83. Once the asymmetric I-V was obtained, the simulated "death-ray" results were not sensitive to factor of 10 changes in $\sigma_\perp$.

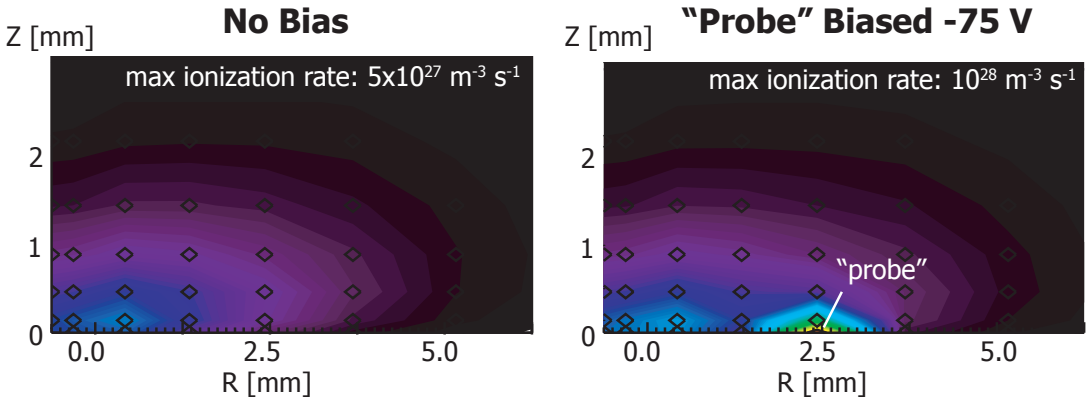

Figure 85: Spatial distribution of the ionization source density $S_{iz} = n_e n_g \langle \sigma v \rangle_{iz}$ is shown. A strongly localized (< 0.25 mm) ionization source is formed at the biased probe tip. The main cause of this elevated electron temperature near this location, which has a strong effect on the ionization rate for this temperature range, fig. 84. (figure modified from [25])

Figure 86: Poloidal profiles of pressure in front of UEDGE "probe" biased to -75 V. The plasma pressure at the divertor, as measured by the experimental Langmuir probe ($p + \rho v^2$), is twice the "upstream" value (as typically seen in experimental "death-rays"). This pressure gradient is sustained by the plasma-neutral momentum exchange (R_{in}). (figure modified from [25])

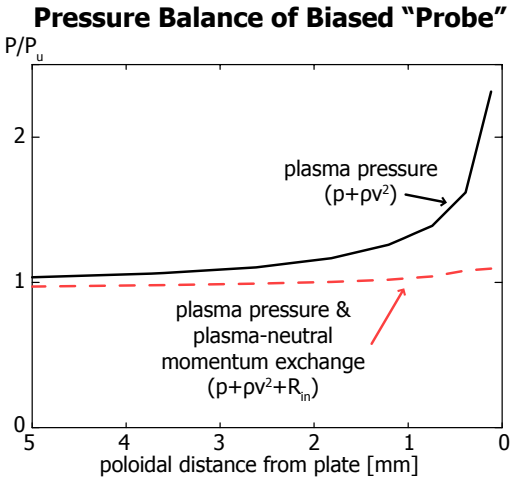

UEDGE simulations reproduce the "death-ray" over-pressure and indicate that ionization of neutrals is a key factor. The physical picture is that:

1. The neutrals are "blown" into a toroidal "wind" through charge-exchange collisions with ions.
2. Negative bias of the simulated Langmuir probe increases the local electron temperature, fig. 84.
3. Encountering the region of elevated T_e the neutral "wind" is ionized (figs. 84 and 85) and deposits its momentum.

The factor of ~ 2 over-pressure is successfully reproduced by the code, fig. 86. It is the ion-neutral friction force associated with the ionization, $R_{in} = m_i S_{iz} u_{n\|}$ (with m_i the ion mass, S_{iz} the ionization source, and $u_{n\|}$ the neutral velocity parallel to the magnetic field), which balances the parallel gradient of increased plasma pressure.

The simulation overestimates some of the effects of plasma probe perturbation, possibly due to using a 2D toroidally symmetric model

of the probe. The simulated ion saturation current increases as the negative bias is increased past $-30\,V$, which is a consequence of both n and T_e increasing locally at the probe. On the other hand, the experimental ion saturation current remains relatively constant, albeit with large fluctuations, through biasing to $-200\,V$, fig. 83. Preliminary simulations indicate that increasing the divertor electron temperature by a few eV decreases the magnitude of the "death-ray"; as expected because the response of ionization rate to changes in T_e becomes less steep at higher T_e.

6.4 DISCUSSION

Although the measurements of sheath heat flux in the sheath-limited regime (section 6.1.2) are the most convincing confirmation to-date in a tokamak (and have since been matched in DIII-D [5] and JET [14]), the measurements in the other edge regimes still leave open questions on the function of the Langmuir probes. The experimentally measured sheath heat flux transmission coefficient systematically decreased with increasing core density to the point where in the detached divertor it was well below the theoretical minimum. Yet the probes still had "reasonable" I-V characteristics.

A new theory was put forth, implicating the Langmuir probe in disturbing the local plasma. The probe bias restricts electrons from exhausting their heat flux to the surface, raises local electron temperature, and increases ionization of neutrals which are then collected by the probe. The mechanisms proposed in this theory were confirmed with 2D plasma-neutral fluid simulations. Although the simulations were a qualitative match, there remains some quantitative discrepancies (especially the simulated I-V not saturating with decreasing bias).

This theory was developed to explain the "death-ray", it could also explain the lack of agreement with sheath heat flux in the other regimes. The "death-ray" case sticks out because there is a clear apparent over-pressure from the divertor to upstream. However, in the high-recycling and detached regimes, there is another issue due to uncertainty in profile mapping. Because the SOL cross-field pressure profiles are typically exponential, a false increase in magnitude of one profile could be made to look correct with a small shift in the other profile. For example, if the divertor plasma profile was measured 50 % above its true value ($P_{div}/P_{up} = 1.5$) and the cross-field pressure decay length was $\lambda = 4\,mm$ the effective shift to get the profiles to overlap would be $x_{shift} = 1.6\,mm$ ($x_{shift} = \lambda \ln\left(P_{div}/P_{up}\right)$). This is well within the uncertainties of EFIT magnetic mapping.

Thus, even though the pressure profiles appear to map over at least a portion of the profiles in all regimes, this is no guarantee that the divertor pressure measurements are correct. The disagreement with

the thermal measurements in all but the sheath-limited regimes could be indicating that the Langmuir probe measurements are not representative of the local plasma conditions. Be it the probe-induced overpressure, sensitivity to non-Maxwellian electrons, or perhaps some combination of both.

Another idea briefly discussed, but not pursued in detail, was what if the shadowed area behind the Langmuir probe was being filled in? This is diagramed in fig. 87. Normally the ion saturation current is assumed to arrive along the magnetic field to the probe and arrive on the front surface. The area behind the probe is considered to be shadowed and thus depleted of plasma. Perhaps in this high recycling regime that area fills in with plasma and the effective collecting area increases.

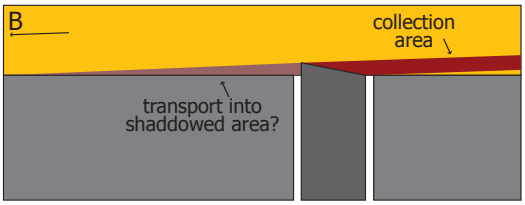

Figure 87: Diagram of a Langmuir probe and its collection area. The angles are to scale: magnetic field is 2° to the divertor surface and the Langmuir probe is 11° to the divertor. Normally only the front face is assumed to collect plasma. However, if the shadowed area behind the probe were to fill with plasma, the effective collection area of the probe would increase.

There are two paths forward in sorting these puzzles: more detailed experiments and more detailed simulations. Presently the DIII-D tokamak is the most attractive device to preform detailed experiments; with its recent success in confirming sheath heat flux theory, its unique divertor Thomson scattering system, and its extensive divertor spectroscopy. Operation of all possible diagnostic systems, much like the simple-as-possible plasmas of a decade ago, would help to sort out what measurements can be trusted and what cannot.

As for simulations, it would be desirable to move beyond fluid simulations and on to kinetic simulations of a probe bias in recycling divertor conditions. The sheath, probe particle collection, and ionization are all inherently kinetic processes. The added detail of a kinetic simulation of a probe biasing in recycling plasma conditions would likely clarify the picture. Given a skilled code experimentalist, it should be straightforward to explore the effects of a probe bias on the local plasma conditions over a range of divertor conditions to see if any sense could be made of the experimental measurements. ⋆

BIBLIOGRAPHY

[1] N. Asakura, K. Shimizu, N. Hosogane, K. Itami, and S. Tsuji. Recycling enhancement with n_e and q_{eff} in high density discharges on JT-60U. *Nuclear Fusion*, 35(4):381–398, 1995.

[2] D. Brunner, M. V. Umansky, B. LaBombard, and T. D. Rognlien. Divertor "death-ray" explained: An artifact of a Langmuir probe operating at negative bias in a high-recycling divertor. *Journal of Nuclear Materials*, 438:S1196–S1199, 2013.

[3] D. Buchenauer, J. W. Cuthbertson, J. A. Whaley, J. D. Miller, J. G. Watkins, R. Junge, W. P. West, and D. N. Hill. Sheath physics study using the divertor materials evaluation system (DiMES) on DIII-D. *Proceedings of the Tenth Topical Conference on High Temperature Plasma Diagnostics*, 66(1):827–829, 1995.

[4] L. Costanzo, J. P. Gunn, T. Loarer, L. Colas, Y. Corre, Ph. Ghendrih, C. Grisolia, A. Grosman, D. Guilhem, P. Monier-Garbet, R. Reichle, H. Roche, and J. C. Vallet. Analysis of energy flux deposition and sheath transmission factors during ergodic divertor operation on Tore Supra. *Journal of Nuclear Materials*, 290-293:840 – 844, 2001.

[5] D. Donovan, D. Buchenauer, J. Watkins, A. Leonard, C. Wong, M. Schaffer, D. Rudakov, C. Lasnier, and P. Stangeby. Experimental measurements of the particle flux and sheath power transmission factor profiles in the divertor of DIII-D. *Journal of Nuclear Materials*, 438:S467–S471, 2013.

[6] S. Elmore, S. Y. Allan, A. Kirk, G. Fishpool, J. Harrison, P. Tamain, M. Kočan, R. Gaffka, R. Stephen, J. W. Bradley, and the MAST Team. Upstream and divertor ion temperature measurements on MAST by retarding field energy analyser. *Plasma Physics and Controlled Fusion*, 54(6):065001, 2012.

[7] A. Herrmann, M. Laux, D. Coster, J. Neuhauser, D. Reiter, R. Schneider, M. Weinlich, and ASDEX-Upgrade Team. Energy transport to the divertor plates of ASDEX-Upgrade during ELMy H-mode phases. *Journal of Nuclear Materials*, 220-222:543 – 547, 1995.

[8] M. A. Jaworski, M. G. Bell, T. K. Gray, R. Kaita, J. Kallman, H. W. Kugel, B. LeBlanc, A. G. McLean, S. A. Sabbagh, V. A. Soukhanovskii, D. P. Stotler, and Surla V. Modification of

the electron energy distribution function during lithium experiments on the National Spherical Torus Experiment. *Fusion Engineering and Design*, 2012.

[9] B. Labombard, J. A. Goetz, I. Hutchinson, D. Jablonski, J. Kesner, C. Kurz, B. Lipschultz, G. M. McCracken, A. Niemczewski, J. Terry, A. Allen, R. L. Boivin, F. Bombarda, P. Bonoli, C. Christensen, C. Fiore, D. Garnier, S. Golovato, R. Granetz, M. Greenwald, S. Horne, A. Hubbard, J. Irby, D. Lo, D. Lumma, E. Marmar, M. May, A. Mazurenko, R. Nachtrieb, H. Ohkawa, P. O'Shea, M. Porkolab, J. Reardon, J. Rice, J. Rost, J. Schachter, J. Snipes, J. Sorci, P. Stek, Y. Takase, Y. Wang, R. Watterson, J. Weaver, B. Welch, and S. Wolfe. Experimental investigation of transport phenomena in the scrape-off layer and divertor. *Journal of Nuclear Materials*, 241-243:149 – 166, 1997.

[10] B. LaBombard, J. W. Hughes, N. Smick, A. Graf, K. Marr, R. McDermott, M. Reinke, M. Greenwald, B. Lipschultz, J. L. Terry, D. G. Whyte, S. J. Zweben, and Alcator C-Mod Team. Critical gradients and plasma flows in the edge plasma of Alcator C-Mod. *Physics of Plasmas*, 15(5):056106, 2008.

[11] B. LaBombard, J. L. Terry, J. W. Hughes, D. Brunner, J. Payne, M. L. Reinke, I. Cziegler, R. Granetz, M. Greenwald, I. H. Hutchinson, J. Irby, Y. Lin, B. Lipschultz, Y. Ma, E. S. Marmar, W. L. Rowan, N. Tsujii, G. Wallace, D. G. Whyte, S. Wolfe, S. Wukitch, G. Wurden, and the Alcator C-Mod Team. Scaling of the power exhaust channel in Alcator C-Mod. *Physics of Plasmas*, 18:056104, 2011.

[12] L. L. Lao, H. St. John, R. D. Stambaugh, A. G. Kellman, and W. Pfeiffer. Reconstruction of current profile parameters and plasma shapes in tokamaks. *Nuclear Fusion*, 25(11):1611, 1985.

[13] J. Marki, R. A. Pitts, T. Eich, A. Herrmann, J. Horacek, F. Sanchez, and G. Veres. Sheath heat transmission factors on TCV. *Journal of Nuclear Materials*, 363-365:382 – 388, 2007.

[14] S. Marsen, L. Aho-Mantila, S. Brezinsek, T. Eich, C. Giroud, M. Groth, S. Jachmich, B. Sieglin, and JET EFDA Contributors. Divertor heat load in JET-comparing Langmuir probe and IR data. In *40th EPS Conference on Plasma Physics, Espoo, Finland*, 2013.

[15] R. D. Monk, A. Loarte, A. Chankin, S. Clement, S. J. Davies, J. K. Ehrenberg, H. Y. Guo, J. Lingertat, G. F. Matthews, M. F. Stamp, and P. C. Stangeby. Interpretation of ion flux and electron temperature profiles at the JET divertor target during high recycling and detached discharges. *Journal of Nuclear Materials*, 241-243:396 – 401, 1997.

[16] T. D. Rognlien, J. L. Milovich, M. E. Rensink, and G. D. Porter. A fully implicit, time dependent 2-D fluid code for modeling tokamak edge plasmas. *Journal of Nuclear Materials*, 196-198:347 – 351, 1992.

[17] M. J. Schaffer, A. V. Chankin, H. Y. Guo, G. F. Matthews, and R. Monk. Pfirsch-Schlüter currents in the JET divertor. *Nuclear Fusion*, 37:83, 1997.

[18] P. C. Stangeby. A problem in the interpretation of tokamak Langmuir probes when a fast electron component is present. *Plasma Physics and Controlled Fusion*, 37(9):1031–1037, 1995.

[19] P. C. Stangeby. *The Plasma Boundary of Magnetic Fusion Devices*. IoP Publishing, 2000.

[20] P. C. Stangeby, J. D. Elder, J. A. Boedo, B. Bray, N. H. Brooks, M. E. Fenstermacher, M. Groth, R. C. Isler, L. L. Lao, S. Lisgo, G. D. Porter, D. Reiter, D. L. Rudakov, J. G. Watkins, W. P. West, and D. G. Whyte. Interpretive modeling of simple-as-possible-plasma discharges on DIII-D using the OEDGE code. *Journal of Nuclear Materials*, 313:883–887, 2003.

[21] D. Storek and K. W. Gentle. Accurate measurement and interpretation of the heat flux to the divertor in TEXT Upgrade. *Nuclear Fusion*, 41(1):1–9, 2001.

[22] D. P. Stotler, R. A. Vesey, D. P. Coster, C. F. F. Karney, B. LaBombard, B. Lipschultz, C. S. Pitcher, and R. Schneider. Coupled Monte Carlo neutral–fluid plasma simulation of Alcator C-Mod divertor plasma near detachment. *Journal of Nuclear Materials*, 266:947–952, 1999.

[23] S. Takamura, S. Mizoshita, and N. Ohno. Suppression of secondary electron emission from the material surfaces with grazing incident magnetic field in the plasma. *Physics of Plasmas*, 3(12):4310–4312, 1996.

[24] S. Takamura, M. Y. Ye, T. Kuwabara, and N. Ohno. Heat flows through plasma sheaths. *The 39th Annual Meeting of Division of Plasma Physics of APS*, 5(5):2151–2158, 1998.

[25] M. V. Umansky, D. Brunner, B. LaBombard, and T. D. Rognlien. Modeling of local edge plasma perturbations induced by a biased probe. *Contributions to Plasma Physics*, 52(5-6):417–423, 2012.

7

ASSESSMENT OF ION SENSITIVE PROBE OPERATION

At the outset, the ion sensitive probe was intended to be one of the main diagnostics used to explore boundary the boundary ion temperature. However, in its present form, the C-Mod ISP is not able to measure the ion temperature. This chapter explores space charge and its implications for ISP measurements as well as gives guidance for successful implementation.

Initial analysis of the ISP I-V characteristics produced ion temperatures that were consistent with expectations: it seemed to follow the expected exponential decay (section 2.6.1):

$$I_C = \begin{cases} I_o & V \leqslant V_p \\ I_o \, e^{-\frac{eZ(V-V_p)}{k_B T_i}} & V > V_p \end{cases}, \tag{61}$$

as well as $T_i \approx 3 \times T_e$, as anticipated by reasonable estimates of SOL heat transport [47] and in line with what has previously measured in tokamaks [29]. But a systematic comparison with ion temperatures inferred by Charge eXchange Recombination Spectroscopy (CXRS) over a range of plasma densities suggested that the ion sensitive probe was not following the main ion T_i as expected, section 5.2. More careful consideration of the data (see fig. 88) demonstrates that the C-Mod ISP I-V matches the classic Child-Langmuir 1D space charge current response [31] (shifted by the plasma potential V_p):

$$I_{SC} = \frac{4\epsilon_o}{9}\sqrt{\frac{2e}{m}}\frac{S}{d^2}\left(V_p - V\right)^{3/2}. \tag{62}$$

The $V^{3/2}$ curve of space charge limited current does a remarkably good job of quantitatively fitting the observed I-V response, recognizing that are no free parameters in the expression: d and S are given by probe geometry, m is the deuterium mass, and V_p is given where I goes to zero. That the probe is space charge limited is further supported by the observation that at the voltage where $I \approx 0$ corresponded to the plasma potential as calculated by Langmuir probe measurements (section 5.4).

It is not surprising that the C-Mod ISP is space charge limited. If the classic picture of the ISP holds, i. e., electrons are completely disallowed from the probe volume (the space in front of the Collector magnetically shielded by the Guard) and only ions exist there, then given the probe geometry ($d = 0.25\,\text{mm}$) and plasma density

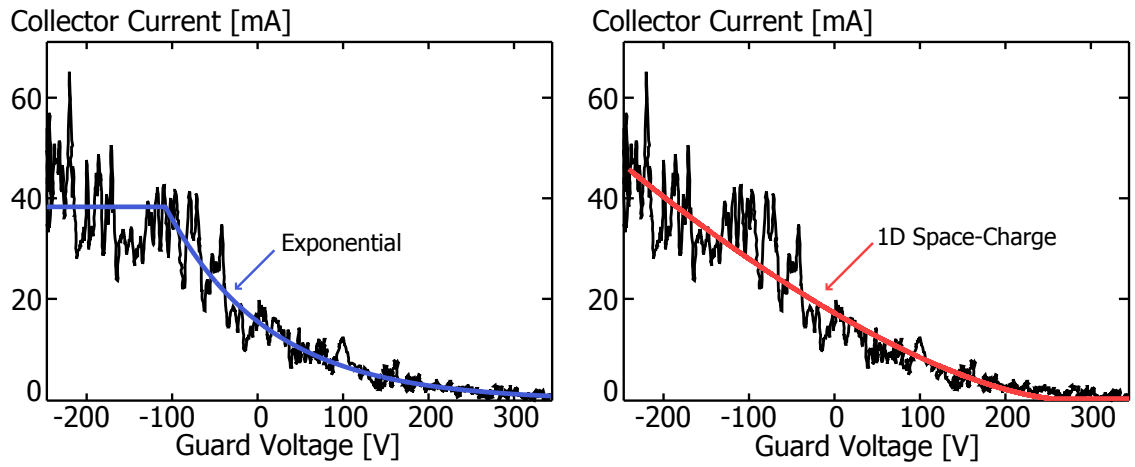

Figure 88: Example of an experimental I-V characteristic from the C-Mod ISP ($T_e \approx 40\,eV$ & $n \approx 0.6 \times 10^{20}\,m^{-3}$). On the left is a "best-fit" of eq. (61), typically used to infer the ion temperature. The 1D Child Langmuir equation (eq. (62)) is overlaid on the same data on the right. This remarkably good match, with no free parameters, indicates that the probe is likely space charge limited and the temperature fit on the left is erroneous.

($n > 10^{18}\,m^{-3}$) it should be space charge limited. The space charge limited current (eq. (62)) at a bias of 100 V below the plasma potential is 1.4 mA. The expected current to the surface at $T_i = 100\,eV$ and $n = 10^{19}\,m^{-3}$ is 3.1 mA, given approximately by the 1-way Maxwellian flux ($1/4 n \sqrt{8 k_B T_i/\pi m_i}$) times the Collector surface area. Prompted by this result, we have surveyed the literature and found many ISPs also operating at the 1-D space charge limit. In fact, many ISPs report ion current collection *significantly in excess* of the Child-Langmuir 1D space charge limit [12, 14, 15, 19, 23, 28, 36, 41, 48].

The goals of this chapter are to address the following three questions:

1. Why did the space charge limited C-Mod ISP I-V data produce a temperature profile that, at first look using the standard fitting technique, seemed reasonable?

2. How can an ISP collect ion current in excess of the 1D space charge limit?

3. What is the operational space (probe bias, plasma temperature and density) in which an ISP can reliably be operated and avoid space charge limits?

This remainder of this chapter is organized as follows: section 7.1 reviews I-V characteristics expected from an ISP in both classic and space charge limited regimes and discusses space charge considerations for previous ISP measurements that are reported in the literature. In section 7.2, we show how the C-Mod ISP I-V characteristics, while being erroneously interpreted as a classic ISP response, can produce an apparent ion temperature profile that looks reasonable. Sec-

tion 7.4 proposes two physical mechanisms in which ISPs may collect ion current that exceeds the 1D space charge limit: (1) inclusion of 2D geometry effects and (2) electrons $\vec{E} \times \vec{B}$ drifting into the probe volume. Kinetic simulations of 1D space charge limited current collection with finite ion temperature are presented in section 7.5. These simulations are used to understand the range of ion temperature and density in which the classic interpretation of the ISP I-V characteristic may be justified. In section 7.6 we conclude with recommendations for a successful implementation of an ISP for ion temperature measurements.

7.1 SURVEY OF ISP SPACE CHARGE

An analogous situation to the space charge physics of the vacuum diode (section 2.4) may be considered for the ion sensitive probe. In the simplest picture, the Guard disallows any electrons into the probe volume. The plasma acts as an anode, releasing ions into the probe volume. The Collector acts as a cathode; at high positive bias it restricts ion collection and low positive bias or negative bias it allows ions to flow more freely to the probe. But, for sufficiently high ion density, the space charge potential of the ions within the probe volume will restrict their flow.

7.1.1 *Experimental Evidence of Space Charge*

As shown in fig. 88, using the Collector area ($S = 7\,mm^2$) and recess distance ($d = 0.25\,mm$), the 1D space charge limited current (eq. (62)) is an excellent fit to the C-Mod ISP I-V data. That the I-V was not an exponential decay but was space charge limited was initially obscured by the large-scale plasma fluctuations. Averaging over multiple I-V sweeps (fig. 89), the agreement with the 1D Child-Langmuir Law becomes much clearer. Looking at I-Vs through the whole probe scan (fig. 90) reveals that the probe follows the Child-Langmuir Law through the SOL. This indicates that the assumptions of 1D space charge limits are good and the fitted exponential decay is unlikely to be representative of the ion temperature.

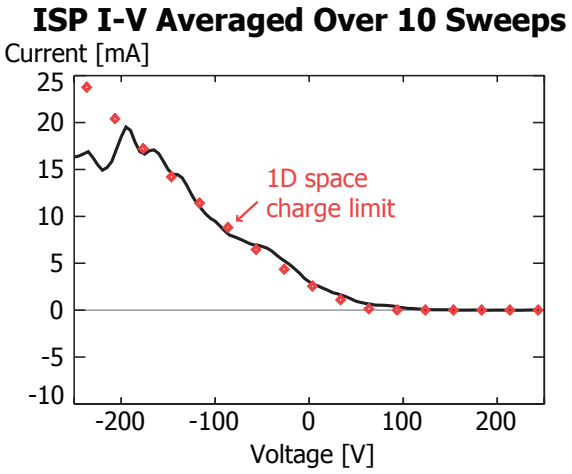

Figure 89: Average over 10 ISP I-V sweeps during dwell scan (at $T_e \approx 15\,eV$ and $n \approx 0.15 \times 10^{20}\,m^{-3}$) and comparison to 1D Child-Langmuir space charge equation. At the most negative bias ($< 200\,V$) the divergence from the Child-Langmuir Law is likely due to the ion flux to the probe saturating.

The C-Mod ISP is not the only ISP to meet or exceed the 1D space charge limit. Through extensive survey of the ISP literature we have located at

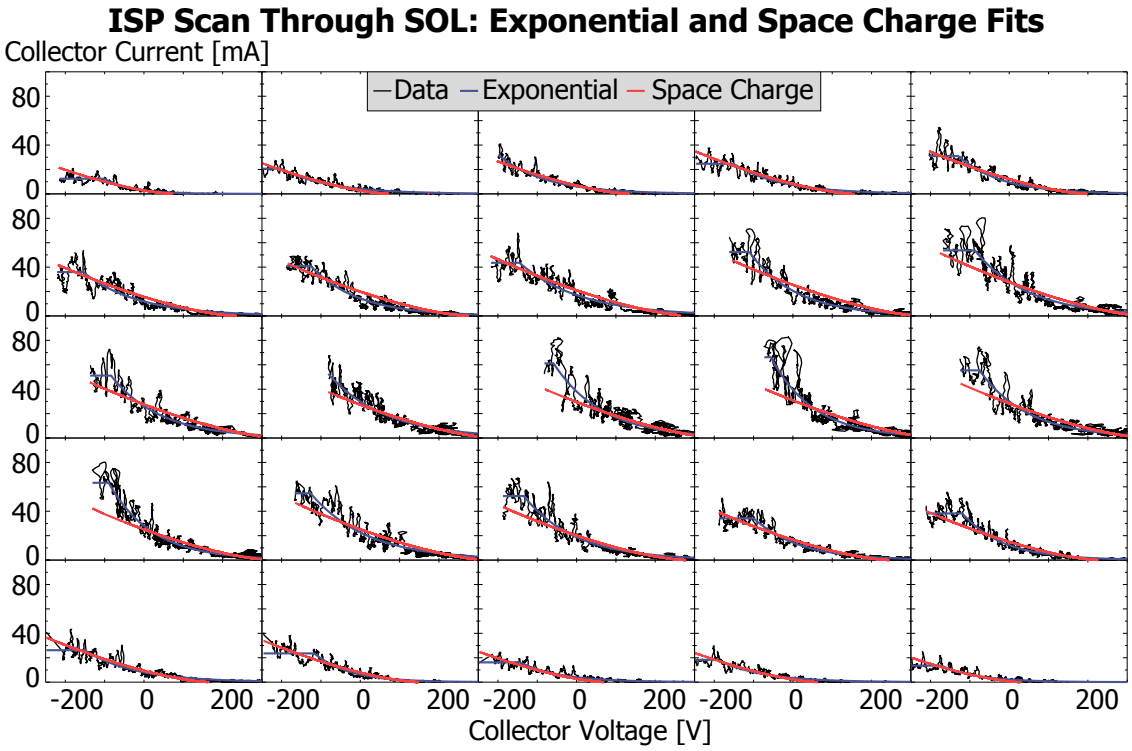

Figure 90: Comparison of exponential (blue) and space charge limited (red) fits to ISP I-Vs (black) through a scan through the SOL. Increasing time reads like text: from left-to-right, top-to-bottom. Far SOL parameters: $T_e \approx 10\,\text{eV}$ & $n \approx 0.1 \times 10^{20}\,\text{m}^{-3}$, near SOL parameters: $T_e \approx 60\,\text{eV}$ & $n \approx 1.0 \times 10^{20}\,\text{m}^{-3}$. Since the Grid card is limited to $\sim 60\,\text{mA}$ the voltage drops when this current is approached. With this the Collector is no longer biased below the Guard and proper operation cannot be ensured. All data in these graph where the voltage did not keep up with demand was removed.

least nine ISPs that have exceeded it [12, 14, 15, 19, 23, 28, 36, 41, 48]. Some of them report ion currents that are a factor of 100 higher than the 1D limit [36, 41, 48]. However, very few of these studies noted the excess. To attempt to identify a physical explanation as to how an ISP can exceed the 1D space charge limit, we restrict our attention to data reported from ISPs that meet the following criteria:

1. They are a classic ISP having only a Guard electrode and a Collector. Some ISPs have an insulating Guard (Ball-Pen Probe) [2], an additional electrodes for secondary electron control [21, 32, 45], or a grid over the Guard [7, 23, 32, 39], all of which could influence the particle trajectories within the probe in different ways.

2. The probe collected only net ion current over its entire bias range. Although this does not guarantee against electron collection, it is the best that can be done to ensure that an electron current contribution is not confusing the 1D space charge calculation.

The magnitude of the ion current collection relative to the 1D space charge limit was estimated as follows: a reference voltage was identified from the I-V characteristic as the point where the current decayed to zero or was 2 to 3 orders of magnitude below the peak current, whichever was most obvious from the data. The voltage difference (ΔV) was computed from the reference voltage and the voltage corresponding to peak current (I_{max}). This peak current and voltage difference were inputted to the 1D space charge limit equation (including the ion mass, with mass number M), yielding the required ratio of geometry parameters, S/d^2, to satisfy the limit:

$$\frac{S}{d^2} = \frac{9}{4\epsilon_0}\sqrt{\frac{M m_p}{2e}}\frac{I_{max}}{\Delta V^{3/2}}, \tag{63}$$

with m_p the proton mass. Taking this ratio of S/d^2 and dividing it by the actual ratio of S/d^2 derived from the probe geometry, we find the factor in which a given probe exceeds the space charge limit. This factor is shown in the last column of table 4. It is remarkable that some ISPs can exceed the 1D space charge limit by such a large amount. However, as is discussed in section 7.4.2, a likely explanation is that electrons drift into the probe volume, effectively reducing the distance, d, in the space charge formula.

The observation of an ion sensitive probe collecting at or above the 1D space charge limit has been discussed by only a few authors. Finite element simulations were performed in Ref. [21], indicating that space charge had a minimal effect on the I-V within the simulatied experimental parameters. Ref. [32] considered space charge limits on the classic Langmuir formulation [31], but concluded that

Table 4: List of ISPs that exceed the 1D space charge limit. This data is only taken from "classic" ISPs with two electrodes biased such that there are no regions of net electron collection. The S/d^2 in the second-to-last column is the effective geometry ratio from the 1D Child Langmuir equation required to satisfy the current values (I_{max}). The "ratio" is the ratio of the geometry factor implied from the I-V to the actual geometry, that is, it is the effective factor which the probe exceeds the classic 1D space charge limit. See the text for full descriptions of the quantities.

Experiment	S[mm²]	d[mm]	$\frac{S}{d^2}$ 1D	I_{max}[A]	ΔV[V]	M	$\frac{S}{d^2}$	ratio
NAGDIS-II [41]	0.20	1.0	0.20	6×10^{-5}	5	4	197.0	1000
DIONISOS [48]	4.96	5.0	0.20	5×10^{-4}	50	4	52.0	262
DIONISOS [36]	17.3	5.0	0.69	1×10^{-4}	30	40	70.7	102
TBR-1 [14]	0.50	0.7	1.03	1×10^{-3}	80	1	25.7	25.0
TBR-1 [15]	0.50	0.5	2.01	5×10^{-4}	55	1	22.5	11.1
TPD [28]	0.50	0.3	5.58	7×10^{-5}	15	4	44.3	7.93
MPX [23]	0.24	3.0	2.64	2×10^{-5}	16	4	11.5	4.35
LHD [19]	0.20	1.0	0.20	3×10^{-5}	100	2	0.779	3.97
C-Mod [12]	7.07	0.25	113.0	5×10^{-2}	500	2	116.0	1.03

the space charge potential was less than a few volts for their densities ($10^{16}\,m^{-3}$). Ref. [36] also considered the probe in the context of the Child-Langmuir law, finding that the ISP exceeded the 1D space charge limit by 3 orders of magnitude. It was mentioned that it would be necessary to have electrons within the probe volume in order to exceed the limit by such a large margin. $\vec{E} \times \vec{B}$ electron drift was identified as a possible mechanism.

Although the shape of the expected I-V characteristic (an exponential decay: $I \propto e^{-eV/k_B}$) may look very similar to that of space charge limited current ($I \propto V^{3/2}$), distinct differences can be seen when these curves are plotted with linear-linear or log-linear axes. For linear-linear graphs, space charge is seen as a nearly linear increase in the current collected with decreasing bias. Features like this can be seen in Refs. [2, 7, 8, 12, 15, 19, 23, 34, 36, 41]. This feature is seen to continue to the most negative bias range of the graph or to the point where the probe reaches ion saturation, depending on the degree of space charge and bias range. On a log-linear graph in which there are no space charge effects, the I-V characteristic exhibits two distinct straight lines, one for ion saturation and one for the exponential decay. When the probe is space charge limited, the distinct corner between these two lines is replaced by a smooth, rounded knee; this feature can be identified in Refs. [19, 23, 25, 27, 28, 38, 45].

The I-Vs of some ISPs show no signs of space charge [21, 32, 39]. While the I-V characteristics of other ISPs indicate collected electrons (for example Ball-Pen Probes, which have an insulating Guard that does not completely eliminate electrons, only reduces their flux), which may obscure whether they are space charge limited or not [1,

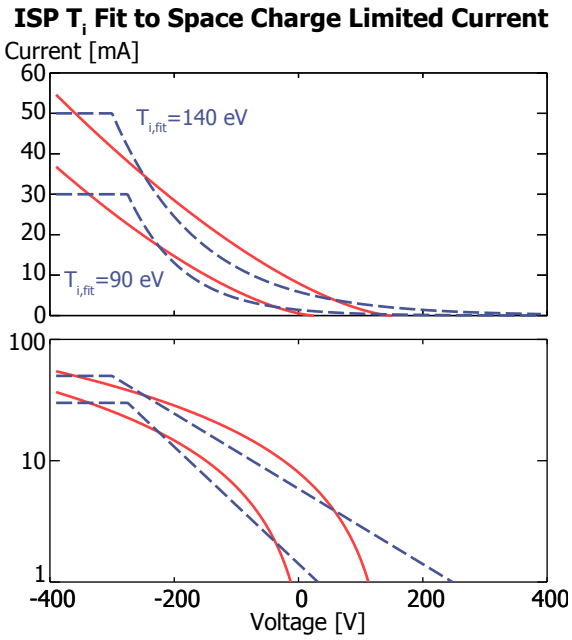

Figure 91: ISP exponential decay I-V responses (dashed blue lines, eq. (61)) are fitted to synthetic I-V characteristics generated by the 1D Child-Langmuir Law (solid red lines, eq. (62)) at two different plasma potentials. The values of T_i/Z, I_o, and V_p are returned by the fitting algorithm (section 4.3.2.2). Since the exponential fit is performed only over a finite voltage range, an increase in the plasma potential (i. e., the voltage where the space charge limited current goes to zero) results in an increase in the fitted ion temperature. Linear-linear (top panel) and log-linear scales (bottom) are shown to clearly illustrate the differences between exponential and space charge limited I-V responses.

5, 6, 11, 15, 17, 22, 37, 40, 49]. Finally, no I-Vs are given for [3, 4, 9, 10, 16, 20, 24, 26, 44] and thus we are unable to assess whether they displayed space charge limited characteristics.

Often the space charge potential is small enough to not affect the entire I-V. At a high enough bias, a probe can operate in a regime where the space charge potential is negligible, regaining the exponential decay (this is explored quantitatively through simulations in section 7.5). Some ISPs report very smooth I-V characteristics, allowing the space charge limited region to be recognized and fitting an exponential only to the unaffected, large positive bias region of the slope [2, 19, 23, 25, 27, 28, 38]. ISP I-V characteristics in Refs. [7, 45] are fitted over an intermediary portion of the I-V, ignoring the space charge rounding as well as the high positive bias region. In Ref. [45] this was done to avoid what was thought to be a population of hot ions. The region of the I-V fit was not shown in Refs. [8, 15, 34, 36, 41].

7.2 C-MOD ISP SPACE CHARGE PROFILES

To understand why the fitted T_i profile increased as the probe plunged deeper into the plasma, reconsider the 1D space charge limit equation (eq. (62)). The only quantity in this equation that changes as the ISP scans through the SOL is the plasma potential V_p. The plasma potential profiles remain unchanged over the course of the density scan as did the erroneous ISP ion temperature measurements.

To understand how a changing plasma potential could cause an apparent change in the ion temperature, first we form synthetic, space charge limited I-Vs from eq. (62), using the ISP probe geometry and

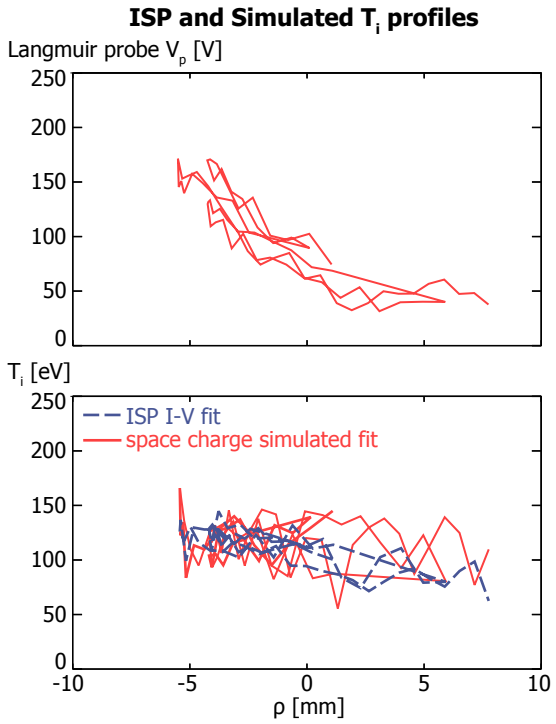

Figure 92: Top panel—Langmuir probe-inferred plasma potential profile. Bottom panel—Comparison of the ion temperatures that result from fitting ISP I-V experimental data (dashed blue line) and those that result from fitting a simulated space charge limited I-V response, accounting for the measured local plasma potential (solid red line). See text for a description of how the space charge simulated fit was calculated.

the plasma potentials as measured by the Langmuir probe. Then we least-squares fit the synthetic I-Vs, using the exponential decay formula (eq. (61)) over the typical bias range ($-390\,\mathrm{V} < V_C < 390\,\mathrm{V}$), yielding a fitted ion temperature for each plasma potential. Examples of this fitting technique are shown for two different plasma potentials in fig. 91.

Figure 92 shows a comparison of the T_i values that result from fitting the synthetic space charge limited I-V characteristics to the T_i values resulting from fitting to the actual ISP I-V characteristics. The profiles overlay almost identically. The increase in "temperature" as the probe plunged deeper into the plasma is apparently due to the increasing plasma potential. As the plasma potential increases, the position of the space charge limited I-V curve shifts in voltage bias. For high plasma potentials, a higher T_i results from a fit to the data. The fact that the fitted ion temperature happened to be around what was expected was an unfortunate coincidence. ●

7.3 DETAILED ASSESSMENT OF ISP OPERATION

Insight into the operation of the C-Mod ISP may be gained by mapping out all voltage combinations between the Collector and Guard. To do this we scanned them at two different frequencies (Collector 2000 Hz and Guard 20 Hz), see fig. 93. From this time series data we created a 2D contour plot of Collector and Guard currents versus the bias on both electrodes, see fig. 94, from which we may interpolate to any voltage sweep. Regions of net electron collection are red and

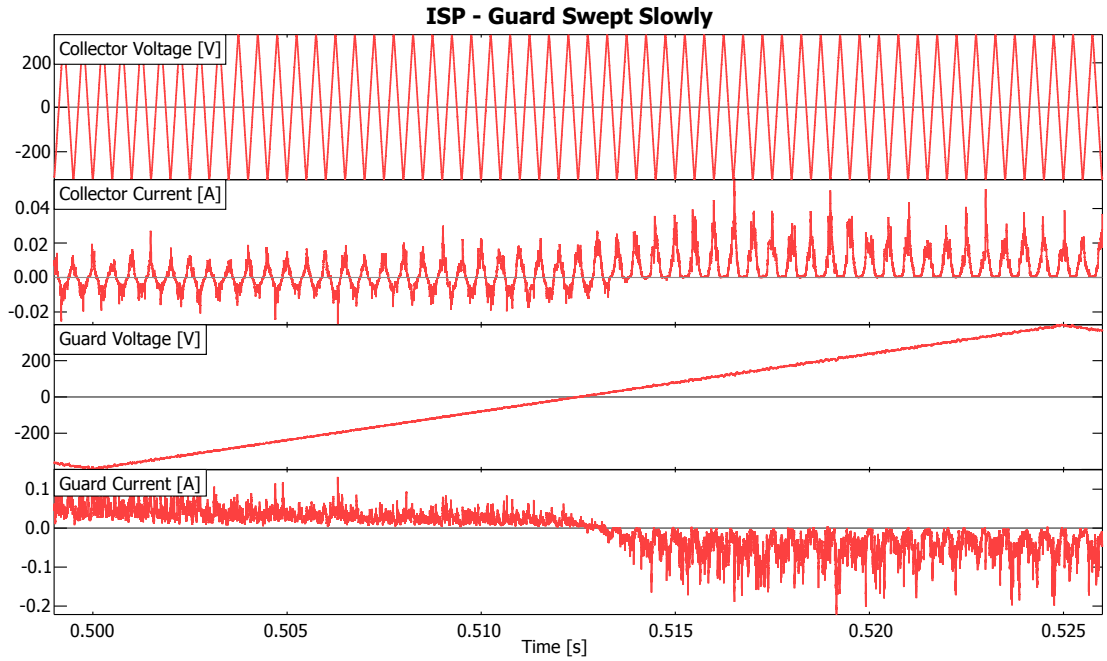

Figure 93: Raw current and voltage traces of ISP with Guard and Collector swept at two different rates (20 Hz to 2000 Hz, respectively). Data is used in fig. 94 and subsequent figures to explore operational space of the C-Mod ISP.

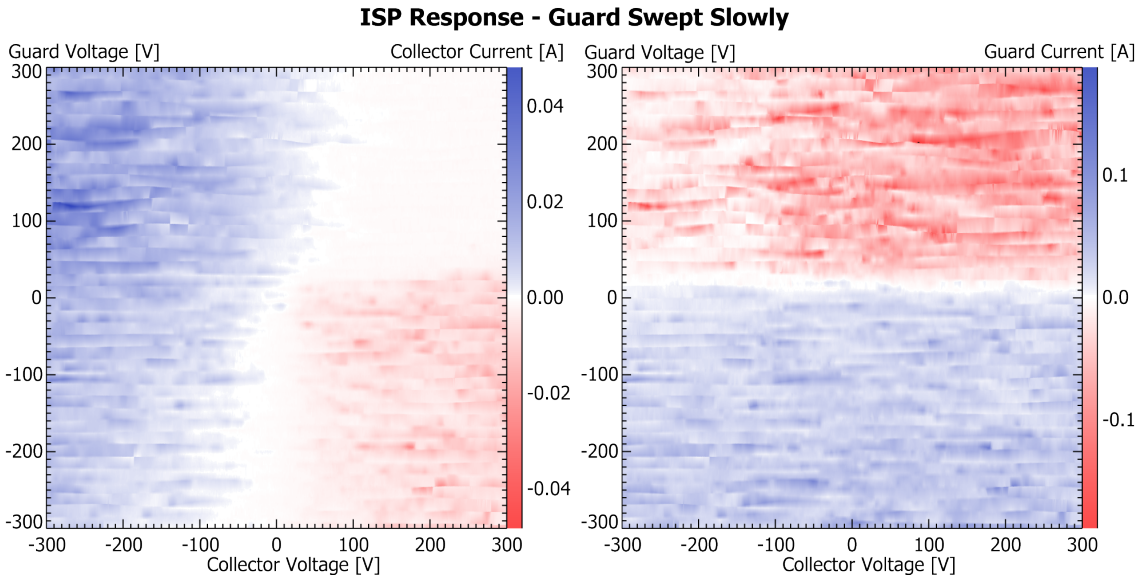

Figure 94: 2D contour plots of the C-Mod ISP operation (Collector ion collection is space charge limited). Collector current is on the left and Guard current is on the right. Blue is net ions collected, red is net electrons collected. This plot was created from the data in fig. 93 by sweeping the voltage on the Guard slowly (20 Hz) and the Collector quickly (2 kHz), nearly identical results are obtained when the bias rates are switched.

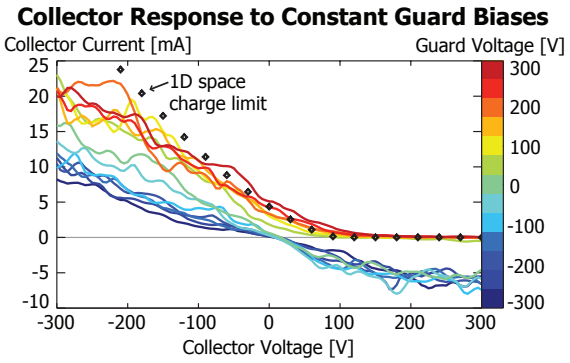

Figure 95: Horizontal lineout of ISP Collector current at constant Guard biases from fig. 94. Top panel is with linear current scale, bottom panel logarithmic. Overlaid dots are of 1D space charge limited current with probe geometry

regions of net ion collection are blue. The small-scale features are due to plasma fluctuations. Parameters for the measurements in these figures were: deuterium plasma with $n = 1.5 \times 10^{19}\,m^{-3}$, $T_e = 15\,eV$, $B = 5\,T$.

Since the C-Mod ISP in its current configuration is space charge limited, the plasma potential is no longer at the transition from saturated ion current to exponential decay, but near the knee where the current decays to zero [36, 37]. From fig. 94 a few features are immediately evident. The floating potential of the Guard, seen as the white line cutting horizontally across the right plot, is insensitive to the bias of the Collector. The operation of the Collector depends strongly on whether the Guard is biased above or below its floating potential. When the Guard is biased below its floating potential, the Collector can collect net electrons. When the Guard is biased above its floating potential, the Collector collects only net ions.

Taking lineouts of fig. 94 allows for more clear and quantitative comparison of various bias arrangements. First taking lineouts of the Collector current at constant Guard bias (horizontal lines on fig. 94) we have fig. 95. At Guard biases above its floating potential the Collector current has relatively the same shape, following nearly that of the Child-Langmuir 1D limit. However, the magnitude of these curves does tend to increase with increasing Guard bias. This may be because as the Guard is biased more positive, it collecting more electrons. It may be pulling the electrons down to regions near enough to the Collector to negate part of the ion space charge there, allowing more ions to flow to the Collector.

When the Guard is biased below its floating potential the current to the Collector changes significantly, now it can collect net electrons. For negative Collector bias it retains essentially the same slope as when the Guard is biased above its floating potential (where it was likely space charge limited) but at a reduced current. It retains this nearly linear slope through collection of net electrons to a Collector bias of $\sim 200\,V$. The significance of it being linear is not known, but the resistance is approximately $30\,k\Omega$. Electron collection eventually saturates as the Collector biases above $\sim 200\,V$. These curves are unchanged for any bias of the Guard below $-100\,V$.

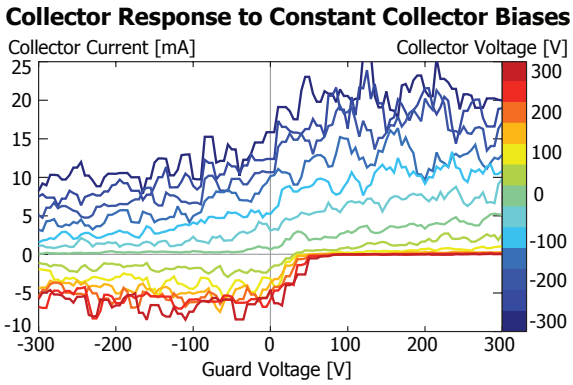

Figure 96: Horizontal lineout of ISP Collector current at constant Collector biases (swept Guard) from fig. 94. The Guard determines whether the Collector can receive electrons or not, only at Guard biases above its floating potential is the Collector guaranteed to not collect electrons.

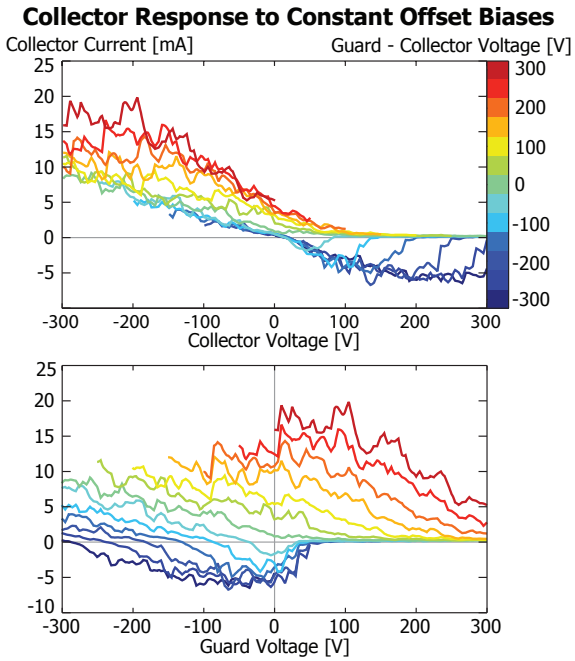

Figure 97: Diagonal lineout of ISP Collector current at constant offset bias between the Collector and Guard from fig. 94. This more closely represents what is done in practice in experiment. Top two panels are plotted against the Collector voltage; bottom is plotted against the Guard voltage.

The Guard controls whether the Collector receives electrons or not. At Guard biases above its floating potential it drains electrons from the surrounding plasma, effectively shorting out any equipotential surfaces from connecting to the Collector. At biases below its floating potential the Guard no longer shorts out the electrons and the equipotential surfaces from the plasma may connect to the Collector, allowing it to collect net electrons.

Moving on to consider lineouts at constant Collector bias (vertical lines on fig. 94) we have fig. 96. For Guard biases above its floating potential and strongly negative Collector bias ($< -100\,\mathrm{V}$) the Collector current is generally constant for a given negative Guard bias. When the Collector is biased positively (approximately above the Guard floating potential) it collects net electrons. The location of the electron knee is not uniquely determined but dependent on the bias. It becomes more well-defined and moves to higher potential as the Collector voltage increases.

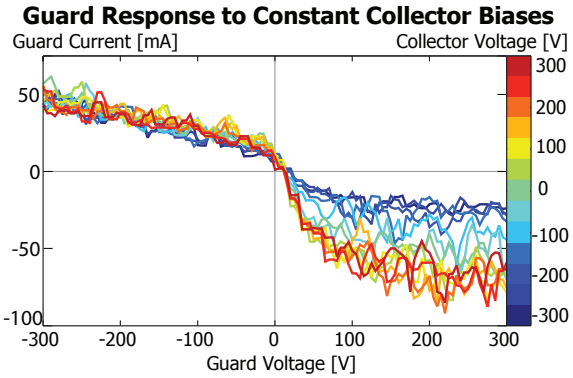

Figure 98: Vertical lineout of ISP Guard current at constant Collector biases from fig. 94. The floating potential from the Guard is unchanged by the Collector bias as is its ion "saturation" region. However strong negative biasing of the Collector does reduce the electron flux to the Guard.

Moving on to the more typical ISP bias arrangement of sweeping the Collector and Guard together but with a fixed offset we have fig. 97 (diagonal lines with slope $1\,\mathrm{V\,V^{-1}}$ on fig. 94). This figure is plotted against both the Collector and Guard voltage. The standard practice is to bias the Collector with just enough voltage above the Guard to ensure no regions of net electrons collected (i. e., a diagonal line with slope $1\,\mathrm{V\,V^{-1}}$ that does not pass through the red region on fig. 94); which typically ends up being a few volts. From this figure it is quite clear that the resulting curve not only depends on the magnitude of the bias difference, but which electrode voltage the data is plotted against. If plotted against the Collector voltage the location of the ion-side knee is broad and increases with increased bias difference. If plotted against the Guard voltage the location of the electron-knee shifts to higher voltages as the bias difference is increased. The electron knee is better defined than the ion knee.

We may also examine how the Collector affects the Guard current, fig. 98 (made from vertical lineouts of the right panel in fig. 94). The Guard floating potential remains unchanged for all Collector voltages. The net ion current collected as Guard biases below its floating potential also remain unchanged for all Collector biases. Only when the Guard is biased positively, collecting net electrons, does the Collector bias change the Guard current. As the Collector voltage sweeps from $\sim 0\,\mathrm{V}$ to $-150\,\mathrm{V}$ the Guard electron current is reduce by $\sim 2/3$. It is not yet understood why the current changes in this way. In this region it may be expected that as the Collector sweeps negative it would reject electrons and pull in ions. If it were pushing electrons to and pulling ions away from the Guard the trend would be the opposite of what is seen, The Guard current decrease with the decreasing Collector bias.

Although these trends are seen for the space charge limited C-Mod ISP, they may not hold true for an ISP below the space charge limit. It remains to be seen whether the Guard truly does just determine whether or not the electrons can reach the Collector or if it influence the ion current as well. Repeating this exercise of sweeping out all biases between the Guard and Collector should be illuminating to the operation of an ISP below the space charge limit.

7.4 ION COLLECTION EXCEEDING 1D SPACE CHARGE LIMITS

While the C-Mod ISP was found to collect ion current at a level quantitatively consistent with the Child-Langmuir space charge limit, other ISPs have exceeded it. This may be due to two reasons:

1. 2D effects: As the aspect ratio of the probe decreases (deeper recess and/or smaller collector diameter) the magnitude of the peak space charge potential in the probe volume decreases. Also, since the space charge in the region around the perimeter of the probe volume must necessarily be small (to satisfy the boundary condition set by the Guard potential there), ion current can freely flow to the Collector in this region.

2. Departure from perfect magnetic shielding of the electrons: The simple picture of how the Guard shields electrons from the probe volume is not complete. It has been demonstrated through experiments [25, 28, 48] and simulations [18, 30] that electrons can $\vec{E} \times \vec{B}$ drift along equipotential surfaces that dip down into the probe volume. If equipotential surfaces dip down into the probe volume close to the Collector, this effectively decreases the distance that the ions must travel through the space charge zone, increasing the space charge limited current.

7.4.1 *2D Extension of Space Charge Limit*

The reduced space charge potential at the edges of a 2D beam can allow "wings" of current, exceeding the traditional 1D limit. Although it is not solvable analytically like the 1D space charge limit, physical insight into the 2D problem has been gained through simulations. 2D space charge was modeled in Ref. [50] in which electrons were emitted between finite parallel plates of width w and separation d. An infinitely strong magnetic field confined the electrons to move only in the direction between the plates. It was found that the current traversing the plates, normalized to the 1D limit, was well described for $0.1 < w/d < 30$ by:

$$\frac{I}{I_{SC}} = 1 + 0.23\frac{d}{w} - 0.0067\left(\frac{d}{w}\right)^2. \tag{64}$$

For the C-Mod ISP with an aspect ratio of $w/d = 12$ the additional current ratio due to 2D effects as given by eq. (64) is 1.02. This increase is below what can be detected experimentally. In the other extreme of aspect ratio is an ISP from LHD [19] with an aspect ratio of 0.5, which results in an increase of 1.4 above the 1D limit. The LHD ISP displayed clear signs of space charge limited current: the current increased nearly linearly with negative bias and was a factor of ~ 2.3 above the 1D space charge limit. An exceptionally narrow probe with

an aspect ratio of 0.1 could exceed the 1D space charge limit by a factor of ~ 4; however this is nowhere near enough to account for probes that exceed the limit by orders of magnitude.

A 2D space charge distribution has an additional complication: now all the ions arriving on the Collector are no longer retarded by the same potential. Although the lower potential at the boundaries allows more total ion current to the probe, the center potential remains nearly the same as in the 1D limit. Therefore the I-V characteristic remains affected by the space charge potential, except for when the bias of the Collector exceeds the highest potential in the probe volume. Thus while 2D effects allow more ion current to be collected, appearing to circumvent the problem associated with the 1D space charge limit, the effects do not extend the bias range over which a classic, exponential decay, I-V characteristic would be recovered.

7.4.2 $\vec{E} \times \vec{B}$ *Drift of Electrons into the Probe Volume*

What if electrons were not perfectly shadowed by the Guard and able to drift into the probe volume? This would effectively decrease the spacing, d, which strongly influences the 1D space charge limit. If the electrons could dip down to 90 % of the distance to the Collector in the probe volume, then the 1D space charge limit would increase by a factor of 100, enough to account for the discrepancy seen in some experiments. $\vec{E} \times \vec{B}$ drift of electrons into the probe volume but not to the Collector was seen in PIC simulations [18, 30] (also see figs. 12 and 13); although the space charge potential was likely not dominating for both simulations ($n \approx 10^{18}\,m^{-3}$). The degree to which the electrons may travel into the probe volume is likely controlled by how fast they travel along field lines (i. e., their thermal velocity, $v_{th} = \sqrt{2k_B T_e/m_e}$) compared to how fast they $\vec{E} \times \vec{B}$ drift into the probe volume.

The $\vec{E} \times \vec{B}$ velocity is determined by the strength of the electric field within the probe and the external magnetic field. The electric field is set up by the self-consistent profiles of electrons and ions within the probe volume—a complicated problem beyond the scope of this work. However, a reasonable estimate may be that the electric field at the probe entrance is on order that of a uniform charge distribution of ions within the probe volume: $|E| \approx end/2\epsilon_o$). Thus the $\vec{E} \times \vec{B}$ drift velocity can be estimated as $v_{\vec{E}\times\vec{B}} \approx end/2\epsilon_o B$. The ratio of the $\vec{E} \times \vec{B}$ velocity to the thermal velocity is:

$$\frac{v_{\vec{E}\times\vec{B}}}{v_{th}} \approx \sqrt{\frac{m_e}{2k_B T_e}} \frac{end}{2\epsilon_o B}. \tag{65}$$

It is valid to assume that the electrons $\vec{E} \times \vec{B}$ drift: by design, the electron Larmor radius ρ_e is smaller than the probe recess ($\rho_e < d$).

Table 5: Parameters used to estimate the ratio electron $\vec{E} \times \vec{B}$ to thermal velocities for the ISP probes listed in table 4. "Ratio" is the factor by which the ISP appears to exceed the 1D Child-Langmuir Law. ISPs that exhibit a large ion collection current relative to the 1D space charge limit (first column) tend to have large $\vec{E} \times \vec{B}$ to thermal velocity ratios (last column).

Experiment	ratio	$n[m^{-3}]$	$T_e[eV]$	$B[T]$	$v_{\vec{E}\times\vec{B}}[m\,\mu s^{-1}]$	$v_{th}[m\,\mu s^{-1}]$	$\frac{v_{\vec{E}\times\vec{B}}}{v_{th}}$
NAGDIS-II [41]	1000	6×10^{18}	4	0.1	542.0	1.19	457.0
DIONISOS [48]	262	1.2×10^{18}	22	0.04	1360	2.78	487
DIONISOS [36]	102	1×10^{18}	15	0.04	1130	2.30	492
TBR-1 [14]	25.0	1×10^{18}	12	0.4	15.8	2.05	7.70
TBR-1 [15]	11.1	1×10^{18}	25	0.4	11.3	2.96	3.81
TPD [28]	7.93	2.5×10^{17}	4.7	0.4	1.69	1.29	1.32
MPX [23]	4.35	2×10^{15}	2	0.035	1.15	0.839	1.85
LHD [19]	3.97	3×10^{18}	8	3	9.04	1.68	5.39
C-Mod [12]	1.03	1.5×10^{19}	50	5	6.78	4.19	1.62

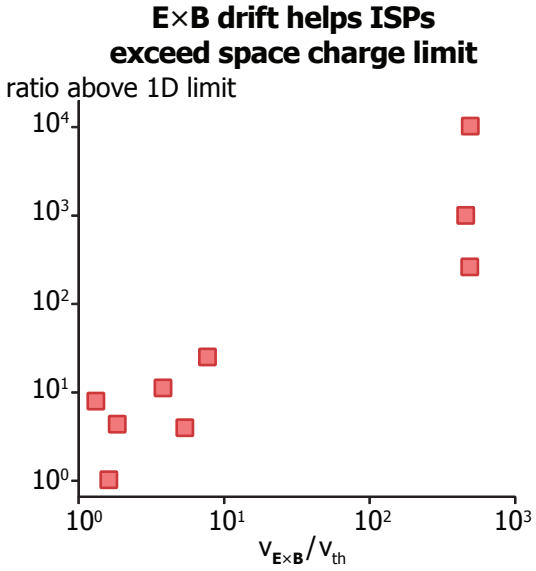

Figure 99: ISP probes tend to greatly exceed the apparent 1D space charge limit when the $\vec{E} \times \vec{B}$ electron drift velocity exceeds the electron thermal velocity. This is consistent with electrons drifting into the probe volume, neutralizing the ion space charge and decreasing the effective recess distance, d, of the Collector. Data is taken from tables 4 and 5. Since the data in this figure and those tables is taken from characteristic values in published papers, there is considerable uncertainty (at least a factor of 2) in relating the parameters to each other. Thus the data should not be taken as strict points but as more of a cloud which follows this trend.

Thus ρ_e is smaller than the characteristic scale of the potential in the probe and the electrons will $\vec{E} \times \vec{B}$ drift within the volume.

Table 5 shows estimates of the electron $\vec{E} \times \vec{B}$ to thermal velocities from eq. (65) for the ISP probes listed in table 4. Local plasma conditions used for this estimate are also shown. A comparison of the ratio of current above the 1D limit (table 5, first column) to the velocity ratio (table 5, last column) is presented in fig. 99. It is clear that the probes which greatly exceed the 1D space charge limit also had a high velocity ratio: the electrons could easily drift into the probe volume and reduce the space charge. On the other hand, probes close to the 1D space charge limit had a thermal velocity exceeding the $\vec{E} \times \vec{B}$ drift velocities, i.e., with electrons tending to follow the field lines and not straying too far into the probe volume.

Note that the velocity ratio depends on n/B. The density dependence may be seen in fig. 90, where at the highest densities (deepest part of the scan and highest V_p) the experimental I-V appears to exceed the 1D limit by a small factor. The strength of the magnetic field can determine whether the electrons can drift into the probe volume. In a strong magnetic field like that in Alcator C-Mod ($B \approx 5\,T$), the electrons are held tight to the magnetic field, barely drifting down into the probe volume and the 1D space charge limit is a good approximation. On the other hand in DIONISOS, with a comparably weak magnetic field ($B \approx 0.04\,T$), the ISP can easily exceed the apparent 1D space charge limit by a factor of 100 or more. However, as with the 2D effects, the fact that the ISP collects current above the 1D limit does not mean that the I-V characteristic can be interpreted as being that of a classic, exponential decay; T_i values fitted using this assumption must be treated with caution.

7.5 1D KINETIC SIMULATIONS

Now that we feel that we understand the C-Mod ISP measurements and how other ISPs exceeded the 1D space charge limit, we wish to explore the operational space of an ISP as a T_i diagnostic, i. e., define the plasma conditions under which an ISP can be successfully used to measure ion temperatures.

Even if an ISP is nominally space charge limited, at sufficiently high bias the I-V characteristic should regain an exponential decay. This is because the space charge potential has a finite value. There will be a potential at which the Collector once again becomes the highest in the system and controls the particle collection. Additionally, for a Maxwellian energy distribution, the exponential tail of the I-V should extend to essentially infinite voltage, although with an exponentially decreasing current. Thus, a space charge limited ISP can, in principle, measure the ion temperature. However the technical challenge is to

build a system that can bias to sufficiently high voltage while also measuring very low ion current.

Although, relying on only the high-energy tail of ions may give misleading results. The sensitivity of Langmuir probe measurements to a small population of high-energy electrons has been well established [46]. Only the high energy ions make it past the space charge potential and using this technique would render the ISP sensitive to deviations from a single-temperature Maxwellian distribution.

To study this problem, we have constructed a 1D kinetic numerical simulation of probe particle collection in the presence of space charge. Through these simulations we seek to learn:

1. What does an I-V characteristic look like when only moderate space charge effects are present and what impact does it have on our interpretation?

2. When the probe is in the space charge limited regime, what is the minimum bias needed to regain the exponential decay of the I-V characteristic for a given density and temperature?

While the model is designed to simulate ion flow through the electron-free region of the ion sensitive probe, the results obtained here are applicable to other problems of interest. In particular, they may be used for the electron-free region of a retarding field analyzer or other ion collecting probes. For instance, the space charge rounding of the knee of an RFA I-V characteristic, as was seen in Ref. [35], where issues of space charge limited current were considered in depth.

7.5.1 *Simulation Setup*

For these simulations we use the commercial Finite Element Method (FEM) program COMSOL [13]. For this problem we consider the probe volume to be free of electrons. It is simplified to one dimension in both space and velocity. We assume that the ions are collisionless within the probe volume. For $T_i = 100\,\mathrm{eV}$ and $n = 10^{19}\,\mathrm{m}^{-3}$ the mean time between deuterium ion-ion collisions is:

$$\begin{aligned}\tau_{ii} &\approx 5 \times 10^{10} T_i^{3/2}/n \\ &\approx 5 \times 10^{-6}\,\mathrm{s},\end{aligned} \tag{66}$$

and the time for an ion to cross the probe is:

$$\begin{aligned}\tau_p &\approx d/\sqrt{k_B T_i/m_i} \\ &\approx 4 \times 10^{-9}\,\mathrm{s}.\end{aligned} \tag{67}$$

Ions are injected from the plasma side of the domain with a half-Maxwellian distribution. Their motion within the domain is controlled both by their space charge potential and the potential applied to the

Collector, which fully absorbs all incident ions. The flux to the Collector is compared to the incident flux as a function of bias on the collector, yielding I-V characteristics that span the full operation of an ISP, from classic exponential I-V to space-charge limited I-V.

The self-consistent motion of ions within their space charge is described by the Vlasov-Poisson system of equations:

$$v_y \frac{\partial w}{\partial y} + \frac{F}{m} \frac{\partial w}{\partial v_y} = 0, \tag{68}$$

$$\frac{\partial^2 V}{\partial y^2} = -\frac{Ze}{\epsilon_o} n, \tag{69}$$

$$n = \int_{-\infty}^{\infty} w \, dv_y, \tag{70}$$

$$F = -Ze \frac{\partial V}{\partial y}, \tag{71}$$

with m the particle mass, F the force on the particles, Ze the charge, ϵ_o the permittivity of free space, w the 1D velocity distribution function, n the density, y the spatially dependent variable (direction parallel to Collector surface normal), and v_y the velocity.

To make the analysis simpler and the solutions general, we normalize the equations as follows. Thermal velocity is defined as:

$$v_t = \sqrt{\frac{2k_B T}{m}}. \tag{72}$$

To normalize the Poisson equation, we consider the potential that results due to a uniform 1D charge distribution (n_o) between grounded planes located at $y = 0$ and $y = d$:

$$V = \frac{Zen_o}{2\epsilon_o} y \left(d - y\right). \tag{73}$$

The maximum potential, given at $y = d/2$, is used as a normalization parameter:

$$V_{max} = \frac{Zen_o d^2}{8\epsilon_o}. \tag{74}$$

The normalized variables for position, velocity, and potential are:

$$\begin{aligned} y' &= \frac{y}{d}, \\ v' &= \frac{v}{v_t}, \\ V' &= \frac{e}{k_B T} V. \end{aligned} \tag{75}$$

Where d is the system length. Removing the primes for clarity, we have the normalized equations:

$$v_y \frac{\partial w}{\partial y} - \frac{Z}{2} \frac{\partial V}{\partial y} \frac{\partial w}{\partial v_y} = 0, \tag{76}$$

$$\frac{\partial^2 V}{\partial y^2} = \frac{8 e V_{max}}{k_B T} \int_{v_{y,min}}^{v_{y,max}} w \, dv_y. \tag{77}$$

With $v_{y,min}$ and $v_{y,max}$ the minimum and maximum normalized velocities in the domain, here set to ± 10.

The boundary conditions on the distribution function are as follows. A forward-going half-Maxwellian from the left boundary (the plasma):

$$w(0, v_y) = \frac{n_o}{v_t} \sqrt{\frac{1}{\pi}} e^{-v_y^2} \quad v_y > 0. \tag{78}$$

No backward-going particles originate from the right boundary:

$$w(1, v_y) = 0 \; v_y < 0. \tag{79}$$

The distribution function is forced to zero at the velocity extremes:

$$w(y, v_{y,min}) = (y, v_{y,max}) = 0. \tag{80}$$

The normalized boundary conditions on the potential are:

$$V(0) = 0, \tag{81}$$

$$V(1) = V_{bias}, \tag{82}$$

with V_{bias} the probe bias voltage normalized to temperature.

Equations (76) and (77) are numerically unstable when solved with the FEM [42]. That is, there are spikes in the distribution function near large gradients. Fortunately a very similar simulation has been already been implemented in COMSOL [51] (beware of typos in the original work). In that work, electrons moved between two charged plates and had Brownian collisions with a background fluid. This

situation can be modeled by Kramer's equation [43], which is very similar to eq. (76):

$$v_y \frac{\partial w}{\partial y} + \frac{F}{m}\frac{\partial w}{\partial v_y} = \nu \left(w + v_y \frac{\partial w}{\partial v_y} + \frac{k_B T_f}{m}\frac{\partial^2 w}{\partial v_y^2} \right). \tag{83}$$

Where ν is the collision frequency and T_f is the temperature of the background fluid. Given a large enough collision frequency, any distribution will damp to the background temperature. We can also make use of the collision terms to damp numerical instabilities by setting it small enough to not disturb the initial distribution. For convenience we take the ion temperature to be equal to the background fluid temperature ($T = T_f$), producing the normalized equation:

$$v_y \frac{\partial w}{\partial y} - \frac{Z}{2}\frac{\partial V}{\partial y}\frac{\partial w}{\partial v_y} = \gamma \left(w + v_y \frac{\partial w}{\partial v_y} + \frac{\partial^2 w}{\partial v_y^2} \right). \tag{84}$$

With γ an effective damping constant given by:

$$\gamma = \frac{\nu d}{v_t}. \tag{85}$$

To find the minimum damping factor needed to obtain a stable numerical solution, a top-hat distribution ($w(0, v_y) = 1, 1 < v_y < 2$ and $w(0, v_y) = 0$, otherwise) was released into the simulation domain. The damping factor was increased until the numerical instabilities were smoothed out, yet the top-hat distribution remained unchanged as it traversed the simulation domain. This minimum normalized damping value was found to be $\gamma = 10^{-3}$.

To solve these equations we make use of the "double-dogleg" solver in COMSOL, which is optimized for nonlinear problems, and implement an adaptive mesh that improves resolution in areas of large gradients in the distribution. The simulation is solved on two finite element domains. The modified Vlasov equation is solved on a 2D domain of space y and velocity v_y. The Poisson equation is solved on a 1D domain of space y. The distribution function is integrated over velocity space to make the density available to the Poisson equation. The potential is projected over velocity to make it available to the modified Vlasov equation.

To simulate the sweeping of the probe bias and fully resolve the exponential decay of the I-V characteristic, we step through values of eV_{bias}/k_BT from -4 to 4. To simulate a variation in density for a given probe geometry, eV_{max}/k_BT is stepped from 0.03 to 30 for each probe bias sweep. The results of these scans are shown in fig. 100. Below $eV_{max}/k_BT = 0.03$ the space charge potential is small and irrelevant. Above $eV_{max}/k_BT = 30$ the space charge dominates the potential and the exponential decay is all but gone.

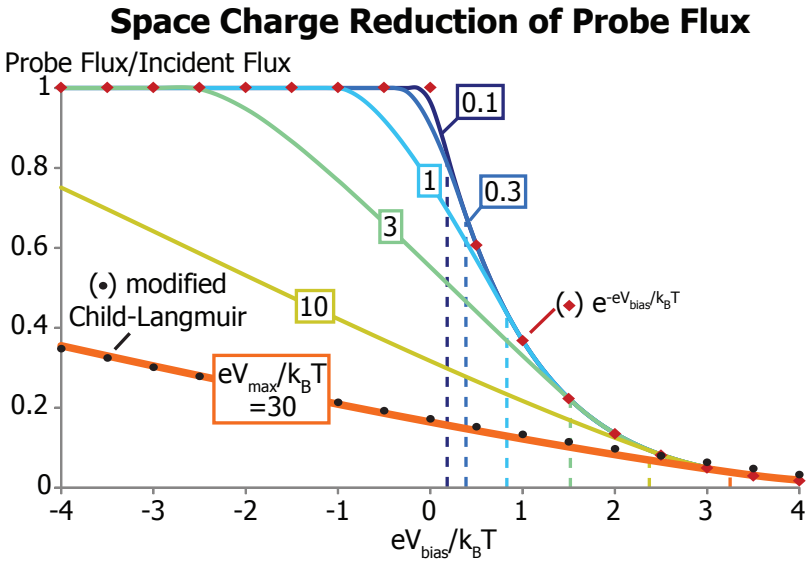

Figure 100: Results of a 1D kinetic simulation of space charge limited probe collection. The exponential decay (red diamonds) is the limit of no space charge. Child-Langmuir space charge limited current with modifications for finite temperature is also shown (black circles). Colored lines are the result of the simulation, indicating severe rounding of the I-V as the space charge potential increase relative to the plasma temperature. Vertical dashed lines indicate a "critical" voltage bias, i. e., a bias voltage above which the I-V characteristic remains within 5 % of the ideal exponential response

In order to verify that our numerical procedure is quantitatively accurate, simulations for both the low and high space charge limits are checked against known solutions (see diamonds and circles in fig. 100). At very low space charge the simulated current matches the ISP exponential decay, eq. (61). At very high space charge we compare it to the Child-Langmuir Law adjusted for finite temperature, eq. (43). To compare eq. (43) to the simulation, it must be normalized to the Maxwellian flux incident into the probe domain. Normalizing to V_{max} we find:

$$\frac{I_{SC}}{I_{incident}} = \frac{\sqrt{\pi}}{9} \frac{\left(\frac{eV_{bias}}{k_B T}\right)^{\frac{3}{2}}}{\frac{eV_{max}}{k_B T}} \tag{86}$$

This current ratio is plotted for the case of $eV_{max}/k_B T = 30$ in fig. 100. We find good agreement between the numerical simulation and the analytic formula in this space charge dominant limit.

7.5.2 *Implications for T_i Measurements with the C-Mod ISP*

From the graphs of normalized probe flux, we can find a critical voltage ($eV_{crit}/k_B T$) above which the probe must be biased to sweep out the portion of the I-V characteristic that remains within 5 % of the ideal exponential response. In practice the I-V characteristic must be sampled over a voltage range of one or two $k_B T_i/e$ in order to fit the

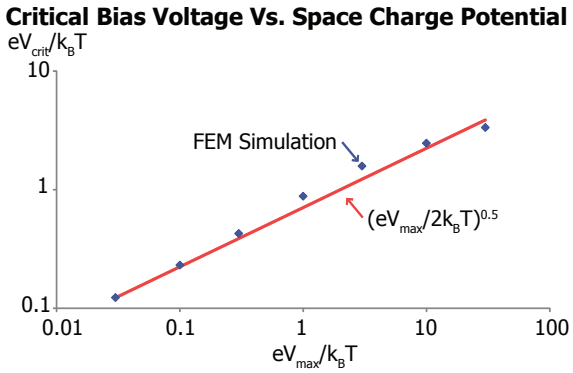

Figure 101: Normalized critical bias voltages from fig. 100 are plotted versus space charge potential. Critical bias is the voltage where the I-V departs from the classic exponential decay by 5 %, i. e., it is the minimum critical bias (V_{crit}) needed to sweep out at least a part of the exponential decay. Overlaid is an analytic fit to the simulation data. This is used in fig. 102 to quantify the minimum bias for the C-Mod ISP in terms of plasma parameters.

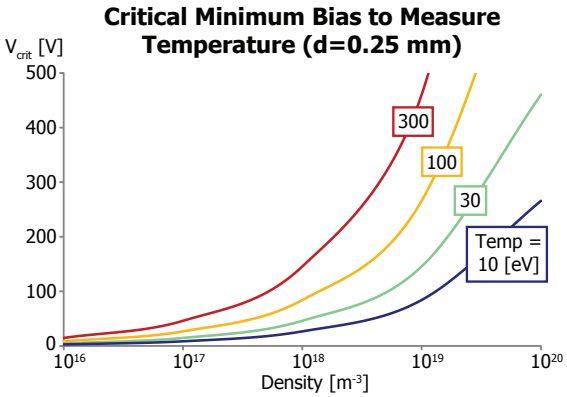

Figure 102: Minimum critical bias, from eq. (87), needed to sweep out the exponential part of the I-V for the C-Mod ISP. The present C-Mod ISP system is unable to access the primary region of interest ($T_i \approx 100\,eV$, $n > 10^{19}\,m^{-3}$).

exponential decay. This critical voltage is shown as dashed lines on fig. 100 and plotted versus V_{max} in fig. 101. We find the following analytic relation to be a reasonable fit to the simulation results:

$$\frac{eV_{crit}}{k_B T} = \sqrt{\frac{1}{2}\frac{eV_{max}}{k_B T}}. \tag{87}$$

This critical bias is the worst-case voltage. If electrons were able to drift into the probe volume V_{crit} would be reduced. However a problem this complicated is outside the scope of this work.

From eqs. (74) and (87), we can recast the critical bias voltage in terms of plasma density and ion temperature:

$$V_{crit} = \frac{d}{4}\sqrt{\frac{n k_B T}{\epsilon_o}} \tag{88}$$

Figure 102 shows curves of critical bias voltage as a function of density and temperature, using the recess distance of the C-Mod ISP ($d = 0.25\,mm$). The curve labeled 100 eV is the most relevant one for C-Mod boundary plasma conditions, with densities varying from a few $10^{18}\,m^{-3}$ to $10^{20}\,m^{-3}$. It is clear that a significant Collector bias is required to recover an exponential decay. The bias must be swept past 200 V at the low densities and well over 500 V for the high densities near the separatrix.

This is not good news for recovering T_i from the present C-Mod ISP data. Although, as now set up, our system can sweep to 400 V, the critical bias at our densities corresponds about 3 to 4 times the e-

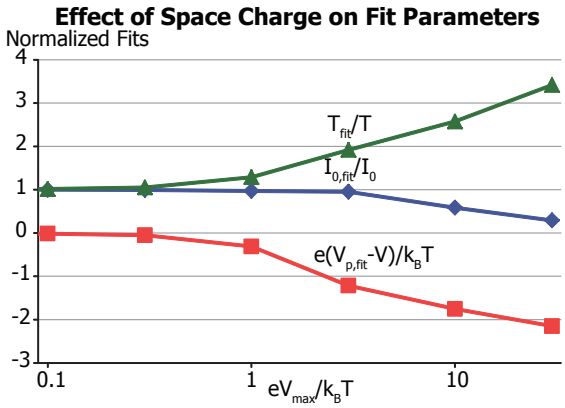

Figure 103: Result of fitting an exponential decay (eq. (61)) to the simulation data of fig. 100 with varying amounts of space charge. The voltage bias of the exponential fit is restricted to $-3 < eV_{bias}/k_BT < 3$. As the relative space charge is increased, the the ratio of the fitted temperature to the actual temperature increases (green triangles), the ratio of the fitted ion saturation current to the actual ion saturation current decreases (blue diamonds), and the shift of the fitted plasma potential relative to the actual plasma potential decreases (red squares, normalized to the actual temperature).

folding voltage. In addition, the voltage must be swept much higher than this critical bias to sweep out a portion of the I-V characteristic with enough data to fit an exponential decay length. The challenge is that the collected ion current is very low in this regime and that the plasma typically exhibits large amplitude (order unity) fluctuations in plasma density. At the present time, the dynamic range of the ISP current sensing electronics is too low to resolve an exponential decay in this region of high bias.

7.5.3 *Effect of Space Charge on Fitting Parameters*

As shown in fig. 88, the plasma fluctuations make the experimentally measured I-V depart from the simple analytic fit. This presents a challenge to the experimentalist in discerning where the space charge limited current region ends and the exponential decay begins. For instance, looking at the curve labeled $eV_{max}/k_BT = 1$ in fig. 100, the difference between the space charge affected curve and the pure exponential decay are minor, and would be nearly imperceptible to the human eye (or software fitting algorithms) when plasma fluctuations, such as those in fig. 88, are superimposed.

The effect of fitting an exponential decay (eq. (61)) to marginally space charge limited I-V characteristics is shown in fig. 103. Here we limit the fitting range to $-3 < eV_{bias}/k_BT < 3$ to more closely represent the typical bias range of the C-Mod ISP. It is assumed that the fitting program is unaware of the break between space charge limited and exponential; thus it fits over this entire range. In the limit of very low space charge ($eV_{max}/k_BT < 1$) the fitting parameters are relatively unaffected. At even slight space charge ($eV_{max}/k_BT = 1$) the fitted temperature is already 40 % higher than the actual ion temperature.

When the probe is strongly space charge limited ($eV_{max}/k_BT > 10$), not only is the fitted temperature much higher than it should be ($> 2\times$) but the fitted plasma potential is very low: $\sim -2k_BT/e$ below the actual V_p. This may be used as a simple check on whether space

charge is affecting the probe, especially when the probe departs from the 1D space charge limit (due to geometry or electrons $\vec{E} \times \vec{B}$ drifting into the probe volume) or when there are no other checks on the ion temperature: if the fitted V_p is much lower than what is expected, it is very likely that the probe is space charge limited.

There are only two ways around the problem of fluctuations obscuring the transition from space charge limited to exponential decay: 1) sweep the bias much faster than the plasma fluctuations such that they are fully resolved or 2) sweep slowly enough to average over the fluctuations. In a high power-density tokamak like C-Mod these both present challenges. The first method is ideal because all of the physics of the turbulence in the fluctuations remains. However it is extremely challenging to switch the voltage this fast ($\sim 1\,\mu s$) and measure the low currents at voltages above V_{crit}. Sweeping slowly also presents challenges. In order to tolerate the intense heat flux of experimental fusion plasma, the probe must move quickly through the plasma ($\sim 1\,m\,s^{-1}$) [12]. But this requires the probe bias to be swept fast enough to resolve the spatial variation in the plasma conditions. Thus it is unlikely that a probe can be swept both fast enough to resolve spatial changes in T_i while also sweeping slowly enough to average over the temporal fluctuations.

7.6 WHAT DOES IT TAKE TO MAKE SUCCESSFUL T_i MEASUREMENTS WITH AN ISP?

Given that space charge effects become important for probes in high density plasma and high magnetic field (due to the arrest of electrons from $\vec{E} \times \vec{B}$ drifting into the probe volume), what does it take to make successful ion temperature measurements with an ISP? We have shown that a low aspect ratio probe (deep and narrow) will allow it to exceed the 1D space charge limit, but it is unlikely that this will improve the minimum bias necessary to overcome the space charge potential. Operating in a weak magnetic field (not a choice for tokamaks) causes electrons to have a much stronger $\vec{E} \times \vec{B}$ drift velocity. This allows them to enter into the probe volume, neutralize the ion space charge, and allow ion current collection that may be hundreds of times larger than the 1D space charge limit. However, just because the probe can operate above the 1D limit does not guarantee that the I-V is representative of the ion energy distribution.

Ideally there would be an independent check on the ISP measurement, preferably from another well accepted technique, such as an RFA or spectroscopy. At the very least, when space charge is likely, the probe should be swept at sufficiently high bias to regain the exponential portion of the I-V. Although this technique should be treated with caution, as it would be very sensitive to a small population of hot ions.Exceeding the space charge affected bias region by at least 2 tem-

perature e-foldings would increase confidence in the fitted temperature. Based on our kinetic simulations, this would require sweeping well past 500 V for densities above $10^{19}\,m^{-3}$ with the present C-Mod ISP.

The strongest tool for increasing the space charge current limit is the recess distance of the Collector. However it cannot be made arbitrarily small. It must be greater than the electron Larmor radius to prevent direct electron collection ($\sim$ 0.01 mm for the C-Mod boundary). In practice this distance must be greater to prevent electron collection via misalignments in the probe with respect to the magnetic field and variation of the magnetic field direction as the probe is scanning in the plasma.

It is possible that the diameter of the C-Mod ISP geometry could be reduced to accommodate smaller recess distances. We found that setting $d = 0.10$ mm with the present geometry led to net electron current on the Collector, despite it being biased at voltages below the Guard—the bias arrangement necessary to prevent $\vec{E} \times \vec{B}$ collection of electrons by the Collector. This may be due to misalignments within the probe drive system, allowing direct collection of electrons flowing along magnetic field lines. Increasing the distance to $d = 0.25$ mm eliminated electron current. The ratio of the present probe diameter (3 mm) to recess height (0.25 mm) allows a 4.8° misalignment; for $d = 0.10$ mm the alignment tolerance drops to 1.9°. On the other hand, a probe with a much smaller diameter would allow for a smaller recess height while maintaining the same robustness against misalignments. Decreasing the probe diameter to 0.6 mm would allow the recess height to be reduced to 0.05 mm (close to the limit of the electron Larmor radius). The factor of 5 decrease in d would decrease the critical bias potential by a factor of 5 (eq. (88)), perhaps putting high density ($n > 10^{19}\,m^{-3}$) T_i measurements within reach.

One could envision an improved ISP with a grid over the Guard, such as in Refs. [7, 23, 32, 39]. Keeping the Guard at a very strong negative voltage would serve three purposes: 1) it would reject plasma electrons from getting to the Collector and would return secondary electrons back to the Collector (it wouldn't prevent secondary electrons from the grid getting to the Collector); 2) it would be in ion saturation, thus giving a measurement of density fluctuations to which the Collector current could be normalized (although it must be shown that the Collector sweeping behind it, rejecting ions, does not change the current to the Guard); and most importantly, (3) it may allow the probe to operate at densities much higher than would be allowed if it was used without the grid. This would be accomplished in two ways. First it would serve to reduce the free flux of ions due to the finite transparency of the grid. The ions would be turned into beamlets the size of the grid holes. Secondly, it would serve to reduce the relative peak of the space charge potential. Pulling down the potential at the

grid can negate the space charge potential, much like sweeping the probe to high enough voltages such that it can eventually overcome the space charge potential. This is a technique used in RFAs [33]. This cannot be done with a gridless ISP because biasing the Guard below the Collector allows the electrons to $\vec{E} \times \vec{B}$ drift onto the Collector. However, the most important design consideration with respect to the grid is that it must able to handle the extreme heat flux and not limit the probe's operation. ⋆

BIBLIOGRAPHY

[1] J. Adámek, J. Horacek, H. W. Müller, R. Schrittwieser, M. Tichy, A. H. Nielsen, and The ASDEX-U Team. Fast ion temperature measurements using ball-pen probes in the SOL of ASDEX Upgrade during L-mode. In *38th EPS Conference on Plasma Physics*, 2011.

[2] J. Adámek, M. Kočan, R. Pánek, J. P. Gunn, E. Martines, J. Stöckel, C. Ionita, G. Popa, C. Costin, J. Brotánková, R. Schrittwieser, and G. Van Oost. Simultaneous measurements of ion temperature by segmented tunnel and Katsumata probe. *Contributions to Plasma Physics*, 48(5):395–399, 2008.

[3] J. Adámek, M. Peterka, T. Gyergyek, P. Kudrna, M. Ramisch, U. Stroth, J. Cavalier, and M. Tichỳ. Application of the ball-pen probe in two low-temperature magnetised plasma devices and in torsatron TJ-K. *Contributions to Plasma Physics*, 53(1):39–44, 2013.

[4] J. Adámek, V. Rohde, H. W. Müller, A. Herrmann, C. Ionita, R. Schrittwieser, F. Mehlmann, J. Stöckel, J. Horacek, J. Brotánková, and ASDEX Upgrade Team. Direct measurements of the plasma potential in ELMy H-mode plasma with ball-pen probes on ASDEX Upgrade tokamak. *Journal of Nuclear Materials*, 390-391:1114 – 1117, 2009.

[5] J. Adámek, J. Stöckel, I. Duran, M. Hron, R. Panek, M. Tichy, R. Schrittwieser, C. Ionita, P. Balan, E. Martines, and G. Van Oost. Comparative measurements of the plasma potential with the ball-pen and emissive probes on the CASTOR tokamak. *Czechoslovak Journal of Physics*, 55:235–242, 2005.

[6] J. Adámek, J. Stöckel, M. Hron, J. Ryszawy, M. Tichy, R. Schrittwieser, C. Ionita, P. Balan, E. Martines, and G. Oost. A novel approach to direct measurement of the plasma potential. *Czechoslovak Journal of Physics*, 54:C95–C99, 2004.

[7] W. E. Amatucci, D. N. Walker, G. Ganguli, D. Duncan, J. A. Antoniades, J. H. Bowles, V. Gavrishchaka, and M. E. Koepke. Velocity-shear-driven ion-cyclotron waves and associated transverse ion heating. *Journal of Geophysical Research*, 103(A6):11711, 1998.

[8] R. Armstrong, Å. Fredriksen, E. Grønvoll, D. Batani, A. Galassi, and F. Pisani. Measurements of ion temperature in weakly ionized, steady-state plasmas. *Physics Essays*, 10(3):483–491, 1997.

[9] T. Bisong, M. Zhibin, S. Wulin, W. Zhenhui, C. Hong, and W. Jianhua. Measurement of ion parameters by ion sensitive probe in ECR plasma. *Plasma Science and Technology*, 13(1):68, 2011.

[10] G. Böhm, B. Kampmann, and H. Schulüter. Measurements with an ion-sensitive probe in stationary RF-discharges of stellarator configuration. *Physics Letters A*, 70(5):413–415, 1979.

[11] G. Bousselin, J. Cavalier, J. F. Pautex, S. Heuraux, N. Lemoine, and G. Bonhomme. Design and validation of the ball-pen probe for measurements in a low-temperature magnetized plasma. *Review of Scientific Instruments*, 84(1):013505–013505, 2013.

[12] D. Brunner, B. LaBombard, R. Ochoukov, and D. Whyte. Scanning ion sensitive probe for plasma profile measurements in the boundary of the Alcator C-Mod tokamak. *Review of Scientific Instruments*, 84:053507, 2013.

[13] COMSOL Inc. 1 New England Executive Park, Suite 350, Burlington, MA 01803, `www.comsol.com`.

[14] R. P. da Silva and I. C. Nascimento. Simultaneous measurement of ion and electron temperatures in the scrape-off layer of a small tokamak. *Review of Scientific Instruments*, 62(11):2700–2708, 1991.

[15] R. P. da Silva, I. C. Nascimento, Jr. D. F. da Cruz, and A. Hershcovitch. Electrostatic ion probe for tokamak-plasma-edge diagnostic. *Review of Scientific Instruments*, 57(9):2205–2209, 1986.

[16] A. de Cambrier, G. A. Collins, P. A. Duperrex, A. Heym, F. Hofmann, Ch. Hollenstein, B. Joye, R. Keller, A. Lietti, J. B. Lister, F. B. Marcus, J. M. Moret, S. Nowak, A. Pochelon, W. Simm, and S. Veprek. Alfven wave heating on TCA. In *Proccedings of the 4th International Symposium on Heating in Toroidal Plasmas, International School of Plasma Physics and ENEA, Rome, March 21-28*, volume 310, pages 137–152, 1984.

[17] Mohamed El Shaer. *Plasma De Bord Dans un Tokamak Mesures et Simulation Numerique Application au Chauffage Hybride du Plasma de WEGA*. PhD thesis, L'Universite Scientifique et Medicale de Grenoble, June 1981.

[18] N. Ezumi. PIC simulation of the motion of plasma around ion sensitive probes. *Contributions to Plasma Physics*, 41(5):488–493, 2001.

[19] N. Ezumi, S. Masuzaki, N. Ohno, Y. Uesugi, S. Takamura, and LHD Experimental Group. Ion temperature measurement using an ion sensitive probe in the LHD divertor plasma. *Journal of Nuclear Materials*, 313-316:696 – 700, 2003.

[20] N. Ezumi, K. Todoroki, T. Kobayashi, K. Sawada, N. Ohno, M. Kobayashi, S. Masuzaki, and Y. Feng. Particle transport measurements in the LHD stochastic magnetic boundary plasma using Mach probes and ion sensitive probe. *Journal of Nuclear Materials*, 415(1):S430–S432, 2011.

[21] S. Falabella and A. W. Molvik. Ion temperature measurements on TMX-U using a gridless electrostatic analyzer. *Review of Scientific Instruments*, 61(7):1892–1899, 1990.

[22] Ambrogio Fasoli. *Study of Wave-Particle Interaction from the Linear Regime to Dynamical Chaos in a Magnetized Plasma*. PhD thesis, Ecole Polytechnique Federale de Lausanne, 1993.

[23] T-Y. Hsieh, E. Kawamori, and Y. Nishida. Pure ion current collection in ion sensitive probe measurement with a metal mesh guard electrode for evaluation of ion temperature in magnetized plasma. *Review of Scientific Instruments*, 84(2):023502, 2013.

[24] P. Javel, G. Muller, A. v.H. von Oordt, and U. Weber. Wave propagation and RF plasma heating near and above the lower hybrid frequency in the W II A stellarator. In *Proccedings of the 7th European Conference on Controlled Fusion and Plasma Physics*, page 147, 1975.

[25] I. Katsumata. Ion temperature measurements of cesium plasma by ion sensitive probe. *Annual Review of Institute of Plasma Physics Japan*, 76, 1966-1967.

[26] I. Katsumata. Direct measurement of ion temperature by ion sensitive probe. *Annual Review of Institute of Plasma Physics Japan*, 59, 1967-1968.

[27] I. Katsumata. A measurement of $T_{i\perp}$ of Ba plasma in a Q-machine. *Proccedings of 3rd International Conference on Quiescent Plasmas, Elisinore September 20-24*, page 374, 1971.

[28] I. Katsumata. A review of ion sensitive probes. *Contributions to Plasma Physics*, 36(S1):73–79, 1996.

[29] M. Kočan, J. P. Gunn, S. Carpentier-Chouchana, A. Herrmann, A. Kirk, M. Komm, H. W. Müller, J. Y. Pascal, R. A. Pitts, V. Rohde, P. Tamain, and ASDEX Upgrade and Tore Supra Teams. Measurements of ion energies in the tokamak plasma boundary. *Journal of Nuclear Materials*, 415(1):S1133–S1138, 2011.

[30] M. Komm, J. Adámek, R. Dejarnac, J. P. Gunn, and Z. Pekarek. Transport of electrons in the tunnel of an ion sensitive probe. *Plasma Physics and Controlled Fusion*, 53:015005, 2011.

[31] I. Langmuir and K. T. Compton. Electrical discharges in gases Part II. Fundamental phenomena in electrical discharges. *Review of Modern Physics*, 3:191–257, Apr 1931.

[32] M. J. McCarrick, R. F. Ellis, M. Koepke, and R. P. Majeski. Perpendicular ion energy analyzer for hot-ion plasmas. *Review of Scientific Instruments*, 56(7):1463–1464, 1985.

[33] A.W. Molvik. Large acceptance angle retarding-potential analyzers. *Review of Scientific Instruments*, 52(5):704–711, 1981.

[34] R. W. Motley and T. Kawabe. Energy analysis of cesium ions in a Q machine. *Physics of Fluids*, 14:1019, 1971.

[35] Robert Thomas Nachtrieb. *Ion Mass Spectrometry on the Alcator C-Mod tokamak*. PhD thesis, Massachusetts Institute of Technology, 2000.

[36] R. Ochoukov, D. G. Whyte, B. Lipschultz, B. LaBombard, and S. Wukitch. Interpretation and implementation of an ion sensitive probe as a plasma potential diagnostic. *Review of Scientific Instruments*, 81(10):10E111, 2010.

[37] R. Ochoukov, D. G. Whyte, B. Lipschultz, B. LaBombard, and S. Wukitch. Interpretation and implementation of an ion sensitive probe as a plasma potential diagnostic on Alcator C-Mod. *Journal of Nuclear Materials*, 415:S1143–S1146, 2010.

[38] K. Odajima, H. Kimura, H. Maeda, and K. Ohasa. Measurement of ion temperature in scrape-off layer with Katsumata probe. *Japanese Journal of Applied Physics*, 17(7):1281–1282, 1978.

[39] M. Oertl, H. Störi, and R. Hatakeyama. A small electrostatic retarding field energy analyzer with compensating differentiation circuit. *Journal of Applied Physics*, 51(3):1431–1434, 1980.

[40] Y. Ohtsu and N. Wakita. A simple hollow probe for monitoring ion-beam energy in processing plasmas. *Measurement Science and Technology*, 21, 2010.

[41] K. Okazaki, H. Tanaka, N. Ohno, N. Ezumi, Y. Tsuji, and S. Kajita. Measurement of ion and electron temperatures in plasma blobs by using an improved ion sensitive probe system and statistical analysis methods. *Review of Scientific Instruments*, 83(2):023502, 2012.

[42] L. Pichler, A. Masud, and L. A. Bergman. Numerical solution of the Fokker–Planck equation by finite difference and finite element methods—A comparative study. In *Computational Methods in Stochastic Dynamics*, pages 69–85. Springer, 2013.

[43] Hannes Risken. *Fokker-Planck Equation*. Springer, 1989.

[44] R. Schrittwieser, C. Ionita, J. Adamek, J. Stockel, J. Brotankova, E. Martines, G. Popa, C. Costin, L. van de Peppel, and G. van Oost. Direct measurements of the plasma potential by Katsumata-type probes. *Czechoslovak Journal of Physics*, 56, 2006.

[45] T. Sekine, T. Saito, Y. Tatematsu, T. Yasuoka, H. Ikegami, D. Nagai, K. Nozaki, M. Ichimura, H. Higaki, and T. Cho. Ion measurement of the edge plasma in the GAMMA10 tandem mirror device with an ion sensitive probe. *Review of Scientific Instruments*, 75(10):4317–4319, 2004.

[46] P. C. Stangeby. A problem in the interpretation of tokamak Langmuir probes when a fast electron component is present. *Plasma Physics and Controlled Fusion*, 37(9):1031–1037, 1995.

[47] P. C. Stangeby, J. M. Canik, and D. G. Whyte. The relation between upstream density and temperature widths in the scrape-off layer and the power width in an attached divertor. *Nuclear Fusion*, 50:125003, 2010.

[48] R. M. Sullivan, R. Ochoukov, and D. G. Whyte. Internal physics of the ion-sensitive probe. *Journal of Nuclear Materials*, 438:S1253–S1256, 2013.

[49] K. Uehara, A. Tsushima, H. Amemiya, and JFT-2M Group. Direct measurement of ion behavior using modified ion sensitive probe in tokamak boundary plasma. *Journal of the Physics Society of Japan*, 66:921–924, 1997.

[50] J. J. Watrous, J. W. Luginsland, and M. H. Frese. Current and current density of a finite-width, space-charge-limited electron beam in two-dimensional, parallel-plate geometry. *Physics of Plasmas*, 8:4202, 2001.

[51] W. B. J. Zimmerman. *Multiphysics Modeling with Finite Element Methods*. World Scientific, 2006.

8

ASSESSMENT OF ION HEAT TRANSPORT IN THE BOUNDARY

Although there have been systematic measurements of the boundary ion to electron transport ratio, see section 2.3.2, none have been compared to simulations. The goal of this chapter is to use simulations to understand how the experimentally measured upstream ion to electron temperature ratio changes with edge collisionality. Section 8.1 presents profiles of upstream T_i (CXRS) and T_e (Langmuir probe) over a core density scan along with estimates of divertor T_i from sheath heat flux measurements. A 1D fluid model has been constructed to explore these trends, section 8.2. It models electron and ion heat transport including convection, conduction (with flux limits), and electron-ion coupling. Parallel transport in the model is successfully benchmarked against the 2D plasma-neutral fluid code UEDGE, section 8.3. Comparison of the 1D model to these experimental measurements in section 8.4 reveals the need to include kinetic effects to explain the large ratio of upstream T_i to T_e at high Kn (Knudsen number, ratio of mean free path to system scale length λ/L). •

8.1 EDGE ION TEMPERATURE IN C-MOD

A dedicated set of discharges were performed to study the relative levels of ion and electron heat transport in Alcator C-Mod. Plasmas examined here were run in lower-single null with the ∇B-drift towards the active x-point. The toroidal field was $B_t = 5.4\,T$ and the plasma current was $I_p = 0.8\,MA$. Deuterium was the main fuel and the density was scanned from $\bar{n}_e = 0.6 \times 10^{20}\,m^{-3}$ to $1.8 \times 10^{20}\,m^{-3}$ (Greenwald fraction: $\bar{n}_e/n_G = 0.12$ to 0.35). No auxiliary heating was used; these plasmas where ohmic L-mode.

The arrangement of experimental diagnostics is shown in fig. 104. The upstream ion temperature is taken from CXRS measurements. Since the Langmuir probe temperature measurements are much less scattered than Thomson scattering, they are used for upstream electron temperature. One of the biggest challenges in comparing profiles of measurements from different locations is mapping them along magnetic flux surfaces. It is sometimes necessary to shift the Langmuir probe profiles relative to the Thomson profiles by up to 2 mm in flux surface space in order for the electron density and temperature profiles to match [13]. In studies with the CXRS of transport in moderate- to high-collisionality H- and I-mode plasmas—where the pedestal electrons and ions are expected to be strongly coupled—

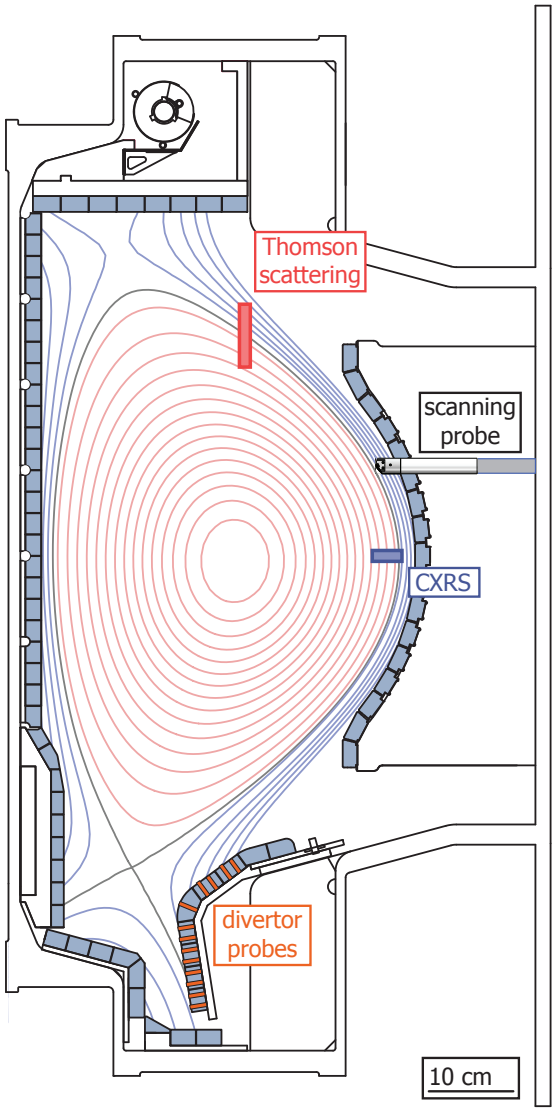

Figure 104: Poloidal cross section of the Alcator C-Mod tokamak showing the locations of the divertor and scanning probes as well as the volumes of plasma sampled by the Thomson scattering and CXRS (poloidal and toroidal viewing).

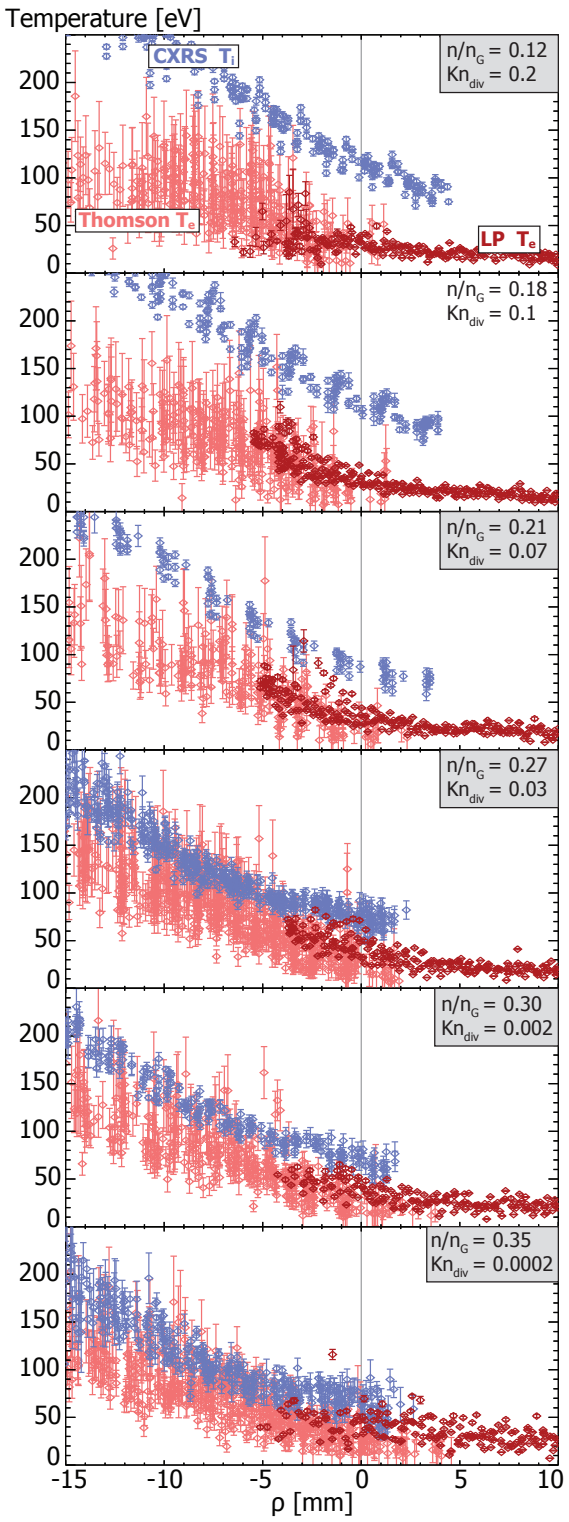

Figure 105: Poloidal-viewing CXRS T_i profiles (blue) plotted with Thomson and Langmuir probe T_e profiles (red). Profiles are not shifted relative to each other. Core plasma density is systematically varied from low values (top) to high values (bottom). As the density increases, the CXRS T_i profiles approach the Thomson T_e profiles, as expected from increased coupling between the ions and electrons along with decreasing kinetic effects on the ions.

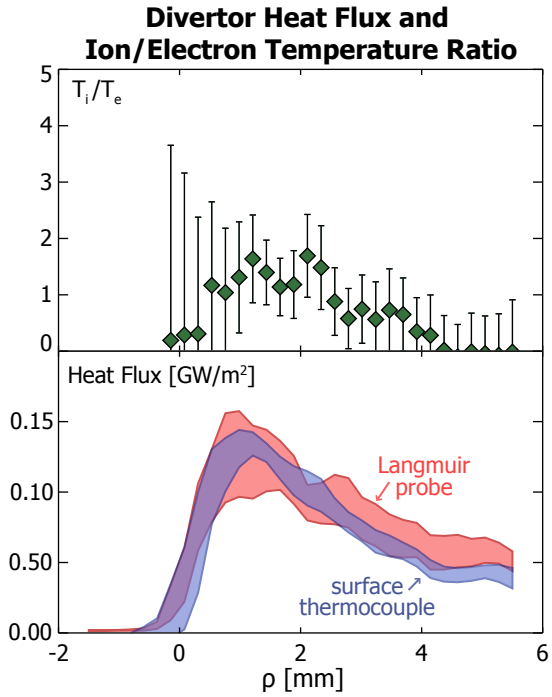

Figure 106: Bottom panel—divertor heat flux profiles from surface thermocouple measurements (blue) and Langmuir probes plus sheath theory (red) assuming $T_i = T_e$. These results are obtained by combining 4 repeated discharges. The vertical span of the banded regions represent the mean data ± 1 standard deviation. These values are propagated through the sheath heat flux transmission equation (eq. (60)) to calculate the divertor ion to electron temperature ratio—top panel.

the CXRS profile needs to be systematically shifted out in ρ a few millimeters to align them [15]. The profiles in fig. 105 are presented unshifted.

As seen in fig. 105 there is a decreasing trend in T_i/T_e with increasing core density. At the lowest core density and highest Kn the ion temperature exceeds the electron temperature by a factor of ~ 4. At the highest core density and lowest Kn the temperature ratio decreases to ~ 1.8.

Although C-Mod has no direct measurements of divertor ion temperature, it may be inferred through comparison of surface thermocouple and Langmuir probe measurements along with sheath heat flux theory. The theory for heat flux through a plasma-wall sheath is well developed: section 2.2.3 and chapter 6. Since the sheath heat flux depends on the local ratio of ion to electron temperature, eq. (60), the ion temperature may be inferred by comparing measurements. Because the ions account for about only one third of the total heat flux, the uncertainty in this ion temperature estimate is high.

To reduce uncertainties, divertor profiles from four repeated discharges in the sheath limited regime were combined. The bands in the bottom panel of fig. 106 represent the mean heat flux profiles from these discharges ± 1 standard deviation; the Langmuir probe profile is plotted assuming $T_i = T_e$. These values are propagated through the sheath heat flux equation to calculate T_i/T_e in the divertor (top panel of fig. 106). Near the strike point the data are consistent with T_i/T_e values in the range $0.5 \lesssim T_i/T_e \lesssim 2$ while further out in the SOL $T_i/T_e \ll 1$. Even in this low collisionality, sheath-limited regime, near the strike point ($T_e \approx 40\,\text{eV}$ & $n \approx 0.6 \times 10^{20}\,\text{m}^{-3}$) the electrons

and ions are marginally coupled ($\tau_{eq}/\tau_{SOL} \approx 1.3$). The T_i/T_e values near the strike point are consistent with divertor RFA measurements at MAST where $T_i \approx T_e$ for ohmic plasma [8]. These values provide a sufficient constraint on the divertor T_i for the 1D simulations presented in section 8.4.

8.2 1D NUMERICAL MODEL FOR ION AND ELECTRON TEMPERATURE PROFILES

We have developed a 1D model of parallel heat transport in the SOL to systematically explore what the upstream ion and electron temperatures should be, given divertor conditions and assumptions about heat flux limiters. The model includes conservation of mass, parallel momentum and electron and ion energy balance in a simplified form, capturing the dominant physics. Ion and electron temperature profiles deduced from the model are found to agree well with simulations from the 2D UEDGE transport code, as discussed in section 8.3.

We follow the 1D fluid SOL modeling techniques laid out in Chapter 11 of Ref. [22], implementing a 4^{th} order Runge-Kutta integration technique (RK45) that uses an imbedded 5^{th} order Runge-Kutta as an error estimate [19]. Based on the error, the step size is automatically adjusted, taking small steps in regions of large changes and large steps over regions of small changes. The simulation domain is half of a symmetric SOL of length L_x with the divertor located at $x = 0$. The equations of the 1D model are as follows.

Continuity equation:

$$\frac{d}{dx}(nv) = S_p, \tag{89}$$

with n the density and v the fluid velocity (distinct from the thermal velocity v_{th}). S_p is the net volumetric particle source which is assumed to have the form:

$$S_p = S_{po}\, e^{-x/L_s}, \tag{90}$$

where L_s is the characteristic scale length of the particle source along the field line from the plate. S_{po} is adjusted such that $v(x = L_x) = 0$, and its magnitude is given entirely by the divertor boundary conditions: $\int_o^{L_x} S_p\, dx = -n_t v_t$, see fig. 107.

Conservation of momentum:

$$\frac{d}{dx}(m_i n v^2 + n k_B T_e + n k_B T_i) = 0, \tag{91}$$

with sources/sinks of momentum neglected. Terms containing m_e are small compared to m_i and not included.

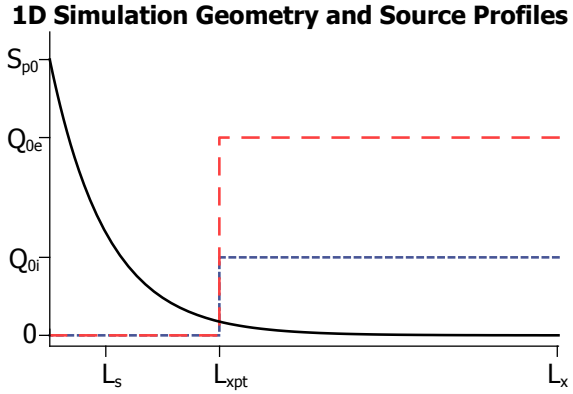

Figure 107: Schematic of the source profiles used in the 1D simulation. The solid black line is the particle source, the dashed red line is the electron energy source, and the dotted blue line is the ion energy source. The magnitude of the particle source is set by the divertor temperature and density along with $v = 0$ at the mid-plane. The magnitudes of the energy sources are set by the sheath heat flux, the balance of equipartition, and having $\frac{dT}{dx} = 0$ at the mid-plane. The ion energy source is typically lower than the electron due to its lower sheath heat flux transmission coefficient.

Electron and ion energy balances:

$$\frac{d}{dx}\left(\frac{5}{2}nk_BT_ev + q_{\|e}\right) = -Q_{eq} + Q_{o,e}, \tag{92}$$

$$\frac{d}{dx}\left(\frac{5}{2}nk_BT_iv + \frac{1}{2}m_inv^3 + q_{\|i}\right) = Q_{eq} + Q_{o,i}, \tag{93}$$

with the heat fluxes ($q_{\|(e,i)}$) given by the flux limited expression, eq. (15). The electron-ion equilibration heat exchange term is given by [22]:

$$Q_{eq} = \frac{Z^2e^4\sqrt{m_e}\ln\Lambda}{3\pi\sqrt{2\pi}\epsilon_0 m_i}n^2\frac{k_BT_e - k_BT_i}{(k_BT_e)^{3/2}}, \tag{94}$$

with Z the ion charge (we use $Z = 1$), $\ln\Lambda$ the Coulomb logarithm, and ϵ_0 the permittivity of free space. The leading fraction is taken to be $2.51 \times 10^{-14}\,kg^{1.5}\,m^6\,s^{-4}$.

The electron and ion energy sources ($Q_{o(e,i)}$) are uniform over the region from the x-point (L_{xpt}) to the mid-point (L_x) and zero otherwise, see fig. 107. Initially their values are set to the target (sheath) heat flux divided by the distance from the x-point to the mid-point ($Q_{o(e,i)} = q_{t(e,i)}/\left(L_x - L_{xpt}\right)$, subscript "t" indicates quantities evaluated at the divertor $x = 0$). These values are iterated, while maintaining energy balance, until both the electron and ion parallel temperature gradients at the midplane are essentially zero (i. e., below a threshold $< 0.1\,eV\,m^{-1}$). At high Kn, little energy is exchanged between the electrons and ions and no iterations are needed. However at lower Kn, the equipartition term becomes important and iterations are necessary.

We apply the Bohm criterion at the sheath boundary:

$$M_t \equiv \frac{v_t}{\sqrt{\frac{k_B T_{e,t} + k_B T_{i,t}}{m_i}}} \geqslant 1. \tag{95}$$

The fluid velocity must meet or exceed the sound speed at the sheath. For most cases simply having $M_t = 1$ is sufficient. However, for some cases with low target temperature and high target density $M_t = 1$ causes discontinuities in the solution and a solution with $M_t > 1$ must be found [10, 14, 17, 21, 22]. We find that the RK45 method has trouble integrating through the transonic region, almost exclusively due to the $1/2 m_i n v^3$ term in the ion energy balance (eq. (94)). However the regions away from the transonic region were solved properly and not affected by the discontinuity. More clever techniques that start the integration from the sonic transition point would likely be successful [6, 7, 14]. Fortunately none of the data presented in this study needed the supersonic transition, so the simple model and numerical technique is sufficient.

Sheath heat flux boundary conditions are given by [22]:

$$q_{t(e,i)} = \gamma_{(e,i)} n_t v_t k_B T_{t,e}. \tag{96}$$

With the electron sheath heat flux transmission coefficient given by:

$$\gamma_e = 2 + \frac{eV_{sh}}{k_B T_{t,e}} \approx 5, \tag{97}$$

and the ion sheath heat flux transmission coefficient, allowing for $M_t > 1$:

$$\gamma_i = \frac{1}{k_B T_{t,e}} \left(\frac{5}{2} k_B T_{t,i} + \frac{1}{2} m_i v_t^2 \right). \tag{98}$$

Although $\gamma_i = 2.5 T_i / T_e$ is often used based on results from kinetic simulations [22], the additional $1/2 m_i v_t^2$ term helps the numerics, ensuring that ion temperature gradient does not go negative at the surface.

8.3 COMPARISON OF 1D NUMERICAL MODEL WITH UEDGE

We performed four UEDGE simulations to benchmark the 1D heat transport model, ensuring that the code solves the parallel transport equations with sufficient accuracy and that it reproduces the heat flux limiters implemented in 2D simulations. Two simulations are for high-Kn cases ($Kn = 4$) where electrons and ions should be weakly

coupled and two are for low-Kn ($Kn = 0.04$) where electrons and ions should be strongly coupled. Both the high- and low-Kn cases were run with heat flux limits ($\alpha = 0.21$) and without ($\alpha = \infty$).

The UEDGE simulations were run using a standard C-Mod plasma equilibrium (lower single null, $B_t = 5.4\,T$, $I_p = 0.8\,MA$) with the C-Mod divertor geometry. The only difference between the high- and low-Kn cases was a change of the density boundary condition inside the LCFS from $0.4 \times 10^{20}\,m^{-3}$ to $0.8 \times 10^{20}\,m^{-3}$. A net SOL power of 0.55 MW (0.8 MW ohmic minus 0.25 MW radiation) was divided equally among the ions and electrons. Standard sheath heat flux and Bohm boundary conditions were used. Drifts were kept off to aid in fast convergence. The fluid neutral model was implemented with 100 % recycling boundary condition. Cross-field transport is anomalous; as such the transport coefficients are usually adjusted to match experimentally measured profiles. Since we were only interested in exploring parallel transport and not cross-field profiles, the cross field transport coefficients were left as Bohm transport ($T_e/16eB$).

An accurate comparison of the parallel transport requires the effective cross-field sources in the two simulations to be similar. Thus, since the 1D simulation assumed that the parallel velocity at the midplane was zero, we picked the UEDGE flux tube with the velocity profile that most closely matched this. Then we take the UEDGE values of L_x, L_{xpt}, along with n, T_e, and T_i at the divertor in this flux tube, and input them into the 1D simulation. The only parameter that was free to be adjusted was the source scale length, L_s. It was changed such that the UEDGE and 1D simulation velocity and density profiles nearly matched (2 m for the high-Kn and 1 m for the low-Kn cases).

The UEDGE and 1D simulation temperature profiles from these four cases are shown in fig. 108. The 1D numerical model is found to produce ion and electron temperature profiles that are in excellent agreement with that from UEDGE. In the high-Kn case, it is quite clear that the heat flux limiters make a large difference for the ion temperature profile, increasing the peak temperature by $\sim$ 70 %. Yet the electron temperature profile remains relatively unchanged. This is consistent with other simulations [4, 5, 9, 20]. On the other hand, for the low-Kn case the ion temperature profile only slightly increased, by $\sim$ 10 %. The electron profile again remains relatively unchanged.

The effects of equipartition of energy between electrons and ions are clear from these graphs. In the high-Kn cases the electron and ion temperatures are within 25 % of each other in the divertor and quickly diverge moving upstream. In the low-Kn cases, both species remain at essentially the same temperature to a distance of at least 0.5 m away from the divertor. The coupling is particularly strong in the low-Kn regime because a sharp temperature gradient near the divertor target is necessary to conduct the heat flux. In this case, pres-

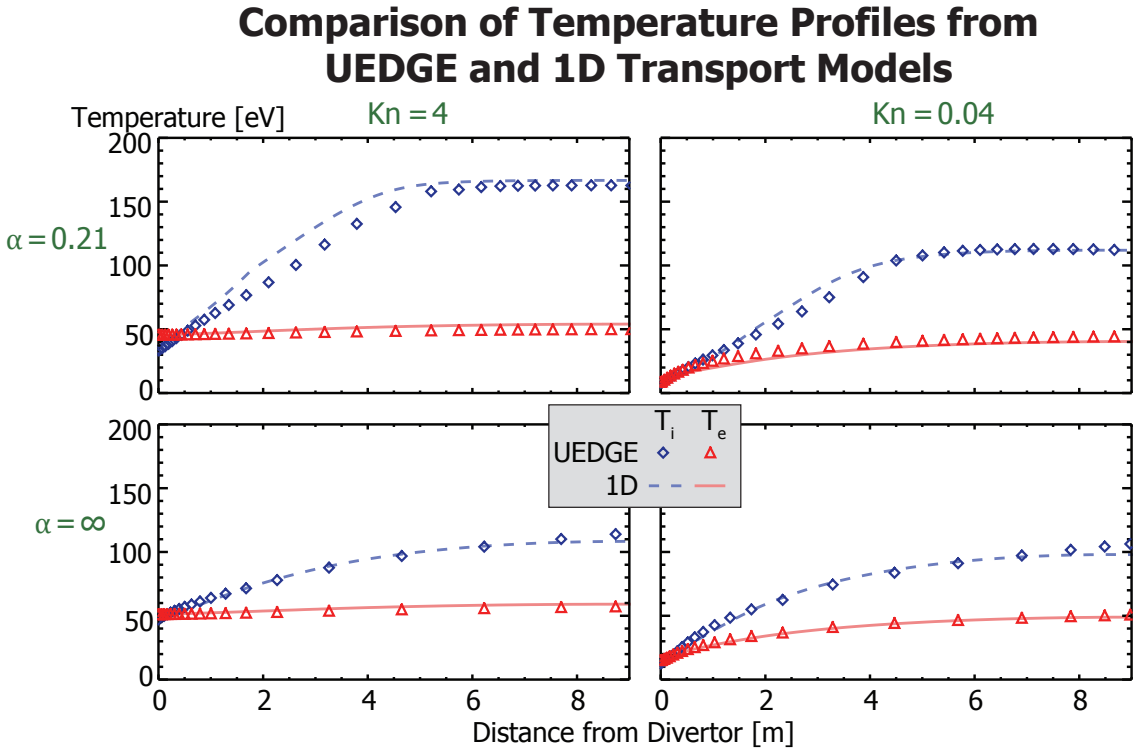

Figure 108: Comparison of the 1D heat transport model and the 2D plasma code UEDGE. Left two plots are for high-Kn cases and the right two are for low-Kn. The top row are simulations with heat flux limiters and the bottom row are without. Given similar source profiles, the 1D model (T_i dashed blue lines, T_e solid red line) and UEDGE (T_i blue diamonds, T_e red triangles) produce very similar temperature profiles over this wide parameter range. These results confirm that the 1D simulation solves the parallel transport accurately and implements heat flux limiters consistent with UEDGE.

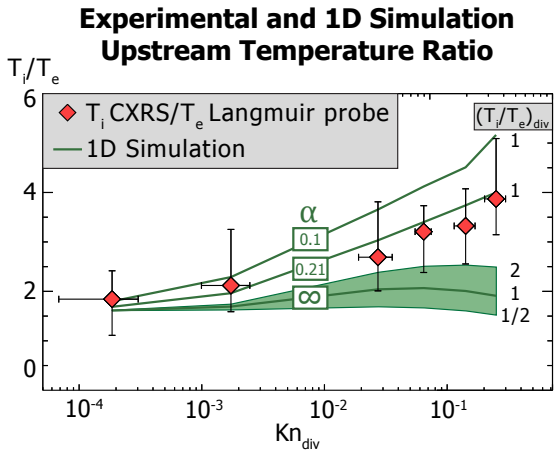

Figure 109: Comparison of experimental and simulated upstream ion to electron temperature ratios plotted against the Knudsen number evaluated in the divertor ($Kn_{div} = c_s/\tau_{ii}L \propto T_i^2/nL$, calculated assuming $T_i = T_e$). The ratio approaches unity as Kn decreases due to increased coupling between the ions and electrons. At high-Kn the experimentally measured temperature ratio is not adequately described by the fluid model alone; kinetic corrections (i. e., finite values of α, the flux limiter in a fluid model) are necessary to match the temperature ratio.

sure balance requires the density to increase sharply near the divertor target. The combined effect of temperature decrease and density increase strongly enhances coupling between the electrons and ions.

Having benchmarked our 1D heat transport model and the ion and electron profiles that it produces, we now proceed to compare its output with experimental measurements.

8.4 COMPARISON OF EXPERIMENTAL AND SIMULATED UPSTREAM TEMPERATURE RATIO

The experimentally measured values of the upstream temperature ratio are shown in fig. 109. The profiles were not shifted, taking the values outputted at $\rho = 0$ as calculated by EFIT. The error bars in $T_{u,i}/T_{u,e}$, indicate the extreme values given by ± 3 mm relative shifts of the electron and ion temperature profiles. If anything, the systematic shift previously needed in the CXRS profile suggests that $T_{u,i}/T_{u,e}$, may be towards the higher end of the range.

The inputs to the simulation are: the target electron and ion temperatures ($T_{t(e,i)}$), target density (n_t), SOL half-length (L_x), SOL particle source length (L_s), as well as the electron and ion heat flux limits ($\alpha_{(e,i)}$). Target electron temperature, T_e, and density, n_e, were taken from Langmuir probe measurements near the strike point. Target ion temperature is estimated from sheath heat flux measurements, fig. 106. For simulations with no heat flux limiters, the divertor ion temperature was set equal to 1/2, 1, and 2 times the divertor electron temperature. For simulations with heat flux limits the divertor ion temperature was set equal to the divertor electron temperature.

From the simple 1D simulations of the SOL and our experimental measurements we see that the upstream temperature ratio is much higher than that inferred from Spitzer heat conduction ($\alpha_{(e,i)} = \infty$) at high-Kn. The model under predicts the temperature ratio by a factor of 2. Increasing the divertor ion temperature to be twice the divertor

electron temperature has little effect. But inclusion of the heat flux limiter ($\alpha_{(e,i)} = 0.21$) brings the model into agreement with the high-Kn data. This value of $\alpha_{(e,i)}$ is consistent with those reported in kinetic simulations [1, 2, 11, 18]. Although, uncertainty in the divertor ion temperature prevents a precise value to be identified for the heat flux limiter. For the low-Kn cases, as expected, the heat flux limiters have little effect on the upstream temperature ratio and the fluid model gives a good prediction of the experimental temperature ratio.

A comment must be made concerning divertor Langmuir probe measurements made near detachment conditions; they often report electron pressures that are twice the upstream value when $5\,\text{eV} \leqslant T_e \leqslant 15\,\text{eV}$ [3, 12, 16]. As discussed in chapter 6, this phenomenon has been identified as an artifact of the Langmuir probe; its electrical bias can disturb the local plasma conditions in this regime [3, 23]. The $Kn \approx 2 \times 10^{-3}$ data point in fig. 109 may be affected by this phenomenon. However, the upstream temperature ratio is a weak function of Kn in this regime, and factors of 2 differences in the divertor density here do not change our conclusions.

While a reasonable match between model and experiment is obtained using a heat flux limiter factor of ~ 0.2, these results do not say that the Spitzer-Harm/free-streaming harmonic average model is the correct prescription for kinetic corrections at high values of Kn. Kinetic simulations clearly show that the harmonic average model is sensitive to α and unable to match profile details. Thus, to accurately describe parallel heat flux in the boundary plasma, kinetic simulations are necessary. However, these new experimental results do provide some assurance and guidance. Flux-limited fluid transport models can be a useful tool for simulating boundary physics when more precision than the 2-point model is desired and the full computational complexity of a full kinetic treatment is too burdensome and its improved accuracy unnecessary.

A brief note should be made about implications for simulations in reactor-scale devices. To minimize surface erosion, the divertor electron temperature must be below $\sim 5\,\text{eV}$ and the surface heat flux is limited to $\sim 10\,\text{MW}\,\text{m}^{-2}$. Thus a reactor-scale device will have divertor conditions like those in the far left of fig. 109. Yet, ITER, and likely reactor are about $10\times$ bigger than C-Mod. Thus they will have even lower Kn and kinetic limits may not be as necessary to get good predictions of the upstream temperature ratio. ⋆

BIBLIOGRAPHY

[1] Z. Abou-Assaleh, J. P. Matte, T. W. Johnston, and R. Marchand. Fokker-Planck modelling of edge plasma near the neutralizer plate in a tokamak. *Contributions to Plasma Physics*, 32(3-4):268–272, 1992.

[2] Z. Abou-Assaleh, M. Petravic, R. Vesey, J. P. Matte, and T. W. Johnston. Non-local transport in a tokamak plasma divertor with recycling. *Contributions to Plasma Physics*, 34(2-3):175–179, 1994.

[3] D. Brunner, M. V. Umansky, B. LaBombard, and T. D. Rognlien. Divertor "death-ray" explained: An artifact of a Langmuir probe operating at negative bias in a high-recycling divertor. *Journal of Nuclear Materials*, 438:S1196–S1199, 2013.

[4] A. V. Chankin, D. P. Coster, R. Dux, Ch. Fuchs, G. Haas, A. Herrmann, L. D. Horton, A. Kallenbach, M. Kaufmann, Ch. Konz, K. Lackner, C. Maggi, H. W. Müller, J. Neuhauser, R. Pugno, M. Reich, and W. Schneider. SOLPS modelling of ASDEX upgrade H-mode plasma. *Plasma Physics and Controlled Fusion*, 48(6):839, 2006.

[5] D. P. Coster, X. Bonnin, B. Braams, D. Reiter, R. Schneider, and the ASDEX Upgrade Team. Simulation of the edge plasma in tokamaks. *Physica Scripta*, T108(T108):7, 2004.

[6] H. De Sterck. Critical point analysis of transonic flow profiles with heat conduction. *SIAM Journal on Applied Dynamical Systems*, 6(3):645–662, 2007.

[7] H. De Sterck, S. Rostrup, and F. Tian. A fast and accurate algorithm for computing radial transonic flows. *Journal of Computational and Applied Mathematics*, 223(2):916–928, 2009.

[8] S. Elmore, S. Y. Allan, A. Kirk, G. Fishpool, J. Harrison, P. Tamain, M. Kočan, R. Gaffka, R. Stephen, J. W. Bradley, and the MAST Team. Upstream and divertor ion temperature measurements on MAST by retarding field energy analyser. *Plasma Physics and Controlled Fusion*, 54(6):065001, 2012.

[9] W Fundamenski. Parallel heat flux limits in the tokamak scrape-off layer. *Plasma Physics and Controlled Fusion*, 47(11):R163, 2005.

[10] P. J. Harbour and A. Loarte. Departures from sonic flow at the sheath on a divertor target or limiter. *Contributions to Plasma Physics*, 34(2-3):312–316, 1994.

[11] S. A. Khan and T. D. Rognlien. Thermal heat flux in a plasma for arbitrary collisionality. *Physics of Fluids*, 24:1442, 1981.

[12] B. Labombard, J. A. Goetz, I. Hutchinson, D. Jablonski, J. Kesner, C. Kurz, B. Lipschultz, G. M. McCracken, A. Niemczewski, J. Terry, A. Allen, R. L. Boivin, F. Bombarda, P. Bonoli, C. Christensen, C. Fiore, D. Garnier, S. Golovato, R. Granetz, M. Greenwald, S. Horne, A. Hubbard, J. Irby, D. Lo, D. Lumma, E. Marmar, M. May, A. Mazurenko, R. Nachtrieb, H. Ohkawa, P. O'Shea, M. Porkolab, J. Reardon, J. Rice, J. Rost, J. Schachter, J. Snipes, J. Sorci, P. Stek, Y. Takase, Y. Wang, R. Watterson, J. Weaver, B. Welch, and S. Wolfe. Experimental investigation of transport phenomena in the scrape-off layer and divertor. *Journal of Nuclear Materials*, 241-243:149 – 166, 1997.

[13] B. LaBombard, J. W. Hughes, D. Mossessian, M. Greenwald, B. Lipschultz, J. L. Terry, and the Alcator C-Mod Team. Evidence for electromagnetic fluid drift turbulence controlling the edge plasma state in the Alcator C-Mod tokamak. *Nuclear Fusion*, 45(12):1658, 2005.

[14] O. Marchuk and M. Z. Tokar. Modeling of supersonic plasma flow in the scrape-off layer. *Journal of Computational Physics*, 227(2):1597–1607, 2007.

[15] K. D. Marr, B. Lipschultz, P. J. Catto, R. M. McDermott, M. L. Reinke, and A. N. Simakov. Comparison of neoclassical predictions with measured flows and evaluation of a poloidal impurity density asymmetry. *Plasma Physics and Controlled Fusion*, 52(5):055010, 2010.

[16] R. D. Monk, A. Loarte, A. Chankin, S. Clement, S. J. Davies, J. K. Ehrenberg, H. Y. Guo, J. Lingertat, G. F. Matthews, M. F. Stamp, and P. C. Stangeby. Interpretation of ion flux and electron temperature profiles at the JET divertor target during high recycling and detached discharges. *Journal of Nuclear Materials*, 241-243:396 – 401, 1997.

[17] A. V. Nedospasov and M. Z. Tokar. Engineering aspects of a tokamak-reactor divertor operation with strong recycling. *Proceedings of the Fusion Reactor Design and Technology, IAEA, Yalta*, page 113, 1986.

[18] D. E. Post, K. Borrass, J. D. Callen, et al. ITER Documentation Series No. 21. *ITER Physics (International Atomic Energy Agency, Vienna)*, 1991.

[19] W. H. Press, S. A. Teukolsky, W. T. Vetterling, and B. P. Flannery. *Numerical Recipes 3rd Edition: The Art of Scientific Computing*. Cambridge University Press, 2007.

[20] G. J. Radford. The application of moment equations to scrape off layer plasmas. *Contributions to Plasma Physics*, 32(3-4):297–302, 1992.

[21] P. C. Stangeby. Subsonic and supersonic divertor solutions. *Plasma Physics and Controlled Fusion*, 33(6):677, 1991.

[22] P. C. Stangeby. *The Plasma Boundary of Magnetic Fusion Devices*. IoP Publishing, 2000.

[23] M. V. Umansky, D. Brunner, B. LaBombard, and T. D. Rognlien. Modeling of local edge plasma perturbations induced by a biased probe. *Contributions to Plasma Physics*, 52(5-6):417–423, 2012.

9

CONCLUSIONS

This thesis work has made key contributions in the following areas:

Diagnostic Development

- Development of two ion temperature probes—a retarding field analyzer and an ion sensitive probe—able to survive the extreme heat flux in the boundary of Alcator C-Mod.
- New state-of-the-art retarding field analyzer design. The entrance slit is an order of magnitude (1.7 mm versus ~ 20 mm) closer to the tip of the probe than previous designs. This allows the C-Mod retarding field analyzer make measurements up to the last closed flux surface.
- Detailed assessment of ion sensitive probe operation, including 1D kinetic simulations, clarifying its operation and demonstrating the regimes in which its measurements may be trusted. This research has uncovered some serious flaws in previous work reported in the literature.
- Implementation and refinement of divertor heat flux diagnostics–surface thermocouples and calorimeters. Diagnostics were benchmarked against each other and IR thermography, confirming the heat flux measurements.

Boundary Plasma Physics

- The first systematic comparison of boundary ion temperature measurements and simulation over a large collisionality span, clearly demonstrating the limits of the fluid model in describing ion heat transport at low collisionality. Kinetic corrections are derived from the data and found to be consistent with that expected from kinetic computations.
- Verification of sheath heat flux theory with unprecedented accuracy. The sheath heat flux transmission coefficient has been notoriously difficult to measure in tokamaks, causing doubts to its validity. The divertor heat flux profiles measured with surface thermocouples overlayed that inferred from Langmuir probes using sheath heat flux theory across the entire divertor "footprint", giving confidence to this very important theory.
- Clarifying Langmuir probe operation in high-recycling divertor conditions. The divertor heat flux diagnostics demonstrated

that the "death-ray"—an apparent divertor over-pressure—was localized to the Langmuir probes. A new theory for this phenomena was developed: the Langmuir probe bias restricted electron heat exhaust, increasing local electron temperature and thus ionization of neutrals in front of the probe. A collaboration was set up which tested and confirmed this mechanism using plasma-neutral fluid simulations of a biased probe.

The engineering and scientific developments in this thesis have been published in seven peer reviewed papers [1, 2, 3, 4, 5, 6, 7].

9.1 ASSESSMENT OF ION HEAT TRANSPORT

Understanding of electron heat transport in the boundary of tokamaks is relatively mature. Upstream and divertor measurements of electron temperature are regularly obtained with Langmuir probes and/or Thomson scattering. Ion heat transport has not been so thoroughly investigated. Edge ion temperature measurements are rarer than electron temperature. Ion probes can be both more challenging to build and interpret than Langmuir probes. Spectroscopic techniques have relatively poor resolution and rely on the impurity being well-coupled to the main ion. Because of these challenges and limitations, systematic measurements of edge ion temperature are infrequent.

In the few studies, there is an almost universal trend of ion temperature exceeding the electron temperature at low core density (or high Knudsen number, the ratio of mean free path to system scale length: $Kn = \lambda/L$). As the core density increases (Kn decreases) the ion temperature converges on the electron temperature. The most sophisticated analyses to-date have demonstrated that the ion temperature approaches the electron temperature as the ion to electron equilibration time approaches the boundary dwell time. However, none of these analyses explored the cause(s) of high ion to electron temperature ratio at high Kn. A simple fluid model would indicate that the measured ratios exceeding 3 would imply much greater heat flux in the ion channel.

9.1.1 *Development of Ion Temperature Probes*

To asses ion heat transport in Alcator C-Mod two new probes were created, a retarding field analyzer and an ion sensitive probe (section 3.3). The retarding field analyzer is a well-accepted diagnostic to measure the ion temperature across the field of plasma physics. But, with its major faces normal to the magnetic field and incident heat flux, it is poor at handling heat flux. On the other hand, the major faces of the ion sensitive probe are tangent to the magnetic field and incident heat flux. But, particle collection is complicated because the

magnetic field is nearly tangent to the probe surface. The ion sensitive probe ion temperature measurements have been benchmarked in some low density ($< 10^{18}\,m^{-3}$) plasmas but proper operation in high density ($> 10^{18}\,m^{-3}$) plasmas had yet to be confirmed. An important focus of this thesis was therefore assessing the operation of the ion sensitive probe in C-Mod scrape-off layer conditions.

Alcator C-Mod has the most extreme boundary heat flux of any present tokamak, easily exceeding $100\,MW\,m^{-2}$. This required very careful design of the probes to handle the heat flux. Simulations of the probes plunging through the exponential heat flux profile of the boundary were created in the finite element code COMSOL, see section 3.3.6. Probe geometry was optimized to handle the heat flux while still meeting physics requirements for proper ion temperature measurements. The ion sensitive probe is able to plunge to a simulated peak heat flux of $\sim 700\,MW\,m^{-2}$ (same as the high heat flux Langmuir probe) and the retarding field analyzer to $\sim 400\,MW\,m^{-2}$. The retarding field analyzer in particular was a large improvement in state of the art: the entrance slit is ten times closer to the tip than in any previous design. This maximizes the distance into the plasma which the measurement can be made.

Initial plans were to use the retarding field analyzer to benchmark the ion sensitive probe—taking charge exchange recombination spectroscopy data as a tie-breaker—and then scan the ion sensitive probe deeper into the plasma. However, operation of the probes was limited due to the early closure of Alcator C-Mod. Experimental focus was given to the ion sensitive probe due to its superior heat flux handling.

After the experimental campaign was completed the ion sensitive probe measurements were found to be space charge limited and unable to measure the ion temperature (chapter 7). This prompted an in depth examination of the ISP literature. At least 17 out of $>$ 40 ion sensitive probe data reported in the literature showed signs of space charge, with only 3 publications considering its deleterious effect on measurements.

A 1D kinetic simulation was created in COMSOL to explore the effects of ion space charge on the ISP I-V (section 7.5). These simulations were used to investigate how fitting the traditional exponential decay to a moderately space charge limited I-V might over-estimate the temperature and under-estimate the plasma potential. The simulations were also used to show under what plasma temperature and density conditions the probe bias would exceed the space charge potential and regain the exponential I-V. For the present C-Mod ISP this would have to be over 500 V, well beyond the available bias. Based on this knowledge, modifications to the probe geometry were identified that would allow a high heat flux ion sensitive probe to measure the ion temperature up to the last closed flux surface in C-Mod.

The RFA did remarkably well, surviving all the way to the last closed flux surface. RFA electron temperature profiles matched that measured with a Langmuir probe. There was not enough RFA data to do a full investigation of the edge ion temperature due to the challenges of getting it operational on a constrained time frame. However, it was sufficient to benchmark CXRS measurements of B^{5+} T_i at the lowest edge collisionality (section 5.2), where B^{5+} ions are least likely to be coupled to the main fuel. Thus measurements indicate that the CXRS impurity ion temperature can be used as a proxy for the main ion temperature for the ion heat flux transport studies. In addition, a simple calculation of the B^{5+}-D^{+} equilibration time reveals that they should be coupled.

9.1.2 *Comparison of Simulated and Experimental Heat Transport*

Although there was not sufficient probe ion temperature measurements to systematically study ion heat transport, the CXRS was good enough to explore trends of the upstream temperature ratio. Over a volume-averaged density scan from $0.6 \times 10^{20}\,m^{-3}$ to $1.8 \times 10^{20}\,m^{-3}$ the ratio of CXRS T_i to Langmuir probe T_e at the last closed flux surface decreased from ~ 4 to ~ 1.8, see section 8.1.

A 1D fluid heat transport simulation was created to compare to the edge electron and ion temperature measurements. It includes convection, flux limited heat conduction, and electron-ion energy exchange. The 1D simulation was benchmarked against the 2D fluid code UEDGE over a wide range of parameters with excellent agreement, see section 8.3. In comparing the simulations to experimental measurements, inputs to the 1D simulation were the divertor Langmuir probe measurements of n and T_e along with estimations of T_i from sheath heat flux measurements. The simulation with no heat flux limiters ($\alpha = \infty$) shows good agreement with the upstream temperature ratio at low Kn, but is off by a factor of ~ 2 at high Kn (section 8.4). With the addition of heat flux limiters, agreement with the upstream temperature ratio is achieved at high Kn while agreement at low Kn is maintained. The best agreement is achieved with heat flux limits at about the same value found with kinetic simulations ($\alpha \approx 0.2$). However, because of uncertainty in the mapping of T_i to T_e and the divertor ion temperature, a precise empirical value for the heat flux limit cannot be given.

9.2 CONFIRMATION OF SHEATH HEAT FLUX

The sheath heat flux transmission coefficient is one of the most important parameters in the boundary plasma. It is a parameter computed from a kinetic theory of plasma heat flux transport to the first wall, relating the heat flux to local values of plasma temperature and density.

The sheath heat flux transmission coefficient is used in all edge fluid codes as the boundary condition on heat flux. It is crucial to have confidence in this theory, given that the boundary heat flux is expected to be near the engineering limits of power exhaust in reactor-scale devices.

Direct experimental measurements of the sheath heat flux transmission coefficient—from independent measurements of the heat flux and plasma conditions—can increase our confidence in the theory. However, in the past, experimental measurements have only increased confusion. The sheath heat flux transmission coefficient should be around 7, yet previously measured values have ranged over an order of magnitude, from 2 to 20. Values above 7 might be explained with large secondary electron emission or an ion temperature much greater than the electron temperature. The lowest values, on the other hand, cannot be explained so simply. The lower bound allowed by theory, in the limit of ions much colder than electrons, is 5. A measured value of 2 would suggest that there is no sheath.

9.2.1 *Implementation of Heat Flux Diagnostics*

Among today's experiments, Alcator C-Mod presents a unique opportunity to study sheath heat flux. It has reactor-level parallel heat flux, exceeding $100\,\mathrm{MW\,m^{-2}}$, and a vertical, refractory metal divertor plates; identical conditions to ITER. As part of the Department of Energy FY2010 Joint Research Target to measure the heat flux footprint, an array of surface thermocouples and calorimeters were designed for the Alcator C-Mod divertor by B. LaBombard, J. Payne, and N. Mucic. A significant portion of this thesis focused on implementation, refinement, and analysis of data from these diagnostics (sections 3.1, 3.2, 4.1 and 4.2). Both the surface thermocouples and calorimeters needed improvements before they were reliable.

Surface thermocouples are a novel diagnostic: the thermojunction is directly on the surface, allowing for an unambiguous calculation of the surface heat flux. This is the first successful implementation of surface thermocouples on a fusion experiment. Proper grounding of surface thermocouples in a tokamak is important. The initial version of the surface thermocouples had large, spurious spikes of positive and negative heat flux. The source of the erroneous heat flux was found through comparisons with Langmuir probe measurements. An additional voltage was generated when the boundary currents connected to ground through the surface thermocouple stainless steel mount. Propagation of this voltage through the thermal analysis resulted in the erroneous heat flux. A short was implemented to reroute the current. With the short in place the measurements had no spurious heat flux spikes.

The calorimeters are thermally isolated molybdenum cylinders with an embedded thermocouple. A comparison of the measured thermocouple response with thermal modeling of the expected response demonstrated a large discrepancy. This difference was tracked down to a thick (few mm) stainless steel sheath on the thermocouples which significantly damped the thermal response. A new, unsheathed thermocouple was designed and implemented. The new thermocouple had much better time response which allowed for a precise calculation of the deposited energy.

The energy deposition measurements from the calorimeters were an important check on the surface thermocouples. The calorimeters confirmed that the surface thermocouples correctly measured the energy deposition, see section 5.1, and thus the surface thermocouple heat flux measurements could be trusted. In addition, applying the same energy deposition measurement technique to the thermocouples embedded in the divertor and limiter tiles produced excellent whole-machine energy balance.

The surface thermocouples were crucial for measuring sheath heat flux. Most of the previous measurements used an IR camera, which is susceptible to surface layers. That is, the IR emission is from a surface layer that may be in poor thermal contact with the bulk material. The effect can be simulated by allowing for an effective surface resistance in the thermal modeling. The resistance is a free parameter in the thermal modeling and is tuned to remove negative heat fluxes during transients; this also effects the magnitude of the positive heat flux. The surface thermocouples do not exhibit this phenomena and thus do not need the thermal resistance in the heat flux calculation. The lack of a free parameter in the heat flux modeling along with the calorimeter benchmarking, means we are supremely confident in the surface thermocouple heat flux measurements.

The formula for sheath heat flux transmission was recast from the floating value to one for a grounded divertor in terms of the Langmuir probe measured ground current measurement. This was an important development as the ground current increases sheath heat flux by $\sim 50\,\%$ in C-Mod in the sheath-limited regime. With the additional ground current terms there is excellent agreement between the surface thermocouple and Langmuir probe heat flux measurements, see section 6.1. These measurements are the first confirmation of sheath heat flux theory over the entire profile in a tokamak. The sheath heat flux measurements also allowed estimation of the divertor ion temperature, placing it in the range $0.5T_e < T_i < 2T_e$.

9.2.2 *Clarification of Langmuir Probe Measurements in High-Recycling Divertor*

In addition to confirming sheath heat flux theory, the surface thermocouples were used to show where Langmuir probe measurements fail. The surface thermocouples showed that the Langmuir probe divertor over-pressure known as the "death-ray" was localized to the Langmuir probe and connected to the unphysical sheath heat flux transmission coefficient values ($\gamma < 5$), see section 6.1. The "death-ray" was discovered in C-Mod before the thermal diagnostics were installed. It was thought to be caused by neutrals, which were collisionally-coupled to ions, ionizing in a local region of raised electron temperature. However, there was no known source of elevated electron temperature.

As a result of this thesis work a new theory for these phenomena has been proposed (section 6.2): the Langmuir probe in ion saturation changes the boundary condition on electron heat flux which raises the local electron temperature. The higher electron temperature increases the ionization of neutrals directly in front of the probe in this high-recycling divertor. A collaboration with M. V. Umansky was set up test this theory (section 6.3). He used UEDGE to simulate the biased probe in a high-recycling divertor. The factor of 2 over-pressure was reproduced. The simulations revealed that it was the strong coupling of momentum between the ions and neutrals which supported the over-pressure. These results show that Langmuir probe measurements in high-recycling divertor conditions should be treated with strong caution.

9.3 FUTURE WORK

As with many other theses, this work shines light on new areas to explore.

The pursuit of an ion sensitive probe to measure the ion temperature in high density plasmas should continue. Guidance to the operational space of a probe was given by the 1D kinetic simulations. A probe with a sufficiently small diameter would allow for shallow Collector recess distance yet still protect against misalignments. The smaller recess distance will allow a much higher space charge limited current and thus operation in high density plasmas. In addition, an ion sensitive probe with a grid over the Guard could be useful. Keeping the grid at very negative bias would at least partially cancel out the space charge potential. It must be made sure that the grid is sufficiently robust to handle the heat flux; perhaps it will be shadowed slightly by the surrounding probe head.

Ion sensitive probes have been used over a wide range of relative length scales (electron & ion Larmor radii and mean free path, Debye

length, as well as probe radius and recess distance). Although the 1D approximation was good for the C-Mod ion sensitive probe, experimental measurements indicate that 3D effects are likely important for other probes. Perhaps new insights could be gained in using a 3D simulation code to explore particle collection in an ion sensitive probe over a variety of length scales.

Since the retarding field analyzer could survive in the boundary of C-Mod, it could survive in any other present experiment. Placement of the slit 1.7 mm from the tip of the probe puts it almost an order of magnitude closer than any past probe, allowing it to make measurements deeper into the plasma. Implementing this new retarding field analyzer design would benefit any tokamak.

This thesis focused on only comparing fluid simulations to experimental measurements because of the relative simplicity in implementation of a fluid code. However, kinetic corrections to the fluid simulations leave much to be desired. The next step is clearly to set up kinetic simulations, such as XGC0 or PARISOL, and compare them to edge measurements. The sensitivity of ion temperature to edge collisionality presents a great opportunity for comparison. In addition, since kinetic effects are so important for understanding retarding field analyzer measurements, a retarding field analyzer synthetic diagnostic inserted into the kinetic simulations would provide insight into operation of the probe.

There should be wider use of the surface thermocouples and the calorimeters. Because of their great success on C-Mod, surface thermocouples are being considered for instillation at the other two US tokamaks, NSTX and DIII-D. They provide an excellent alternative to IR thermography, not having issues with negative heat flux, resolution, or view-access. Adoption of calorimeters would further increase confidence in other thermal measurements.

The largest drawback to the surface thermocouples has been reliability. Some surface thermocouples work the entire campaign and some are inoperable at instillation, with no obvious differences (electrical or visual). If their mechanism(s) of failure could be understood and reliability improved, they could become a standard part of edge plasma diagnostics.

Additionally, the idea of an electrically isolated, biasable surface thermocouple was thrown around at C-Mod. This would allow measurements of the plasma parameters and heat flux in one location.

Although the UEDGE fluid simulations captured the Langmuir probe induced over-pressure of the "death-ray", it would be interesting to explore it in a kinetic simulation. The physics of electron impact ionization and charge exchange as well as particle transport in the SOL are inherently kinetic processes in which the fluid equations may be a crude approximation. It would be insightful to simulate a Langmuir probe with a swept bias over a wide range of plasma con-

ditions. Perhaps measurements are not only adversely effected in the "death-ray" but in other regimes as well. ⋆

BIBLIOGRAPHY

[1] D. Brunner and B. LaBombard. Surface thermocouples for measurement of pulsed heat flux in the divertor of the Alcator C-Mod tokamak. *Review of Scientific Instruments*, 83(3):033501–033501, 2012.

[2] D. Brunner, B. LaBombard, R. M. Churchill, J. Hughes, B. Lipschultz, R. Ochoukov, T. D. Rognlien, C. Theiler, M. V. Umansky, J. Walk, and D. Whyte. Comparison of ion temperature measurements in the boundary of the Alcator C-Mod tokamak and implications for ion fluid heat flux limiters. *Plasma Physics and Controlled Fusion*, 55:095010, 2013.

[3] D. Brunner, B. LaBombard, R. Ochoukov, R. Sullivan, and D. G. Whyte. Space charge limits of ion sensitive probes. *submitted to Plasma Physics and Controlled Fusion*, 2013.

[4] D. Brunner, B. LaBombard, R. Ochoukov, and D. Whyte. Scanning ion sensitive probe for plasma profile measurements in the boundary of the Alcator C-Mod tokamak. *Review of Scientific Instruments*, 84:053507, 2013.

[5] D. Brunner, B. LaBombard, R. Ochoukov, and D. Whyte. Scanning retarding field analyzer for plasma profile measurements in the boundary of the Alcator C-Mod tokamak. *Review of Scientific Instruments*, 84(3):033502, 2013.

[6] D. Brunner, B. LaBombard, J. Payne, and J. L. Terry. Comparison of heat flux measurements by IR thermography and probes in the Alcator C-Mod divertor. *Journal of Nuclear Materials*, 415(1):S375–S378, 2011.

[7] D. Brunner, M. V. Umansky, B. LaBombard, and T. D. Rognlien. Divertor "death-ray" explained: An artifact of a Langmuir probe operating at negative bias in a high-recycling divertor. *Journal of Nuclear Materials*, 438:S1196–S1199, 2013.

A

DERIVATION OF SHEATH HEAT FLUX TRANSMISSION COEFFICIENT

Here is presented a derivation of the sheath heat flux transmission coefficient (γ) following closely the technique of Stangeby [1]. The sheath heat flux transmission coefficient is often given for a floating surface. This simplifies the derivation but is not proper for most tokamak surfaces, which are typically grounded. So we include the changes to sheath heat flux due to non-zero current flowing through the sheath. For simplicity in relating to probe measurements the formula is derived in terms of the ratio of ground current (J_{gnd}) to ion saturation current (J_{sat}). Also included are terms due to ion charge (Z) and secondary electron emission (δ_e).

The ion current (J_i) through a sheath to a surface is given by the Bohm condition, that is the ions flow in at the speed of sound ($c_s = \sqrt{k_B\left(ZT_e + T_i\right)/m_i}$):

$$J_i = en_{i,se}\sqrt{\frac{k_B\left(ZT_e + T_i\right)}{m_i}}. \tag{99}$$

With $n_{i,se}$ the ion density at the sheath edge, k_B the Boltzmann constant, T_e and T_i the electron and ion temperatures, and m_i the ion mass. This is simply related to the ion flux through the sheath by:

$$J_i = eZ\Gamma_i \tag{100}$$

The net electron current density to a surface, including secondary electron emission, is given by the forward going Maxwellian flux reduced by the Boltzmann factor:

$$J_e = \frac{1}{4}en_{e,se}\left(1-\delta_e\right)\sqrt{\frac{8k_BT_e}{\pi m_e}}\,e^{eV/k_BT_e}. \tag{101}$$

With $n_{e,se}$ the electron density at the sheath edge, m_e the electron mass, and V the voltage drop of the sheath. The electron current is simply related to the electron flux through the sheath by:

$$J_e = e\Gamma_e \tag{102}$$

Defining the sheath edge as a neutral plasma gives:

$$Zn_{i,se} = n_{e,se}. \tag{103}$$

The total current density ($J(V) = J_i - J_e$) through the sheath as a function of the voltage drop is:

$$J(V) = en_{se}\sqrt{\frac{k_B(ZT_e + T_i)}{m_i}} - \frac{1}{4}en_{se}(1-\delta_e)\sqrt{\frac{8k_BT_e}{\pi m_e}}e^{eV/kT_e}. \quad (104)$$

In ion saturation ($J(V=-\infty) = J_{sat}$) the electron current to the surface becomes zero giving:

$$J_{sat} = en_{se}\sqrt{\frac{k_B(ZT_e + T_i)}{m_i}} \quad (105)$$

Substituting eq. (105) into eq. (104) and rearranging:

$$e^{eV/kT_e} = \sqrt{2\pi\frac{m_e}{m_i}\left(Z + \frac{T_i}{T_e}\right)}\frac{1 - J(V)/J_{sat}}{1-\delta_e}. \quad (106)$$

The ion heat flux to the surface includes terms due to ion flux ($2.5k_BT_i\Gamma_i$, with the 2.5 factor found through kinetic simulations [1]) and ion acceleration through the sheath ($eZV\Gamma_i$):

$$q_{i,surf}(V) = \Gamma_i(2.5k_BT_i + eZV). \quad (107)$$

A Langmuir probe measures the ion saturation current, so relating this to the current:

$$q_{i,surf}(V) = \frac{J_{sat}}{e}\left(2.5k_B\frac{T_i}{Z} + eV\right). \quad (108)$$

Adding in V from eq. (106):

$$q_{i,surf}(V) = \frac{k_BT_eJ_{sat}}{e} \times \left\{2.5\frac{T_i}{ZT_e} + \ln\left[\sqrt{2\pi\frac{m_e}{m_i}\left(Z + \frac{T_i}{T_e}\right)}\frac{1 - J(V)/J_{sat}}{1-\delta_e}\right]\right\}. \quad (109)$$

The electron heat flux is from the flux of plasma electrons through the sheath ($2k_BT_e\Gamma_e$) and ignores the (minimal) energy lost by secondary electrons:

$$q_{e,surf}(V) = \frac{2k_BT_e}{e}\frac{1}{4}n_{se}\sqrt{\frac{8k_BT_e}{\pi m_e}}e^{eV/k_BT_e}. \quad (110)$$

Again, substituting in V from eq. (106):

$$q_{e,surf}(V) = 2\frac{1 - J(V)/J_{sat}}{1-\delta_e}\frac{k_B T_e J_{sat}}{e}. \tag{111}$$

The total heat flux to the surface, adding eq. (109) and eq. (111):

$$\begin{aligned} q_{surf}(V) = \frac{k_B T_e J_{sat}}{e} \times \Bigg\{ & 2.5\frac{T_i}{Z T_e} \\ & + 2\frac{1 - J(V)/J_{sat}}{1-\delta_e} \\ & + \ln\left[\sqrt{2\pi\frac{m_e}{m_i}\left(Z + \frac{T_i}{T_e}\right)}\frac{1 - J(V)/J_{sat}}{1-\delta_e}\right] \Bigg\} \end{aligned} \tag{112}$$

Now, defining the sheath heat flux transmission coefficient as:

$$\gamma = \frac{q_{surf}}{k_B T_e J_{sat}/e}, \tag{113}$$

we find

$$\begin{aligned} \gamma(V) = 2.5\frac{T_i}{Z T_e} & + 2\frac{1 - J(V)/J_{sat}}{1-\delta_e} \\ & + \ln\left[\sqrt{2\pi\frac{m_e}{m_i}\left(Z + \frac{T_i}{T_e}\right)}\frac{1 - J(V)/J_{sat}}{1-\delta_e}\right]. \end{aligned} \tag{114}$$

Finally the sheath heat flux transmission coefficient to a grounded divertor (defined as the current collected by a Langmuir probe at zero bias $J_{gnd} = J(V = 0)$) is given by:

$$\begin{aligned} \gamma = 2.5\frac{T_i}{Z T_e} & + 2\frac{1 - J_{gnd}/J_{sat}}{1-\delta_e} \\ & + \ln\left[\sqrt{2\pi\frac{m_e}{m_i}\left(Z + \frac{T_i}{T_e}\right)}\frac{1 - J_{gnd}/J_{sat}}{1-\delta_e}\right]. \end{aligned} \tag{115}$$

⋆

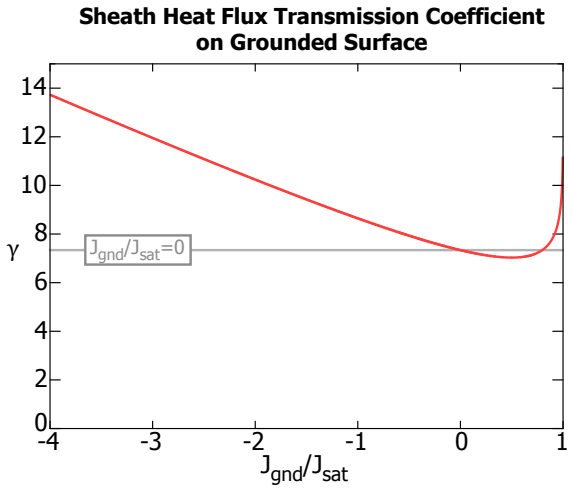

Figure 110: Dependence of sheath heat flux transmission coefficient on the ground current normalized to the ion saturation current.

BIBLIOGRAPHY

[1] P. C. Stangeby. *The Plasma Boundary of Magnetic Fusion Devices*. IoP Publishing, 2000.

COLOPHON

This document was typeset using `classicthesis` developed by André Miede (although aspects were changed to comply with the MIT thesis standards and the author's personal preferences). The style was inspired by Robert Bringhurst's seminal book on typography "*The Elements of Typographic Style*". `classicthesis` is available for both LaTeX and LyX:

http://code.google.com/p/classicthesis/

Final Version as of August 8, 2013 (`classicthesis` version 4.1).

Hermann Zapf's *Palatino* and *Euler* type faces (Type 1 PostScript fonts *URW Palladio L* and *FPL*) are used. The "typewriter" text is typeset in *Bera Mono*, originally developed by Bitstream, Inc. as "Bitstream Vera". (Type 1 PostScript fonts were made available by Malte Rosenau and Ulrich Dirr.)